The Chemical and Physical Impacts of Magma Ocean Solidification: Insights into Lunar Magma Ocean Solidification, Mantle Formation, and Mantle Evolution.

A Dissertation Presented for the

Doctor of Philosophy

Degree

The University of Tennessee, Knoxville

Jesse L. Scholpp

May 2025

Copyright © 2025 by Jesse L. Scholpp

All rights reserved.

DEDICATION

I dedicate this to my wife and my family; I could not have done this without their unwavering support and love. I also dedicate this to my late friend and undergraduate research assistant, Olivia Wilkerson; her endless curiosity, love of geology, and goofy personality was always a welcomed reminder of why I love doing research and advising undergraduate researchers.

ACKNOWLEDGEMENTS

I want to thank my advisor, Nick Dygert, for his support and guidance over the last four and a half years. I am grateful for the opportunity to work with and learn from him. I am also profoundly thankful for his support whenever I presented him with highly ambitious project ideas that required significant effort on his part. I thank my committee, Molly McCanta, Anna Szynkiewicz, and Colin Jackson, for their support during my degree. I would also like to thank those who have mentored me throughout my geoscience journey and are why I am where I am today- Jeffrey Ryan and John Shervais.

I would like to thank those who assisted me with my laboratory work and research- Allan Patchen, Hirochika Sumino, Graham Pearson, Andy Dufrane, Sarah Woodland, Noah Hooper, Olivia Wilkerson, Sabrina Sanders, and Kydin Keylock. I would like to thank the University of Tennessee, the National Science Foundation (NSF), and the National Aeronautics and Space Administration (NASA) for funding and allowing me to conduct my research and follow my curiosity.

I would like to give a special thanks to the International Ocean Discovery Program (IODP) Expedition 391 science team members who helped keep me from going insane during the two-month-long Covid quarantine cruise- Katie Potter, Aaron Avery, John Shervais, Wendy Nelson, Sonia Tikoo-Schantz, Harsha Thoram, Kevin Gaastra, and Mike Widdowson. Without all of you, I would have never made it through the craziness of that expedition.

I would also like to thank all the incredible faculty, staff, and graduate students in the Department of Earth, Environmental, and Planetary Sciences who have supported me over the last four and a half years. To my friends- Stephen Hill, Allison Rogers, John

Fulginiti, Cameron Harris, Emily Roberts, Dian Ji, Micki Recchuiti, Noah Hooper, Olivia Wilkerson, Sabrina Sanders, Rachel Huk, Gabby Boggs, Udit Basu, Nick Brey, Sonja Schmoyer, Justin Hardin, Ben Alexander, Claire Mondro, and Tyler and Nadine Grambling, thank you for your friendship. Whether it was office and lab shenanigans, venting sessions over drinks, or dark humor when nothing was going right, all of you kept me going.

And finally, I am incredibly grateful for all my family's unwavering love and support. Mom and Dad, you always believed in me even and encouraged me when I felt lost and didn't know what I was going to do with my life. I am genuinely grateful for everything you've done for me, and I could never have done this without you. To my sister, Sami, thank you for always being there when I needed you and listening when I needed someone to vent to about my research problems, even if it sounded like gibberish to you. To my wife, Kendall, thank you for being my biggest fan and encouraging me when I felt like I was just wasting my time and money getting this degree. Thank you for financially and emotionally supporting me over the last three years. Thank you for taking care of me when I was working 14-hour days and was too exhausted to take care of myself. I would have never survived this process without you.

ABSTRACT

Solidification of a lunar magma ocean (LMO) after a giant planetary collision event formed the Moon's gravitationally unstable juvenile mantle. Hybridization of the lunar mantle during the overturn of late-crystallized Ti- rich ilmenite-bearing cumulates (IBC) in the lunar interior is called upon to explain the variable Ti and REE abundances of melts. We experimentally investigated hybridization reactions in experiments that juxtapose an IBC glass against presynthesized dunite in a reaction couple at temperatures of 1100-1300 $^{\circ}$C and pressures of 0.5-2.02 GPa for 0.33-31.66 hours. We then model chemical fractionation during LMO solidification, mantle hybridization, and partial melting of hybridized and unhybridized cumulates to evaluate the formation of lunar basalts, picritic glasses, and crustal cumulates. Subsolidus experiments produce garnet in the IBC at 2 GPa. Supersolidus experiments exhibit dissolution of olivine material into the IBC melt and the formation of clinopyroxene at the IBC melt-dunite interface. Simple numerical simulations suggest that mechanical mixing may be required in addition to dissolution-precipitation reactions to produce volumetrically significant hybridized mantle sources capable of producing lunar melts over geologically relevant timescales. Geochemical models indicate that plagioclase floatation efficiency during LMO solidification and crustal formation must be >90% to explain the negative Eu anomaly demonstrated by lunar melts. Melting models demonstrate that unhybridized cumulates could produce low-Ti melts, and hybridized garnet-free sources can generate many intermediate to high-Ti melts. The Heavy Rare Earth Element depleted compositions of some high-Ti lunar melts require a ~0.25-5% garnet component in the downwelling IBC or hybridized sources. The need for garnet combined with isotope ratios of high-Ti lunar

basalts indicates the cumulate overturn is likely required. Geochemical models of LMO solidification also demonstrate that the Moon likely contains <86% of the Earth's K budget. This K depletion significantly decreases radiogenic heat production within the Moon since K is the primary heat-producing element (HPE) in most planets. Geochemical models also demonstrate that >90% of the lunar HPE budget should initially be concentrated in the lunar crust and upper mantle cumulates following LMO solidification.

TABLE OF CONTENTS

INTRODUCTION AND LITERATURE REVIEW 1

Lunar Magma Ocean Formation and Solidification 2

LMO Solidification Products and Their Physical Effects 3

References 6

CHAPTER 1 Experimental Insights into the Mineralogy and Melt-Rock Reactions Produced by Lunar Cumulate Mantle Overturn 12

Abstract 13

1.1 Introduction 14

1.2 Methods 18

1.2.1 Starting Materials 18

1.2.2 Experiments 19

1.2.3 Analysis of Run Products 21

1.3 Results 25

1.3.1 Near Solidus Experiments 26

1.3.1.1 Products and Growth Textures 26

1.3.1.2 Phase Chemistry 28

1.3.2 Supersolidus Experiments 34

1.3.2.1 Group A Products and Growth Textures 34

1.3.2.2 Group A Mineral and Melt Chemistry 36

1.3.2.3 Group B Products and Growth Textures 37

1.3.2.4 Group B Mineral and Melt Chemistry 39

1.3.3 Step-Cooled Experiment 39

1.3.3.1 Products and Growth Textures 39
1.3.3.2 Mineral and Melt Chemistry 40
1.4 Discussion 42
1.4.1 Dissolution-precipitation reactions and IBC liquid crystallization 42
1.4.1.1 Dunite Assimilation 42
1.4.1.2 Crystallization in the IBC melt 45
1.4.2 Dissolution, Diffusion, and Advection 46
1.4.2.1 Solid-State Diffusion 46
1.4.2.2 Dunite Dissolution Rates, and Effects of Dunite Dissolution on IBC Liquid 49
1.4.2.3 Vein Formation 56
1.4.3 Phase Equilibria 56
1.4.3.1 Fe-Ti Oxides 58
1.4.3.2 Garnet 59
1.5 Implications for the Lunar Mantle 60
1.5.1 Metamorphic Reactions 61
1.5.2 Formation of Hybridized Mantle Sources 62
1.6 Summary and Conclusions 67
1.7 Acknowledgements 68
References 69
Appendix A 90

CHAPTER 2 Trace Element and Isotopic Evolution of the Lunar Interior During Magma Ocean Solidification, Cumulate Overturn, and Subsequent Melting: Insights into Lunar Melt Sources 105
Abstract 106
2.1 Introduction 108
2.2 Geochemical Modeling 114
2.2.1 Model Assumptions: Lunar Bulk Composition 114
2.2.2 Lunar Magma Ocean Solidification Models 115
2.2.3 LMO Solidification Products 125
2.2.4 Eu anomalies of LMO cumulates and cumulate melts 132
2.2.4.1 Residual LMO liquids and their relation to “KREEP” 133
2.2.5 Partial Melting Models 134
2.2.6 Partial Melting of Initial LMO Cumulates 136
2.3 Mantle Hybridization After Cumulate Mantle Overturn 143
2.3.1 Mineralogy of the Downwelling IBC Material 144
2.3.2 Partial Melting of Downwelling IBC 146
2.3.3 LMO Cumulate Hybridization 151
2.3.4 Partial Melting of Hybridized Mantle Sources 159
2.3.5 Effect of Garnet on Hybridized Source Melt Chemistry 159
2.3.5.1 Mechanical Mixing with Solid IBC Material 159
2.3.5.2 Garnet-Free IBC 163
2.3.5.3 Garnet-Bearing IBC 166

2.3.5.4 Summary of Partial Melting Models Assuming No Late Cumulate Mixing (Scenarios #1-#5) 167
2.3.6 Early Mixing During LMO Solidification 170
2.3.6.1 Partial Melting of a Thickened IBC 173
2.3.6.2 Partial Melting Source Hybridized by a Thickened IBC 173
2.3.6.3 Summary of Partial Melting Models Assuming Late Cumulate Mixing Occurred (Scenarios #6-#7) 174
2.4 Parameters That Could Affect Model Results 175
2.4.1 LMO Cumulate Mineralogy 175
2.5 Garnet in the Lunar Mantle 178
2.5.1 Garnet in a primitive lunar mantle reservoir? 178
2.5.2 Garnet's Relationship with Cumulate Overturn 180
2.6 Effect of Cumulate Overturn Sm-Nd and Lu-Hf Isotopes 181
2.7 Conclusions 185
2.8 Acknowledgements 187
2.9 Open Research Statement 187
References 188
Appendix B 207
CHAPTER 3 An Evaluation of the Lunar K/Th Ratio Using Geochemical Modeling: Implications for the Moon's Thermal Evolution 237
Abstract 238
3.1 Introduction 238

3.2 Geochemical Modeling 242
3.2.1 Modeling Parameters for LMO Solidification 242
3.2.2 Radiogenic Element Partitioning 244
3.3 Modeled HPE Distributions and Ratios 244
3.3.1 Lunar HPE Distribution 244
3.3.2 Constraining The Lunar K/Th Ratio 249
3.4 Thermal Evolution Models 254
3.4.1 Thermal Diffusion and Heat Production Model 254
3.4.2 Density, Conductivity, and Heat Capacity Assumptions 258
3.4.3 P-T Conditions of the Lunar Mantle 261
3.4.4 HPE and Thermal Distributions Before and After Overturn 261
3.5 Thermal Modeling Results 263
3.6 Mechanisms That Could Prolong Lunar Thermal Evolution 269
3.7 Conclusions 271
References 273
Appendix C 291
CONCLUSIONS 314
Lunar Mantle Hybridization During Cumulate Overturn 314
Magma Ocean Solidification And The Formation Of Lunar Basalt Sources 315
Concentration And Distribution Of Lunar Heat Producing Elements 316
VITA 318

LIST OF TABLES

Table 1.1. Starting material compositions (wt%) measured by electron microprobe from this study compared with ilmenite-bearing cumulate compositions from previous studies. 20

Table 1.2. Starting materials and run conditions. 22

Table 1.3. Interface dissolution and exchange measurements from melt-rock reaction experiments. 29

Table 1.4. Pre-reaction IBC composition compared with post-reaction melt compositions averaged from data collected across the entire IBC half of the diffusion couple..... 30

Table 1.5. Effective binary diffusion coefficients (EBDC) of MgO, FeO, MnO, Al_2O_3, TiO_2, and CaO for dunite dissolution in IBC melt at 1200ºC, 0.55 GPa. 51

Table 2.1. Phase proportions in LMO cumulates based on findings from Charlier et al. (2018), assuming no plagioclase or quartz floatation. 117

Table 2.2. Assumed LMO starting composition and mineral-melt partition coefficients for magma ocean solidification models. 119

Table 2.3. Average REE+Hf abundances and ratios for modeled LMO cumulate layers and IBC material assuming 90% plagioclase floatation efficiency. 127

Table 2.4. Model assumptions for mantle hybridization and partial melting scenarios and associated figures. 137

Table 2.5. Estimated major element compositions of IBC material for plagioclase floatation efficiencies of 80%, 90%, and 98%. 145

Table 2.6. Mineral-melt partition coefficients for partial melting calculations. 152

Table 2.7. Phase proportions of hybridized mantle sources in melting models. 160

Table 3.1. Comparison of assumed present day bulk moon HPE concentrations from previous studies. 240

Table 3.2. Phase proportions in LMO cumulates based on results from Charlier et al. (2018), assuming 95% plagioclase and 100% quartz floatation efficiency. 243

Table 3.3. Mineral-melt partition coefficients for Th, U, and K used in magma ocean solidification models. 245

Table 3.4. Atomic Mass (u), Half-life ($T_{1/2}$), Present-Day Fractional Abundance (X_{iso}), Heat-Effective Decay Energy per Atom (E_H), and Specific Heat Production (H) of ^{40}K, ^{232}Th, ^{235}U, and ^{238}U from Ruedas (2017). 259

Table 3.5. Parameter assumptions used in thermal evolution calculations in this study. 260

LIST OF FIGURES

Figure 1.1. Schematic illustrating assemblies used in near solidus and melt-rock reaction experiments utilized in this work. IBC refers to half of the reaction couple with the ilmenite bearing cumulate composition. 24

Figure 1.2. Representative BSE images and elemental maps highlighting minerals and reactions produced in near solidus experiments MRx#1, MRx#3, and MRx#8. 27

Figure 1.3. Pyroxene compositions from melt-rock reaction experiments projected as components..... 32

Figure 1.4. Garnet compositions from near solidus experiments conducted in this study compared to terrestrial and lunar relevant compositions..... 33

Figure 1.5. Representative BSE images and elemental maps highlighting minerals and reaction features in supersolidus experiments MRx#10 and MRx#12..... 38

Figure 1.6. Representative BSE image and elemental map highlighting minerals and reaction features produced in step-cooled supersolidus experiment MRx#13..... 41

Figure 1.7. Experimental glasses plotted in relation to olivine-wollastonite-quartz basalt ternary diagrams from Longhi (1991). 44

Figure 1.8. Fe-Mg exchange profiles across the IBC-dunite interface from near solidus experiments with modeled diffusion curves..... 47

Figure 1.9. Elemental concentration profiles in the IBC melt from the reaction interface (i.e., 0 μm) to the top of the experiment (or top of the glass-dominated region of the experiment). Modeled diffusion profiles for MRx#9 with respect to (a) MgO, (b) FeO, (c) MnO, (d) Al_2O_3, (e) TiO_2, and (f) CaO mol% are represented by the dashed line. 53

Figure 1.10. Dunite dissolution rates plotted against the square root of time..... 55

Figure 1.11. Ilmenite bearing cumulate phase diagram based on the observations from this work and previous experimental studies testing IBC and Ti-rich lunar relevant compositions (Haggerty and Lindsley, 1970; Friel et al., 1977; Wyatt, 1977; Van Orman and Grove, 2000; Xirouchakis et al., 2002; Mallik et al., 2019)..... 57

Figure 1.12. Comparison of glasses from melt-rock reaction experiments to lunar picritic glasses (TiO_2 mol% vs Mg# (a.) and Al_2O_3 mol% vs Mg#(b.)). 64

Figure 2.1. Schematic figure of lunar evolution up to the point of cumulate overturn and mantle hybridization..... 110

Figure 2.2. Trace element comparison between evolving magma ocean cumulates, residual magma ocean liquids, lunar picritic glasses, and lunar KREEP basalts.... 130

Figure 2.3. Evolution of LMO residual melt and cumulates during fractional crystallization of the LMO compared to picritic lunar glass and basalt compositions. 131

Figure 2.4. Models for partial melting of primary (i.e., unhybridized) LMO cumulates assuming 90% plagioclase floatation (Reference Scenario 0). 135

Figure 2.5. Models demonstrating the effect of plagioclase floatation and fO_2 on Eu anomaly (Eu/Eu*) formation in partial melts of LMO cumulates. 142

Figure 2.6. IBC mineralogy at 1150°C and 2 GPa calculated using thermodynamic models assuming plagioclase floatation efficiencies of 80-98%..... 147

Figure 2.7. Models demonstrating the effect of plagioclase floatation and fO_2 on Eu anomaly (Eu/Eu*) formation in partial melts of garnet-free IBC material and garnet-free hybridized sources. 150

Figure 2.8. Partial melts of garnet-free and garnet-bearing hybridized sources, assuming that during hybridization, the IBC material was below its solidus and was mechanically mixed into EMOC. 161

Figure 2.9. Partial melting models for garnet-free and garnet-bearing sources that were hybridized by partial melts from downwelling garnet-free IBC prior to subsequent melting. 164

Figure 2.10. Partial melting models for garnet-free hybridized sources that were hybridized by partial melts from a garnet-bearing IBC prior to subsequent melting. 168

Figure 2.11. Partial melting models for a hybridized source and IBC, assuming a thickened layer of IBC material did not experience melting during the hybridization process (i.e., solid-solid mechanical mixing) prior to subsequent melting. 171

Figure 2.12. Comparison of measured and modeled Lu-Hf and Sm-Nd isotopic compositions for lunar mantle sources. 183

Figure 3.1. Distribution of Heat Producing Elements (HPE) and heat production potential following LMO solidification if the LMO extends to the lunar core-mantle boundary. 248

Figure 3.2. Comparison of the Th and K abundances observed in lunar samples with geochemical models for LMO solidification and mantle cumulate partial melting. 251

Figure 3.3. Pre- and post-overturn HPE (a) and temperature (b) distributions tested in thermal evolution models from this study. 262

Figure 3.4. Post 4.35 Ga thermal evolution of the upper (top row), middle (middle row), and lower lunar mantle (bottom row) for scenarios with and without lunar cumulate overturn (left and right columns)..... 264

LIST OF ATTACHMENTS

Attachment Ch1SupportingTables.xlsx contains supplementary information on the major element compositions of minerals and melt from high pressure experiments discussed in Chapter 1.

INTRODUCTION AND LITERATURE REVIEW

All large rocky planets within our solar system are believed to experience a magma ocean stage during differentiation. As protoplanets accrete material and grow, the combined heat of accretion (heat released by many high energy impacts) and radiogenic heating related to the decay of short-lived radionuclides present during the early solar system, e.g., ^{26}Al) partially melts the precursor material within planetary bodies. If the planetesimals do not grow fast enough, there is not enough accretionary heat generated or insulating material to retain the radiogenic heat that is produced to initiate partial melting and magma ocean formation. This results in the formation of undifferentiated to partially differentiated chondritic dwarf planets and is the reason why chondritic meteorites that exhibit variable degrees of thermal alteration exist. Protoplanets that accrete quickly and reach the size of Vesta (diameter of ~500 km) retain a significant portion of their accretionary and radiogenic heat resulting in partial melting and eventual magma ocean generation (e.g., Urey, 1955; Fish et al., 1960; Lee et al., 1976; LaTourrette and Wasserburg, 1998; Elkins-Tanton, 2012). Depending on the size of the protoplanet, the magma ocean may be a relatively thin and short-lived lens of melt or a deep molten layer that spans a significant portion of the body's interior and solidifies over millions of years (Mars and Mercury sized bodies or larger). The solidification of these deep magma oceans strongly influences the distribution of elements throughout planetary interiors and further influences post-magma ocean mantle dynamics.

While this planetary differentiation process is believed to occur within large rocky bodies throughout the solar systems, our inability to easily access such bodies makes it

difficult test and refine models of magma ocean solidification and post-solidification mantle evolution. In addition, the active tectonic environment on Earth (i.e., subducting plates, mountain build collisions, and rifting continents) results in significant geochemical overprinting, erasing Earth's magma ocean related geochemical information. Fortunately, the Moon also had a deep magma ocean thought to extended throughout much of the lunar interior. As the Moon lacks evidence of active tectonic processes, chemical signatures related to magma ocean solidification are believed to be retained within the recovered Apollo sample suite and collected lunar meteorites.

This work is composed of three chapters that explore early lunar evolution and its chemical effects on the lunar mantle. Three chapters describe experimental and model-based approaches to improve our understanding of lunar melt basalt chemistry, lunar mantle chemistry, and post-magma ocean mantle processes.

Lunar Magma Ocean Formation and Solidification

The lunar magma ocean (LMO) is believed to have formed after an impact between the proto-Earth and a large (perhaps Mars sized) planetary body, resulting in the ejection of rocky material and eventual accretion of the Moon (Canup, 2004, 2012; Elkins-Tanton and Hager, 2005; Hiesinger and Head, 2006; Elkins-Tanton, 2012; Young et al., 2016; Thiemens et al., 2019; Cano et al., 2020). It is still debated when exactly this impact occurred; however, radiometric age estimates suggest that the impact occurred after 4.5 Gyr and before 4.36 Gyr (Kruijer and Kleine, 2017; Borg et al., 2022; Borg and Carlson, 2023 and references therein). This provides a ~140 Myr range in which the Moon could have formed and suggests the Moon formed tens of millions of years after

the other planetary bodies (e.g., 4.56-4.54 Gyr: Kleine et al., 2002; Schoenberg et al., 2002; Yin et al., 2002; Kleine et al., 2004; Markowski et al., 2007). Given the short half-life ^{26}Al (~0.7 Myr), the giant impact and accretionary heating are the primary thermal contributors to LMO formation (Canup, 2004, 2008).

The estimated depth of the LMO varies significantly depending on the constraints considered (e.g., 200-1000 km; Solomon and Longhi, 1977; Elkins-Tanton et al., 2011); however, recent work using gravity and experimental petrology-based crustal thickness estimates indicate that the LMO was likely ≥600 km (Charlier et al., 2018). Magma ocean cooling models indicate that ~80% of the LMO would solidify within ~1000 yr after accretion (Elkins-Tanton et al. 2011), while the last 20% of the LMO could take 100-400 myr to solidify completely due to the insulating effects of the plagioclase floatation crust and radiogenic heating via U, Th and K decay (Solomon and Longhi 1977; Maurice et al. 2020, 2024).

LMO Solidification Products and Their Physical Effects

Mineral stratification in the post-LMO cumulate mantle is controlled by the phase saturation sequence and phase density, if the LMO fractionally solidified. Lunar magma ocean crystallization experiments show consistent trends with olivine as the dominant crystallizing phase during early magma ocean solidification (Elardo et al. 2011; Elkins-Tanton et al. 2011; Lin et al. 2017; Charlier et al. 2018; Rapp and Draper 2018). This is followed by olivine and orthopyroxene as the SiO_2 concentration in the melt increases (Elkins-Tanton et al. 2011; Charlier et al. 2018). After 60-70% magma ocean crystallization, high-Ca pyroxenes (i.e., pigeonite and augite) and plagioclase (i.e.,

anorthite) become saturated. Since plagioclase is less dense than the melt from which it crystallized, it will float to the top of the LMO and form an anorthosite crust (Wood et al. 1970; Walker and Hays 1977; Dygert et al. 2017). Ilmenite ($FeTiO_3$) and possibly other Fe-Ti oxides (e.g., Ulvöspinel ($TiFe_2O_4$), Armalcolite ($(Mg,Fe)Ti_2O_5$)) begin to crystallize at 90-95% magma ocean solidification and likely continue to precipitate until the end of magma ocean solidification (Elkins-Tanton et al. 2011; Lin et al. 2017; Charlier et al. 2018).

After LMO solidification, the Moon is thought to have had an olivine-rich dunite surrounding the core, harzburgite above the dunite layer, a clinopyroxene- and ilmenite-bearing cumulate (IBC) layer atop the harzburgite, and an incompatible element enriched residual melt region or cumulate near or above the IBC layer, all beneath an anorthosite crust (Snyder et al. 1992; Hess and Parmentier 1995; Shearer et al., 2006; Elkins-Tanton et al. 2011, 2012; Dygert et al. 2017, Rapp and Draper 2018). The late (shallow) precipitation of dense IBC produces a gravitationally unstable lunar mantle stratigraphy, with less dense ilmenite-free cumulates beneath the dense IBC (Snyder et al. 1992; Hess and Parmentier 1995; Elkins-Tanton et al. 2011; Zhang et al. 2017; Li et al. 2019). Recent studies indicate that the gravitationally unstable stratigraphy in the lunar mantle would have resulted in cumulate overturn (Zhang et al. 2017; Li et al. 2019; Maurice et al. 2024). In this scenario, dense shallow cumulates flow into the deep lunar interior as viscous solids, perhaps after progressive thickening of the IBC layer by downwelling of small-scale IBC instabilities into the underlying mantle (Hess and Parmentier, 1995; Li et al., 2019). The overturn of IBC into the lunar mantle would juxtapose sinking IBC

against deep mafic mantle cumulates, where mechanical mixing or chemical reactions could generate hybridized mantle sources.

References

Borg, L.E., Brennecka, G.A., and Kruijer, T.S., 2022, The origin of volatile elements in the Earth–Moon system: Proceedings of the National Academy of Sciences, v. 119, p. e2115726119, doi:10.1073/pnas.2115726119.

Borg, L.E., and Carlson, R.W., 2023, The Evolving Chronology of Moon Formation: Annual Review of Earth and Planetary Sciences, v. 51, p. 25–52, doi:10.1146/annurev-earth-031621-060538.

Cano, E.J., Sharp, Z.D., and Shearer, C.K., 2020, Distinct oxygen isotope compositions of the Earth and Moon: Nature Geoscience, v. 13, p. 270–274, doi:10.1038/s41561-020-0550-0.

Canup, R.M., 2008, Accretion of the Earth: Philosophical Transactions of the Royal Society A: Mathematical, Physical and Engineering Sciences, v. 366, p. 4061–4075, doi:10.1098/rsta.2008.0101.

Canup, R.M., 2012, Forming a Moon with an Earth-like Composition via a Giant Impact: Science, v. 338, p. 1052, doi:10.1126/science.1226073.

Canup, R.M., 2004, Origin of the terrestrial planets and the Earth-Moon system: Physics Today, v. 57, p. 56–62.

Charlier, B., Grove, T.L., Namur, O., and Holtz, F., 2018, Crystallization of the lunar magma ocean and the primordial mantle-crust differentiation of the Moon: Geochimica et Cosmochimica Acta, v. 234, p. 50–69, doi:10.1016/j.gca.2018.05.006.

Dygert, N., Lin, J.-F., Marshall, E.W., Kono, Y., and Gardner, J.E., 2017, A Low Viscosity Lunar Magma Ocean Forms a Stratified Anorthitic Flotation Crust With Mafic Poor and Rich Units: Geophysical Research Letters, v. 44, p. 11,282-11,291, doi:10.1002/2017GL075703.

Elardo, S.M., Draper, D.S., and Shearer, C.K., 2011, Lunar Magma Ocean crystallization revisited: Bulk composition, early cumulate mineralogy, and the source regions of the highlands Mg-suite: Geochimica et Cosmochimica Acta, v. 75, p. 3024–3045, doi:10.1016/j.gca.2011.02.033.

Elkins-Tanton, L.T., 2012, Magma Oceans in the Inner Solar System: Annual Review of Earth and Planetary Sciences, v. 40, p. 113–139, doi:10.1146/annurev-earth-042711-105503.

Elkins-Tanton, L.T., Burgess, S., and Yin, Q.-Z., 2011, The lunar magma ocean: Reconciling the solidification process with lunar petrology and geochronology: Earth and Planetary Science Letters, v. 304, p. 326–336, doi:10.1016/j.epsl.2011.02.004.

Elkins-Tanton, L.T., and Hager, B.H., 2005, Giant meteoroid impacts can cause volcanism: Earth and Planetary Science Letters, v. 239, p. 219–232, doi:10.1016/j.epsl.2005.07.029.

Fish, R.A., Goles, G.G., and Anders, E., 1960, The Record in the Meteorites. III. on the Development of Meteorites in Asteroidal Bodies.: \apj, v. 132, p. 243, doi:10.1086/146918.

Hess, P.C., and Parmentier, E.M., 1995, A model for the thermal and chemical evolution of the Moon's interior: implications for the onset of mare volcanism: Earth and Planetary Science Letters, v. 134, p. 501–514, doi:10.1016/0012-821X(95)00138-3.

Hiesinger, H., and Head, J.W., III, 2006, New Views of Lunar Geoscience: An Introduction and Overview: Reviews in Mineralogy and Geochemistry, v. 60, p. 1–81, doi:10.2138/rmg.2006.60.1.

Kleine, T., Mezger, K., Münker, C., Palme, H., and Bischoff, A., 2004, 182Hf-182W isotope systematics of chondrites, eucrites, and martian meteorites: Chronology of core formation and early mantle differentiation in Vesta and Mars1 1Associate editor: R. J. Walker: Geochimica et Cosmochimica Acta, v. 68, p. 2935–2946, doi:10.1016/j.gca.2004.01.009.

Kleine, T., Münker, C., Mezger, K., and Palme, H., 2002, Rapid accretion and early core formation on asteroids and the terrestrial planets from Hf–W chronometry: Nature, v. 418, p. 952–955, doi:10.1038/nature00982.

Kruijer, T.S., and Kleine, T., 2017, Tungsten isotopes and the origin of the Moon: Earth and Planetary Science Letters, v. 475, p. 15–24, doi:10.1016/j.epsl.2017.07.021.

LaTourrette, T., and Wasserburg, G.J., 1998, Mg diffusion in anorthite: implications for the formation of early solar system planetesimals: Earth and Planetary Science Letters, v. 158, p. 91–108, doi:10.1016/S0012-821X(98)00048-X.

Lee, T., Papanastassiou, D.A., and Wasserburg, G.J., 1976, Demonstration of ^{26}Mg excess in Allende and evidence for ^{26}Al: Geophysical Research Letters, v. 3, p. 41–44, doi:10.1029/GL003i001p00041.

Li, H., Zhang, N., Liang, Y., Wu, B., Dygert, N.J., Huang, J., and Parmentier, E.M., 2019, Lunar Cumulate Mantle Overturn: A Model Constrained by Ilmenite Rheology: Journal of Geophysical Research: Planets, v. 124, p. 1357–1378, doi:10.1029/2018JE005905.

Lin, Y., Tronche, E.J., Steenstra, E.S., and van Westrenen, W., 2017, Evidence for an early wet Moon from experimental crystallization of the lunar magma ocean: Nature Geoscience, v. 10, p. 14–18, doi:10.1038/ngeo2845.

Markowski, A., Quitté, G., Kleine, T., Halliday, A.N., Bizzarro, M., and Irving, A.J., 2007, Hafnium–tungsten chronometry of angrites and the earliest evolution of planetary objects: Earth and Planetary Science Letters, v. 262, p. 214–229, doi:10.1016/j.epsl.2007.07.035.

Maurice, M., Tosi, N., and Hüttig, C., 2024, Small-Scale Overturn of High-Ti Cumulates Promoted by the Long Lifetime of the Lunar Magma Ocean: Journal of Geophysical Research: Planets, v. 129, p. e2023JE008060, doi:10.1029/2023JE008060.

Maurice, M., Tosi, N., Schwinger, S., Breuer, D., and Kleine, T., 2020, A long-lived magma ocean on a young Moon: Science Advances, v. 6, doi:10.1126/sciadv.aba8949.

Rapp, J.F., and Draper, D.S., 2018, Fractional crystallization of the lunar magma ocean: Updating the dominant paradigm: Meteoritics & Planetary Science, v. 53, p. 1432–1455, doi:10.1111/maps.13086.

Schoenberg, R., Kamber, B.S., Collerson, K.D., and Eugster, O., 2002, New W-isotope evidence for rapid terrestrial accretion and very early core formation: Geochimica et Cosmochimica Acta, v. 66, p. 3151–3160, doi:10.1016/S0016-7037(02)00911-0.

Shearer, C.K. et al., 2006, Thermal and Magmatic Evolution of the Moon: Reviews in Mineralogy and Geochemistry, v. 60, p. 365–518, doi:10.2138/rmg.2006.60.4.

Snyder, G.A., Taylor, L.A., and Neal, C.R., 1992, Combined equilibrium and fractional crystallization of a magma ocean and formation of the upper mantle of the Moon, *in* Lunar and Planetary Science Conference, v. 23.

Solomon, S.C., and Longhi, J., 1977, Magma oceanography. I-Thermal evolution, *in* Lunar and planetary science conference proceedings, v. 8, p. 583–599.

Thiemens, M.M., Sprung, P., Fonseca, R.O.C., Leitzke, F.P., and Münker, C., 2019, Early Moon formation inferred from hafnium–tungsten systematics: Nature Geoscience, v. 12, p. 696–700, doi:10.1038/s41561-019-0398-3.

Urey, H.C., 1955, The cosmic abundances of potassium, uranium, and thorium and the heat balances of the earth, the moon, and mars*: Proceedings of the National Academy of Sciences, v. 41, p. 127–144, doi:10.1073/pnas.41.3.127.

Walker, D., and Hays, J.F., 1977, Plagioclase flotation and lunar crust formation: Geology, v. 5, p. 425–428, doi:10.1130/0091-7613(1977)5<425:PFALCF>2.0.CO;2.

Wood, J.A., Dickey Jr, J.S., Marvin, U.B., and Powell, B.N., 1970, Lunar anorthosites and a geophysical model of the moon: Geochimica et Cosmochimica Acta Supplement, v. 1, p. 965.

Yin, Q., Jacobsen, S.B., Yamashita, K., Blichert-Toft, J., Télouk, P., and Albarède, F., 2002, A short timescale for terrestrial planet formation from Hf–W chronometry of meteorites: Nature, v. 418, p. 949–952, doi:10.1038/nature00995.

Young, E.D., Kohl, I.E., Warren, P.H., Rubie, D.C., Jacobson, S.A., and Morbidelli, A., 2016, Oxygen isotopic evidence for vigorous mixing during the Moon-forming giant impact: Science, v. 351, p. 493, doi:10.1126/science.aad0525.

Zhang, N., Dygert, N., Liang, Y., and Parmentier, E.M., 2017, The effect of ilmenite viscosity on the dynamics and evolution of an overturned lunar cumulate mantle: Geophysical Research Letters, v. 44, p. 6543–6552, doi:10.1002/2017GL073702.

CHAPTER 1 EXPERIMENTAL INSIGHTS INTO THE MINERALOGY AND MELT-ROCK REACTIONS PRODUCED BY LUNAR CUMULATE MANTLE OVERTURN

A version of this Chapter was originally published by Jesse L. Scholpp and Nicholas Dygert:

Scholpp, J.L., and Dygert, N., 2024, Experimental insights into the mineralogy and melt-rock reactions produced by lunar cumulate mantle overturn: *Contributions to Mineralogy and Petrology, v. 179, p. 58,* doi:10.1007/s00410-024-02134-z.

Abstract

Hybridization of the lunar mantle during the overturn (sinking) of Fe- and Ti-rich ilmenite-bearing clinopyroxenite cumulates (IBC) in the lunar interior is called upon to explain the high TiO_2 abundances of lunar basalts. Chemical reactions that occur after juxtaposition of IBC and mantle peridotite are poorly constrained. We experimentally investigated these reactions in experiments that adjoin an IBC glass against presynthesized dunite in a reaction couple at temperatures of 1100-1300 $^{\circ}$C and pressures of 0.5-2.02 GPa for 0.33-31.66 hr. These conditions produced experiments near and well above the solidus temperature of the IBC. Near solidus experiments produce garnet in the IBC at 2 GPa. Supersolidus experiments exhibit dissolution of olivine material into the IBC melt and the formation of clinopyroxene at the IBC melt-dunite interface. Dunite dissolution is attributed to the olivine undersaturated composition of the IBC melt. In both near- and supersolidus experiments, compositional variations produced by solid-state diffusion across the IBC melt-dunite interface are observed. When pressure increases, temperature decreases, or IBC melts become closer to olivine saturation, dissolution slows, and the effects of solid-state diffusion in the dunite become more evident. Similar chemical exchange reactions would occur in the lunar mantle as

downwelling IBC and lunar peridotites are juxtaposed by cumulate overturn. Hybridized lunar mantle sources are expected to contain 47-84% normative peridotite and 16-53% IBC. Simple numerical simulations suggest that in addition to dissolution-precipitation reactions, mechanical mixing may be required to produce volumetrically significant hybridized mantle sources over geologically-relevant timescales.

1.1 Introduction

The origin and formation mechanisms of lunar mare basalt and picritic glass mantle sources have been debated since analysis of Apollo returned samples revealed that the basalts exhibit variable TiO_2 and REE concentrations with a wide range of Mg#s (Mg# = (molar Mg/(Mg+Fe))x100) (Delano, 1986; Haskin and Warren, 1991; Shearer et al., 1991; Shearer and Papike, 1993; Papike et al., 1998; Neal, 2001; Shearer et al., 2015). This chemical variation is attributed to the chemical diversity of lunar mantle sources (e.g., Lucey et al., 1998; Giguere et al., 2000; Shearer et al., 2015). Lunar mantle sources may have formed after solidification of a lunar magma ocean (LMO), which would produce layers of mafic cumulates (olivine and then olivine and orthopyroxene) beneath clinopyroxene and ilmenite-bearing cumulates of more evolved residual magma ocean liquids. Despite the mineralogical diversity of these LMO cumulate layers, they individually cannot explain the compositions of many mare basalt sources (Snyder et al., 1992; Elardo et al., 2011; Elkins-Tanton et al., 2011; Lin et al., 2017; Charlier et al., 2018). Thus, a post-LMO solidification mantle hybridization mechanism is invoked to effectively mix shallow and deep magma ocean cumulates to account for the mare basalt and picritic glass chemical compositions (Hess and Parmentier, 1995; Singletary and

Grove, 2008; Thacker et al., 2009; Yao and Liang, 2012; Mallik et al., 2019). This work explores processes that control mantle hybridization inferred to produce lunar basalt sources.

Magma ocean crystallization experiments testing a bulk Moon with an LPUM-like composition show consistent trends during magma ocean solidification with olivine as the initial crystallizing phase (Elardo et al., 2011; Elkins-Tanton et al., 2011; Lin et al., 2017; Charlier et al., 2018; Rapp and Draper, 2018). This is followed by olivine (Ol) and orthopyroxene (Opx) as the SiO_2 concentration in the melt increases (Elkins-Tanton et al., 2011; Charlier et al., 2018). At 60-70% crystallization of the magma ocean, high-Ca pyroxene (i.e., pigeonite and augite) and plagioclase (i.e., anorthite) become saturated. Since plagioclase is less dense than the melt from which it crystallized, it will float to the top of the LMO and form an anorthosite crust (Wood et al., 1970; Walker and Hays, 1977; Dygert et al., 2017). Ilmenite ($FeTiO_3$) and possibly other Fe-Ti oxides (e.g., Ulvöspinel ($TiFe_2O_4$), Armalcolite ($(Mg,Fe)Ti_2O_5$)) begin to crystallize at 90-95% magma ocean solidification and likely continue to precipitate until the end of magma ocean solidification (Elkins-Tanton et al., 2011; Lin et al., 2017; Charlier et al., 2018). Although high-pressure crystallization experiments with TWM-like starting compositions have produced garnet as an LMO cumulate (Elardo et al., 2011; Jing et al., 2022, Kraettli et al., 2022), garnet has not been observed in crystallization experiments assuming an LPUM-like bulk Moon composition regardless of the pressure. Thus, if we assume the LMO had an LPUM-like composition, garnet is likely to have been absent from the initial magma ocean cumulates.

Mineral stratification in the post-LMO cumulate mantle is controlled by the phase saturation sequence and phase density due to fractional crystallization of the solidifying LMO. After LMO solidification, the Moon is thought to have had an olivine-rich dunite surrounding the core, harzburgite above the dunite layer, a clinopyroxene- (Cpx) and ilmenite-bearing cumulate (IBC) atop the harzburgite, and an incompatible element enriched (i.e., KREEP- Potassium, Rare Earth Element, and Phosphorous) residual melt region or cumulate near or above the IBC layer, all beneath an anorthosite crust (Snyder et al., 1992; Hess and Parmentier, 1995; Elkins-Tanton et al., 2011, 2012; Dygert et al., 2017, Rapp and Draper, 2018). The late, shallow precipitation of dense IBC produces a gravitationally unstable lunar mantle stratigraphy, with less dense ilmenite-free cumulates beneath the dense IBC (for reference, ilmenite is ~4720 kg/m^3, magnesian olivine is ~3400 kg/m^3, magnesian orthopyroxene is ~3300 kg/m^3 at atmospheric pressure) (Snyder et al., 1992; Hess and Parmentier, 1995; Elkins-Tanton et al., 2011; Zhang et al., 2017; Li et al., 2019). Elkins-Tanton et al. (2002) argue the overturn of solidified IBC is unlikely given the viscosities and temperatures of mantle cumulates, and other studies argued it might be inefficient owing to the IBC viscosity (Zhao et al., 2019), but recent studies that account for the low viscosity of ilmenite relative to lunar mantle silicates (Dygert et al., 2016; Tokle et al., 2021), suggest that the gravitationally unstable stratigraphy would have resulted in cumulate overturn (Zhang et al., 2017; Li et al., 2019; Maurice et al., 2024). These recent studies indicate that dense shallow cumulates flow into the deep lunar interior as viscous solids, perhaps after progressive thickening of the IBC layer by downwelling of small-scale IBC instabilities into the underlying mantle (Hess and

Parmentier, 1995; Li et al., 2019). The overturn of IBC into the lunar mantle would juxtapose sinking IBC against deep mafic mantle cumulates, where mechanical mixing or chemical reactions could generate hybridized mantle sources.

Although multiple lunar basalt formation mechanisms have been proposed (e.g., Hubbard and Minear, 1975), mantle hybridization is considered a capable mechanism for forming sources of high-Ti lunar basalts and picritic glasses (Ringwood and Kesson, 1976; Hess and Parmentier, 1995; Wagner and Grove, 1997; Van Orman and Grove, 2000; Elkins-Tanton et al., 2002). Hybridization is invoked to explain the Ti- and REE-rich compositions of the lunar basalts (relative to mafic cumulates of a lunar magma ocean) and high Mg#s (relative to that estimated for the IBC) (e.g., Singletary and Grove, 2008; Grove and Krawczynski, 2009; Krawczynski and Grove, 2012; Brown and Grove, 2015). Previous studies have estimated the composition of the hybridized sources by mixing various proportions of late LMO cumulates and mafic cumulates (Singletary and Grove, 2008; Thacker et al., 2009; Yao and Liang, 2012; Mallik et al., 2019) and investigated the phase equilibria of the downwelling IBC (Van Orman and Grove, 2000; Mallik et al., 2019). While these studies provide a first order understanding of the starting material and possible end products of the hybridization process, they do not explore the chemical reactions that control the hybridization process.

This study experimentally investigates the chemical reactions that occur during the cumulate overturn as downwelling IBC melts and mushes interact with mafic cumulates. The experiments indicate that the primary processes contributing to hybridization are the dissolution of mafic material and solid-state diffusion between

cumulates. The experimental results also constrain metamorphic phase relations in the downwelling IBC, which indicate garnet would form in the lunar mantle during cumulate mantle overturn events.

1.2 Methods

1.2.1 Starting Materials

Experiments tested the mineralogy and mineral reactions that occurred between dunite representing early lunar magma ocean cumulates and an ilmenite-bearing cumulate (IBC) under supersolidus and near solidus conditions (for the IBC). The IBC composition in this study represents a late lunar magma ocean cumulate comprising 85% normative hedenbergite clinopyroxene and 15% normative ilmenite (Longhi and Ashwal, 1985; Snyder et al., 1992; Hess and Parmentier, 1995). The assumed pyroxene composition is an average of LMO-relevant pyroxene compositions NJD-20, HB-1, HB-4 from Dygert et al. (2014), while the assumed ilmenite composition is an average of LMO-relevant ilmenite compositions NJD-22M, NJD-19M, NJD-17M, NJD-15M from Dygert et al. (2013). Reagent-grade metal oxide and carbonate powders were used to prepare the IBC starting composition. The powders were weighed and ground in a mortar and pestle for 12 hours, then decarbonated in a furnace at 800°C for 24 hours. Following the decarbonation, the powder was conditioned at an oxygen fugacity (fO_2) relevant to the lunar mantle, which is close to the iron-wüstite (IW) buffer (Sato, 1979; Weitz et al., 1997; Nicolis and Rutherford, 2009). The powder was placed in a gas mixing furnace at 800°C in a gas mixture with subequal volumes of CO_2 and H_2 (Deines, 1974) to achieve

an fO_2 approximating IW. The IBC cumulate melt has a Ti-, Al-, and Fe-rich composition with an Mg# of 4.96 $\pm$ 0.12 (**Table 1.1**).

A lunar-relevant mafic cumulate composition represented by a terrestrial dunite was prepared using mineral separates from a mantle xenolith (Dygert et al., 2019). The dunite consists of olivine mineral separates with trace amounts of Opx, Cpx, and minor spinel from the crushed mantle xenolith. The dunite separates were ground in ethanol, dried, and stored in a 200°C vacuum oven for at least 12 hours to drive off adsorbed water. The olivine from the dunite used in reaction experiments has an Mg# of 90.83 $\pm$ 0.07 (**Table 1.1**).

1.2.2 Experiments

Experiments were conducted at the University of Tennessee using a 150-ton end-loaded piston cylinder apparatus equipped with a computerized pressure holding system. Assembly designs are similar to those utilized by Morgan and Liang (2005) and Wang et al. (2013). Experiments were run in graphite-lined molybdenum capsules, which were previously demonstrated to approach lunar-relevant value fO_2s near the IW buffer for similarly preconditioned starting materials (Ji and Dygert, 2024). Dunite and IBC materials were presynthesized before running the reaction experiments. The IBC materials were heated to 1300°C at 1 GPa for 2 hours and then quenched to a glass. Dunite was annealed at 1200°C at 1 GPa for 24 hours to texturally equilibrate. The presynthesized runs were then sectioned latitudinally, polished, and reaction couples were prepared by juxtaposing the IBC glass against the dunite.

Table 1.1. Starting material compositions (wt%) measured by electron microprobe from this study compared with ilmenite-bearing cumulate compositions from previous studies.

	IBC (This Study)		Dunite (This Study)		TiCum (VO&G' 00)	TiCum (M' 19)	TiCum Est (C' 18)
	Avg.	σ	Avg.	σ			
SiO_2	38.03	0.15	41.42	0.27	41.61	41.90	32.40
TiO_2	6.83	0.10	0.01	0.01	9.10	9.10	12.63
Al_2O_3	6.26	0.08	0.05	0.02	2.80	3.24	5.51
Cr_2O_3	0.26	0.01	0.12	0.01	0.00	0.01	0.03
MgO	0.91	0.02	49.90	0.15	7.50	7.95	4.34
CaO	13.91	0.10	0.20	0.02	8.20	8.48	5.38
MnO	1.05	0.02	0.14	0.01	0.00	0.03	0.40
FeO	31.21	0.09	8.98	0.05	29.60	28.90	39.15
NiO	0.00	0.00	0.40	0.03	0.00	0.00	0.00
Na_2O	0.29	0.02	0.01	0.00	0.00	0.02	0.15
K_2O	0.00	-	0.00	-	0.00	0.02	0.01
Total	98.75	0.23	101.22	0.35	98.81	99.65	100.00
Mg#	4.96	0.12	90.83	0.07	31.11	32.90	16.49

Mg# = (Mg/(Mg+Fe))x100
VO&G' 00 - Van Orman and Grove (2000)
M' 19 - Mallik et al. (2019)
C' 18 - Charlier et al. (2018)
TiCum Est - Estimated composition of the ilmenite-bearing cumulate from Charlier et al. (2018) determined with the modal mineral abundances and mineral compositions from crystallization experiments (LPUM/02-3 gl). Composition assumes 80% floation of plagioclase and quartz based on the findings of the study.

Reaction couples were held together using platinum foil and placed in experimental assemblies composed of crushable MgO spacers within a graphite resistance heater and Pyrex sleeve, using outer NaCl salt sleeves as a confining material, with the IBC glass above the dunite (**Figure 1.1**). No pressure correction was applied. Temperature was monitored using calibrated D-type W-Re thermocouples, and no emf correction was applied.

Eight of the experiments were run in a three-step, heat-dwell-quench sequence to examine whether a reaction would occur between the halves of the reaction couple (**Table 1.2**). These eight experiments were run at temperatures between 1100 and 1300°C at pressures between 0.55 and 2.02 GPa for durations of 20 min to 24 hr. One experiment (MRx#13) was run as a five-step, heat-dwell-cool-dwell-quench sequence to examine the effects of dunite dissolution on a hybridized cumulate (**Table 1.2**). This experiment was run at 2.02 GPa and had an initial 6 hr dwell period at 1300°C, followed by a 1 hr and 40 min cooling period, which cooled the experiment at a rate of 1 °C/min. The cooling period decreased the temperature to 1200°C, and the experiment dwelled at this temperature for 24 hr before quenching (**Table 1.2**).

1.2.3 Analysis of Run Products

Run products were extracted from assembles, mounted in epoxy resin, cut lengthwise with a low-speed saw, and polished. Imaging and mineral chemistry measurements were conducted using the Cameca SX100 electron probe microanalyzer (EPMA) at the University of Tennessee, Knoxville.

Table 1.2. Starting materials and run conditions.

Experiment	Starting Materials	P (GPa)	T (^{o}C)	Duration (hr)	Temperature Path (^{o}C)	Run Products	Assimilation	Group
MRx#1	IBC+Dunite	2.02	1200	6	0 (70^{o}C/min) ➔ 1200 (6 hr) ➔ Quench	Grnt+Cpx+Fe-Ti Oxide^	No	N/A
MRx#3	IBC+Dunite	1.99	1100	6	0 (70^{o}C/min) ➔ 1100 (6 hr) ➔ Quench	Grnt+Cpx+Ilm+Usp	No	N/A
MRx#5	IBC+Dunite	0.55	1200	6	0 (70^{o}C/min) ➔ 1200 (6 hr) ➔ Quench	Glass+Cpx	Yes	A
MRx#8	IBC+Dunite	2.02	1150	24	0 (70^{o}C/min) ➔ 1150 (24 hr) ➔ Quench	Grnt+Cpx+Ilm	No	N/A
MRx#9	IBC+Dunite	0.55	1200	0.33	0 (70^{o}C/min) ➔ 1200 (0.33 hr) ➔ Quench	Glass+Cpx*	Yes	A
MRx#10	IBC+Dunite	0.55	1200	24	0 (70^{o}C/min) ➔ 1200 (24 hr) ➔ Quench	Glass+Cpx	Yes	A
MRx#11	IBC+Dunite	0.55	1100	24	0 (70^{o}C/min) ➔ 1100 (24 hr) ➔ Quench	Cpx+Usp+Glass	No	B

Table 1.2. Continued.

Experiment	Starting Materials	P (GPa)	T (^{o}C)	Duration (hr)	Temperature Path (^{o}C)	Run Products	Assimilation	Group
MRx#12	IBC+Dunite	2.02	1300	1	0 (70^{o}C/min) ➔ 1300 (1 hr) ➔ Quench	Cpx+Fe-Ti Oxide^	Yes	A
MRx#13	IBC+Dunite	2.02	1300-1200	31.66	0 (70^{o}C/min) ➔ 1300 (6 hr) ➔ (-1^{o}C/min)➔ 1200 (24 hr) ➔ Quench	Glass+Cpx	Yes	N/A

^FeTi-Oxide indicates that High-Z phases were present in the reaction products; however, the grain size of the phases made analysis impossible.
*Cpx indicates that silicate crystals were present in the reaction products; however, the grain size of the crystals made analysis impossible.
Olivine (Ol), Orthopyroxene (Opx), Clinopyroxene (Cpx), Garnet (Grnt), Ilmenite (Ilm), Ulvöspinel (Usp)
Group A supersolidus experiements exhibit significant evidence of dunite dissolution.
Group B supersolidus experiments lacked clear evidence of dissolution.

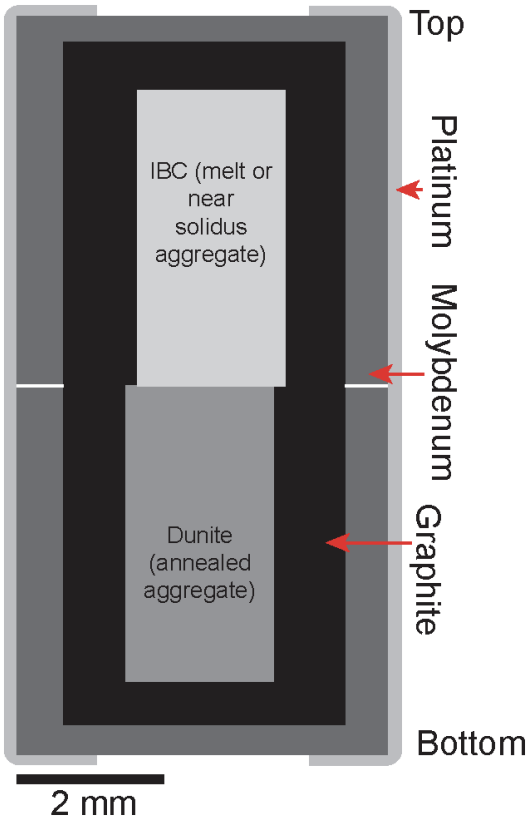


Figure 1.1. Schematic illustrating assemblies used in near solidus and melt-rock reaction experiments utilized in this work. IBC refers to half of the reaction couple with the ilmenite bearing cumulate composition.

For quantitative wavelength dispersive spectroscopy (WDS) mineral analyses, operating conditions were 15kV and 30 nA, with a spot size of 1 μm. For glass analysis, a defocused 10 μm beam was used, and operating conditions were 15kV and 20 nA. X-ray counts were measured for 30-40 seconds on the peak position of each element and 10 seconds on background. Natural and synthetic standards were used for calibration, and the ZAF matrix correction was applied. X-ray maps of the reaction interface were created with the Phenom XL at the University of Tennessee, Knoxville. For qualitative energy dispersive spectroscopy (EDS) mapping, operating conditions were 15kV and 30 nA, under a 1 Pa vacuum, with a spot size of 2 μm. The count time per spot was set to 20 ms for variably sized areas of interest with a resolution of 1024×1024 pixels. Since the mapping area and resolution determine the point density, the point density ranges from 0.1 μm to 2 μm among maps.

1.3 Results

Experiments juxtaposing the IBC glass and dunite in this study are presented in three groups: (1) near solidus experiments, (2) supersolidus dunite dissolution experiments, and (3) a dunite dissolution-solidification experiment. (**Table 1.2**). In all cases, the dunite half of the reaction couple was below its melting temperature; near solidus and supersolidus refer to the behavior of the IBC side of the reaction couple. Near solidus experiments are classified as experiments that contain $\leq$1% melt in the IBC half of the couple, while supersolidus experiments have $>$30% melt in the IBC half of the couple. The melt proportion was determined using volumetric estimates from chemical maps where the minerals and melt are easily distinguished. ImageJ was the image

processing software used for these calculations. Results for each experimental group are discussed separately. All chemical data collected from each experiment are reported in attached file Ch1SupportingTables.xlsx.

1.3.1 Near Solidus Experiments

1.3.1.1 Products and Growth Textures

Experiments MRx#1, MRx#3, and MRx#8 were run under near solidus conditions (**Table 1.2**), with trace amounts of a low-degree interstitial melt in the IBC side of the reaction couple. These experiments produce Cpx and garnet with variable amounts of Fe-Ti oxides (i.e., ulvöspinel and ilmenite) throughout the IBC side of the reaction couple (**Figure 1.2a**). Growth textures of Cpx and garnet crystals are often subhedral. Ilmenite and ulvöspinel exhibit subhedral and anhedral growth textures. Garnets often contain inclusions of Cpx and Fe-Ti oxides and are difficult to distinguish from Cpx in BSE images owing to the similar average atomic number of the minerals in this system (**Figure 1.2b**). Ulvöspinel and ilmenite often form as inclusions within garnet and in the interstitial space between garnet and Cpx crystals. Trace amounts of low-degree interstitial melt are present along the edge of the IBC material (MRx#8) (**Figure 1.2a**) and between crystals (MRx#1) (**Figure 1.2d**). Garnet represents ~19% of the IBC half of the reaction couple in these high-pressure experiments, while Cpx and Fe-Ti oxides represent ~78% and ~3% respectively. Low-degree interstitial melt makes up <1% of the material in the IBC side of experiments MRx#1 and MRx#8, while MRx#3 appears to be free of interstitial melt.

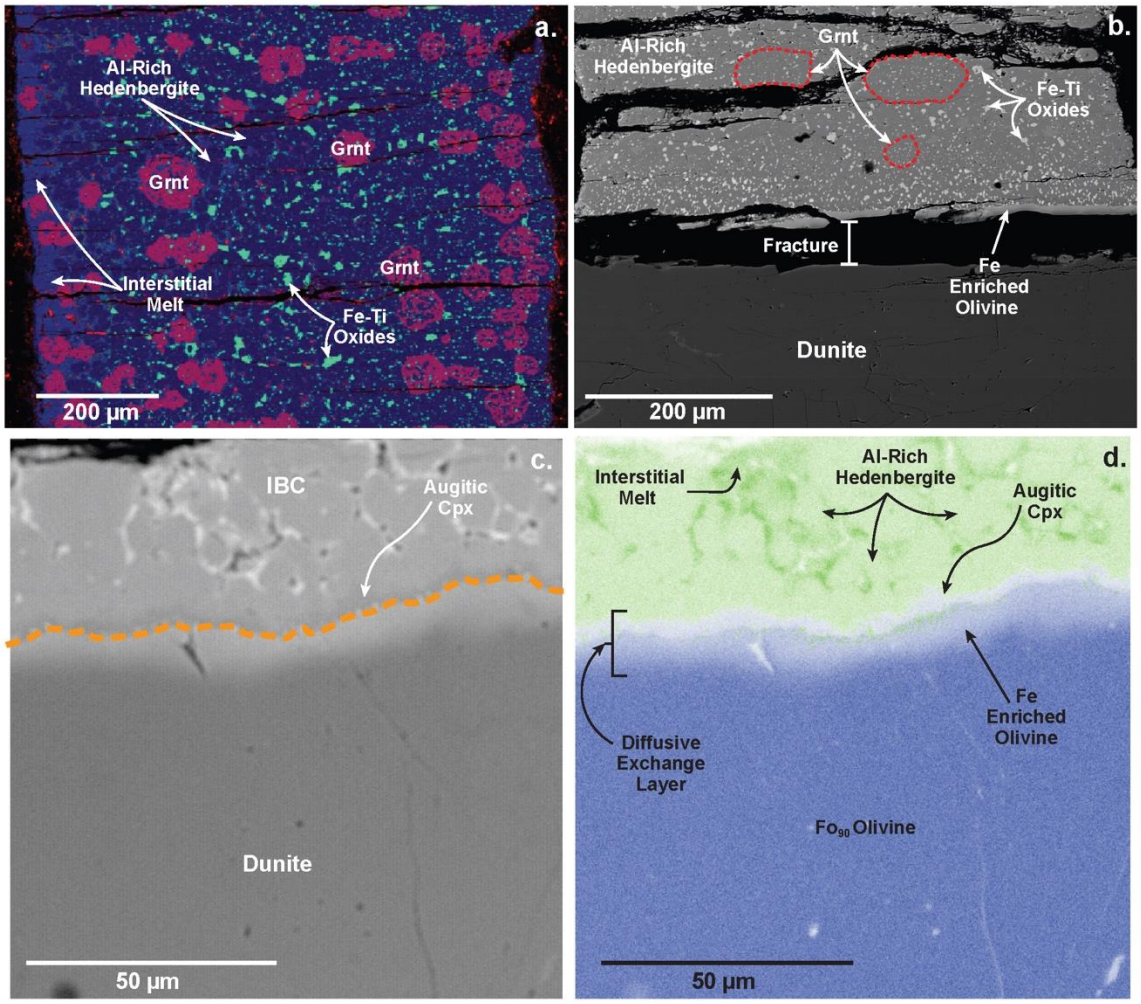


Figure 1.2. Representative BSE images and elemental maps highlighting minerals and reactions produced in near solidus experiments. (a) False color image of the IBC half of the reaction couple in MRx#8, showing garnet (red), clinopyroxene (dark blue), Fe-Ti oxides (green), and Ti- and Fe-rich low degree interstitial melt on the left side of the experiment (lighter blue). (b) Backscatter electron image of near solidus experiment MRx#3 showing crystalline features in IBC half of the reaction couple, and diffusive exchange boundary at the IBC-dunite interface. The IBC formed Al-rich hedenbergite, garnet (Grnt) (outlined in red), and Fe-Ti oxides. Boundary reactions observed in MRx#1 are shown in (c) and (d). (c) Backscatter electron image of the IBC-dunite reaction interface (orange dashed line). Augitic Cpx that formed via diffusive exchange is labeled. (d) Combined Fe (green) and Mg (blue) false color elemental map of the interface showing the diffusive exchange of Fe and Mg. This chemical exchange resulted in the formation of fayalitic olivine and augitic Cpx (light blue and gray-blue respectively in the elemental maps.

A diffusive exchange layer ~10-60 µm thick is present around the original interface (**Figure 1.2d, A1, and A2**). The thickness of the reactive layer interface appears to increase with time (**Table 1.3**). It should be noted that fractures often form at the interface between halves of the experimental reaction couples, making accurate measurements difficult within and near the reaction boundary. Thus, the dunite boundary thicknesses for MRx#3 and MRx#8 reported in **Table 1.3** represent minimum estimates as material may have been lost during fracture formation, mounting, and polishing.

1.3.1.2 Phase Chemistry

Clinopyroxenes from near solidus experiments have Al and Ti-rich hedenbergitic compositions (**Figure 1.3a**). Garnets produced in the experiments have high almandine (Alm) and grossular (Gro) components with almost no pyrope component (**Figure 1.4**). Garnet from MRx#1 is more grossular normative than garnets from MRx#3 and MRx#8. This may be related to the higher temperature of the MRx#1 experiment. Ulvöspinel and ilmenite were observed in MRx#3; however, ulvöspinel was not observed in MRx#8. High-Z phases are present in MRx#1 and are likely Fe-Ti oxides; however, these phases are typically <3 µm across, so single-phase analysis was impossible. Low-degree interstitial melt in MRx#1 and MRx#8 is TiO_2 and FeO enriched, but SiO_2, Al_2O_3, Cr_2O_3, and MgO depleted relative to the initial IBC composition (**Table 1.4**).

Clinopyroxene crystals that form on the boundary between the dunite and IBC sides of the reaction couple typically have more augitic compositions and plot separately from Cpx that form within the IBC side and far from the boundary (**Figures 1.2c, 1.2d, and 1.3a**).

Table 1.3. Interface dissolution and exchange measurements from melt-rock reaction experiments.

Experiment	P (GPa)	T (^{o}C)	Duration (hr)	Dunite Diffusion Boundary Thickness (μm)			Dissolution distance (μm)			Estimated Dissolution Propagation (m^2/s)	
				n	Avg.	$\boldsymbol{\sigma}$	n	Avg.	$\boldsymbol{\sigma}$	Est.	$\boldsymbol{\sigma}$
MRx#1	2.02	1200	6	6	10	0.36	–	N/A	–	N/A	–
MRx#3	1.99	1100	6	6	10	1.01	–	N/A	–	N/A	–
MRx#5	0.55	1200	6	–	N/A	–	6	313	50.24	1.45E-14	2.33E-15
MRx#8	2.02	1150	24	6	16	4.40	–	N/A	–	N/A	–
MRx#9	0.55	1200	0.33	–	N/A	–	6	30	79.62	2.51E-14	5.00E-15
MRx#10	0.55	1200	24	6	14	7.67	6	394	6.00	4.56E-15	9.22E-16
MRx#11	0.55	1100	24	6	5	1.41	–	N/A	–	N/A	–
MRx#12	2.02	1300	1	6	6	1.77	6	86	15.83	2.38E-14	4.40E-15
MRx#13	2.02	1300-1200	31.66	6	24	4.28	7	201	18.97	N/A	–

Table 1.4. Pre-reaction IBC composition compared with post-reaction melt compositions averaged from data collected across the entire IBC half of the diffusion couple.

	Initial IBC		MRx#1		MRx#5		MRx#8		MRx#9		MRx#10	
	Avg	σ	Avg	σ	Avg	σ	Avg	σ	Avg	σ	Avg	σ
SiO_2	38.03	0.15	34.57	3.67	39.05	0.31	36.31	1.08	38.58	0.58	39.17	0.19
TiO_2	6.83	0.10	11.84	0.39	5.41	0.22	9.57	0.55	6.83	0.22	5.89	0.13
Al_2O_3	6.26	0.08	5.59	0.52	5.16	0.28	3.66	1.20	6.21	0.11	5.50	0.18
Cr_2O_3	0.26	0.01	0.07	0.03	0.25	0.02	0.04	0.02	0.27	0.02	0.25	0.02
MgO	0.91	0.02	0.48	0.19	7.28	0.65	0.33	0.02	1.22	0.85	6.85	0.32
CaO	13.91	0.10	10.38	1.96	12.48	0.32	9.59	2.07	14.39	0.43	12.65	0.15
MnO	1.05	0.02	1.09	0.15	0.94	0.03	1.01	0.04	1.03	0.04	0.92	0.02
FeO	31.21	0.09	34.07	2.06	28.55	0.35	38.84	3.15	30.97	1.36	28.01	0.19
NiO	0.00	0.00	0.04	0.06	0.03	0.02	0.01	0.01	0.01	0.01	0.01	0.01
Na_2O	0.29	0.02	0.49	0.25	0.28	0.03	0.29	0.09	0.30	0.07	0.32	0.05
Total	98.75	0.23	98.62	0.02	99.43	0.31	99.63	0.82	99.80	0.50	99.57	0.31
Mg#	4.96	0.12	2.41	0.81	31.20	1.88	1.48	0.20	6.52	4.50	30.34	0.97

Table 1.4. Continued.

	MRx#11		MRx#13	
	Avg	$\boldsymbol{\sigma}$	Avg	$\boldsymbol{\sigma}$
SiO_2	44.65	0.33	35.21	0.34
TiO_2	3.81	0.15	8.72	0.25
Al_2O_3	9.39	0.26	6.36	0.20
Cr_2O_3	0.01	0.02	0.07	0.01
MgO	0.09	0.01	1.99	0.13
CaO	11.47	0.10	11.28	0.45
MnO	1.18	0.03	1.14	0.03
FeO	27.37	0.37	35.55	0.98
NiO	0.01	0.01	0.01	0.01
Na_2O	0.77	0.03	0.26	0.05
Total	98.76	0.24	100.59	0.36
Mg#	0.60	0.04	9.08	0.74

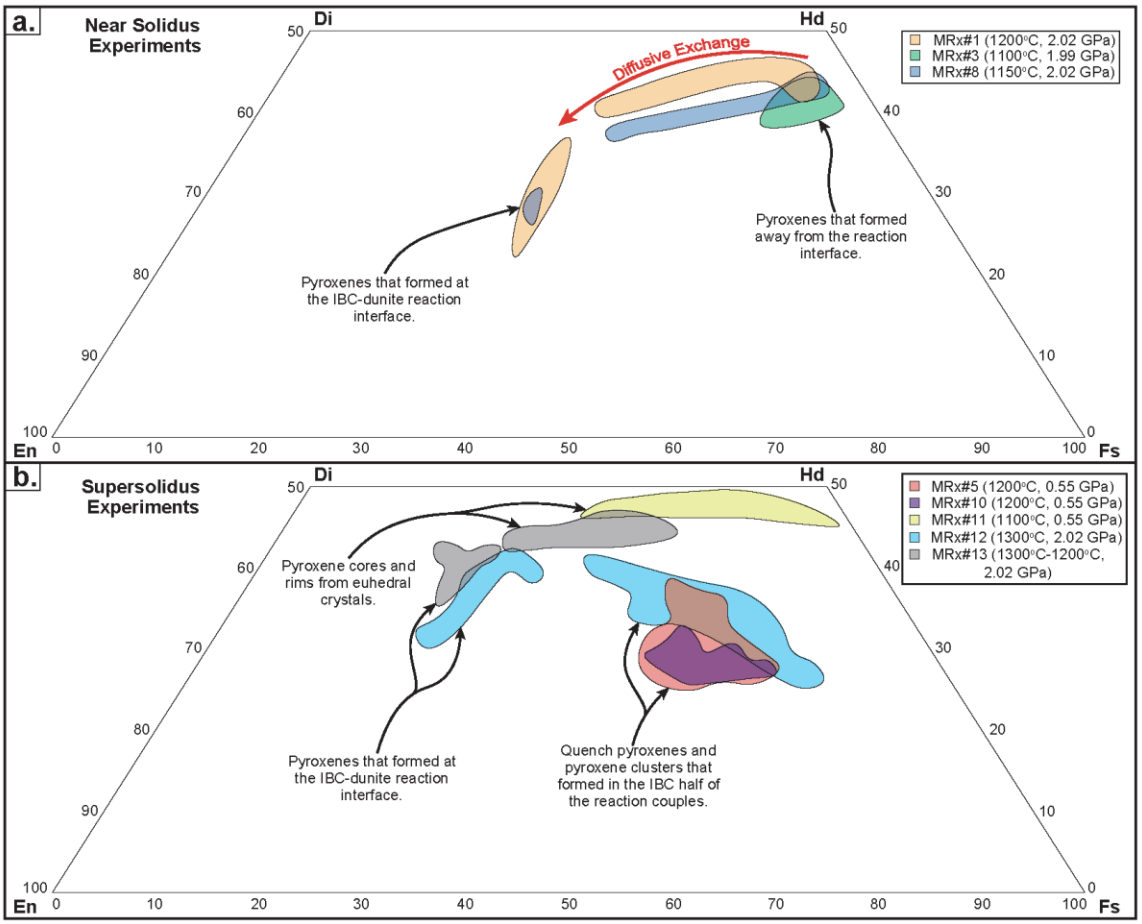


Figure 1.3. Pyroxene compositions from melt-rock reaction experiments projected as components. (a) Pyroxene compositions from near solidus experiments. (b) Pyroxene compositions from supersolidus and dissolution-precipitation experiments. Pyroxenes that formed at the interface plot in separated groups as noted for each experiment (except for IBC-MRx#11, as the interface pyroxenes have similar compositions to the most magnesian cores of euhedral pyroxenes). Mineral end-members: Enstatite (En), Ferrosilite (Fs), Diopside (Di), Hedenbergite (Hd).

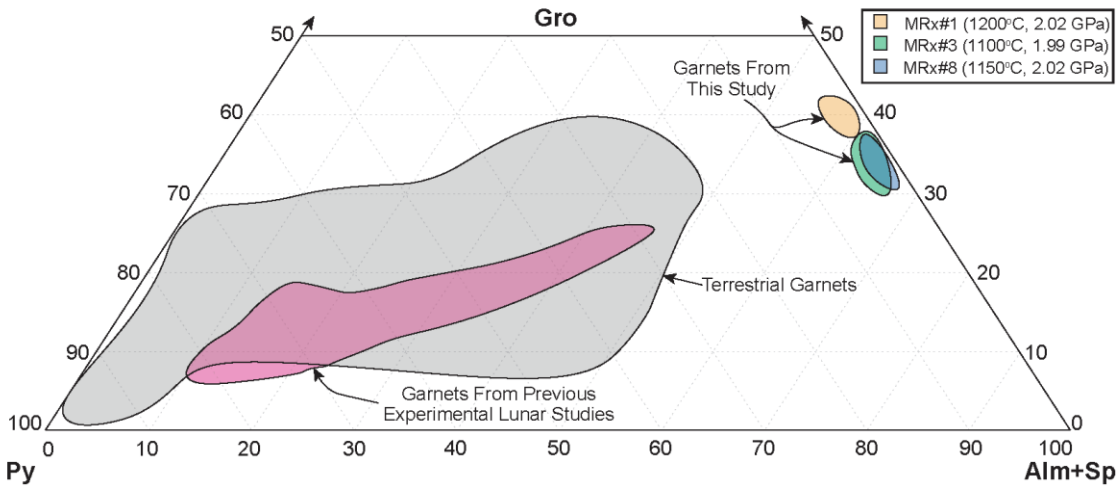


Figure 1.4. Garnet compositions from near solidus experiments conducted in this study compared to terrestrial and lunar relevant compositions. Gray shaded terrestrial garnet region represents data compiled by Sun and Liang (2015). Pink shaded lunar garnet region represents experimental garnets from picritic glass multi-saturation experiments, hybridized lunar mantle source experiments, and lunar magma ocean solidification studies (Elkins-Tanton et al., 2003; Draper et al., 2006; Elardo et al., 2011; Krawczynski and Grove, 2012; Barr and Grove, 2013; Mallik et al., 2019; Kraettli et al., 2022; Jing et al., 2022). Mineral end-members: Almandine (Alm), Spessartine (Sp), Grossular (Gro), Pyrope (Py).

Olivine within the dunite side is more fayalite (Fa) normative at the boundary (**Figures 1.2b-1.2c**), consistent with diffusive chemical exchange between the dunite and IBC. Considering the width of the dunite boundary layer (~30 μm) and the fact that its width increases with experimental duration suggests that it is the product of solid-state diffusive exchange across the reaction couple. As the layer is relatively thin, it is unlikely that the dunite significantly influences the composition of minerals within the IBC side beyond a similarly thin boundary layer adjacent to the dunite. This also indicates that the average pyroxene and garnet compositions in near solidus experiments represent the equilibrium phase compositions within the IBC at the P-T conditions of the given experiment.

1.3.2 Supersolidus Experiments

Supersolidus experiments MRx#5, MRx#9, MRx#10, MRx#11, and MRx#12 are divided into group A (MRx#5, MRx#9, MRx#10, and MRx#12) and group B (MRx#11). Group A experiments were run at 0.55 GPa (1200 °C) and 2 GPa (1300 °C), and all exhibit significant evidence of dunite dissolution. The Group B experiment was run at 0.55GPa (1100 °C) and lacked clear evidence of dissolution (**Table 1.2**). These experimental groups are discussed separately below.

1.3.2.1 Group A Products and Growth Textures

Both low-pressure (i.e., 0.55 GPa) and high-pressure (i.e., ~2 GPa) experiments produce dunite dissolution (assimilation). Evidence of dunite dissolution is evident in backscatter electron (BSE) images where the interface between the dunite and IBC halves of the reaction couple was always offset into the dunite (**Figures 1.5a and 1.5c**). The position of the original polished interface is shown in **Figure 1.5** by the blue line, and the

orange line shows the final position of the interface. The IBC side of the reaction couple exhibits Cpx and/or hybridized melt (i.e., IBC melt that has assimilated dunite material) at the reaction boundary. The IBC side of the reaction couple remained glass-rich in the low-pressure experiments after the quenching process (**Figures 1.5a and 1.5b**). In contrast, the IBC side of the reaction couple in the high-pressure experiments completely crystallized during the quenching process, forming dendritic Cpx (**Figure 1.5c and 1.5d**). An exception is MRx#9 (0.55 GPa), where the IBC side of the reaction couple is almost entirely glassy with some nano-scale crystals throughout.

The Cpx in the hybridized melt exhibits subhedral, anhedral, or dendritic morphologies. Clinopyroxenes in low-pressure experiments MRx#5 and MRx#10 often exhibit sector or patchy zoning and a bight rim around them (**Figure A3**). Clinopyroxene is the only crystallizing phase in MRx#5 and MRx#10. In high-pressure experiment MRx#12, a high-Z phase (presumably an Fe-Ti oxide) is present in the interstitial space between dendritic Cpx; however, crystals were too small to analyze.

MRx#10 exhibits less Cpx crystallization on the IBC side of the reaction interface relative to MRx#5 (**Figures A5 and A6**). MRx#10 also lacks significant Cpx crystallization throughout the IBC side of the reaction couple (**Figures 1.5a and 1.5b**). Clinopyroxene crystals that form on the reaction interface in MRx#5 and MRx#10 are acicular, small, and bright in BSE images (**Figures A3 and A4**). High-pressure experiment MRx#12 contains abundant Cpx on the reaction interface, and the Cpx is dark in BSE images and pale blue in elemental maps (**Figures 1.5c and 1.5d**).

In BSE images, a thin but noticeable diffusive exchange layer is present on the dunite side of the reaction interface in experiments MRx#10 and MRx#12 with a highly irregular thickness representing concentration gradients in Fe and Mg (**Figures 1.5b, 1.5d, and A4**). MRx#5 and MRx#9 do not have analogous layers on the dunite side of the reaction interface (**Figures A3 and A5**). The lack of a diffusive exchange layer on the reaction interface may be related to the rate of dunite dissolution relative to solid-state diffusion and is discussed further in the kinetics of dunite dissolution section below (section 1.4.2).

Small IBC melt veins were observed along the reaction interface of MRx#5 and MRx#12 (**Figures 1.5c, 1.5d, and A3**), and some suspected melt infiltration veins were observed near the reaction interface in MRx#9 and MRx#10 (**Figures A4 and A5**). Veins of melt infiltration are short (<100 μm), have highly irregular shapes, and are usually next to or in the middle of a thicker portion of the dunite interface layers mentioned above. All group A supersolidus experiments also have thin veins of IBC melt along the dunite-graphite interface of the assembly (i.e., the assembly walls) that often propagate to the bottom of the dunite half of the reaction couple. The effects of IBC-dunite interface vein formation on the reaction process are discussed further in sections (1.4.2.2) and (1.4.2.3) below.

1.3.2.2 Group A Mineral and Melt Chemistry

Relative to near solidus experiments, most Cpx crystals in the supersolidus experiments have more enstatite (En) normative and less wollastonite (Wo) normative compositions (**Figure 1.3b**). High-pressure experiment MRx#12 contains Cpx that trend

toward ferrosilite (Fs). These pyroxenes are exclusively found far from the reaction interface in the dendritic region of the experiment. Like the near solidus experiments, Cpx crystals that form on the reaction couple interface in MRx#12 have more augitic compositions and plot separately from Cpx that form within the IBC side and further from the boundary (**Figure 1.5b**). Clinopyroxene crystals that form on the reaction couple interface in experiments MRx#5 and MRx#10 were too small to analyze.

Melt hybridization in MRx#5 and MRx#10 is evidenced by the elevated melt Mg#s of ~30-31 relative to the Mg# of the pre-reaction IBC material (i.e., ~5). Similar melt Mg# elevation is observed near the reaction interface of MRx#9; however, the Mg enrichment is confined to the interface due to the shorter duration of the experiment The Mg#s of hybridized melts in MRx#5, MRx#9, and MRx#10 generally decrease with distance from the reaction interface (see section (1.4.2.2.) for further discussion).

1.3.2.3 Group B Products and Growth Textures

In experiment MRx#11, large Cpx (200-1000 μm) are present throughout the IBC side of the reaction couple. All Cpx within this experiment exhibit skeletal and euhedral morphologies and core-to-rim zoning (**Figure A5**). Euhedral ulvöspinel crystals surround the Cpx and are the only Fe-Ti oxides present in the experiment. MRx#11 contains interstitial melt (i.e., IBC melt that has undergone crystallization and lacks evidence of dunite assimilation) in the form of glass throughout the IBC side of the couple. Glass within this experiment occupies the interstitial space between the large Cpx crystals. Clinopyroxene crystals are abundant at the reaction couple interface and appear to nucleate from the interface, isolating the interface from the evolved melt.

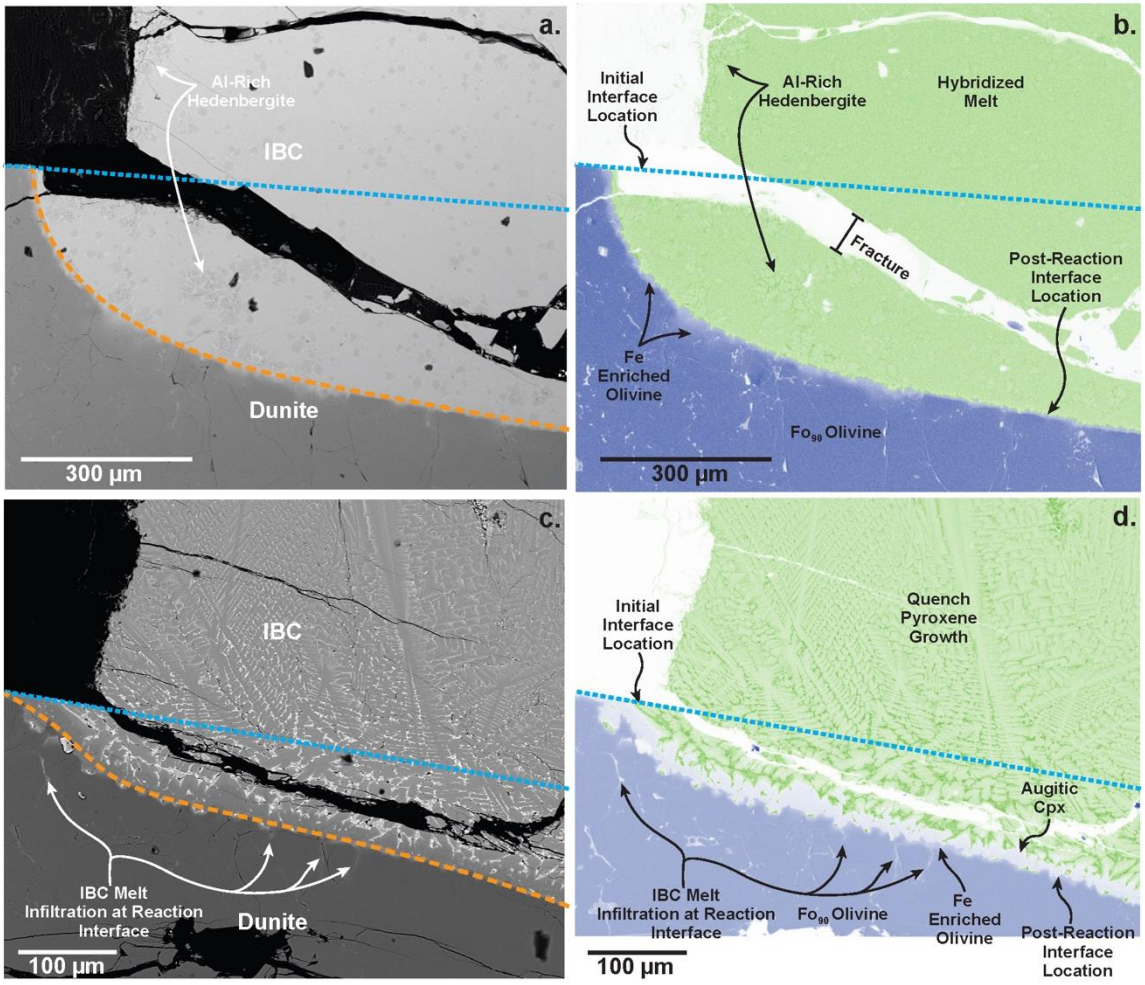


Figure 1.5. Representative BSE images and elemental maps highlighting minerals and reaction features in supersolidus experiments. (a) Backscatter electron image of MRx#10 showing the pre-reaction interface, post-reaction interface, and Al-rich hedenbergite. (b) Combined Fe (green) and Mg (blue) false color elemental map of the reaction interface in MRx#10 with phases and reaction features labeled. (c) Backscatter electron image of MRx#12 showing the pre-reaction interface, post-reaction interface, and possible melt propagation into the dunite along grain boundaries. (d) Combined Fe (green) and Mg (blue) false color elemental map of the reaction interface in MRx#12 with phases and reaction features labeled. In all figures the blue dotted line represents the pre-reaction interface position and in figures (a) and (c) the orange dashed line represents the post-reaction interface position. In both experiments, the IBC-dunite interface has migrated into the dunite side of the reaction couple due to dunite dissolution. In MRx#12 the IBC melt appears to be exploiting grain boundaries to propagate into the dunite resulting in the light gray (c) and light blue (d) streaks indicated in the dunite.

As in the other experiments, there is a thin but obvious diffusive exchange layer on the dunite side of the reaction interface (**Figure A5**). This diffusive exchange layer is thinner (~5 μm) than those observed in 6 hr near solidus experiments (~10 μm) on the dunite side of the interface (**Table 1.3**). IBC melt veins were not observed along the IBC-dunite reaction interface of MRx#11 as in the Group A experiments.

1.3.2.4 Group B Mineral and Melt Chemistry

Clinopyroxene crystals in MRx#11 have more Wo normative compositions than all other experiments (**Figure 1.3b**). Normal zoning occurs in all Cpx crystals with an average core Mg# of 22.5±4.7 and rim Mg# of 9.2±2.7, consistent with progressive Cpx crystallization in the IBC composition. Clinopyroxenes near the interface plot along a continuum with the core and rim compositions from elsewhere in the experiment but have slightly more En normative compositions closer to the interface (**Figure 1.3b**).

Interstitial melt in MRx#11 lacks the TiO_2 and FeO enrichment observed in the low-degree interstitial melt from MRx#8. This is likely due to the extensive crystallization of ulvöspinel in this experiment, which would keep the TiO_2 and FeO concentrations lower relative to oxide-free experiments. Overall, melt within this experiment exhibits SiO_2, Al_2O_3, Na_2O enrichment and TiO_2, Cr_2O_3, MgO, and FeO depletion relative to the initial IBC composition (**Table 1.4**).

1.3.3 Step-Cooled Experiment

1.3.3.1 Products and Growth Textures

Experiment MRx#13 is the only step-cooled experiment (**Table 1.2**). Clinopyroxene is the only phase in the IBC side of the couple large enough to analyze.

Clinopyroxenes are large (500-1500 μm) and exhibit skeletal and euhedral morphologies like those in MRx#11. Clinopyroxenes within the experiment exhibit pronounced core-to-rim zoning, similar to MRx#11.

High-Z phases (presumably Fe-Ti oxides) are present in the interstitial region between large Cpx. The presence of these phases is most apparent near the IBC-dunite interface where Cpx crystals formed in close proximity to each other, and the hybridized interstitial melt (i.e., IBC melt that has assimilated dunite material and undergone crystallization) seems to have undergone more extensive crystallization.

BSE images show that the experiment resulted in extensive dunite dissolution as the IBC-dunite interface migrated into the dunite side of the reaction couple (**Figures 1.6a and 1.6b**). Hybridized interstitial melt is present throughout the IBC side of the experiment. Clinopyroxene crystals are abundant at the reaction couple interface and appear to nucleate from the interface, isolating the interface from the melt. Given the extensive dissolution observed in this experiment, the Cpx crystals likely formed during the cooling step of the experiment, significantly reducing IBC-dunite interaction.

1.3.3.2 Mineral and Melt Chemistry

Clinopyroxene crystals in MRx#13 have unique compositions relative to the other experiments (**Figure 1.3b**). The Cpx are less Fs normative than those observed in the near solidus experiments and MRx#11. The pyroxenes exhibit a continuum of compositions ranging from augitic to hedenbergitic. Clinopyroxene cores have Mg#s of 48.2 ± 5.1, while clinopyroxene rims have Mg#s of 36.3 ± 2.3.

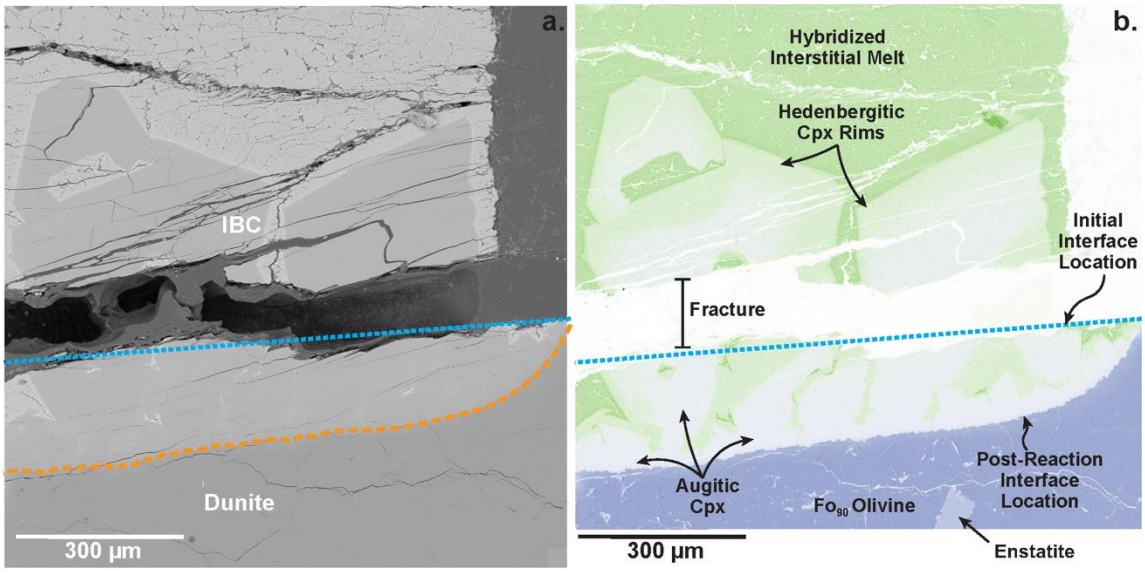


Figure 1.6. Representative BSE image and elemental map highlighting minerals and reaction features produced in step-cooled supersolidus experiment MRx#13. (a) Backscatter electron image of the reaction interface in showing the pre-reaction interface (blue dotted line) and post-reaction interface (orange dashed line). (b) Combined Fe (green) and Mg (blue) false color elemental map of the reaction interface with the pre-reaction interface, phases, and reaction features labeled. The IBC-dunite interface location has migrated into the dunite side of the reaction couple due to dunite dissolution. A rare enstatite crystal within the dunite side of the reaction couple is visible in the elemental map, this grain is unrelated to melt-rock reaction and originates from incomplete mineral separation in the starting material.

Given the morphology and size of the crystals, the core-to-rim zoning perhaps reflects a shift in equilibrium pyroxene compositions as the melt composition evolved due to progressive crystallization.

Hybridized interstitial melt in MRx#13 exhibits TiO_2, MgO, and FeO enrichment and SiO_2, Cr_2O_3, and CaO depletion relative to the initial IBC composition (**Table 1.4**). TiO_2 and FeO enrichment and CaO depletion in the melt is consistent with progressive Cpx crystallization and lack of significant Fe-Ti oxide formation. The elevated Mg# reflects extensive dunite dissolution. Crystallization of Cpx probably decreased the total amount of Mg in the melt given the high Mg# of the pyroxene cores and size of the crystals and low Mg# of the hybridized interstitial melt (i.e., 9.08 ± 0.74).

As in other experiments in this study, the boundary between the IBC and dunite sides of the experiment exhibits evidence of solid-state diffusive exchange. The Cpx at the interface in the IBC side of the reaction couple has an elevated Mg# of ~71. Olivine in the dunite side of the couple is more Fa normative near the interface (Fo ~82).

1.4 Discussion

Here we discuss dissolution-precipitation reactions, followed by an analysis of rates of dissolution and diffusive exchange reactions, and veining. Then we discuss phase equilibria in the subsolidus experiments.

1.4.1 Dissolution-precipitation reactions and IBC liquid crystallization

1.4.1.1 Dunite Assimilation

Propagation of the reaction interface into the dunite and elevated Mg#s of residual melts in experiments MRx#5, MRx#9, MRx#10, and MRx#13 demonstrate a dissolution

reaction produced by Fe-rich melt in contact with an Mg-rich dunite. Dunite dissolution is anticipated according to the low-Mg# (i.e., 25) mare basalt olivine-wollastonite-quartz ternary diagram from Longhi (1991) (**Figure 1.7**). The initial IBC composition is augite normative and plots above the olivine-augite cotectic (**Figure 1.7**). Since the IBC is at supersolidus temperatures in these experiments, olivine dissolves into the IBC melt as the system reacts and equilibrates. This drives the IBC melt towards a more olivine normative composition, shifting the composition toward the olivine-augite cotectic (**Figure 1.7**). This reaction proceeds following Eq 1.1:

$$IBC\ Melt + \ Olivine \ \rightarrow \ Hybridized\ Melt \pm Clinopyroxene, \qquad (1.1)$$

with olivine dissolution progressing until eventual olivine saturation in the hybridized melt. This hybridization process can be modeled by assuming modal mixing between the initial IBC composition and the dunite. Melt compositions from experiments MRx#5 and MRx#10 are consistent with 10-15% dunite assimilation, while melt compositions from MRx#9 are consistent with 0-5% assimilation (**Figure 1.7**). Most melt compositions from experiments MRx#5 (6 hr) and MRx#10 (24 hr) cluster around the olivine-augite cotectic, and the estimated dissolution rates for these experiments decrease with experiment duration (**Table 1.3**). These observations suggest that dissolution occurs at rates that decrease as the melt composition approaches the olivine-augite cotectic (see section (1.4.2.2) below for further discussion).

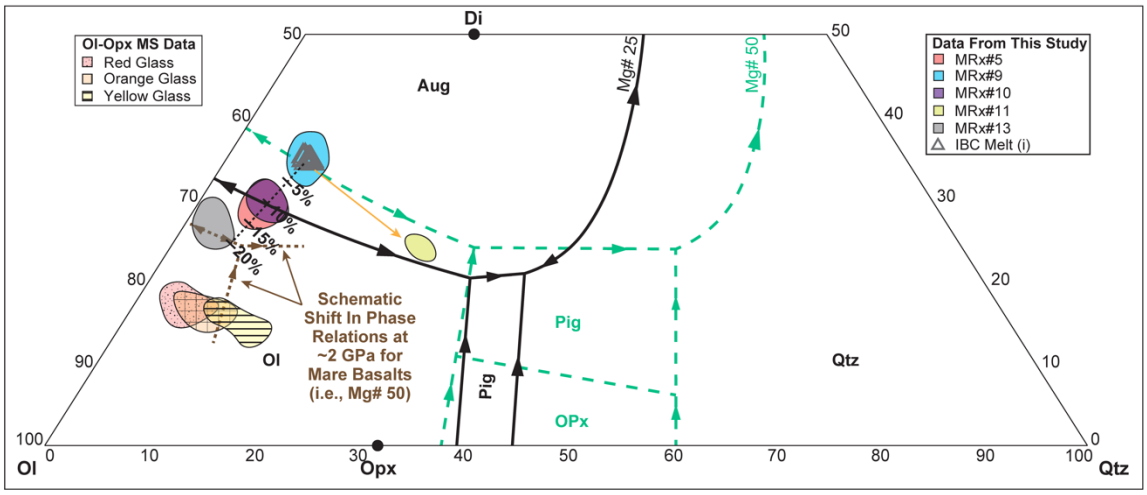


Figure 1.7. Experimental glasses plotted in relation to olivine-wollastonite-quartz basalt ternary diagrams from Longhi (1991). The thin black dotted line and shows the trajectory of a simple mixing model for modal dunite addition to the initial IBC liquid between 1% and 20%. Orange solid arrow shows the trajectory for equilibrium crystallization. Solid black phase boundaries and arrows are from basalt projections in a system with an Mg# of 25 and mare basalt relevant alkali components at atmospheric pressure. Dashed green phase boundaries and arrows are from mare basalt relevant projections in a system with an Mg# of 50 at atmospheric pressure. The brown dotted lines are schematic of a pressure related shift in the phase relations for Mg# 50 mare basalts as pressure increases. The schematic boundaries are based on the observations from lunar glass multi-saturation experiments (Krawczynski and Grove, 2012; Brown and Grove, 2015) and previous studies of basalt phase equilibria (Stolper 1980; Longhi, 1982; Elthon and Scarfe, 1984). The dotted shaded region represents experimental lunar red glass data for melts at the Ol-Opx saturation point (for pressures of 1.7-2.3 GPa) (Krawczynski and Grove, 2012). The cross-hatched shaded region represents experimental lunar orange glass data for melts at the Ol-Opx saturation point (for pressures of 1.9-2.33 GPa) (Krawczynski and Grove, 2012). The striped shaded region represents experimental lunar yellow glass data for melts at the Ol-Opx saturation point (for pressures of 1.7-2.3 GPa) (Brown and Grove, 2015). Given inferred relationships between mare basalts and lunar picritic glasses and similar Mg#s, these melts define the position of the Ol-Opx cotectic position for Mg# 50 mare basalts (dashed green lines) at pressures of 1.7-2.33 GPa. If the Ol-Opx cotectic shifts towards normative olivine as Mg# increases (as the data imply), the Ol-Pig-Aug peritectic and Ol-Aug cotectic should experience a similar shift in position given the observations from previous studies (Stolper, 1980; Longhi, 1982; Elthon and Scarfe, 1984). Phases: Olivine (Ol), Orthopyroxene (Opx), Diopside (Di), Augite (Aug), Pigeonite (Pig), Quartz (Qtz).

As dissolution proceeds, the Mg# of the reacting melt increases. It is well known that Mg# variations cause phase boundaries to shift, and stability fields of phases can shrink or expand (e.g., Stolper and Walker, 1980; Longhi, 1982, 1991; Elthon and Scarfe, 1984) (**Figure 1.7**). Previous studies indicate that the olivine-low Ca pyroxene-augite peritectic shifts toward olivine as pressure increases. Similarly, increasing pressure shifts the olivine-augite cotectic downward toward the olivine-silica binary on the phase diagram (**Figure 1.7**).

1.4.1.2 Crystallization in the IBC melt

Experiment MRx#11 lacks evidence of dunite dissolution and contains a significant melt fraction, in addition to Cpx and ulvöspinel (**Figure A6**). Melt from this experiment plots between the IBC starting material and the Mg# 25 ternary olivine-pigeonite-augite peritectic, which indicates that the melt is evolving toward the peritectic (**Figure 1.7**). This shift in composition is consistent with the growth of sizeable euhedral pyroxene and ulvöspinel observed in the experiment.

MRx#13 likely reflects the effects of crystallization after dissolution based on the large size and euhedral morphology of pyroxene crystals from that experiment. Given the extensive pyroxene crystallization observed in MRx#13, the melt is likely at or near the 2 GPa olivine-augite cotectic (**Figure 1.7**) and beginning to evolve to the left (down temperature from a thermal maximum) along the cotectic as crystallization progresses, consistent with predicted evolution trajectories from previous studies. It is difficult to determine how the MRx#13 melt might continue to evolve; however, we speculate that the TiO_2 and FeO enrichment observed in MRx#13 would eventually result in the

stabilization of an Fe-Ti oxide phase. Stabilization of the Fe-Ti oxide would enrich melt in Al_2O_3 and SiO_2 and eventually stabilize an aluminosilicate, perhaps garnet at the conditions of the experimental run, forming a hybridized lunar eclogite (see section (1.4.3) below for further discussion). Further experimental work is required to evaluate this hypothesis.

1.4.2 Dissolution, Diffusion, and Advection

1.4.2.1 Solid-State Diffusion

Near solidus experiments MRx#1, MRx#3, and MRx#8 exhibit compositional variations across the IBC (Cpx) and dunite (olivine) sides of the reaction couple interface consistent with diffusive exchange, with Mg-enriched pyroxene on the IBC side and Fe-enriched olivine on the dunite side. Supersolidus experiments MRx#10, MRx#11, and MRx#12 also exhibit compositional variations on the dunite side of the reaction interface, with Fe-enriched olivine at the interface boundary. However, given the complexity of dissolution shifting the IBC-dunite interface location, crystallization at the interface changing the melt composition, and the multi-step nature of some experiments, no attempt was made to model diffusive interaction for experiments MRx#10, MRx#11, MRx#12, and MRx#13. Diffusive exchange models are applied to near solidus experiments MRx#1 and MRx#8.

In MRx#1 and MRx#8, the IBC side of the couple exhibits a downward shift in Fe/(Fe+Mg)x100, while the dunite side of the couple exhibits an upward shift (**Figure 1.8**). Both experiments exhibit similar interface conditions with compositional variations trending toward molar Fe/(Fe+Mg)x100 values between 40 and 50.

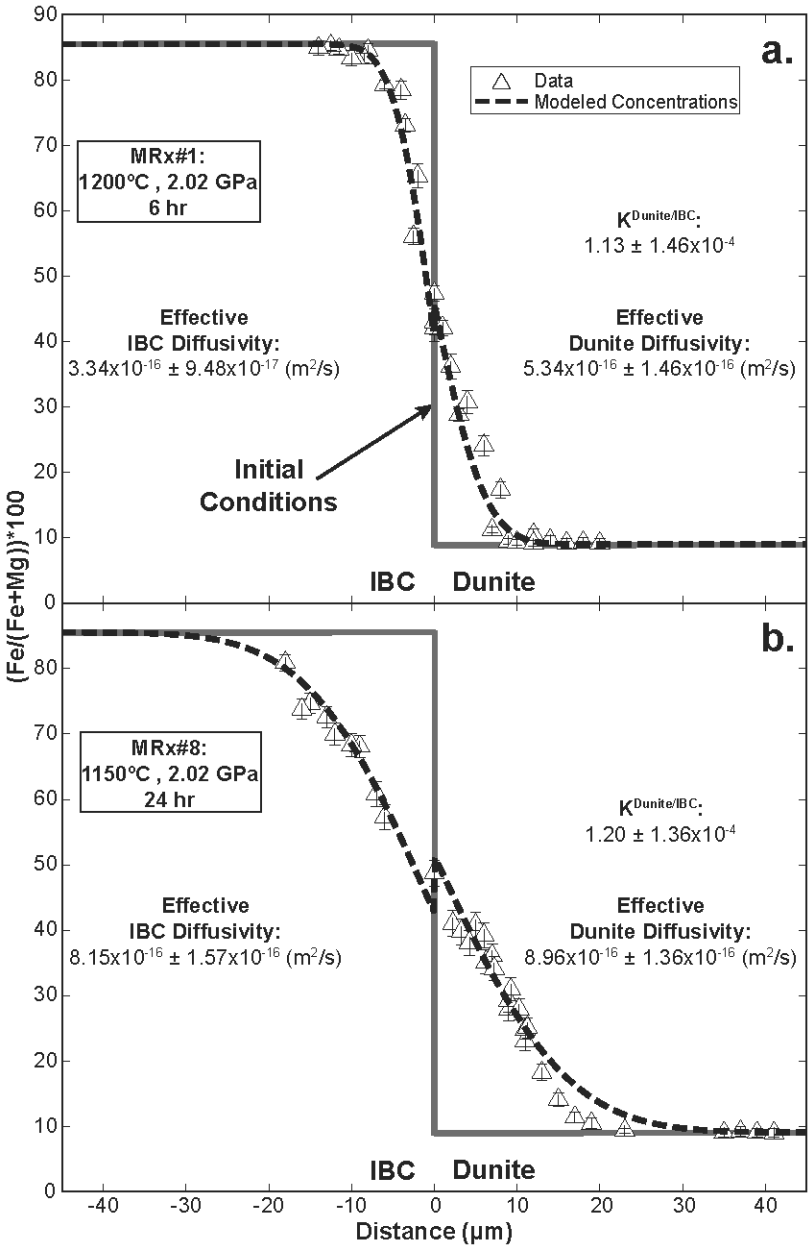


Figure 1.8. Fe-Mg exchange profiles across the IBC-dunite interface from near solidus experiments. (a) Fe-Mg exchange profile from experiment MRx#1. (b) Fe-Mg exchange profile from experiment MRx#8. Gray solid lines show the initial conditions prior to reaction. Dashed lines are modeled concentration profiles for the reaction couple.

Compositional variations in 24 hr experiment MRx#8 (1150°C) are approximately twice the width of the variations in 6 hr experiment MRx#1 (1200°C), 1150°C vs 1200°C respectively. These compositional variations were modeled using an analytical solution to the one-dimensional diffusion equation assuming exchange between two semi-infinite media with differing diffusivities and a partitioning relationship across the interface (Zhang, 2009) (see Appendix A for further details). From MRx#1, we recover an effective diffusivity of $5.34 \times 10^{-16} \pm 1.46 \times 10^{-16}$ m^2/s in the dunite and $3.34 \times 10^{-16} \pm 9.48 \times 10^{-17}$ m^2/s in the IBC (**Figure 1.8a**). The model for MRx#8 recovers an effective diffusivity of $8.96 \times 10^{-16} \pm 1.36 \times 10^{-16}$ m^2/s in the dunite and $8.15 \times 10^{-16} \pm 1.57 \times 10^{-16}$ m^2/s in the IBC (**Figure 1.8b**).

The Fe-Mg diffusion rates for IBC determined by this study are three to four orders of magnitude faster than anticipated at 1200°C to 1100°C for Cpx according to volume diffusion studies (Brady and McCallister, 1983; Fujino et al.1990; Azough and Freer, 2000; Zhang et al., 2010a; Muller et al., 2013). Fe-Mg diffusion in garnet is faster than Cpx; however, the IBC exchange rates from this study are still one to two orders of magnitude faster at the relevant temperatures (Loomis et al., 1985; Chakraborty and Ganguly, 1992; Chakraborty and Rubie, 1996; Ganguly et al., 1998; Perchuk et al., 2009; Borinski et al., 2012; Li et al., 2018). It is possible that the Fe-rich compositions of minerals within the IBC material accelerate diffusive exchange relative to the existing experiments on more magnesian materials, as diffusion through Fe-rich endmembers is often faster than diffusion through Mg-rich endmembers (e.g., Buening and Buseck, 1973; Nakamura and Schmalzried, 1984; Chakraborty, 1997; Dohmen and Chakraborty,

2007). The presence of trace amounts of interstitial melt and polycrystalline nature of the IBC may also affect the diffusion rates on the IBC side of the reaction couple. Grain boundary diffusion is expected to be three orders of magnitude faster than volume diffusion (Farver et al., 1994).

Dunite Fe-Mg diffusion rates determined for MRx#1 and MRx#8 fall within the range of diffusivities determined from previous experimental studies at temperatures between 1200°C and 1100 °C (i.e., 10^{-14} to 10^{-17} m^2/s) (Jurewicz and Watson, 1988; Chakraborty et al., 1994; Chakraborty, 1997; Petry et al., 2004; Dimanov and Wiedenbeck, 2006; Dohmen and Chakraborty, 2007). Faster diffusion rates in MRx#8 appear inconsistent with the 50°C temperature difference between MRx#1 (1200°C) and MRx#8 (1150°C). According to previous olivine diffusion studies, the diffusion rates should be about half an order of magnitude faster in MRx#1 if temperature is the only factor affecting the rate. We interpret the results as demonstrating the dependence of diffusion rate on olivine Fe/Mg content, with fayalitic olivine exchanging Fe for Mg about three orders of magnitude faster than forsterite (Chakraborty, 1997; Dohmen and Chakraborty, 2007). The higher iron content in the diffusive boundary layer increases the exchange rate such that longer experiments have faster effective diffusion rates.

1.4.2.2 Dunite Dissolution Rates, and Effects of Dunite Dissolution on IBC Liquid

Constant temperature (1200°C), low-pressure (0.55 GPa) experiments run for 20 min (MRx#9), 6 hr (MRx#5), and 24 hr (MRx#10) enable us to investigate the dunite dissolution rate as a function of time and compare compositional variations in the coexisting IBC melt affected by dissolution. In the IBC melt, MRx#5 and MRx#10

exhibit unusual MgO, Al_2O_3, and TiO_2 concentration variations that peak ~100-200 (μm) away from the reaction interface, consistent with uphill diffusion. The concentrations of these elements then decline as approximately linear trends away from the peaks toward the end of the IBC half of the reaction couple (**Figures 1.9a, 1.9d-e**). CaO concentrations exhibit similar trends with the lowest concentrations ~100-200 (μm) away from the reaction interface and concentrations that ascend linearly toward the end of the IBC half of the reaction couple (**Figure 1.9f**). These compositional variations may be produced by multi-component diffusion effects, where coupled concentration variations affect diffusion rates and elemental variations (e.g., Zhang, 1993; Morgan et al., 2006; Van Der Laan et al., 1994; Zhang et al., 2010b; Liang, 2010). Modeling multi-component diffusion is beyond the scope of this study.

Dissolution of olivine in the dunite occurs quickly causing the MgO mol% in the IBC melt near the interface to increase to 5.03 ± 0.30 in the 0.33 hr experiment (**Figure 1.9a**, **Table 1.5**). Chemical profiles from MRx#9 were modeled using an analytical solution for one-dimensional diffusion-controlled dissolution into a semi-infinite melt reservoir (e.g., Zhang et al., 1989; Van Orman and Grove, 2000) (**Figure 1.9**) (see Appendix A for further calculation details). Effective binary diffusion coefficients for MgO, FeO, MnO, Al_2O_3, TiO_2, and CaO in the IBC melt were inverted from the compositional observations by a nonlinear least squares regression. The inverted EBDCs of MgO, FeO, MnO, Al_2O_3, TiO_2, and CaO in the IBC melt at 1200°C and 0.55 GPa, all fall between 10^{-10} and 10^{-11} m^2/s, respectively based on data from MRx#9 (**Table 1.5**).

Table 1.5. Effective binary diffusion coefficients (EBDC) of MgO, FeO, MnO, Al_2O_3, TiO_2, and CaO for dunite dissolution in IBC melt at 1200ºC, 0.55 GPa.

	MgO		FeO		MnO		Al_2O_3	
	val.	1**σ**	val.	1**σ**	val.	1**σ**	val.	1**σ**
EBDC (m^2/s)	9.84E-11	1.36E-11	9.67E-11	5.28E-11	3.83E-11	3.57E-11	3.00E-11	1.29E-11
C_0 (mol%)	5.03	0.30	25.61	0.98	0.81	0.12	3.57	0.17
a	0.035	0.003	0.081	0.091	0.120	0.081	0.067	0.004
Dissolution rate ($g\ m^{-2}\ s^{-1/2}$)	1.15	0.13	2.62	3.03	2.43	2.00	1.21	0.27
Average dissolution rate ($g\ m^{-2}\ s^{-1/2}$)	1.84	0.68						

Table 1.5. Continued.

	TiO_2		CaO	
	val.	1**σ**	val.	1**σ**
EBDC (m^2/s)	2.56E-11	1.86E-11	2.02E-11	2.49E-11
C_0 (mol%)	4.54	0.74	13.99	3.66
a	0.125	0.050	0.105	0.079
Dissolution rate ($g\ m^{-2}\ s^{-1/2}$)	2.08	1.12	1.55	1.51
Average dissolution rate ($g\ m^{-2}\ s^{-1/2}$)				

For dissolution rate calculations the estimated melt ρ= 3.286 (g/cm^3). This was determined using the method of Bottinga and Weill (1970). Volume, thermal expansion, and compressibility data from Lange and Carmichael (1987) and Kress and Carmichael (1991) were used for the calculation.

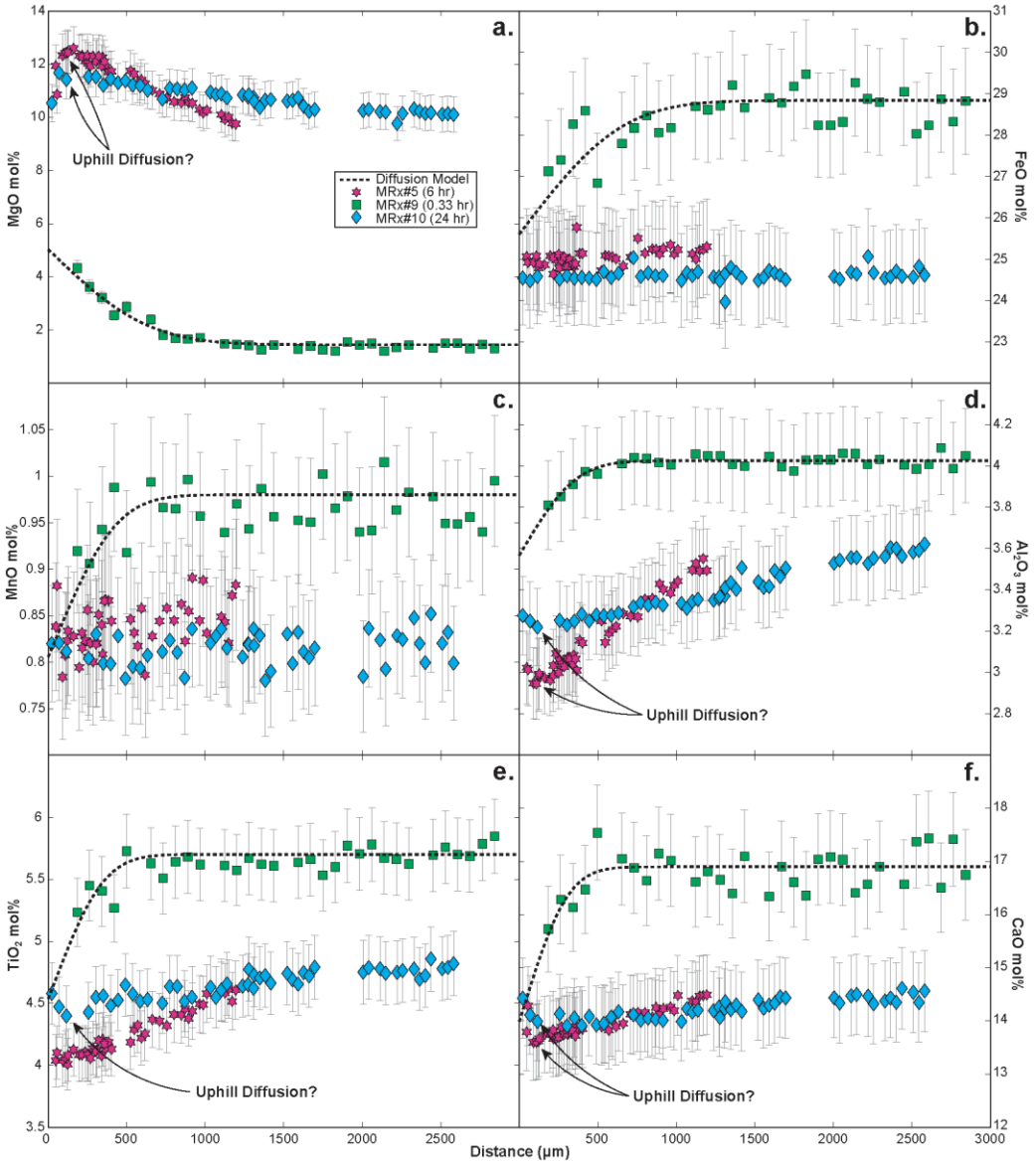


Figure 1.9. Elemental concentration profiles in the IBC melt from the reaction interface (i.e., 0 µm) to the top of the experiment (or top of the glass-dominated region of the experiment). Modeled diffusion profiles for MRx#9 with respect to (a) MgO, (b) FeO, (c) MnO, (d) Al_2O_3, (e) TiO_2, and (f) CaO mol% are represented by the dashed line. In contrast to experiment MRx#9, MRx#5 and MRx#10 exhibit (b) MgO, (d) Al_2O_3, (e) TiO_2, and (f) CaO variations consistent with uphill diffusion at the melt-rock interface, these experiments were run for hours whereas MRx#9 was run for 20 minutes (see legend). Distances for MRx#5, MRx#9, and MRx#10 data were determined by measuring the distance between the reaction interface and first point of the chemical transect. Sizable fractures were present near the interface of MRx#9 and ~1800 µm from the interface in MRx#10 resulting in data gaps. Parameters recovered from MRx#9 diffusion model fits can be found in Table 1.5. All experiments in this figure were run at 0.55 GPa and 1200 ºC.

Van Orman and Grove (2000) calculate similar EBDCs of $1.92x10^{-10} \pm 7.7x10^{-11}$ m^2/s for MgO, $2.5x10^{-11} \pm 6.3x10^{-12}$ m^2/s for Al_2O_3, and $2.87x10^{-11} \pm 1.0x10^{-11}$ m^2/s for TiO_2 at a higher temperature of 1350°C and 1.3 GPa for an analogous melt composition. Using the calculated EBDCs and the relationship between EBDC, mineral density, and the dimensionless parameter a described in Zhang et al. (1989), we estimate a mean dissolution rate of 2.07 ± 0.87 $gm^{-2}s^{-1/2}$ for dunite in MRx#9, within uncertainty of measured mean dissolution rate of 2.18 ± 0.59 $gm^{-2}s^{-1/2}$ for diopside determined by Van Orman and Grove (2000).

Observing the change between the melt-rock interface position before and after the reaction experiments, we estimated the rate of interface retreat with respect experiment duration (**Figure 1.10**) (**Table 1.3**). These data indicate that the rate of interface retreat decreases as experimental duration increases (i.e., dunite dissolution slows over longer periods of time). We speculate that the decreasing dissolution rate is related to the degree of undersaturation of olivine in the IBC melt as it approaches the augite-olivine cotectic (Eq. 1.1). A similar change in dissolution rate was previously observed in low-temperature experimental studies, e.g., labradorite and gibbsite dissolution experiments, where the rate of dissolution decreased by a factor of ~4.5 as the saturation of the mineral in the solution increased (Nagy and Lasaga, 1992; Taylor et al., 2000). The changing dissolution rate may also explain the lack of concentration variations in the dunite along the reaction interface of experiments MRx#9 and MRx#5. The rate of dunite dissolution in these experiments may exceed the rate of diffusive exchange within the dunite, so a diffusive exchange layer never forms in the dunite.

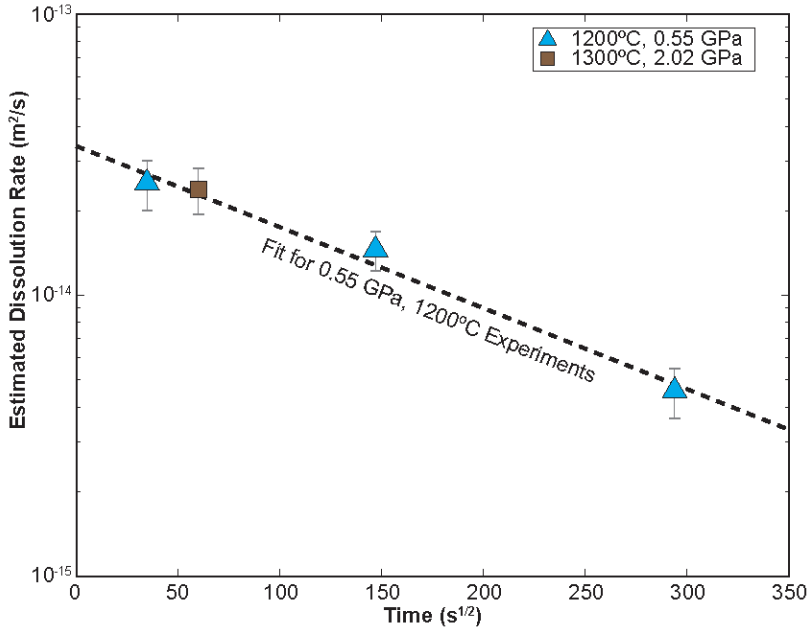


Figure 1.10. Dunite dissolution rates plotted against the square root of time. Experiment MRx#12 was used to calculate the dunite dissolution rate at 1300°C and 2.02 GPa. Experiments MRx#5, MRx#9, and MRx#10 were used to calculate rates at 1200°C and 0.55 GPa.

Concentration variations along the dunite interface of MRx#10 formed because the melt became closer to olivine saturation, at which point the rate of diffusion in olivine exceeded the rate of dunite dissolution.

1.4.2.3 Vein Formation

The formation of veins along the IBC-dunite reaction interface in supersolidus experiments highlights the possible importance of advective infiltration mechanisms on lunar mantle hybridization. Melt infiltration features are often observed at the reaction interface in experimental studies exploring melt-rock reaction (Morgan and Liang, 2003, 2005; Beck et al., 2006; Van Den Bleeken et al., 2010; Pec et al., 2020). These features are similar in scale to the veins in this study but are typically associated with pyroxene dissolution. Veins in MRx#12 appear to follow grain boundaries toward triple junctions (**Figure A7**). We speculate that olivine grain boundaries provide a permeable path for IBC melt to infiltrate the dunite and enhance the dissolution rate. This infiltration and dissolution process explains the jagged texture along the dunite interface. As grain boundaries dissolve, smaller residual cores are left behind.

1.4.3 Phase Equilibria

Supersolidus and near solidus experiments MRx#1, MRx#3, MRx#8, and MRx#11 suggest that both Fe-Ti oxide and silicate mineral phase transitions occur at temperatures between 1100ºC and 1150ºC and pressures above 2.1 GPa (**Figure 1.11**). Below, we compare the observations from this study and previous experimental studies and discuss their implications for IBC phase equilibria.

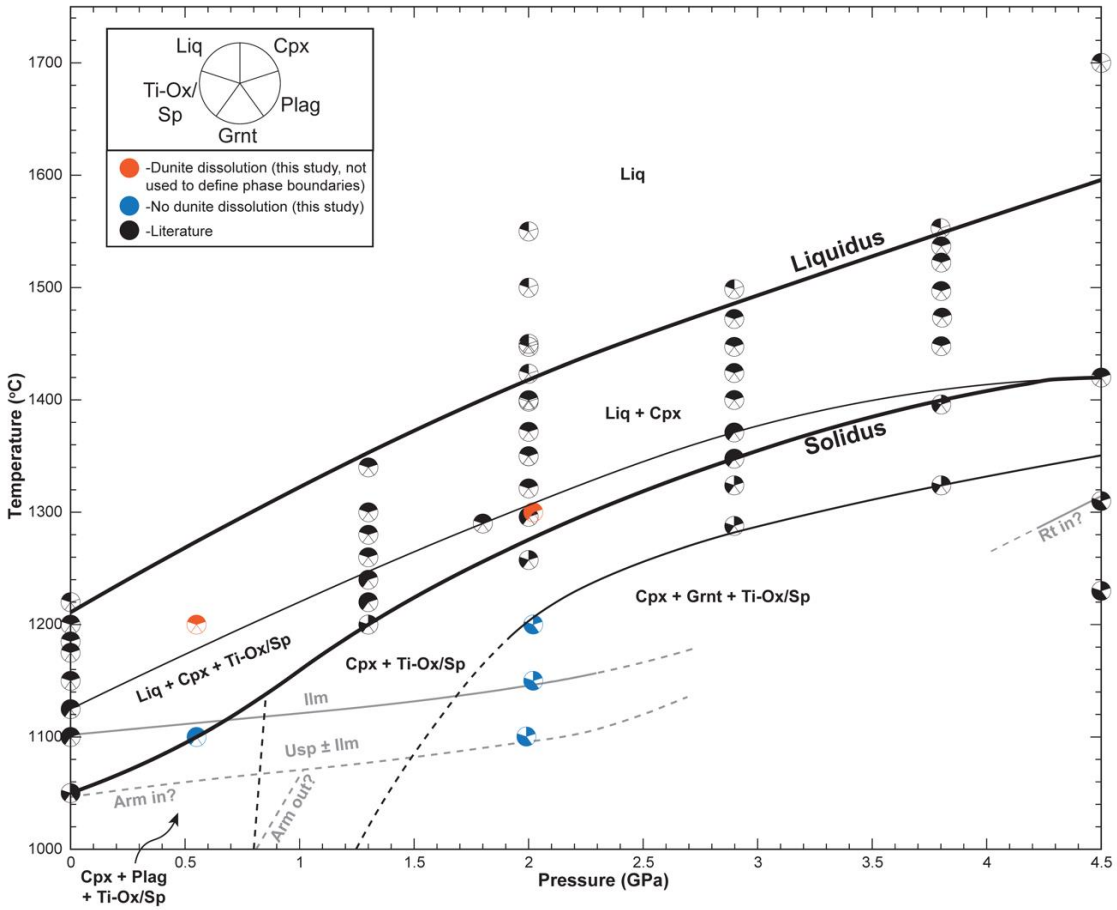


Figure 1.11. Ilmenite bearing cumulate phase diagram based on the observations from this work and previous experimental studies testing IBC and Ti-rich lunar relevant compositions (Haggerty and Lindsley, 1970; Friel et al., 1977; Wyatt, 1977; Van Orman and Grove, 2000; Xirouchakis et al., 2002; Mallik et al., 2019). New experimental data from this study are blue and orange points representing experiments that did not and did exhibit dunite dissolution, respectively. Literature data are shown in black (Wyatt, 1977; Van Orman and Grove, 2000; Mallik et al., 2019). Experiments which resulted in dunite dissolution (orange) were not used to determine phase boundaries for the IBC. Black lines represent silicate assemblage boundaries ± oxides while gray lines indicate Fe-Ti oxide boundaries. Solid lines represent boundaries estimated using data from experiments conducted on IBC-related compositions. Solidus and liquidus are shown as thicker lines. Dashed lines represent phase boundaries inferred from non-IBC specific studies or trajectories of solid lines. Armalcolite phase boundaries in the lower left corner of the diagram are based on the results of Haggerty and Lindsley (1970), Friel et al. (1977), Xirouchakis et al. (2002), and Thacker et al. (2009). Dashed plagioclase stability boundary in the lower left corner of the diagram is an extrapolation based on the plagioclase stability boundary in the modeled TWM phase diagram from Johnson et al. (2021). Phases: Liquid (Liq), Clinopyroxene (Cpx), Plagioclase (Plag), Garnet (Grnt), Fe-Ti Oxide or Spinel (Ti-Ox/Sp), Ilmenite (Ilm), Ulvöspinel (Usp), Armalcolite (Arm), Rutile (Rt).

1.4.3.1 Fe-Ti Oxides

Results from this study and previous work (Van Orman and Grove, 2000; Thacker et al., 2009; Mallik et al., 2019) suggest ulvöspinel stability is temperature dependent, with ulvöspinel absent in high-temperature experiments. Ulvöspinel is absent at 1050°C and 0.0001 GPa (Van Orman and Grove, 2000) and in the 2 GPa experiments from Mallik et al. (2019) and the current study conducted above 1100°C. Existing experimental data show no clear preference for either oxide between 1050°C and 1100°C; however, this may be related to compositional variations in the starting material (i.e., the higher FeO and lower TiO_2 composition in this study (**Table 1.1**) or the fO_2 conditions of the experiments (Anovitz et al., 1985; Shepherd et al., 2022). Given the absence of ulvöspinel in higher temperature experiments, we infer that ilmenite is the only oxide present at temperatures above ~1110°C at atmospheric pressure and ~1140°C at 2 GPa. At P-T conditions beneath the ilmenite-only stability field (i.e., <1110°C at atmospheric pressure and <1140°C at 2 GPa), we infer that ilmenite and ulvöspinel can coexist (**Figure 1.11**).

Armalcolite is a common Fe-Ti oxide observed in lunar rocks (Haggerty, 1973), but was not observed in the experiments from this study. If we consider the results of MgO-FeO-Fe_2O_3-TiO_2 and FeO-Fe_2O_3-TiO_2 system experiments (Haggerty and Lindsley, 1970; Friel et al., 1977), thermodynamic models (Xirouchakis et al., 2002; Xirouchikis, 2007), and peridotitic experiments of Thacker et al. (2009), armalcolite would be expected in MRx#11; however, its absence in this experiment and similar experiments reported by Van Orman and Grove (2000) indicate that armalcolite is not stable within

the IBC-like systems at near-solidus conditions. With a lower metal:anion proportion than ilmenite, the stability of armalcolite may be fO_2-dependent. Experiments of Shepherd et al. (2022), stabilized armalcolite in Ti-rich ferrobasaltic at fO_2 >FMQ, but not at lower, lunar relevant, fO_2 conditions.

1.4.3.2 Garnet

Garnet in the IBC side of the reaction couple at ~2 GPa is novel but may be anticipated given the stability of garnet in terrestrial mafic granulites and eclogites at pressures of ~1.5-2.0 GPa (Cohen et al., 1967; Ito and Kennedy, 1971; Springer and Seck, 1997), which have a bulk composition comparable to the IBC material explored here. Mallik et al. (2019) show that garnet can be stable in an IBC cumulate and synthetic hybridized mantle sources; however, this was at pressures of ~4.5 GPa (i.e., analogous to the lunar core-mantle boundary). Multi-saturation experiments of red and green picritic glasses and Apollo 17 mare basalts indicate that garnet may be stable in the lunar mantle at pressures slightly above 2 GPa (Longhi et al., 1974; Elkins-Tanton et al., 2003; Krawczynski and Grove, 2012; Barr and Grove, 2013). THERMOCALC models for lunar primitive upper mantle (LPUM) and Taylor whole moon (TWM) compositions presented in Johnson et al. (2021) suggest that the garnet stability field may extend closer to ~1.25 GPa at 1000 °C.

Garnets produced in our experiments are almandine normative relative to terrestrial garnets and garnets from previous experimental lunar studies (**Figure 1.4**). This is a consequence of the low Mg# of starting the IBC composition (**Table 1.1**). While the lower Mg# decreases the solidus temperature of the IBC composition in this study

relative to previous work, the new results and literature suggest it has a negligible effect on the pressure at which garnet becomes stable (Longhi et al., 1974; Elkins-Tanton et al., 2003; Krawczynski and Grove, 2012; Barr and Grove, 2013). Considering these results, we infer garnet will be stable in overturned IBC in the lunar interior at pressures around 2 GPa; however, garnet stability may extend toward lower P-T conditions (**Figure 1.11**). This is significant as garnet is not predicted to be a product of lunar magma ocean solidification for bulk Moon compositions with Al_2O_3 contents in agreement with crustal thickness constraints (i.e., LPUM; Elardo et al., 2011; Taylor and Wieczorek, 2014; Charlier et al., 2018). Formation of metamorphic garnet in downwelling IBC during cumulate mantle overturn represents a plausible mechanism for delivering geochemical signatures of garnet to hybridized lunar basalt source regions. This is discussed further in Metamorphic Reactions section below.

1.5 Implications for the Lunar Mantle

Density-driven overturn of late crystallizing IBC would juxtapose the IBC material and mafic early crystallizing LMO cumulates, promoting metamorphic reactions, melting, mineral dissolution, thermal diffusion, and elemental diffusion that led to hybridization of lunar mantle basalt sources. Mechanical mixing due to cumulate overturn or subsequent convective stirring would further mix lunar basalt sources. In this section, we discuss the first-order implications of melt-rock experiments from this study concerning chemical implications of lunar cumulate overturn.

1.5.1 Metamorphic Reactions

Our experiments demonstrate that metamorphic reactions would change the mineralogy of downwelling cumulates during an overturn event. Considering the Fe-Ti oxide phase stability boundaries (**Figure 1.11**), ilmenite is likely the primary oxide phase within the cumulate during cumulate overturn (assuming the thermal profiles from previous studies are reasonable; Elkins-Tanton et al., 2011; Lin et al., 2016; Zhang et al., 2017) (**Figure A8**). Ulvöspinel may be present in the IBC at lower pressures (i.e., before overturn or early in the overturn process); however, the temperature increase which the IBC would experience during overturn makes it unlikely to be stable beyond ~200 km depth in the lunar interior (i.e., 1 GPa). The near-solidus experiments demonstrate the stability of garnet in downwelling IBC under lunar conditions, in contrast to expectations from lunar magma ocean solidification experiments, which found it was only stabilized in the lunar mantle for unrealistically aluminous bulk Moon compositions (Elardo et al., 2011; Jing et al., 2022, Kraettli et al., 2022).

Garnet stability is dependent on the Al_2O_3 abundance of the system and should thereby be affected by the efficiency of plagioclase floatation during magma ocean solidification (e.g., Dygert et al., 2017; Charlier et al., 2018), as more efficient flotation would produce a less aluminous downwelling IBC cumulates. Interestingly, the garnet stability field for the IBC in this study overlaps with the Ol-Opx multi-saturation pressures for lunar picritic glasses (**Figure A8**; Elkins-Tanton et al., 2003; Draper et al., 2006; Krawczynski and Grove, 2012; Barr and Grove, 2013; Brown and Grove, 2015). As stated in the introduction, multiple studies have suggested that the lunar mare basalts

and picritic glasses are the result of mixing between initially deep Mg-rich sources and initially shallow Ti-rich sources in the lunar cumulate pile (Hess and Parmentier, 1995; Van Orman and Grove, 2000; Elkins-Tanton et al., 2002; Longhi, 2006; Singletary and Grove, 2008; Mallik et al., 2019). A downwelling Al and Ti-rich garnet-bearing IBC could mechanically or reactively (by assimilation or diffusive exchange) mix with underlying mafic cumulates and result in the formation of a hybridized source capable of generating mare basalts.

Partial melting of downwelling, garnet-bearing IBC would hybridize the surrounding mantle with melts that have a residual garnet trace element signature, analogous to terrestrial granulite facies melting (Cohen et al., 1967; Springer and Seck, 1997). The results of this study provide strong support for the melting of a metamorphosed IBC, a hybridization mechanism previously suggested by Schmidt and Kraettlli (2022). Beard et al. (1998) argue that the extreme Lu/Hf fractionation observed in mare basalts can be best explained by the melting of a garnet-bearing source followed by continued melting in the spinel stability field. The fractionated REE-patterns with $(Sm/Yb)_N$ up to 3.5 in some of some lunar glasses have been argued to originate from a garnet-bearing source (Neal, 2001). Stabilization of garnet in downwelling IBC provides a mechanism for forming it in the sources of these basalts.

1.5.2 Formation of Hybridized Mantle Sources

Hybridization of the lunar mantle during cumulate overturn likely happens by multiple processes. The downwelling IBC would produce melts as the IBC descended and sank through the hot underlying mantle, increasing in temperature (**Figure A8**).

Results from this study show that IBC melts would be significantly undersaturated with respect to forsteritic olivine, and interactions with the underlying Mg-rich cumulates would result in rapid dissolution. As dissolution progresses, the degree of olivine undersaturation in the IBC melt decreases, and a Mg-enriched hybridized melt forms (Eq. 1.1).

If we assume that olivine is present in the picritic glass source (Longhi et al., 1974; Walker et al., 1977; Delano, 1980, 1986; Elkins-Tanton et al., 2003, Grove and Krawczynski, 2009) and the olivine-liquid $K_{D(Fe/Mg)} \approx 0.34$-$0.23$ (depending on the TiO_2 concentration within the melt) (Roeder and Emslie, 1970; Longhi et al., 1978; Delano, 1980; Xirouchakis et al., 2001; Canil and Bellis, 2008; Krawczynski and Grove, 2012), the picritic glass sources should have Mg# ~68-87. Thus, if mantle hybridization during overturn formed the sources of lunar picritic glasses, the hybridized source must reach compositions containing≥47% normative dunite (**Figure 1.12**). The range of compositions in IBC melts for dissolution experiments MRx#5 and MRx#10 indicate that the IBC material incorporated ~10-15% dunite (**Figures 1.8 and 1.12**). This suggests that 10-15% of dissolution-driven hybridization could occur relatively quickly (i.e., hours to days); however, observations from this study indicate that the hybridization rate may slow significantly after this initial stage. As the degree of olivine undersaturation decreases, the rate of dunite dissolution decreases (**Figures 1.7 and 1.10**) (e.g., Watson, 1982; Zhang et al., 1989; Watson and Baker, 1991; Nagy and Lasaga, 1992; Kerr, 1995; Liang, 2000; Taylor et al., 2000; Zhang and Xu, 2003; Liang, 2010).

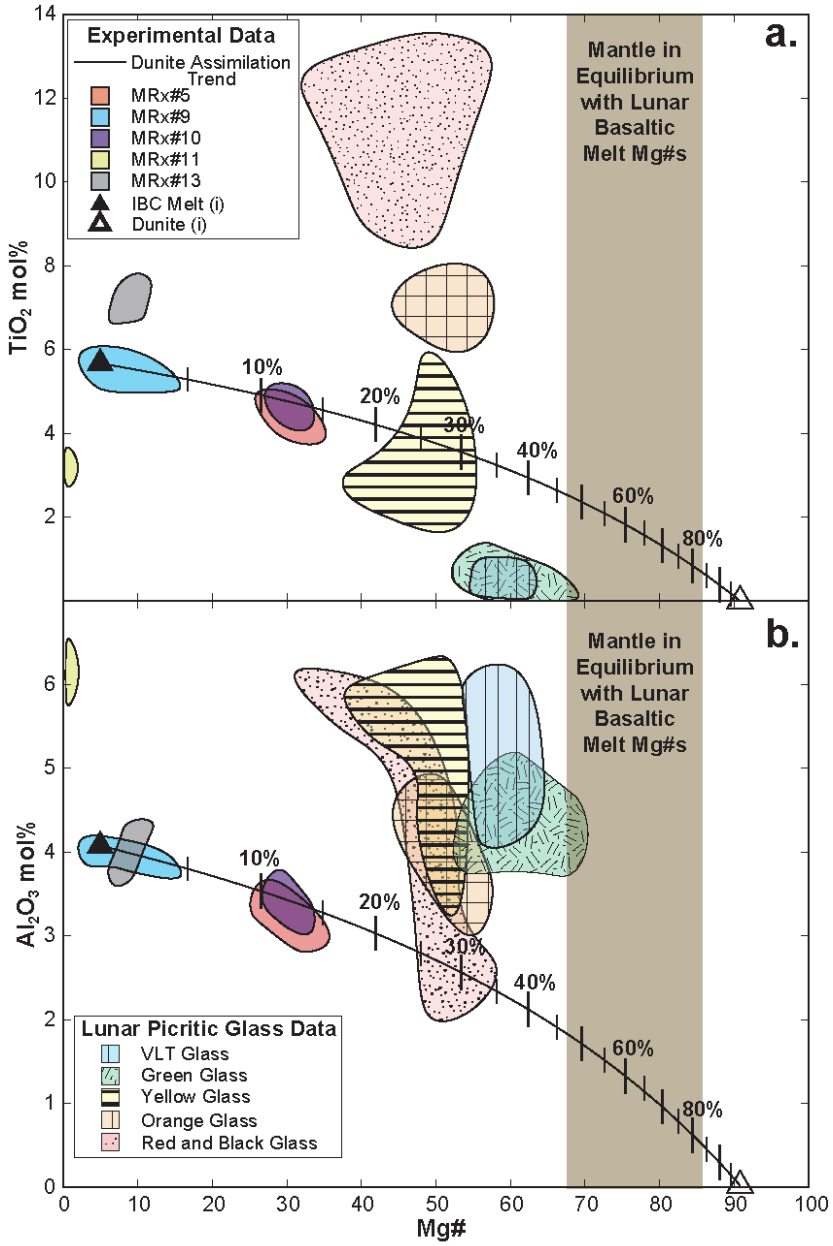


Figure 1.12. Comparison of glasses from melt-rock reaction experiments to lunar picritic glasses (TiO_2 mol% vs Mg# (a.) and Al_2O_3 mol% vs Mg#(b.)). Initial IBC melt composition (filled triangle) and initial dunite composition (open triangle) are located at the ends of a calculated dunite assimilation line (black). Percentages represent the amount of dunite assimilated by the IBC melt relative to the initial mass of the IBC melt. Shaded region each plot represents the range of lunar basalt mantle source Mg#s assuming a $K_{D\,Ol-Liq}^{Fe-Mg} \approx 0.34$-$0.23$, depending on the TiO_2 concentration (Roeder and Emslie, 1970; Longhi et al., 1978; Delano, 1980; Xirouchakis et al., 2001; Canil and Bellis, 2008; Krawczynski and Grove, 2012). Lunar data were compiled from Hughes et al. (1990), Shearer et al. (1991), and Shearer and Papike (1993).

Dunite dissolution will only be an effective hybridization mechanism if the composition of melt near the interface remains olivine undersaturated. Replenishment of IBC melt to the dunite-melt interface would be achieved by porous flow or solid-state advection away from the interface.

Comparing the estimated rates of dissolution (**Figure 1.10**) and diffusion (**Figure 1.9**) from this study (see section (1.4.2.) above for further discussion), at the experimental conditions, diffusive exchange is at least two orders of magnitude slower than dissolution. Given estimated age of the Moon (i.e., ~4.45 Ga: Borg and Carlson, 2023 and references therein), bounds on timescales of LMO solidification (i.e., 1000 yr -400 myr after accretion: Solomon and Longhi, 1977; Elkins-Tanton et al., 2011, Maurice et al., 2020, 2024), bounds on timescales for cumulate overturn events (i.e., 10-600 myr after IBC formation: Zhang et al., 2017; Li et al., 2019; Maurice et al., 2024), and age range of High-Ti mare basalts (i.e., ~3.89-3.61 Ga; Unruh et al., 1984; Paces et al., 1991; Beard et al., 1998; Sprung et al., 2013; Borg et al., 2019), the formation of lunar basalt sources by mantle hybridization must have been achieved within tens to hundreds of millions of years. Over these timescales, diffusive exchange alone could be limited to length scales of cm to meters around the IBC material (Figure A9a). The polycrystalline nature of mantle peridotites means that grain boundary diffusion may increase diffusion rates. Enhanced effective diffusivity owing to multidomain or other diffusion effects could extend the maximum diffusion distance to a few tens of meters over 100 Myr, assuming diffusivities three orders of magnitude faster than the experimental constraints (**Figure A9b**). The efficiency of diffusive hybridization may depend on the scale of the

downwelling IBC plumes. If many plumes form over short wavelengths on the order of kms as predicted by Li et al. (2019), diffusion may be a viable hybridization mechanism over geologically relevant timescales. If the scale of the downwelling IBC instabilities is larger, other mechanisms must be invoked.

Vein formation like that observed along the IBC-dunite interface in supersolidus experiments could enhance the rate of lunar mantle hybridization process. The veins appear to exploit regions of permeability in the mantle material (i.e., the grain boundary between mineral grains). Advection of IBC material through the mantle on scales predicted by previous studies (i.e., Zhang et al., 2017, 2022; Li et al., 2019) could result in strain localization around the downwelling IBC. Strain localization would produce dynamic recrystallization, decreasing grain size in the surrounding mantle material, and producing a greater density of grain boundaries for IBC melt veins to exploit (Van der Wal et al., 1993; Dannberg et al., 2017 and references therein).

If diffusive and dissolutive hybridization mechanisms are insufficiently rapid, mechanical mixing of downwelling IBC and ambient peridotite must be invoked. Poor physical and chemical constraints on material properties related to overturn-driven hybridization make these processes difficult to evaluate. Future studies on (1) the evolving mineralogy of the IBC during P-T changes, (2) melt extraction efficiency from the IBC, (3) the density of the IBC melts, (4) rheological properties of the IBC melt, IBC solid, and surrounding mantle, and strain partitioning among them, (5) lunar mantle and IBC deformation rates, (6) thermal states of the IBC and surrounding mantle would further advance knowledge of lunar mantle hybridization processes.

1.6 Summary and Conclusions

The last phase of lunar magma ocean crystallization would produce Fe- and Ti-rich cumulates that contain dense Fe-Ti oxide phases (i.e., IBC). Fe-Ti oxide formation would make the density of these late crystallizing cumulates greater than underlying early crystallizing mafic (olivine and orthopyroxene-rich) cumulates. This gravitationally unstable density contrast would eventually result in a cumulate overturn event where the overlying IBC would sink through the early crystallizing cumulates. We experimentally investigated the chemical reactions that occur during the cumulate overturn process as downwelling IBC melts and mushes interact with early crystallizing mafic (dunite) cumulates.

Experiments run under near solidus conditions reveal that metamorphic transitions in the downwelling IBC would stabilize garnet in the IBC at pressures around 2 GPa during cumulate mantle overturn events. Near solidus experiments demonstrate solid-state diffusive exchange between the IBC material and dunite. Experiments run under supersolidus conditions demonstrate a dissolution-precipitation reaction involving dissolution of dunite and formation of a hybridized melt ± clinopyroxene, depending on the experimental conditions. In the lunar interior, similar chemical reactions may govern the mantle hybridization process. The rate of dunite dissolution is dependent on the pressure, temperature, and saturation state of olivine in the hybridizing melt. Simple kinetic models indicate that formation of volumetrically significant hybridized lunar mantle sources over geologically relevant timescales may require some amount of mechanical mixing, in addition to the chemical reaction mechanisms constrained in this

study, depending on the scale of downwelling plumes that develop in the Moon's interior during cumulate mantle overturn.

1.7 Acknowledgements

We thank A. Patchen at the University of Tennessee for his assistance with EPMA analysis, and Malcolm Rutherford at Brown University who conditioned the IBC starting materials while a conditioning furnace at the University of Tennessee was under development. The manuscript benefited greatly from the comments and suggestions of the editor Othmar Müntener, as well as, Yanhao Lin and the anonymous reviewer. This work was supported by NASA Solar System Workings award 80NSSC20K0467 to ND.

References

Anovitz, L.M., Treiman, A.H., Essene, E.J., Hemingway, B.S., Westrum, E.F., Wall, V.J., Burriel, R., and Bohlen, S.R., 1985, The heat-capacity of ilmenite and phase equilibria in the system Fe-T-O: Geochimica et Cosmochimica Acta, v. 49, p. 2027–2040, doi:10.1016/0016-7037(85)90061-4.

Azough, F., and Freer, R., 2000, Iron Diffusion in Single-Crystal Diopside: Physics and Chemistry of Minerals, v. 27, p. 732–740, doi:10.1007/s002690000119.

Barr, J.A., and Grove, T.L., 2013, Experimental petrology of the Apollo 15 group A green glasses: Melting primordial lunar mantle and magma ocean cumulate assimilation: Geochimica et Cosmochimica Acta, v. 106, p. 216–230, doi:10.1016/j.gca.2012.12.035.

Beard, B.L., Taylor, L.A., Scherer, E.E., Johnson, C.M., and Snyder, G.A., 1998, The Source Region and Melting Mineralogy of High-Titanium and Low-Titanium Lunar Basalts Deduced from Lu-Hf Isotope Data: Geochimica et Cosmochimica Acta, v. 62, p. 525–544, doi:10.1016/S0016-7037(97)00373-6.

Beck, A.R., Morgan, Z.T., Liang, Y., and Hess, P.C., 2006, Dunite channels as viable pathways for mare basalt transport in the deep lunar mantle: Geophysical Research Letters, v. 33, doi:10.1029/2005GL024008.

Borg, L.E., and Carlson, R.W., 2023, The Evolving Chronology of Moon Formation: Annual Review of Earth and Planetary Sciences, v. 51, p. 25–52, doi:10.1146/annurev-earth-031621-060538.

Borg, L.E., Gaffney, A.M., Kruijer, T.S., Marks, N.A., Sio, C.K., and Wimpenny, J., 2019, Isotopic evidence for a young lunar magma ocean: Earth and Planetary Science Letters, v. 523, p. 115706, doi:10.1016/j.epsl.2019.07.008.

Borinski, S.A., Hoppe, U., Chakraborty, S., Ganguly, J., and Bhowmik, S.K., 2012, Multicomponent diffusion in garnets I: general theoretical considerations and experimental data for Fe–Mg systems: Contributions to Mineralogy and Petrology, v. 164, p. 571–586, doi:10.1007/s00410-012-0758-0.

Bottinga, Y., and Weill, D.F., 1970, Densities of liquid silicate systems calculated from partial molar volumes of oxide components.: Amer. J. Sci., v. 269, p. 169–182, doi:10.2475/ajs.269.2.169.

Brady, J.B., and McCallister, R.H., 1983, Diffusion data for clinopyroxenes from homogenization and self-diffusion experiments: American Mineralogist, v. 68, p. 95–105.

Brown, S.M., and Grove, T.L., 2015, Origin of the Apollo 14, 15, and 17 yellow ultramafic glasses by mixing of deep cumulate remelts: Geochimica et Cosmochimica Acta, v. 171, p. 201–215, doi:10.1016/j.gca.2015.09.001.

Buening, D.K., and Buseck, P.R., 1973, Fe-Mg lattice diffusion in olivine: Journal of Geophysical Research (1896-1977), v. 78, p. 6852–6862, doi:10.1029/JB078i029p06852.

Canil, D., and Bellis, A.J., 2008, Phase equilibria in a volatile-free kimberlite at 0.1 MPa and the search for primary kimberlite magma: Lithos, v. 105, p. 111–117, doi:10.1016/j.lithos.2008.02.011.

Chakraborty, S., 1997, Rates and mechanisms of Fe-Mg interdiffusion in olivine at 980°–1300°C: Journal of Geophysical Research: Solid Earth, v. 102, p. 12317–12331, doi:10.1029/97JB00208.

Chakraborty, S., Farver, J.R., Yund, R.A., and Rubie, D.C., 1994, Mg tracer diffusion in synthetic forsterite and San Carlos olivine as a function of P, T and fO2: Physics and Chemistry of Minerals, v. 21, p. 489–500, doi:10.1007/BF00203923.

Chakraborty, S., and Ganguly, J., 1992, Cation diffusion in aluminosilicate garnets: experimental determination in spessartine-almandine diffusion couples, evaluation of effective binary diffusion coefficients, and applications: Contributions to Mineralogy and Petrology, v. 111, p. 74–86, doi:10.1007/BF00296579.

Chakraborty, S., and Rubie, D.C., 1996, Mg tracer diffusion in aluminosilicate garnets at 750-850° C, 1 atm. and 1300° C, 8.5 GPa: Contributions to Mineralogy and Petrology, v. 122, p. 406–414, doi:10.1007/s004100050136.

Charlier, B., Grove, T.L., Namur, O., and Holtz, F., 2018, Crystallization of the lunar magma ocean and the primordial mantle-crust differentiation of the Moon: Geochimica et Cosmochimica Acta, v. 234, p. 50–69, doi:10.1016/j.gca.2018.05.006.

Cohen, L.H., Ito, K., and Kennedy, G.C., 1967, Melting and phase relations in an anhydrous basalt to 40 kilobars: American Journal of Science, v. 265, p. 475, doi:10.2475/ajs.265.6.475.

Dannberg, J., Eilon, Z., Faul, U., Gassmöller, R., Moulik, P., and Myhill, R., 2017, The importance of grain size to mantle dynamics and seismological observations:

Geochemistry, Geophysics, Geosystems, v. 18, p. 3034–3061, doi:10.1002/2017GC006944.

Deines, P., 1974, Temperature-oxygen fugacity tables for selected gas mixtures in the system C-H-O at one atmosphere total pressure: University Park : College of Earth and Mineral Sciences, Pennsylvania State University, Bulletin 88, 129 p.

Delano, J.W., 1980, Chemistry and liquidus phase relations of Apollo 15 red glass: implications for the deep lunar interior.: Lunar and Planetary Science Conference Proceedings, v. 1, p. 251–288.

Delano, J.W., 1986, Pristine lunar glasses: Criteria, data, and implications: Journal of Geophysical Research: Solid Earth, v. 91, p. 201–213, doi:10.1029/JB091iB04p0D201.

Dimanov, A., and Wiedenbeck, M., 2006, (Fe,Mn)-Mg interdiffusion in natural diopside: effect of pO2: European Journal of Mineralogy, v. 18, p. 705–718, doi:10.1127/0935-1221/2006/0018-0705.

Dohmen, R., and Chakraborty, S., 2007, Fe–Mg diffusion in olivine II: point defect chemistry, change of diffusion mechanisms and a model for calculation of diffusion coefficients in natural olivine: Physics and Chemistry of Minerals, v. 34, p. 409–430, doi:10.1007/s00269-007-0158-6.

Draper, D.S., duFrane, S.A., Shearer, C.K., Dwarzski, R.E., and Agee, C.B., 2006, High-pressure phase equilibria and element partitioning experiments on Apollo 15 green C picritic glass: Implications for the role of garnet in the deep lunar interior:

Geochimica et Cosmochimica Acta, v. 70, p. 2400–2416, doi:10.1016/j.gca.2006.01.027.

Dygert, N., Bernard, R.E., and Behr, W.M., 2019, Great basin mantle xenoliths record active lithospheric downwelling beneath central Nevada: Geochemistry, Geophysics, Geosystems, v. 20, p. 751–772.

Dygert, N., Hirth, G., and Liang, Y., 2016, A flow law for ilmenite in dislocation creep: Implications for lunar cumulate mantle overturn: Geophysical Research Letters, v. 43, p. 532–540, doi:10.1002/2015GL066546.

Dygert, N., Liang, Y., and Hess, P., 2013, The importance of melt TiO2 in affecting major and trace element partitioning between Fe–Ti oxides and lunar picritic glass melts: Geochimica et Cosmochimica Acta, v. 106, p. 134–151, doi:10.1016/j.gca.2012.12.005.

Dygert, N., Liang, Y., Sun, C., and Hess, P., 2014, An experimental study of trace element partitioning between augite and Fe-rich basalts: Geochimica et Cosmochimica Acta, v. 132, p. 170–186, doi:10.1016/j.gca.2014.01.042.

Dygert, N., Lin, J.-F., Marshall, E.W., Kono, Y., and Gardner, J.E., 2017, A Low Viscosity Lunar Magma Ocean Forms a Stratified Anorthitic Flotation Crust With Mafic Poor and Rich Units: Geophysical Research Letters, v. 44, p. 11,282-11,291, doi:10.1002/2017GL075703.

Elardo, S.M., Draper, D.S., and Shearer, C.K., 2011, Lunar Magma Ocean crystallization revisited: Bulk composition, early cumulate mineralogy, and the source regions of

the highlands Mg-suite: Geochimica et Cosmochimica Acta, v. 75, p. 3024–3045, doi:10.1016/j.gca.2011.02.033.

Elkins Tanton, L.T., Van Orman, J.A., Hager, B.H., and Grove, T.L., 2002, Re-examination of the lunar magma ocean cumulate overturn hypothesis: melting or mixing is required: Earth and Planetary Science Letters, v. 196, p. 239–249, doi:10.1016/S0012-821X(01)00613-6.

Elkins-Tanton, L.T., 2012, Magma Oceans in the Inner Solar System: Annual Review of Earth and Planetary Sciences, v. 40, p. 113–139, doi:10.1146/annurev-earth-042711-105503.

Elkins-Tanton, L.T., Burgess, S., and Yin, Q.-Z., 2011, The lunar magma ocean: Reconciling the solidification process with lunar petrology and geochronology: Earth and Planetary Science Letters, v. 304, p. 326–336, doi:10.1016/j.epsl.2011.02.004.

Elkins-Tanton, L.T., Chatterjee, N., and Grove, T.L., 2003, Experimental and petrological constraints on lunar differentiation from the Apollo 15 green picritic glasses: Meteoritics & Planetary Science, v. 38, p. 515–527, doi:10.1111/j.1945-5100.2003.tb00024.x.

Elthon, D., and Scarfe, C.M., 1984, High-pressure phase equilibria of a high-magnesia basalt and the genesis of primary oceanic basalts: American Mineralogist, v. 69, p. 1–15.

Farver, J.R., Yund, R.A., and Rubie, D.C., 1994, Magnesium grain boundary diffusion in forsterite aggregates at 1000°–1300°C and 0.1 MPa to 10 GPa: Journal of Geophysical Research: Solid Earth, v. 99, p. 19809–19819, doi:10.1029/94JB01250.

Friel, J.J., Harker, R.I., and Ulmer, G.C., 1977, Armalcolite stability as a function of pressure and oxygen fugacity: Geochimica et Cosmochimica Acta, v. 41, p. 403–410, doi:10.1016/0016-7037(77)90268-X.

Fujino, K., 1990, Direct determination of cation diffusion coefficients in pyroxene.: Eos, v. 71, p. 943.

Ganguly, J., Cheng, W., and Chakraborty, S., 1998, Cation diffusion in aluminosilicate garnets: experimental determination in pyrope-almandine diffusion couples: Contributions to Mineralogy and Petrology, v. 131, p. 171–180, doi:10.1007/s004100050386.

Giguere, T.A., Taylor, G.J., Hawke, B.R., and Lucey, P.G., 2000, The titanium contents of lunar mare basalts: Meteoritics & Planetary Science, v. 35, p. 193–200, doi:10.1111/j.1945-5100.2000.tb01985.x.

Grove, T.L., and Krawczynski, M.J., 2009, Lunar Mare Volcanism: Where Did the Magmas Come From? Elements, v. 5, p. 29–34, doi:10.2113/gselements.5.1.29.

Haggerty, S.E., 1973, Armalcolite and genetically associated opaque minerals in the lunar samples: Lunar and Planetary Science Conference Proceedings, v. 4, p. 777.

Haggerty, S.E., and Lindsley, D.H., 1970, Stability of the pseudobrookite (Fe2TiO5)-ferropseudobrookite (FeTi2O5) series.: Carnegie Inst. Washington Year Book, v. 68, p. 247–249.

Haskin, L.A., and Warren, P.H., 1991, Lunar chemistry., *in* Lunar sourcebook, v. 4, p. 357–474.

Hess, P.C., and Parmentier, E.M., 1995, A model for the thermal and chemical evolution of the Moon's interior: implications for the onset of mare volcanism: Earth and Planetary Science Letters, v. 134, p. 501–514, doi:10.1016/0012-821X(95)00138-3.

Hubbard, N.J., and Minear, J.W., 1975, A physical and chemical model of early lunar history, *in* Lunar and Planetary Science Conference Proceedings, v. 6, p. 1057–1085.

Hughes, S.S., Delano, J.W., and Schmitt, R.A., 1990, Chemistry of individual mare volcanic glasses: evidence for distinct regions of hybridized mantle and a KREEP component in Apollo 14 magmatic sources.: Lunar and Planetary Science Conference Proceedings, v. 20, p. 127–138.

Ito, K., and Kennedy, G.C., 1971, An Experimental Study of the Basalt-Garnet Granulite-Eclogite Transition, *in* The Structure and Physical Properties of the Earth's Crust, Geophysical Monograph Series, p. 303–314, doi:10.1029/GM014p0303.

Ji, D., and Dygert, N., 2023, Trace element partitioning between apatite and silicate melts: Effects of major element composition, temperature, and oxygen fugacity, and implications for the volatile element budget of the lunar magma ocean: Geochimica et Cosmochimica Acta, doi:10.1016/j.gca.2023.11.004.

Jing, J.-J., Lin, Y., Knibbe, J.S., and van Westrenen, W., 2022, Garnet stability in the deep lunar mantle: Constraints on the physics and chemistry of the interior of the Moon: Earth and Planetary Science Letters, v. 584, p. 117491, doi:10.1016/j.epsl.2022.117491.

Jurewicz, A.J.G., and Watson, E.B., 1988, Cations in olivine, Part 2: Diffusion in olivine xenocrysts, with applications to petrology and mineral physics: Contributions to Mineralogy and Petrology, v. 99, p. 186–201, doi:10.1007/BF00371460.

Kerr, R.C., 1995, Convective crystal dissolution: Contributions to Mineralogy and Petrology, v. 121, p. 237–246, doi:10.1007/BF02688239.

Kraettli, G., Schmidt, M.W., and Liebske, C., 2022, Fractional crystallization of a basal lunar magma ocean: A dense melt-bearing garnetite layer above the core? Icarus, v. 371, p. 114699, doi:10.1016/j.icarus.2021.114699.

Krawczynski, M.J., and Grove, T.L., 2012, Experimental investigation of the influence of oxygen fugacity on the source depths for high titanium lunar ultramafic magmas: Geochimica et Cosmochimica Acta, v. 79, p. 1–19, doi:10.1016/j.gca.2011.10.043.

Kress, V.C., and Carmichael, I.S.E., 1991, The compressibility of silicate liquids containing Fe2O3 and the effect of composition, temperature, oxygen fugacity and pressure on their redox states: Contributions to Mineralogy and Petrology, v. 108, p. 82–92, doi:10.1007/BF00307328.

van der Laan, S., Zhang, Y., Kennedy, A.K., and Wyllie, P.J., 1994, Comparison of element and isotope diffusion of K and Ca in multicomponent silicate melts: Earth and Planetary Science Letters, v. 123, p. 155–166, doi:10.1016/0012-821X(94)90264-X.

Lange, R.A., and Carmichael, I.S.E., 1987, Densities of Na2O-K2O-CaO-MgO-FeO-Fe2O3-Al2O3-TiO2-SiO2 liquids: New measurements and derived partial molar

properties: Geochimica et Cosmochimica Acta, v. 51, p. 2931–2946, doi:10.1016/0016-7037(87)90368-1.

Li, B., Ge, J., and Zhang, B., 2018, Diffusion in garnet: a review: Acta Geochimica, v. 37, p. 19–31, doi:10.1007/s11631-017-0187-x.

Li, H., Zhang, N., Liang, Y., Wu, B., Dygert, N.J., Huang, J., and Parmentier, E.M., 2019, Lunar Cumulate Mantle Overturn: A Model Constrained by Ilmenite Rheology: Journal of Geophysical Research: Planets, v. 124, p. 1357–1378, doi:10.1029/2018JE005905.

Liang, Y., 2000, Dissolution in molten silicates: effects of solid solution: Geochimica et Cosmochimica Acta, v. 64, p. 1617–1627, doi:10.1016/S0016-7037(00)00331-8.

Liang, Y., 2010, Multicomponent Diffusion in Molten Silicates: Theory, Experiments, and Geological Applications: Reviews in Mineralogy and Geochemistry, v. 72, p. 409–446, doi:10.2138/rmg.2010.72.9.

Lin, Y., Tronche, E.J., Steenstra, E.S., and van Westrenen, W., 2017, Evidence for an early wet Moon from experimental crystallization of the lunar magma ocean: Nature Geoscience, v. 10, p. 14–18, doi:10.1038/ngeo2845.

Lin, Y., Tronche, E.J., Steenstra, E.S., and van Westrenen, W., 2016, Solidification Evolution of a Dry Lunar Magma Ocean: Constraints from Experimental Petrology: v. 47, p. 1296.

Longhi, J., 1991, Comparative liquidus equilibria of hypersthene-normative basalts at low pressure: American Mineralogist, v. 76, p. 785–800.

Longhi, J., 1982, Multicomponent phase diagrams and the phase equilibria of basalts, *in* Magmatic Processes of Early Planetary Crusts: Magma Oceans and Stratiform Layered Intrusions, p. 90.

Longhi, J., 2006, Petrogenesis of picritic mare magmas: Constraints on the extent of early lunar differentiation: A Special Issue Dedicated to Larry A. Haskin, v. 70, p. 5919–5934, doi:10.1016/j.gca.2006.09.023.

Longhi, J., and Ashwal, L.D., 1985, Two-stage models for lunar and terrestrial anorthosites: Petrogenesis without a magma ocean: Journal of Geophysical Research: Solid Earth, v. 90, p. C571–C584.

Longhi, J., Walker, D., Grove, T.L., Stolper, E.M., and Hays, J.F., 1974, The petrology of the Apollo 17 mare basalts.: Lunar and Planetary Science Conference Proceedings, v. 1, p. 447–469.

Longhi, J., Walker, D., and Hays, J.F., 1978, The distribution of Fe and Mg between olivine and lunar basaltic liquids: Geochimica et Cosmochimica Acta, v. 42, p. 1545–1558, doi:10.1016/0016-7037(78)90025-X.

Loomis, T.P., Ganguly, J., and Elphick, S.C., 1985, Experimental determination of cation diffusivities in aluminosilicate garnets: Contributions to Mineralogy and Petrology, v. 90, p. 45–51, doi:10.1007/BF00373040.

Lucey, P.G., Taylor, G.J., Hawke, B.R., and Spudis, P.D., 1998, FeO and TiO2 concentrations in the South Pole-Aitken basin: Implications for mantle composition and basin formation: Journal of Geophysical Research: Planets, v. 103, p. 3701–3708, doi:10.1029/97JE03146.

Mallik, A., Ejaz, T., Shcheka, S., and Garapic, G., 2019, A petrologic study on the effect of mantle overturn: Implications for evolution of the lunar interior: Geochimica et Cosmochimica Acta, v. 250, p. 238–250, doi:10.1016/j.gca.2019.02.014.

Maurice, M., Tosi, N., and Hüttig, C., 2024, Small-Scale Overturn of High-Ti Cumulates Promoted by the Long Lifetime of the Lunar Magma Ocean: Journal of Geophysical Research: Planets, v. 129, p. e2023JE008060, doi:10.1029/2023JE008060.

Maurice, M., Tosi, N., Schwinger, S., Breuer, D., and Kleine, T., 2020, A long-lived magma ocean on a young Moon: Science Advances, v. 6, doi:10.1126/sciadv.aba8949.

Morgan, Z., and Liang, Y., 2003, An experimental and numerical study of the kinetics of harzburgite reactive dissolution with applications to dunite dike formation: Earth and Planetary Science Letters, v. 214, p. 59–74, doi:10.1016/S0012-821X(03)00375-3.

Morgan, Z., and Liang, Y., 2005, An experimental study of the kinetics of lherzolite reactive dissolution with applications to melt channel formation: Contributions to Mineralogy and Petrology, v. 150, p. 369–385, doi:10.1007/s00410-005-0033-8.

Morgan, Z., Liang, Y., and Hess, P., 2006, An experimental study of anorthosite dissolution in lunar picritic magmas: Implications for crustal assimilation processes: Geochimica et Cosmochimica Acta, v. 70, p. 3477–3491, doi:10.1016/j.gca.2006.04.027.

Müller, T., Dohmen, R., Becker, H.W., ter Heege, J.H., and Chakraborty, S., 2013, Fe–Mg interdiffusion rates in clinopyroxene: experimental data and implications for Fe–

Mg exchange geothermometers: Contributions to Mineralogy and Petrology, v. 166, p. 1563–1576, doi:10.1007/s00410-013-0941-y.

Nagy, K.L., and Lasaga, A.C., 1992, Dissolution and precipitation kinetics of gibbsite at 80°C and pH 3: The dependence on solution saturation state: Geochimica et Cosmochimica Acta, v. 56, p. 3093–3111, doi:10.1016/0016-7037(92)90291-P.

Nakamura, A., and Schmalzried, H., 1984, On the Fe2+ –Mg2+-Interdiffusion in Olivine (II): Berichte der Bunsengesellschaft für physikalische Chemie, v. 88, p. 140–145, doi:10.1002/bbpc.19840880212.

Neal, C.R., 2001, Interior of the Moon: The presence of garnet in the primitive deep lunar mantle: Journal of Geophysical Research: Planets, v. 106, p. 27865–27885, doi:10.1029/2000JE001386.

Nicholis, M.G., and Rutherford, M.J., 2009, Graphite oxidation in the Apollo 17 orange glass magma: Implications for the generation of a lunar volcanic gas phase: Geochimica et Cosmochimica Acta, v. 73, p. 5905–5917, doi:10.1016/j.gca.2009.06.022.

Paces, J.B., Nakai, S., Neal, C.R., Taylor, L.A., Halliday, A.N., and Lee, D.-C., 1991, A strontium and neodymium isotopic study of Apollo 17 high-Ti mare basalts: Resolution of ages, evolution of magmas, and origins of source heterogeneities: Geochimica et Cosmochimica Acta, v. 55, p. 2025–2043, doi:10.1016/0016-7037(91)90040-C.

Papike, J.J., Ryder, G., and Shearer, C.K., 1998, Lunar samples: Reviews in Mineralogy and Geochemistry, v. 36, p. 5– 01.

Pec, M., Holtzman, B.K., Zimmerman, M.E., and Kohlstedt, D.L., 2020, Influence of Lithology on Reactive Melt Flow Channelization: Geochemistry, Geophysics, Geosystems, v. 21, p. e2020GC008937, doi:10.1029/2020GC008937.

Perchuk, A.L., Burchard, M., Schertl, H.-P., Maresch, W.V., Gerya, T.V., Bernhardt, H.-J., and Vidal, O., 2009, Diffusion of divalent cations in garnet: multi-couple experiments: Contributions to Mineralogy and Petrology, v. 157, p. 573–592, doi:10.1007/s00410-008-0353-6.

Petry, C., Chakraborty, S., and Palme, H., 2004, Experimental determination of Ni diffusion coefficients in olivine and their dependence on temperature, composition, oxygen fugacity, and crystallographic orientation: Geochimica et Cosmochimica Acta, v. 68, p. 4179–4188, doi:10.1016/j.gca.2004.02.024.

Rapp, J.F., and Draper, D.S., 2018, Fractional crystallization of the lunar magma ocean: Updating the dominant paradigm: Meteoritics & Planetary Science, v. 53, p. 1432–1455, doi:10.1111/maps.13086.

Ringwood, A.E., and Kesson, S.E., 1976, A dynamic model for mare basalt petrogenesis, *in* Lunar and Planetary Science Conference Proceedings, v. 7, p. 1697–1722.

Roeder, P.L., and Emslie, R.F., 1970, Olivine-liquid equilibrium: Contributions to Mineralogy and Petrology, v. 29, p. 275–289, doi:10.1007/BF00371276.

Sato, M., 1979, The driving mechanism of lunar pyroclastic eruptions inferred from the oxygen fugacity behaviour of Apollo 17 orange glass.: Lunar and Planetary Science Conference Proceedings, v. 1, p. 311–325.

Schmidt, M.W., and Kraettli, G., 2022, Experimental Crystallization of the Lunar Magma Ocean, Initial Selenotherm and Density Stratification, and Implications for Crust Formation, Overturn and the Bulk Silicate Moon Composition: Journal of Geophysical Research: Planets, v. 127, p. e2022JE007187, doi:10.1029/2022JE007187.

Shearer, C.K., Elardo, S.M., Petro, N.E., Borg, L.E., and McCubbin, F.M., 2015, Origin Of The Lunar Highlands Mg-Suite: An Integrated Petrology, Geochemistry, Chronology, And Remote Sensing Perspective: v. 100, p. 294–325, doi:10.2138/am-2015-4817.

Shearer, C.K., and Papike, J.J., 1993, Basaltic magmatism on the Moon: A perspective from volcanic picritic glass beads: Geochimica et Cosmochimica Acta, v. 57, p. 4785–4812, doi:10.1016/0016-7037(93)90200-G.

Shearer, C.K., Papike, J.J., Galbreath, K.C., and Shimizu, N., 1991, Exploring the lunar mantle with secondary ion mass spectrometry: a comparison of lunar picritic glass beads from the Apollo 14 and Apollo 17 sites: Earth and Planetary Science Letters, v. 102, p. 134–147, doi:10.1016/0012-821X(91)90003-Z.

Shepherd, K., Namur, O., Toplis, M.J., Devidal, J.-L., and Charlier, B., 2022, Trace element partitioning between clinopyroxene, magnetite, ilmenite and ferrobasaltic to dacitic magmas: an experimental study on the role of oxygen fugacity and melt composition: Contributions to Mineralogy and Petrology, v. 177, p. 90, doi:10.1007/s00410-022-01957-y.

Singletary, S., and Grove, T., 2008, Origin of lunar high-titanium ultramafic glasses: A hybridized source? Earth and Planetary Science Letters, v. 268, p. 182–189, doi:10.1016/j.epsl.2008.01.019.

Snyder, G.A., Taylor, L.A., and Neal, C.R., 1992, Combined equilibrium and fractional crystallization of a magma ocean and formation of the upper mantle of the Moon, *in* Lunar and Planetary Science Conference, v. 23.

Solomon, S.C., and Longhi, J., 1977, Magma oceanography. I-Thermal evolution, *in* Lunar and planetary science conference proceedings, v. 8, p. 583–599.

Springer, W., and Seck, H.A., 1997, Partial fusion of basic granulites at 5 to 15 kbar: implications for the origin of TTG magmas: Contributions to Mineralogy and Petrology, v. 127, p. 30–45, doi:10.1007/s004100050263.

Sprung, P., Kleine, T., and Scherer, E.E., 2013, Isotopic evidence for chondritic Lu/Hf and Sm/Nd of the Moon: Earth and Planetary Science Letters, v. 380, p. 77–87, doi:10.1016/j.epsl.2013.08.018.

Stolper, E., and Walker, D., 1980, Melt density and the average composition of basalt: Contributions to Mineralogy and Petrology, v. 74, p. 7–12, doi:10.1007/BF00375484.

Sun, C., and Liang, Y., 2015, A REE-in-garnet–clinopyroxene thermobarometer for eclogites, granulites and garnet peridotites: Chemical Geology, v. 393–394, p. 79–92, doi:10.1016/j.chemgeo.2014.11.014.

Taylor, A.S., Blum, J.D., and Lasaga, A.C., 2000, The dependence of labradorite dissolution and Sr isotope release rates on solution saturation state: Geochimica et Cosmochimica Acta, v. 64, p. 2389–2400, doi:10.1016/S0016-7037(00)00361-6.

Taylor, G.J., and Wieczorek, M.A., 2014, Lunar bulk chemical composition: a post-Gravity Recovery and Interior Laboratory reassessment: Philosophical Transactions of the Royal Society A: Mathematical, Physical and Engineering Sciences, v. 372, p. 20130242, doi:10.1098/rsta.2013.0242.

Thacker, C., Liang, Y., Peng, Q., and Hess, P., 2009, The stability and major element partitioning of ilmenite and armalcolite during lunar cumulate mantle overturn: Geochimica et Cosmochimica Acta, v. 73, p. 820–836, doi:10.1016/j.gca.2008.10.038.

Tokle, L., Hirth, G., Liang, Y., Raterron, P., and Dygert, N., 2021, The Effect of Pressure and Mg-Content on Ilmenite Rheology: Implications for Lunar Cumulate Mantle Overturn: Journal of Geophysical Research: Planets, v. 126, p. e2020JE006494, doi:10.1029/2020JE006494.

Unruh, D.M., Stille, P., Patchett, P.J., and Tatsumoto, M., 1984, Lu-Hf and Sm-Nd evolution in lunar mare basalts: Journal of Geophysical Research: Solid Earth, v. 89, p. B459–B477, doi:10.1029/JB089iS02p0B459.

Van Den Bleeken, G., Müntener, O., and Ulmer, P., 2010, Reaction Processes between Tholeiitic Melt and Residual Peridotite in the Uppermost Mantle: an Experimental Study at 0·8 GPa: Journal of Petrology, v. 51, p. 153–183, doi:10.1093/petrology/egp066.

Van der Wal, D., Chopra, P., Drury, M., and Gerald, J.F., 1993, Relationships between dynamically recrystallized grain size and deformation conditions in experimentally deformed olivine rocks: Geophysical Research Letters, v. 20, p. 1479–1482, doi:10.1029/93GL01382.

Van Orman, J.A., and Grove, T.L., 2000, Origin of lunar high-titanium ultramafic glasses: Constraints from phase relations and dissolution kinetics of clinopyroxene-ilmenite cumulates: Meteoritics & Planetary Science, v. 35, p. 783–794, doi:10.1111/j.1945-5100.2000.tb01462.x.

Wagner, T.P., and Grove, T.L., 1997, Experimental constraints on the origin of lunar high-Ti ultramafic glasses: Geochimica et Cosmochimica Acta, v. 61, p. 1315–1327, doi:10.1016/S0016-7037(96)00387-0.

Walker, D., and Hays, J.F., 1977, Plagioclase flotation and lunar crust formation: Geology, v. 5, p. 425–428, doi:10.1130/0091-7613(1977)5<425:PFALCF>2.0.CO;2.

Walker, D., Longhi, J., Stolper, E., Grove, T., and Hays, J.F., 1974, Experimental Petrology and Origin of Titaniferous Lunar Basalts, *in* Lunar and Planetary Science Conference, Lunar and Planetary Science Conference, v. 5, p. 814.

Wang, C., Liang, Y., Xu, W., and Dygert, N., 2013, Effect of melt composition on basalt and peridotite interaction: laboratory dissolution experiments with applications to mineral compositional variations in mantle xenoliths from the North China Craton: Contributions to Mineralogy and Petrology, v. 166, p. 1469–1488, doi:10.1007/s00410-013-0938-6.

Watson, E.B., and Baker, D.R., 1991, Chemical Diffusion in Magmas: An Overview of Experimental Results and Geochemical Applications, *in* Perchuk, L.L. and Kushiro, I. eds., Physical Chemistry of Magmas, New York, NY, Springer New York, p. 120–151, doi:10.1007/978-1-4612-3128-8_4.

Watson, E.B., Sneeringer, M.A., and Ross, A., 1982, Diffusion of dissolved carbonate in magmas: Experimental results and applications: Earth and Planetary Science Letters, v. 61, p. 346–358, doi:10.1016/0012-821X(82)90065-6.

Weitz, C.M., Rutherford, M.J., and Head, J.W., 1997, Oxidation states and ascent history of the Apollo 17 volcanic beads as inferred from metal-glass equilibria: Geochimica et Cosmochimica Acta, v. 61, p. 2765–2775, doi:10.1016/S0016-7037(97)00119-1.

Wood, J.A., Dickey Jr, J.S., Marvin, U.B., and Powell, B.N., 1970, Lunar anorthosites and a geophysical model of the moon: Geochimica et Cosmochimica Acta Supplement, v. 1, p. 965.

Wyatt, B.A., 1977, The melting and crystallisation behaviour of a natural clinopyroxene-ilmenite intergrowth: Contributions to Mineralogy and Petrology, v. 61, p. 1–9, doi:10.1007/BF00375941.

Xirouchakis, D.M., 2007, Pseudobrookite-group oxide solutions and basaltic melts: The Role of Accessory Minerals in Rocks: Petrogenetic Indicators of Metamorphic and Igneous Processes, v. 95, p. 1–9, doi:10.1016/j.lithos.2006.07.009.

Xirouchakis, D., Hirschmann, M.M., and Simpson, J.A., 2001, The effect of titanium on the silica content and on mineral-liquid partitioning of mantle-equilibrated melts:

Geochimica et Cosmochimica Acta, v. 65, p. 2201–2217, doi:10.1016/S0016-7037(00)00549-4.

Xirouchakis, D., Smirnov, A., Woody, K., Lindsley, D.H., and Andersen, D.J., 2002, Thermodynamics and stability of pseudobrookite-type MgTi2O5 (karrooite): American Mineralogist, v. 87, p. 658–667, doi:10.2138/am-2002-5-608.

Yao, L., and Liang, Y., 2012, An Experimental Study of the Solidus of a Hybrid Lunar Cumulate Mantle: Implications for the Temperature at the Core-Mantle Boundary of the Moon, *in* 43rd Annual Lunar and Planetary Science Conference, Lunar and Planetary Science Conference, p. 2258.

Zhang, Y., 1993, A modified effective binary diffusion model: Journal of Geophysical Research: Solid Earth, v. 98, p. 11901–11920, doi:10.1029/93JB00422.

Zhang, Y., 2009, Geochemical Kinetics: Princetion University Press, 664 p.

Zhang, N., Ding, M., Zhu, M.-H., Li, H., Li, H., and Yue, Z., 2022, Lunar compositional asymmetry explained by mantle overturn following the South Pole–Aitken impact: Nature Geoscience, v. 15, p. 37–41, doi:10.1038/s41561-021-00872-4.

Zhang, N., Dygert, N., Liang, Y., and Parmentier, E.M., 2017, The effect of ilmenite viscosity on the dynamics and evolution of an overturned lunar cumulate mantle: Geophysical Research Letters, v. 44, p. 6543–6552, doi:10.1002/2017GL073702.

Zhang, X., Ganguly, J., and Ito, M., 2010a, Ca–Mg diffusion in diopside: tracer and chemical inter-diffusion coefficients: Contributions to Mineralogy and Petrology, v. 159, p. 175–186, doi:10.1007/s00410-009-0422-5.

Zhang, Y., Ni, H., and Chen, Y., 2010b, Diffusion Data in Silicate Melts: Reviews in Mineralogy and Geochemistry, v. 72, p. 311–408, doi:10.2138/rmg.2010.72.8.

Zhang, Y., Walker, D., and Lesher, C.E., 1989, Diffusive crystal dissolution: Contributions to Mineralogy and Petrology, v. 102, p. 492–513, doi:10.1007/BF00371090.

Zhang, Y., and Xu, Z., 2003, Kinetics of convective crystal dissolution and melting, with applications to methane hydrate dissolution and dissociation in seawater: Earth and Planetary Science Letters, v. 213, p. 133–148, doi:10.1016/S0012-821X(03)00297-8.

Zhao, Y., de Vries, J., van den Berg, A.P., Jacobs, M.H.G., and van Westrenen, W., 2019, The participation of ilmenite-bearing cumulates in lunar mantle overturn: Earth and Planetary Science Letters, v. 511, p. 1–11, doi:10.1016/j.epsl.2019.01.022.

Appendix A

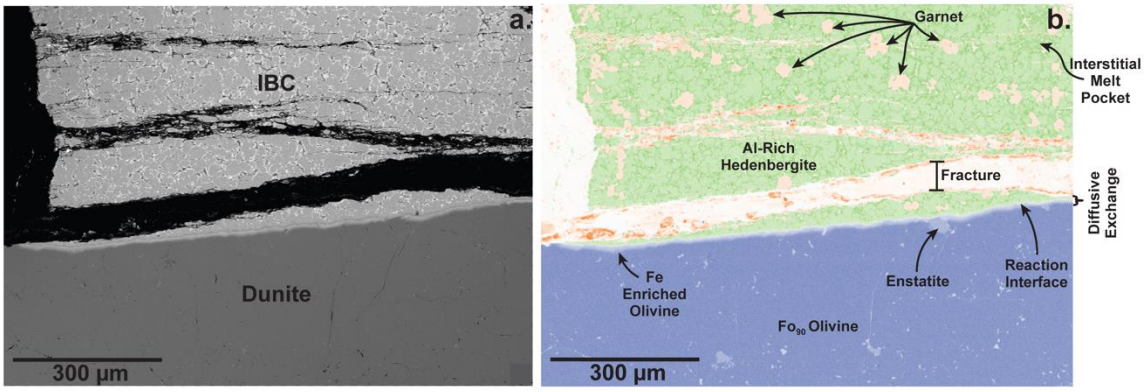


Figure A1. (a) Backscatter electron image of reaction interface in MRx#1. (b) Combined Fe (green), Mg (blue), and Al (orange) false color elemental map of the reaction interface in MRx#1 showing the diffusive exchange boundary and mineral phases labeled. Al-rich hedenbergite crystals are light green and is often surrounded by dark green low degree interstitial melt. Garnets are light orange and are distributed throughout the IBC side of the reaction couple. Rare, dispersed enstatite crystals in the dunite originate from the starting material.

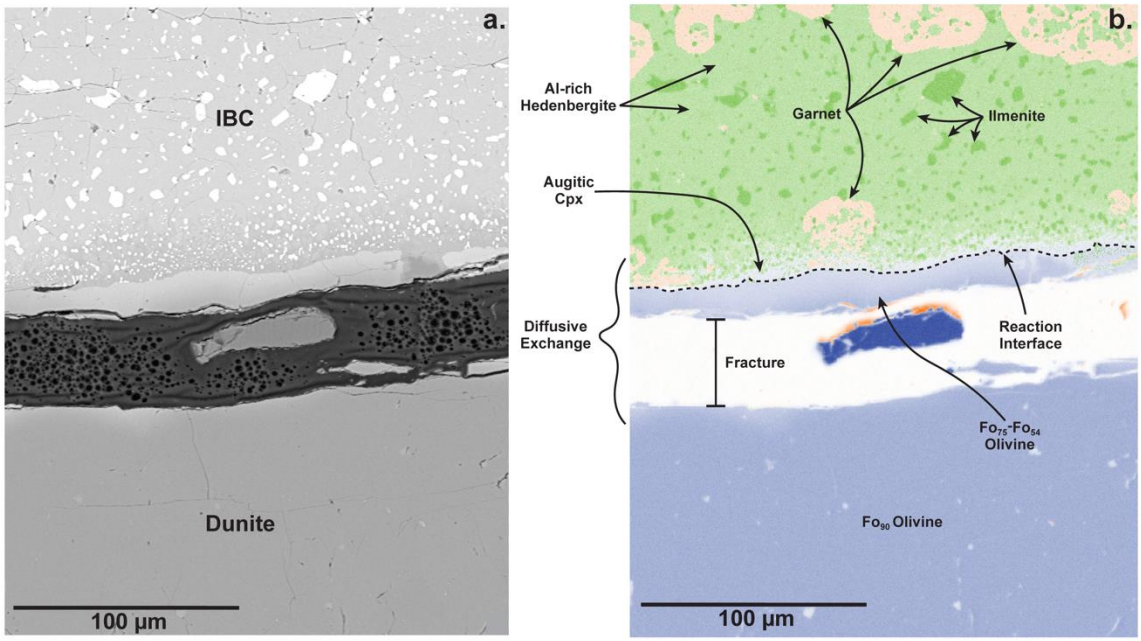


Figure A2. (a) Backscatter electron image of reaction interface in MRx#8. (b) Combined Fe (green), Mg (blue), and Al (orange) false color elemental map of the reaction interface. Al-rich hedenbergite crystals are light green and ilmenite crystals are dark green. Garnets are light orange and are distributed throughout the IBC side of the reaction couple. The black dashed line represents the interface between the IBC and dunite sides of the reaction couple. The light blue material on the IBC side of the reaction interface is augitic Cpx with Mg-enriched compositions. The dark blue fragment in the fracture is a piece of MgO from the experiment assembly that became entrained in the impregnation epoxy during sample preparation for EPMA analysis.

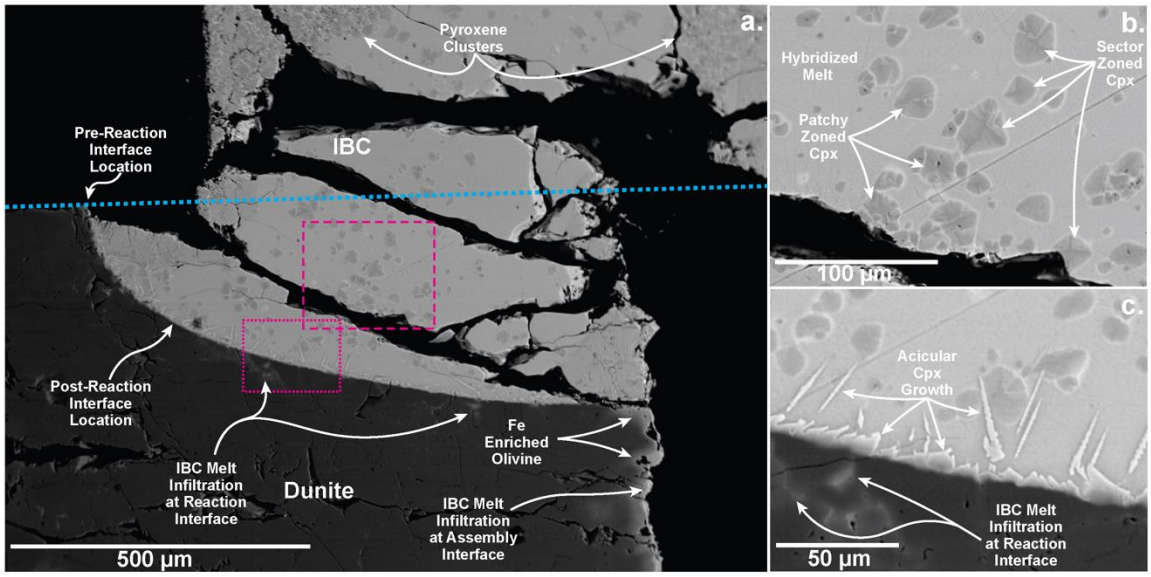


Figure A3. Backscatter electron images of the reaction interface and sector zoned pyroxenes in MRx#5. (a) Reaction interface. The blue dotted line represents the pre-reaction interface position. The box with a pink dashed border highlights the area imaged in (b). The box with a pink dotted border highlights the area of interest imaged in (c). (b) Close-up BSE image of the Cpx crystals that formed away from the interface. (c) Close-up BSE image of the reaction interface. IBC melt infilrated into the dunite at the reaction interface (a and c) and down the right edge of the dunite material at the assembly interface (a). Pyroxenes that form away from the reaction interface form as individual crystals or as crystal clusters (a and c). Bright acicular Cpx crystals nucleate from the reaction interface.

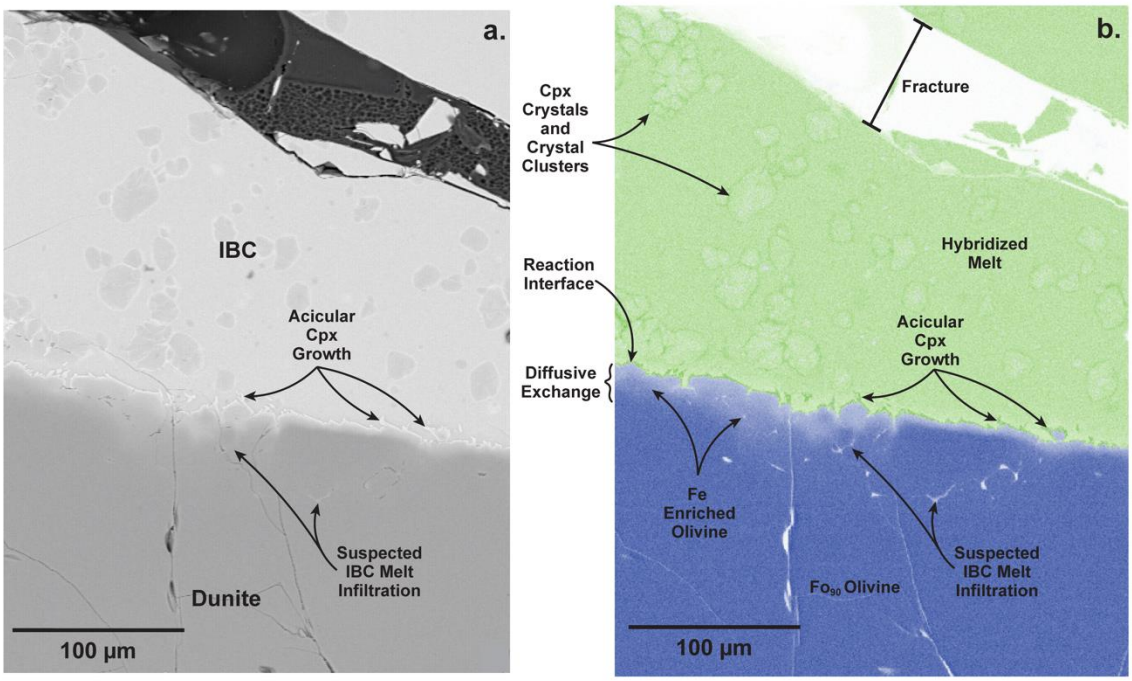


Figure A4. (a) Backscatter electron image of the reaction interface in MRx#10. (b) Combined Fe (green) and Mg (blue) false color elemental map of the reaction interface. A narrow concentration gradient in the olivine produced by diffusive exchange is visible in the dunite side of the reaction couple. Pyroxene crystals are easiest to see in the BSE image (a) and the elemental maps show that their dark green rims are Fe-rich (b). (a) A thin bright layer of Fe-rich acicular Cpx is present on the IBC side of the reaction interface (dark green in elemental map). This layer is likely quench pyroxene growth and likely formed at the same time as the bright Cpx rims.

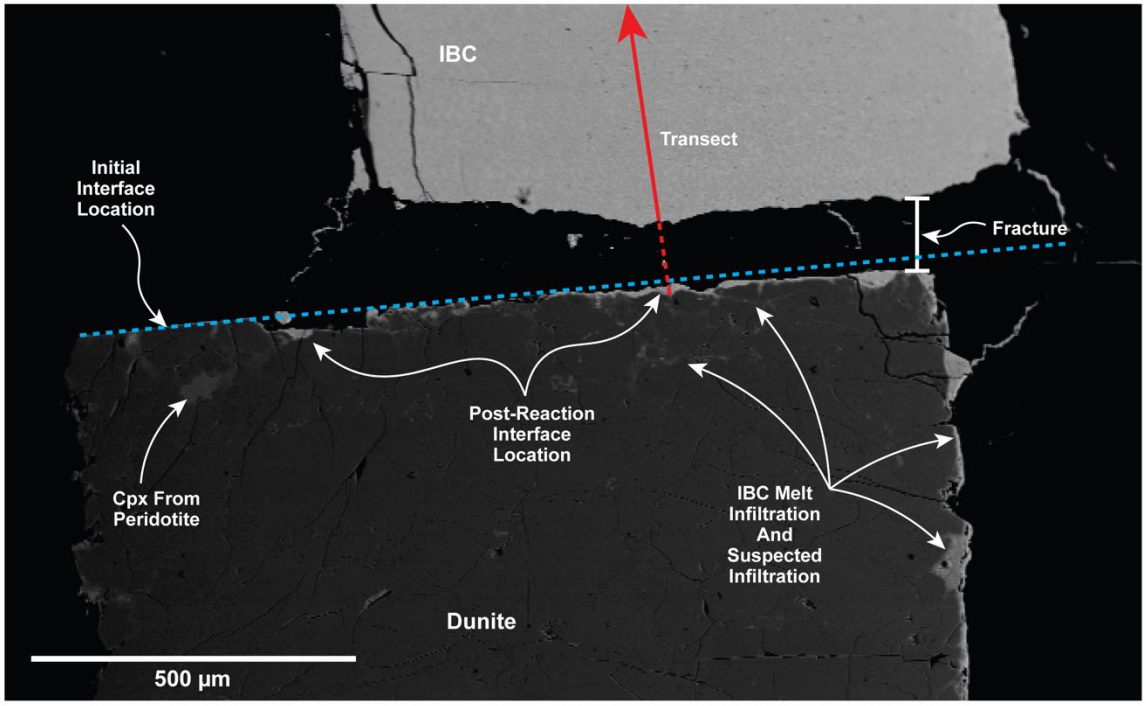


Figure A5. Backscatter electron image of the reaction interface in MRx#9. The chemical transect location for data presented in Figure (1.9) within Chapter 1 is represented by the red line. The location of the initial interface is represented by the blue dotted line. The post-reaction interface is highly irregular and receded into the dunite side of the reaction couple. Melt infiltration can be seen along the right-side edge of the dunite material. A small Cpx crystal is present within the dunite material. This Cpx is the from original peridotite that the natural olivine was sourced from and is not a product of the experimental reaction.

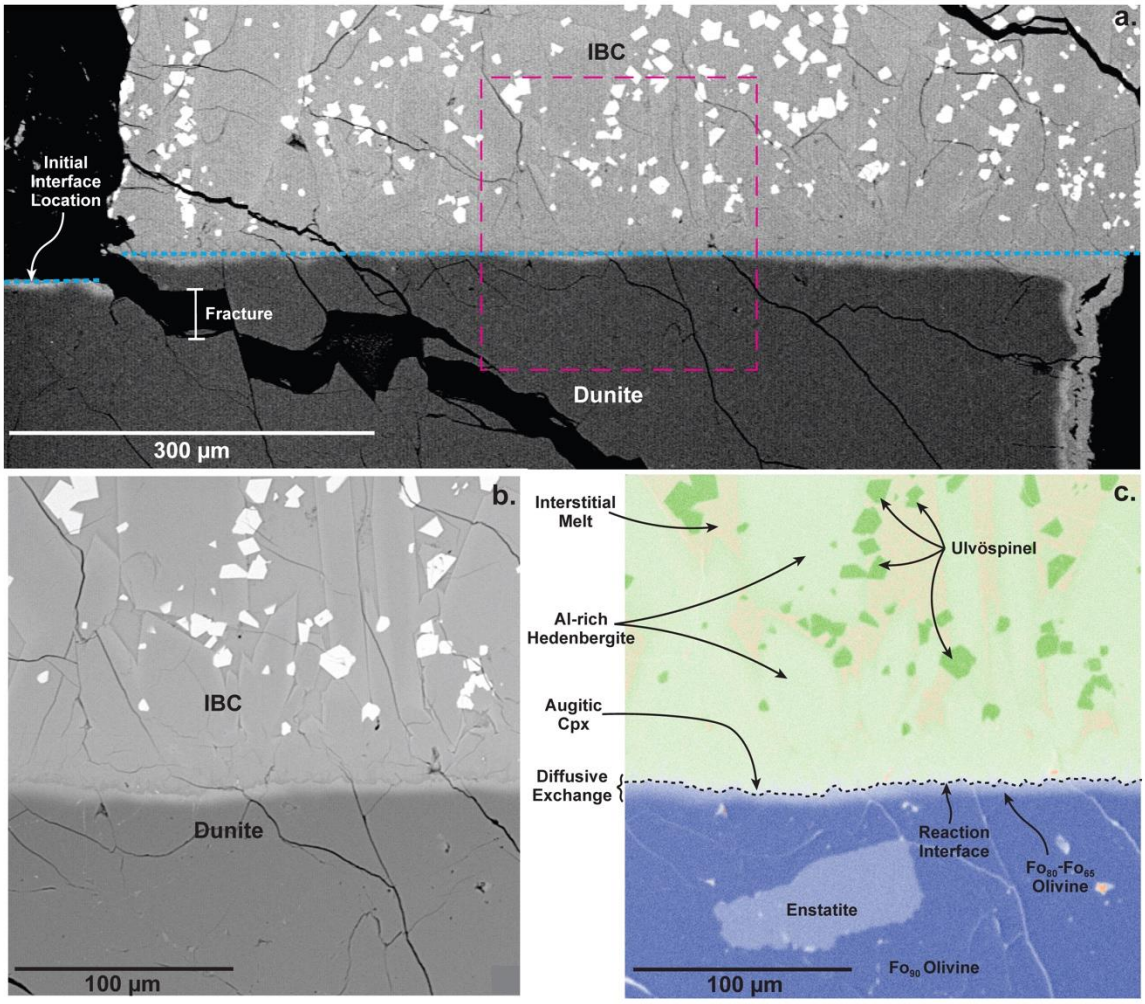


Figure A6. (a) Backscatter electron image of the reaction interface in MRx#11 showing the position of the initial reaction interface (blue dashed line). The box with a pink dashed border highlights an area of interest backscatter imaged in (b) and elemental mapped in (c). (b) Close-up BSE image of the reaction interface in MRx#11. (c) Combined Fe (green), Mg (blue), and Al (orange) false color elemental map of the reaction interface. Al-rich hedenbergite crystals are light green and ulvöspinel crystals are dark green. Interstitial melt is light orange. A rare enstatite crystal within the dunite side of the reaction couple is visible in the elemental map which originates from the natural dunitic starting material. The black dashed line represents the interface between the IBC and dunite sides of the reaction couple. The thin layer of light blue material on the IBC side of the reaction interface is augitic Cpx with Mg-enriched compositions. This material is slightly easier to see in the BSE image (b) as it is a dark layer between light cpx on the IBC side and the light olivine in the dunite side of the reaction interface.

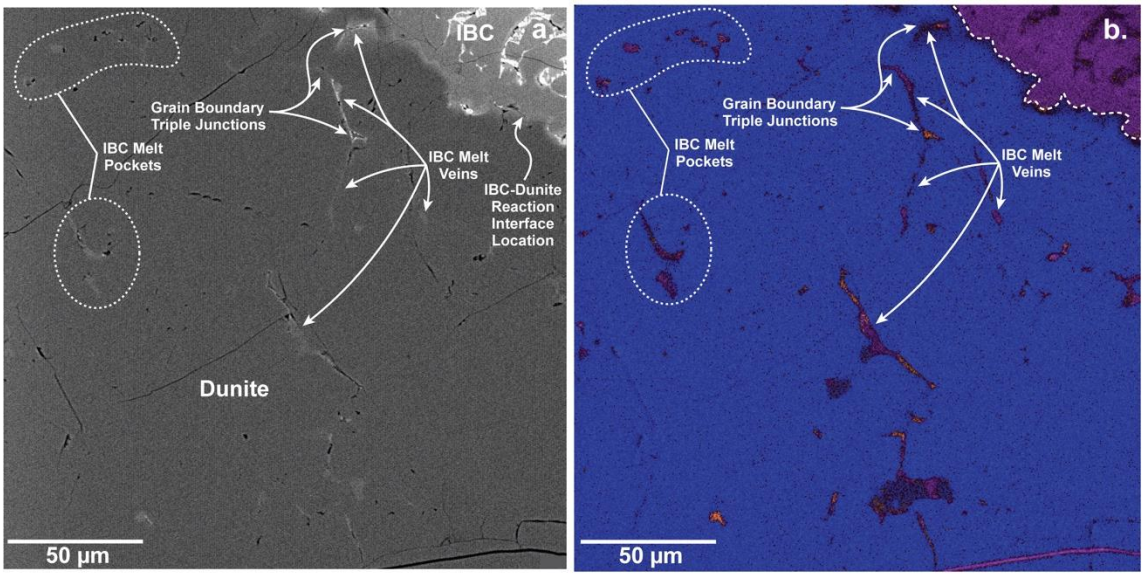


Figure A7. (a) Backscatter electron image of the IBC melt infiltration along grain boundaries in MRx#12. (b) Combined Ca (purple), Mg (blue), and Al (orange) false color elemental map of IBC melt infiltration along grain boundaries at the reaction interface. (b) Dotted white line represents the IBC-dunite reaction interface. IBC melt "pockets" are segments of veins propagating along grain boundaries, perhaps into and out of the view plane in the third dimension.

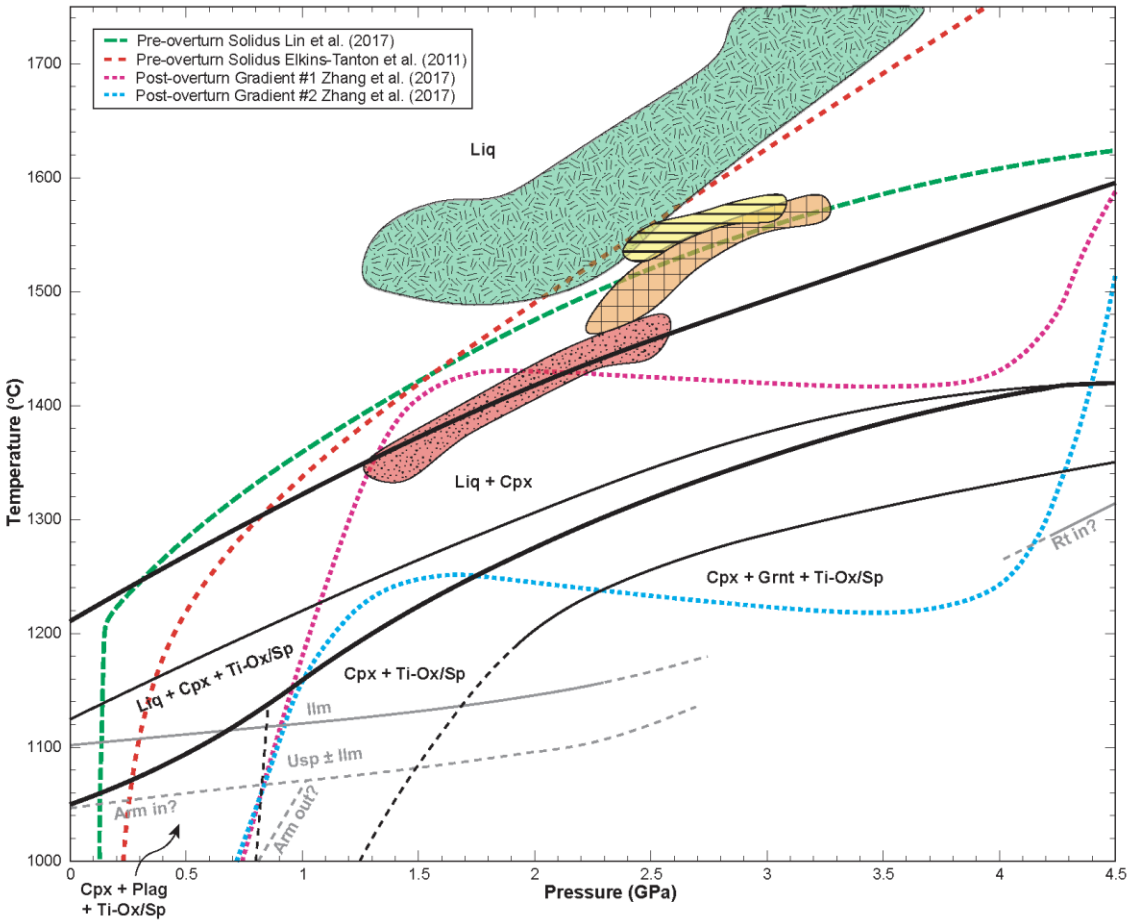


Figure A8. Phase diagram for IBC compared with modeled pre- and post-overturn thermal gradients and Ol-Opx multi-saturation conditions of lunar picritic glasses. Dashed red, green, pink, and light blue lines represent the modeled thermal gradients from previous studies (Elkins-Tanton et al., 2011; Lin et al., 2017, Zhang et al., 2017). Shaded red, orange, yellow, and green regions represent the Ol-Opx multi-saturation conditions of red, orange, yellow, and green picritic glasses (Elkins-Tanton et al., 2003; Draper et al., 2006; Krawczynski and Grove, 2012; Barr and Grove, 2013; Brown and Grove, 2015). Phases: Liquid (Liq), Clinopyroxene (Cpx), Plagioclase (Plag), Garnet (Grnt), Fe-Ti Oxide or Spinel (Ti-Ox/Sp), Ilmenite (Ilm), Ulvöspinel (Usp), Armalcolite (Arm), Rutile (Rt).

Solid-State Diffusion Modeling

In MRx#1 and MRx#8, the IBC side of the couple exhibits a downward shift in Fe/(Fe+Mg)x100, while the dunite side of the couple exhibits an upward shift (**Figure 1.8**). Both experiments exhibit similar interface conditions with compositional variations trending toward molar Fe/(Fe+Mg)x100 values between 40 and 50. Compositional variations in 24 hr experiment MRx#8 (1150°C) are approximately twice width of the variations in 6 hr experiment MRx#1 (1200°C). These compositional variations were modeled using an analytical solution to the one-dimensional diffusion equation assuming exchange between two semi-infinite media with differing diffusivities and a partitioning relationship across the interface (Zhang, 2009).

$$C^L(x,t) = C^L_\infty + \frac{(C^R_\infty - KC^L_\infty)}{1+K\gamma} \cdot erfc\left(\frac{|x|}{2\sqrt{D^L t}}\right), \text{ for } x < 0, \text{ and} \quad \text{(A1a)}$$

$$C^R(x,t) = C^R_\infty + \frac{(KC^L_\infty - C^R_\infty)}{1+K\gamma} \cdot erfc\left(\frac{x}{2\sqrt{D^R t}}\right), \text{ for } x > 0, \quad \text{(A1b)}$$

where $C^L(x,t)$ is the concentration of a given element on the left side of the diffusion couple and $C^R(x,t)$ is the concentration of that element on the right side of the diffusion couple at distance x from the interface at time t. C^L_∞ and C^R_∞ represent the concentration at an infinite distance from the boundary on the left or right side of the diffusion couple. D^L and D^R represent the effective diffusivities of the element on the left or right side of the diffusion couple. The partition coefficient K is the equilibrium concentration variation across the interface ($C^R_{interface}/C^L_{interface}$) and variable γ incorporates the phase densities and diffusivities ($(\rho^R/\rho^L)(D^R/D^L)^{1/2}$). Material densities ρ^R and ρ^L at the experimental P-T conditions were estimated using the third-order Birch-Murnaghan

equation of state and compressibility parameters for Fo90 olivine (Liu and Li, 2006) and hedenbergite (Hu et al., 2015). For both experiments, the calculated densities of Fo90 olivine and hedenbergite are ~3449 kg/m^3 and ~3626 kg/m^3 respectively. The coupled diffusion model assumes that the effective diffusivities differ in the materials on either side of the reaction interface but are constant with time. The effective diffusivities were inverted from the compositional observations by nonlinear least squares regression and are presented in the Solid-State Diffusion subsection of the main text.

Diffusion Through Silicate Melts

Chemical profiles from MRx#9 were modeled using an analytical solution for one-dimensional diffusion-controlled dissolution into a semi-infinite melt reservoir (e.g., Zhang et al., 1989; Van Orman and Grove, 2000) (**Figure 1.10**). The one-dimensional diffusion-controlled dissolution model assumes that the far field and interface melt compositions are constant throughout the dissolution process. Effective binary diffusion coefficients (EBDC) for MgO, FeO, Al_2O_3, and TiO_2 for MRx#9 were modeled using Eq. A2 (also Eq. 3 in Van Orman and Grove, 2000):

$$C(x,t) = C_\infty + \frac{(C_0 - C_\infty)}{erfc(-a)} \cdot erfc\left(\frac{x}{2\sqrt{Dt}} - a\right) \quad \text{(A2)}$$

where C_∞ is the concentration of a given element at infinite distance from the interface, C_0 is the concentration in the melt at the interface, x is the distance from the interface, t is the run duration, D is the effective binary diffusion coefficient in the melt, and $erfc$ is the complementary error function. In application to data from MRx#9, C_0 is assumed to be equal to the composition if the IBC melt at the interface. The variable a from Eq. (A3) is a dimensionless parameter from Zhang et al. (1989) that satisfies:

$$\frac{C_0 - C_\infty}{C_s - C_0} = \sqrt{\pi} a e^{a^2} \cdot erfc(-a) \quad \text{(A3)}$$

where C_s in the concentration in the synthetic dunite. As stated above, the concentration at the interface C_0, is assumed to be constant throughout the experiment. Effective binary diffusion coefficients for MgO, FeO, MnO, Al_2O_3, TiO_2, and CaO in the IBC melt were inverted from the compositional observations by a nonlinear least squares regression and are presented in the Dunite Dissolution Rates, and Effects of Dunite Dissolution on IBC Liquid subsection of the main text.

Diffusion Around The IBC Plume

To model chemical diffusion from an IBC vein or downwelling plume into the ambient mantle we use one-dimensional models for diffusive Fe-Mg exchange. Models were solved numerically using an explicit finite difference method (e.g., Crank, 1975; Ozisik, 1993):

$$C_i^n = \begin{cases} C_{i+1}^{n-1}, & \text{if } i = 0 \\ C_i^{n-1} + \alpha_i (C_{i+1}^{n-1} - 2C_i^{n-1} + C_{i-1}^{n-1}), & \text{if } i = 1,2,\dots,N-1 \\ C_{i-1}^{n-1}, & \text{if } i = N \end{cases} \quad \text{(A4)}$$

where i is the special interval, N is the total number of spatial intervals, n is the time interval, C_i is the concentration at a given interval i, α_i is the scaled diffusivity at a given interval i. The is the dimensionless time is:

$$\alpha_i = \frac{K_i \Delta t}{\Delta x^2} \quad \text{(A5)}$$

where K_i is the diffusivity of the material (m^2/s) at a given interval i, x is the distance between grid points in (m), and Δt is the variation in time between intervals of n in (sec).

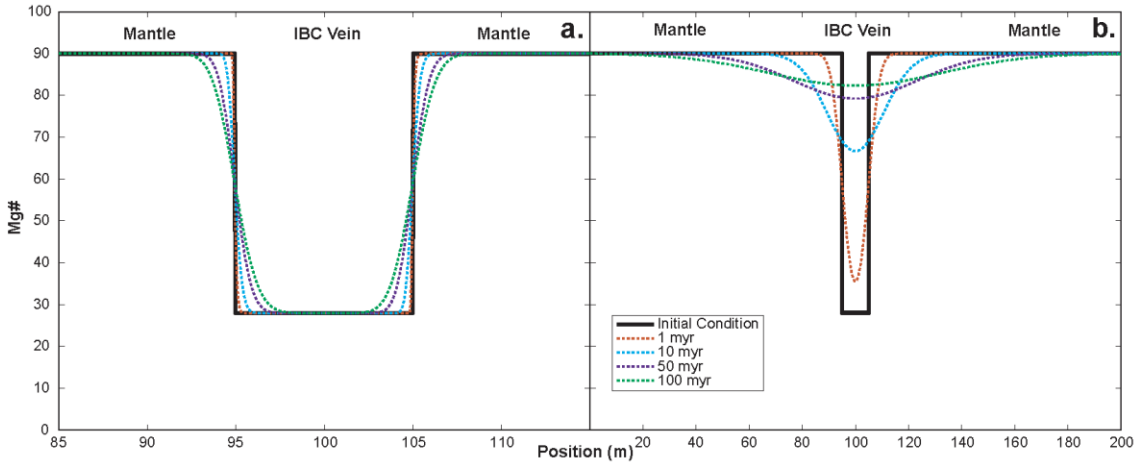


Figure A9. One-dimensional diffusive Fe-Mg exchange simulations modeling interaction between an IBC vein and ambient mantle. (a) Numerical model for vein-mantle Fe-Mg reequilibration where a diffusivity for volume diffusion in olivine at 1200°C is assumed (Dohmen and Chakraborty, 2007). (b) Numerical model for vein-mantle Fe-Mg reequilibration where a three orders of magnitude faster diffusivity is assumed owing to multidomain effects (Farver et al., 1994). Note the different spatial scales in the two figures (the vein has the same width in both cases). Models assume that the vein and surrounding mantle have the same diffusivities, the equilibrium $K_D^{\mathrm{Fe-Mg}}{}_{\mathrm{Mantle-Vein}} = 1$, the initial Mg# of the vein is 28, the initial Mg# of the surrounding mantle is 90, the vein width is 10 m. The assumed diffusivities are 10^{-16} m^2/s in (a) and 10^{-13} m^2/s in (b) (Farver et al., 1994; Dohmen and Chakraborty, 2007).

Appendix A References

Barr, J.A., and Grove, T.L., 2013, Experimental petrology of the Apollo 15 group A green glasses: Melting primordial lunar mantle and magma ocean cumulate assimilation: Geochimica et Cosmochimica Acta, v. 106, p. 216–230, doi:10.1016/j.gca.2012.12.035.

Brown, S.M., and Grove, T.L., 2015, Origin of the Apollo 14, 15, and 17 yellow ultramafic glasses by mixing of deep cumulate remelts: Geochimica et Cosmochimica Acta, v. 171, p. 201–215, doi:10.1016/j.gca.2015.09.001.

Crank, J., 1975, Infinite and Semi-Infinite Media, *in* The Manthematics of Diffusion, Oxford university press, p. 28–43.

Dohmen, R., and Chakraborty, S., 2007, Fe–Mg diffusion in olivine II: point defect chemistry, change of diffusion mechanisms and a model for calculation of diffusion coefficients in natural olivine: Physics and Chemistry of Minerals, v. 34, p. 409–430, doi:10.1007/s00269-007-0158-6.

Draper, D.S., duFrane, S.A., Shearer, C.K., Dwarzski, R.E., and Agee, C.B., 2006, High-pressure phase equilibria and element partitioning experiments on Apollo 15 green C picritic glass: Implications for the role of garnet in the deep lunar interior: Geochimica et Cosmochimica Acta, v. 70, p. 2400–2416, doi:10.1016/j.gca.2006.01.027.

Elkins-Tanton, L.T., Burgess, S., and Yin, Q.-Z., 2011, The lunar magma ocean: Reconciling the solidification process with lunar petrology and geochronology:

Earth and Planetary Science Letters, v. 304, p. 326–336, doi:10.1016/j.epsl.2011.02.004.

Elkins-Tanton, L.T., Chatterjee, N., and Grove, T.L., 2003, Experimental and petrological constraints on lunar differentiation from the Apollo 15 green picritic glasses: Meteoritics & Planetary Science, v. 38, p. 515–527, doi:10.1111/j.1945-5100.2003.tb00024.x.

Farver, J.R., Yund, R.A., and Rubie, D.C., 1994, Magnesium grain boundary diffusion in forsterite aggregates at 1000°–1300°C and 0.1 MPa to 10 GPa: Journal of Geophysical Research: Solid Earth, v. 99, p. 19809–19819, doi:10.1029/94JB01250.

Hu, Y., Dera, P., and Zhuravlev, K., 2015, Single-crystal diffraction and Raman spectroscopy of hedenbergite up to 33 GPa: Physics and Chemistry of Minerals, v. 42, p. 595–608, doi:10.1007/s00269-015-0747-8.

Krawczynski, M.J., and Grove, T.L., 2012, Experimental investigation of the influence of oxygen fugacity on the source depths for high titanium lunar ultramafic magmas: Geochimica et Cosmochimica Acta, v. 79, p. 1–19, doi:10.1016/j.gca.2011.10.043.

Lin, Y., Tronche, E.J., Steenstra, E.S., and van Westrenen, W., 2017, Evidence for an early wet Moon from experimental crystallization of the lunar magma ocean: Nature Geoscience, v. 10, p. 14–18, doi:10.1038/ngeo2845.

Liu, W., and Li, B., 2006, Thermal equation of state of (Mg0.9Fe0.1)2SiO4 olivine: Physics of the Earth and Planetary Interiors, v. 157, p. 188–195, doi:10.1016/j.pepi.2006.04.003.

Özısık, M.N., 1993, Finite-difference Methods, *in* Heat conduction, John Wiley & Sons, p. 436–501.

Van Orman, J.A., and Grove, T.L., 2000, Origin of lunar high-titanium ultramafic glasses: Constraints from phase relations and dissolution kinetics of clinopyroxene-ilmenite cumulates: Meteoritics & Planetary Science, v. 35, p. 783–794, doi:10.1111/j.1945-5100.2000.tb01462.x.

Zhang, Y., 2009, Geochemical Kinetics: Princetion University Press, 664 p.

Zhang, N., Dygert, N., Liang, Y., and Parmentier, E.M., 2017, The effect of ilmenite viscosity on the dynamics and evolution of an overturned lunar cumulate mantle: Geophysical Research Letters, v. 44, p. 6543–6552, doi:10.1002/2017GL073702.

Zhang, Y., Walker, D., and Lesher, C.E., 1989, Diffusive crystal dissolution: Contributions to Mineralogy and Petrology, v. 102, p. 492–513, doi:10.1007/BF00371090.

CHAPTER 2 TRACE ELEMENT AND ISOTOPIC EVOLUTION OF THE LUNAR INTERIOR DURING MAGMA OCEAN SOLIDIFICATION, CUMULATE OVERTURN, AND SUBSEQUENT MELTING: INSIGHTS INTO LUNAR MELT SOURCES

A version of this chapter and the script used in this chapter has been submitted to the Journal of Geophysical Research: Planets, by Jesse L. Scholpp and Nicholas Dygert for publication.

J.L. Scholpp and N. Dygert. (2024b) "A Geochemical Model for Lunar Magma Ocean Solidification." Zenodo, doi:10.5281/zenodo.14172014

J.L. Scholpp and N. Dygert (in review) "Trace Element and Isotopic Evolution of the Lunar Interior During Magma Ocean Solidification, Cumulate Overturn and Subsequent Melting: Insights into Lunar Melt Sources" *The Journal of Geophysical Research: Planets*

Key Points:

- The heavy rare earth element depleted composition of some high-Ti lunar melts requires mantle garnet to explain.
- Plagioclase floatation during lunar magma ocean solidification must be highly efficient to explain the Eu anomaly in lunar melts.
- Cumulate overturn, and mantle hybridization could explain the Lu-Hf and Sm-Nd isotope ratios of lunar basalts.

Abstract

Solidification of a lunar magma ocean (LMO) after a giant impact event formed the Moon's gravitationally unstable juvenile mantle. Hybridization of the lunar mantle during the overturn of late-crystallized Fe- and Ti-rich ilmenite-bearing cumulates (IBC) in the lunar interior is called upon to explain the variable TiO_2 and REE abundances of basalts and picritic melts. We model chemical fractionation during LMO solidification,

mantle hybridization, and partial melting of hybridized and unhybridized cumulates to evaluate the formation of lunar picritic glasses. Solidification models indicate that plagioclase floatation efficiency during LMO solidification must be >90% to explain the negative Eu anomaly demonstrated by lunar picritic glasses. Melting models demonstrate that unhybridized cumulates could produce low-Ti picritic glasses but not high-Ti glasses. Post-hybridization melting models demonstrate that hybridized garnet-free sources can generate elemental ratios of many intermediate to high-Ti lunar picritic glasses. The Heavy Rare Earth Element depleted compositions of orange picritic glasses require a ~0.25-5% garnet component in the downwelling IBC or hybridized sources. If the LMO extended to the core-mantle boundary, garnet may have only formed in the lunar mantle after cumulate overturn occurred. The Lu-Hf and Sm-Nd isotope ratios of lunar samples are consistent with elemental abundances, suggesting the isotopic characteristics of mantle sources reflect primary lunar differentiation. High-Ti basalt isotope ratios can be modeled as hybridized mixtures of late and early crystallizing cumulates. We argue that the combined elemental and isotopic characteristics of high-Ti picritic glasses and basalts are strong evidence of cumulate overturn during early lunar differentiation.

Plain Language Summary

The Moon's magma ocean formed after a giant planetary impact event. Solidification of the lunar magma ocean created an unstable density distribution within the Moon’s mantle. Reorganization of unstable mantle material during overturn events would transport dense rocks from the upper to the lower lunar mantle. This could explain

the varying elemental compositions observed in lunar mantle derived rock (solidified melt) samples. To better understand lunar mantle melt formation, we modeled how elements were separated during magma ocean solidification, mixing of mantle materials during overturn events, and melting of both mixed and unmixed mantle rocks. Our models suggest that more than 90% of certain minerals must have floated to the surface, forming crust during solidification. The models also show that melting of unmixed mantle rocks could have formed low-titanium mantle melts, however; mantle mixing is required to produce intermediate- to high-titanium mantle melts. Some high-titanium mantle melts need a small amount of a mineral called garnet in their source. If the magma ocean was deep, garnet should only form after an overturn event. Isotopic data from lunar rocks support the idea that density reorganization events occurred, with high-titanium basalts showing evidence of mixing between early and late crystallizing materials.

2.1 Introduction

To evaluate what lunar basalt chemistry reveals about the dynamic evolution of the Moon's interior, this study investigates lunar magmatic evolution in a series of forward models conducted in a sequence of three phases: (1) Lunar Magma Ocean (LMO) solidification, (2) gravitational redistribution of LMO cumulates during or after LMO solidification (cumulate mantle overturn), (3) partial melting of lunar mantle sources (with and without garnet). A comparison of measured Rare Earth Element (REE: La-Lu) and Hf abundances, and Sm-Nd and Lu-Hf isotopic compositions of lunar basalts with predictive models provides a means to test hypothesized processes that occurred in the lunar interior during and after the magma ocean stage.

The LMO is believed to have formed after a giant impact between the proto-Earth and another planetary body (Canup, 2004, 2012; Elkins-Tanton and Hager, 2005; Hiesinger and Head, 2006; Elkins-Tanton, 2012; Young et al., 2016; Thiemens et al., 2019; Cano et al., 2020). As the LMO cooled and began to solidify, dense minerals (i.e., olivine (Ol), orthopyroxene (Opx), clinopyroxene (Opx)) settled to the bottom of the magma ocean and the less dense plagioclase (Plag) floated to the top, forming an anorthosite floatation crust **(Figure 2.1a**) (Walker and Hays, 1977; Wood et al., 1970; Elardo et al., 2011; Elkins-Tanton et al., 2011; Dygert et al., 2017; Lin et al., 2016, 2017; Charlier et al., 2018). During the late stages of LMO solidification, the residual LMO melt would have become enriched in incompatible elements (e.g., Ti, K, P), resulting in eventual precipitation of ilmenite ($FeTiO_3$)-bearing cumulates (IBC) and formation of a hypothesized potassium (K), REE, and phosphorous (P)-rich residual liquid thought to have imparted its chemical signature on many lunar samples, commonly referred to as KREEP (Warren and Wasson, 1979; Snyder et al., 1992; Hess and Parmentier, 1995; Elkins-Tanton et al., 2011; Lin et al., 2017; Charlier et al., 2018; Rapp and Draper, 2018) (**Figure 2.1a**).

The origin and formation mechanisms of lunar mare basalt and picritic glass mantle sources have been debated since analysis of Apollo returned samples revealed that the basalts exhibit variable TiO_2 and REE concentrations with a wide range of Mg#s (Mg# = (molar Mg/(Mg+Fe))x100) (Delano, 1986; Haskin and Warren, 1991; Shearer et al., 1991; Shearer and Papike, 1993; Papike et al., 1998; Neal, 2001; Shearer et al., 2015).

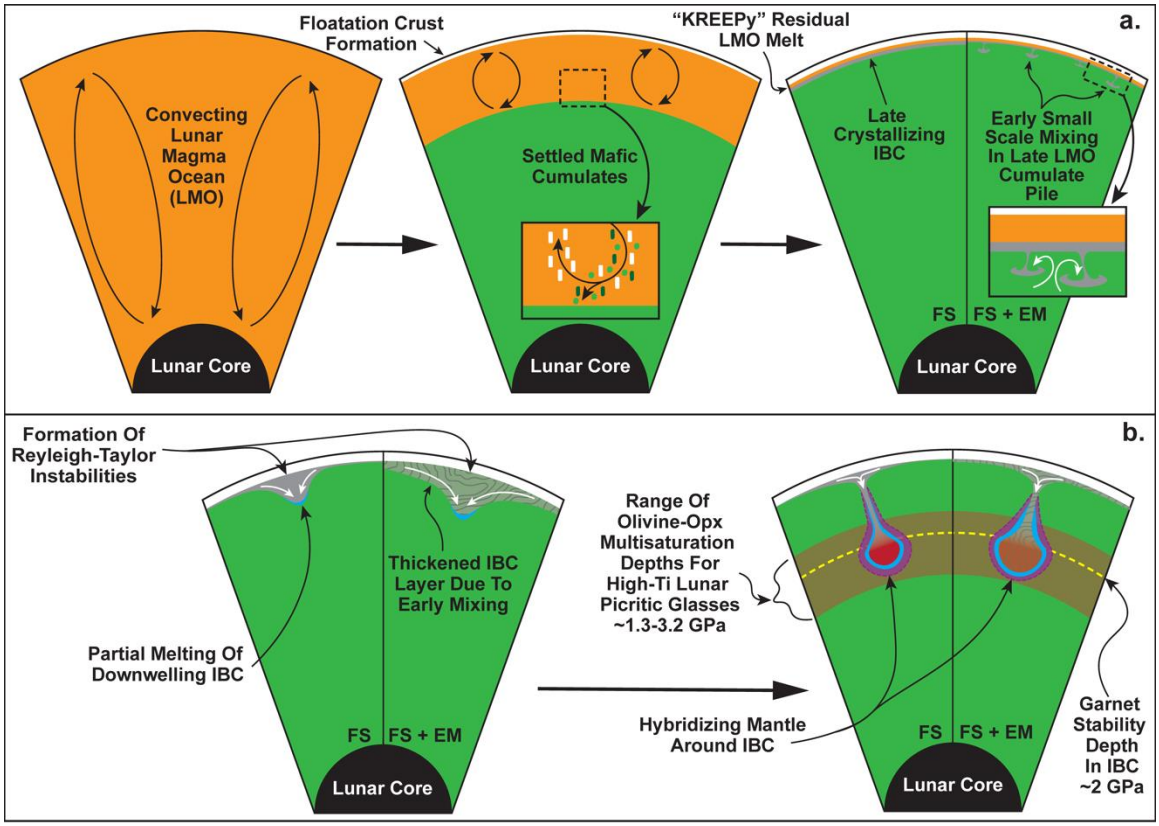


Figure 2.1. Schematic figure of lunar evolution up to the point of cumulate overturn and mantle hybridization. (a) Progressive lunar magma ocean (LMO) solidification forms a juvenile mantle, and crustal cumulates through density-driven crystal settling and floatation. The solidification process results in the eventual formation of late KREEP-rich IBC layers. Depending on the rheologic properties of the settled mafic mantle cumulates, instabilities could form in the IBC layer during late-stage LMO solidification, resulting in a thickened and less ilmenite-rich IBC layer. (b) Following the solidification process, larger Reyleigh-Taylor instabilities in the relatively dense IBC could form and initiate a large-scale cumulate overturn event. Hybridization of the lunar mantle would occur as the downwelling diapirs of IBC material descend into the lunar mantle and chemically and mechanically interact with underlying mafic cumulates. The color change in the IBC material indicates that IBC stabilized garnet during the overturn process. High-Ti glasses: orange, red, and black picritic glass groups. FS- Fractional Solidification, FS + EM- Fractional Solidification + Early Mixing. Features in the Figure are not to scale.

This chemical variation is attributed to the chemical diversity of lunar mantle sources (Delano, 1986; Shearer and Papike, 1993; Lucey et al., 1998; Giguere et al., 2000; Shearer et al., 2015), which may have been a direct product of solidification of the LMO. Despite the mineralogical diversity of anticipated LMO cumulate layers, they individually cannot be invoked as mantle sources capable of producing many mare basalts (Snyder et al., 1992; Elardo et al., 2011; Elkins-Tanton et al., 2011; Lin et al., 2017; Charlier et al., 2018). For example, the lunar orange picritic glasses have Mg#s of 42-55, TiO_2 wt% of 8-14, and REE concentrations 10-150x higher than chondritic values. This requires a mantle source with a relatively Mg-rich composition similar to early crystallizing LMO cumulates and a Ti-rich and REE-rich composition similar to late crystallizing LMO cumulates. Thus, a post-LMO solidification mantle hybridization mechanism is often invoked to effectively mix shallow and deep magma ocean cumulates to account for the mare basalt and picritic glass chemical compositions (Ringwood and Kesson, 1976; Singletary and Grove, 2008; Thacker et al., 2009; Yao and Liang, 2012; Hallis et al., 2014; Mallik et al., 2019).

The late precipitation of dense IBC produces a gravitationally unstable lunar mantle stratigraphy, with less dense ilmenite-free cumulates beneath the dense IBC (Snyder et al., 1992; Hess and Parmentier, 1995; Elkins-Tanton et al., 2011; Zhang et al., 2017; Li et al., 2019). Previous studies indicate that the gravitationally unstable stratigraphy would have resulted in cumulate overturn, where dense shallow cumulates flow into the deep lunar interior as viscous solids, perhaps after progressive thickening of the IBC layer which occurred as the IBC precipitated, where the IBC sank directly into

the underlying mafic cumulates before LMO solidification completed (Hess and Parmentier, 1995; Zhang et al., 2017; Li et al., 2019) (**Figure 2.1b**). The overturn of IBC into the lunar mantle would juxtapose sinking IBC against deep mafic mantle cumulates, where a combination of mechanical mixing and "assimilation" (exchange produced by diffusion and dissolution-precipitation reactions) could generate hybridized mantle sources (Hess and Parmentier 1995; Van Orman and Grove, 2000; Elkins-Tanton et al., 2002; Singletary and Grove, 2008; Brown and Grove, 2015; Mallik et al., 2019; Scholpp and Dygert, 2024a).

Previous studies of lunar mare basalts hypothesized that heavy REE (HREE: Er-Lu) depletions observed in some basalts and picritic glasses may be related to garnet in the lunar mantle (Beard et al., 1998; Neal, 2001; Draper et al., 2006); however, this hypothesis is often refuted given the high pressures required to stabilize garnet in experiments on lunar materials (Longhi et al., 1974; Elkins-Tanton et al., 2003; Draper et al., 2006; Elardo et al., 2011; Krawczynski and Grove, 2012; Barr and Grove, 2013; Mallik et al., 2019; Kraettli et al., 2022; Jing et al., 2022). The recent work of Scholpp and Dygert (2024a) demonstrates that garnet should stabilize in late-crystallizing lunar magma ocean (LMO) cumulates during and after hypothesized cumulate overturn events (Hess and Parmentier, 1995; Zhang et al., 2017; Li et al., 2019). This lends support to the hypothesis from Schmidt and Kraettlli (2022) that a partial melting process akin to terrestrial granulite facies melting of mafic rocks (Cohen et al., 1967; Springer and Seck, 1997) and subsequent mantle hybridization could explain the HREE depletion observed in some lunar basalts and picritic glasses (**Figure 2.1b**).

In this work, geochemical models primarily attempt to constrain processes producing the geochemical characteristics of lunar picritic glasses as they represent near-primary quenched melts (Delano, 1986; Shearer and Papike, 1993; Papike et al., 1998) that originated deep within the lunar interior (Elkins-Tanton et al., 2003, Draper et al., 2006; Krawczyncski and Grove, 2012; Barr and Grove, 2013; Brown and Grove, 2015). The relative lack of fractional crystallization in their petrogenetic history makes the picritic glasses suitable for evaluating lunar internal processes, in contrast to mare basalts, which suffered extensive crystal fractionation (Neal et al., 1994; Snyder et al., 1997; Hallis et al., 2014). Using experimentally determined LMO cumulate solidification sequences (Charlier et al., 2018) and up-to-date lunar trace element partition coefficients, we model chemical fractionation during LMO solidification, mantle hybridization, and partial melting. We investigate the effects of partial melting on primary (i.e., unhybridized) LMO cumulates and hybridized cumulate sources. We consider multiple hybridization scenarios in which modal partial melts of IBC material or unmelted IBC material are mechanically mixed into early magma ocean cumulates (EMOC) to generate hybridized mantle sources. We then apply modal partial melting models to the hybridized sources, evaluating the effect of the presence or absence of garnet in the hybridized sources and IBC material to determine the trace element and isotopic compositions of melts they would produce.

2.2 Geochemical Modeling

2.2.1 Model Assumptions: Lunar Bulk Composition

While there are multiple estimates of the bulk composition of the LMO (Taylor and Bence, 1975; Taylor, 1982; Wanke and Dreibus, 1982; Jones and Delano, 1989; O'Neill, 1991; Longhi, 2003; Warren, 2005), the Lunar Primitive Upper Mantle (LPUM; Longhi, 2003) and Taylor Whole Moon (TWM; Taylor, 1982) compositions are presently the most widely tested and debated compositional endmembers. Due to the Al-rich nature of the TWM composition, recent studies have concluded that this composition would require an unrealistically shallow magma ocean to account for the geophysical estimates of lunar crustal thickness (Wieczorek et al., 2006, 2013), as deep or whole Moon magma oceans with a TWM bulk composition would generate overly thick lunar crusts (Longhi, 2006; Charlier et al., 2018).

Using the recent GRAIL-derived crustal thickness estimates and crust/mantle mass balance calculations, Taylor and Wieczorek (2013) conclude that the abundance of Al_2O_3 (a refractory element) in the bulk silicate Moon is roughly equal to that of the Earth. Assuming that the Moon has an Earth-like refractory element abundance, they also estimate the abundance of K in the lunar mantle, demonstrating that the Moon is K-depleted relative to Earth. Thus, the LPUM composition has emerged as a preferred model for the Moon's bulk composition as it has refractory element abundances similar to Earth's upper mantle composition (Hart and Zindler, 1986) and is depleted in volatile alkali elements (i.e., Na and K) (Longhi, 2003).

Given the abovementioned observations, we assume that LMO solidification follows a crystallization sequence experimentally constrained by Charlier et al. (2018) for an LPUM-like composition. Solidification models in this study assume that the starting REE and Hf in the initial LMO are equal to the estimated Bulk Silicate Earth (BSE) composition from Sun and McDonough (1995).

2.2.2 Lunar Magma Ocean Solidification Models

Trace element fractionation during LMO crystallization was modeled assuming Rayleigh fractionation using Eq.s 2.1 and 2.2:

$$C_L^i = C_{L_0}^i F^{(D_{Bulk}^i - 1)}\,, \tag{2.1}$$

$$C_S^i = C_L^i \times D_{Bulk}^i\,, \tag{2.2}$$

where C_L^i represents the concentration of element i, $C_{L_0}^i$ is the composition of the initial liquid, C_S^i represents the concentration in the solid, F is the fraction of melt remaining, and D_{Bulk}^i is the bulk partition coefficient between crystals and liquid. For an assemblage of phases, D_{Bulk}^i can be calculated with Eq. 2.3:

$$D_{Bulk}^i = D_\alpha^i(X_\alpha) + D_\beta^i(X_\beta) + D_\gamma^i(X_\gamma) + \ldots, \tag{2.3}$$

where D_α^i is the partition coefficient for element i in phase α, X_α is the modal proportion of phase a in the group of crystallizing phases. Fractional crystallization assumes that crystals form within the LMO and settle out to form cumulates at the base of the magma ocean. By definition, in a fractional crystallization scenario, crystals in the cumulate pile are not in equilibrium with the magma ocean residual liquid except at the moment they form. To conserve mass, D_{Bulk}^i in this model must account for previously removed

crystallizing phases as the magma ocean evolves. Recalculating the D^{i}_{Bulk} at intervals j after a first interval a:

$$D^{i,ab}_{Comb} = \frac{D^{i,a}_{Bulk}(1-F_a)+D^{i,b}_{Bulk}(F_a-F)}{(1-F)}, \quad (2.4)$$

$$D^{i,abc}_{Comb} = \frac{D^{i,a}_{Bulk}(1-F_a)+D^{i,b}_{Bulk}(F_a-F_b)+D^{i,c}_{Bulk}(F_b-F)}{(1-F)}, \quad (2.5)$$

and so forth, where $D^{i,j}_{Bulk}$ is the bulk partition coefficient for a given element during a part of the crystallization sequence at an extent of melt F. For the first interval a, the melt fraction at which crystallization interval a ends is F_a. $D^{i,ab}_{Comb}$ represents the combined bulk partition coefficient for a second crystallization interval b, crystallization sequence b occurs for melt fractions between F_a and F_b. $D^{i,abc}_{Comb}$ represents the combined bulk partition coefficient for a third crystallization interval c, crystallization interval c occurs for melt fractions between F_b and F_c.

The crystallization sequence assumed in this study is similar to the experimental results of Charlier et al. (2018). Magma ocean solidification occurs in a six-stage progression of fractionating phases (**Table 2.1**). Olivine is the only crystallization phase from F = 1 to F = 0.49, Ol and Opx crystallize from F = 0.49 to F = 0.22, Ol, Opx, pigeonite (Pig), and Plag crystallize from F = 0.22 to F = 0.19, and Cpx (i.e., augite), Pig, and Plag crystallize from F = 0.19 to F = 0.05. The last two stages of solidification are assumed to crystallize Cpx, Pig, Plag, and quartz (Qtz) from F = 0.05 to F = 0.02, and fayalitic Ol, Cpx, Plag, Qtz, and Ilm crystallize from F = 0.02 to F = 0.

Table 2.1. Phase proportions in LMO cumulates based on findings from Charlier et al. (2018), assuming no plagioclase or quartz floatation.

Phases	Stage 1	Stage 2	Stage 3	Stage 4	Stage 5	Stage 6
Ol	0.990	0.099	0.050	0.000	0.000	0.198
Opx	0.000	0.891	0.198	0.000	0.000	0.000
Cpx	0.000	0.000	0.000	0.198	0.198	0.158
Pig	0.000	0.000	0.248	0.317	0.248	0.000
Plag	0.000	0.000	0.495	0.475	0.446	0.416
Qtz	0.000	0.000	0.000	0.000	0.099	0.099
Ilm	0.000	0.000	0.000	0.000	0.000	0.119
Melt	0.010	0.010	0.010	0.010	0.010	0.010

*Stage 1: F= 1-0.49, Stage 2: F= 0.49-0.22, Stage 3: F= 0.22-0.19, Stage 4: F= 0.19-0.05, Stage 5: F= 0.05-0.02, Stage 6: F= 0.02-0

Olivine (Ol), Orthopyroxene (Opx), Clinopyroxene (Cpx), Pigeonite (Pig), Plagioclase (Plag), Ilmenite (Ilm), Quartz (Qtz)

Table 2.1 documents the mineral proportions for each crystallization step, and entrainment of 1% interstitial melt is assumed for magma ocean cumulates similar to Snyder et al. (1992). The mineral proportions, which are shown in **Table 2.1**, do not account for plagioclase and quartz floatation, which is thought to form the anorthosite crust on the Moon (e.g., Synder et al., 1992; Suckale et al., 2012; Dygert et al., 2017). To account for the effect of plagioclase flotation on the LMO cumulates, this study evaluated flotation efficiencies of 80%, 90%, and 98% (Dygert et al., 2017; Charlier et al., 2018). To account for this effect on the trace element patterns in the LMO cumulates, the D_{Bulk} for the LMO cumulates was scaled appropriately using modal abundances accounting for 80% (**Table B1**), 90% (**Table B2**), and 98% (**Table B3**) plagioclase removal.

Partition coefficients for each mineral phase during solidification were compiled from experimental studies of terrestrial and lunar synthetic analogs (Pertermann et al., 2004; Dalou et al., 2012; Dygert et al., 2013; Brey et al., 2015; Snape et al., 2022) or they were calculated using lattice strain-based partitioning models and lunar relevant mineral compositions (Sun and Liang, 2013a, 2013b; Dygert et al., 2014; Sun et al., 2017; Dygert et al., 2020). Mineral-melt partition coefficients and compositional calculation parameters for LMO solidification models are reported in **Table 2.2**.

The lunar mantle's oxygen fugacity (fO_2) can affect Eu partitioning during LMO solidification (Dygert et al., 2020). The assumed lunar mantle fO_2 in this study is ~IW (i.e., roughly equal to iron-wüstite redox buffer), and partition coefficients were calculated correspondingly.

Table 2.2. Assumed LMO starting composition and mineral-melt partition coefficients for magma ocean solidification models.

Element	LMO (ppm)	ref.	Ol (D)	Ol (D)	Ol (D)
La	0.648	a	7.96E-06	5.31E-06	2.01E-06
Ce	1.675	a	3.45E-05	2.63E-05	1.19E-05
Pr	0.254	a	1.16E-04	9.86E-05	5.19E-05
Nd	1.25	a	1.73E-04	1.52E-04	8.42E-05
Sm	0.406	a	3.50E-04	3.28E-04	1.98E-04
Eu	0.154	a	9.76E-04	9.02E-04	4.52E-04
Gd	0.544	a	1.64E-03	1.76E-03	1.29E-03
Tb	0.099	a	3.09E-03	3.51E-03	2.77E-03
Dy	0.674	a	4.74E-03	5.60E-03	4.67E-03
Y	4.3	a	7.32E-03	9.00E-03	7.90E-03
Ho	0.149	a	7.07E-03	8.66E-03	7.57E-03
Er	0.438	a	1.02E-02	1.30E-02	1.19E-02
Tm	0.068	a	1.40E-02	1.82E-02	1.73E-02
Yb	0.441	a	1.98E-02	2.65E-02	2.64E-02
Lu	0.0675	a	2.38E-02	3.25E-02	3.30E-02
Hf	0.238	a	4.00E-03	4.00E-03	4.00E-03
Stage			1	2	3
T (ºC)			1550	1400	1230
P (GPa)			2	1.2	0.5
Fo			92.7	87.5	83.4
Al^{ol}			0.00255	0.00468	0.00503
$X\mathrm{Ti}^{melt}$			-	-	-
Al^{T}			-	-	-
Al^{M1}			-	-	-
Ca^{M2}			-	-	-
Mg^{M2}			-	-	-
Mg^{M1}			-	-	-
Fe^{M1}			-	-	-
XCa			-	-	-
XNa			-	-	-
D_0			-	-	-
r_0			-	-	-
E			-	-	-
D(Ti)			-	-	-
Log(fO_2)			-8.38	-9.72	-11.57
Sample/ Experiment			LPUM 2.015	LPUM0.55 B1288	LPUM88 HAO2-5

Table 2.2. Continued.

Element	Ol (D)	ref.	Opx (D)	Opx (D)	ref.
La	5.63E-07	b, Cal.	8.45E-04	1.07E-03	d, Cal.
Ce	4.45E-06	b, Cal.	1.74E-03	2.27E-03	d, Cal.
Pr	2.47E-05	b, Cal.	3.35E-03	4.52E-03	d, Cal.
Nd	4.33E-05	b, Cal.	6.10E-03	8.44E-03	d, Cal.
Sm	1.17E-04	b, Cal.	1.52E-02	2.20E-02	d, Cal.
Eu	1.14E-04	Sup.	9.88E-03	7.06E-03	e, Cal.
Gd	1.03E-03	b, Cal.	2.90E-02	4.36E-02	d, Cal.
Tb	2.51E-03	b, Cal.	3.83E-02	5.85E-02	d, Cal.
Dy	4.60E-03	b, Cal.	4.89E-02	7.60E-02	d, Cal.
Y	8.48E-03	b, Cal.	5.61E-02	8.79E-02	d, Cal.
Ho	8.07E-03	b, Cal.	5.97E-02	9.41E-02	d, Cal.
Er	1.36E-02	b, Cal.	7.02E-02	1.12E-01	d, Cal.
Tm	2.12E-02	b, Cal.	7.98E-02	1.29E-01	d, Cal.
Yb	3.44E-02	b, Cal.	8.83E-02	1.44E-01	d, Cal.
Lu	4.47E-02	b, Cal.	9.56E-02	1.57E-01	d, Cal.
Hf	4.00E-03	c	3.14E-02	4.90E-02	d, Cal.
Stage	6		2	3	
T (ºC)	1020	l	1400	1230	l
P (GPa)	0.08	l	1.2	0.5	l
Fo	11.4	l & m	-	-	
Al^{ol}	0.00078	l & m	-	-	
$X\mathrm{Ti}^{melt}$	-		0.0192	0.0219	l
Al^{T}	-		0.0675	0.1067	l
Al^{M1}	-		0.0715	0.0515	l
Ca^{M2}	-		0.0717	0.0989	l
Mg^{M2}	-		0.7064	0.6312	l
Mg^{M1}	-		0.8965	0.9321	l
Fe^{M1}	-		0.0018	0.0034	l
XCa	-		-	-	
XNa	-		-	-	
D_0	-		-	-	
r_0	-		-	-	
E	-		-	-	
D(Ti)	-		-	-	
$\mathrm{Log}(fO_2)$	-14.54		-9.72	-11.57	
Sample/ Experiment	LPUM/0.4-1.5 gl HA02-0.8	l & m	LPUM0.55 B1288	LPUM88 HAO4-5	l

Table 2.2. Continued.

Element	Cpx (D)	Cpx (D)	Cpx (D)	ref.	Pig (D)	ref.
La	1.97E-02	2.37E-02	3.44E-02	f, Cal.	5.68E-03	g, Cal.
Ce	2.87E-02	3.52E-02	5.29E-02	f, Cal.	1.15E-02	g, Cal.
Pr	3.98E-02	4.97E-02	7.70E-02	f, Cal.	2.05E-02	g, Cal.
Nd	5.28E-02	6.70E-02	1.06E-01	f, Cal.	2.47E-02	g, Cal.
Sm	7.80E-02	1.01E-01	1.67E-01	f, Cal.	3.44E-02	g, Cal.
Eu	1.68E-01	1.73E-01	2.08E-01	e, Cal.	5.84E-02	g, Cal.
Gd	9.83E-02	1.29E-01	2.17E-01	f, Cal.	7.03E-02	g, Cal.
Tb	1.07E-01	1.41E-01	2.38E-01	f, Cal.	9.37E-02	g, Cal.
Dy	1.13E-01	1.49E-01	2.54E-01	f, Cal.	1.14E-01	g, Cal.
Y	1.15E-01	1.53E-01	2.61E-01	f, Cal.	1.37E-01	g, Cal.
Ho	1.17E-01	1.55E-01	2.64E-01	f, Cal.	1.35E-01	g, Cal.
Er	1.18E-01	1.57E-01	2.68E-01	f, Cal.	1.59E-01	g, Cal.
Tm	1.18E-01	1.57E-01	2.68E-01	f, Cal.	1.82E-01	g, Cal.
Yb	1.17E-01	1.55E-01	2.64E-01	f, Cal.	2.10E-01	g, Cal.
Lu	1.14E-01	1.52E-01	2.58E-01	f, Cal.	2.27E-01	g, Cal.
Hf	7.32E-02	1.14E-01	2.66E-01	f, Cal.	6.81E-02	h
Stage	4	5	6		3, 4, 5, 6	
T (ºC)	1215	1130	1020	l	-	
P (GPa)	0.5	0.3	0.08	l	-	
Fo	-	-	-		-	
Al^{ol}	-	-	-		-	
$X\mathrm{Ti}^{melt}$	-	-	-		-	
Al^{T}	0.0845	0.0627	0.0598	l	-	
Al^{M1}	0.0488	0.0167	0.0124	l	-	
Ca^{M2}	0.4183	0.4442	0.6385	l	-	
Mg^{M2}	-	-	-		-	
Mg^{M1}	-	-	-		-	
Fe^{M1}	-	-	-		-	
*X*Ca	-	-	-		-	
*X*Na	-	-	-		-	
D_0	-	-	-		0.38	g
r_0	-	-	-		0.759	g
E	-	-	-		198	g
D(Ti)	-	-	-		-	
$\mathrm{Log}(fO_2)$	-11.75	-12.87	-14.54		-	
Sample/ Experiment	LPUM88 HAO2-5	LPUM/02-5 HA02-3	LPUM/0.4-1.5 gl HA02-0.8	l	Eu14-17	g

Table 2.2. Continued.

Element	Plag (D)	Plag (D)	Plag (D)	Plag (D)	ref.
La	1.11E-02	8.46E-03	5.80E-03	7.14E-03	i, Cal.
Ce	1.04E-02	7.90E-03	5.39E-03	6.63E-03	i, Cal.
Pr	9.35E-03	7.08E-03	4.80E-03	5.89E-03	i, Cal.
Nd	8.13E-03	6.11E-03	4.09E-03	5.02E-03	i, Cal.
Sm	5.82E-03	4.28E-03	2.80E-03	3.41E-03	i, Cal.
Eu	6.41E-01	9.61E-01	1.40E+00	1.58E+00	g, Cal.
Gd	4.00E-03	2.88E-03	1.83E-03	2.22E-03	i, Cal.
Tb	3.22E-03	2.29E-03	1.43E-03	1.73E-03	i, Cal.
Dy	2.55E-03	1.78E-03	1.10E-03	1.32E-03	i, Cal.
Y	2.19E-03	1.52E-03	9.25E-04	1.11E-03	i, Cal.
Ho	2.02E-03	1.40E-03	8.46E-04	1.01E-03	i, Cal.
Er	1.61E-03	1.10E-03	6.55E-04	7.80E-04	i, Cal.
Tm	1.30E-03	8.74E-04	5.13E-04	6.08E-04	i, Cal.
Yb	1.06E-03	7.05E-04	4.08E-04	4.82E-04	i, Cal.
Lu	8.81E-04	5.79E-04	3.30E-04	3.89E-04	i, Cal.
Hf	2.46E-04	2.46E-04	2.46E-04	2.46E-04	i
Stage	3	4	5	6	
T (ºC)	1215	1130	1040	1020	l
P (GPa)	0.5	0.3	0.15	0.08	l
Fo	-	-	-	-	
Al^{ol}	-	-	-	-	
$X\mathrm{Ti}^{melt}$	-	-	-	-	
Al^{T}	-	-	-	-	
Al^{M1}	-	-	-	-	
Ca^{M2}	-	-	-	-	
Mg^{M2}	-	-	-	-	
Mg^{M1}	-	-	-	-	
Fe^{M1}	-	-	-	-	
XCa	0.9406	0.8833	0.8029	0.7445	l
XNa	0.0594	0.1138	0.1916	0.2424	l
D_0	-	-	-	-	
r_0	-	-	-	-	
E	-	-	-	-	
D(Ti)	-	-	-	-	
Log(fO_2)	-11.75	-12.87	-14.22	-14.54	
Sample/ Experiment	LPUM88 HAO2-5	LPUM/02-5 HA02-3	LPUM/02-3 gl HAO4-1.5	LPUM/0.4-1.5 gl HA02-0.8	l

Table 2.2. Continued.

Element	Ilm (D)	ref.	Qtz (D)	ref.	Int-Mlt (D)
La	6.42E-06	j, Cal.	1.30E-02	k	1
Ce	3.12E-05	j, Cal.	9.90E-03	k	1
Pr	1.16E-04	j, Cal.	9.10E-03	k	1
Nd	1.80E-04	j, Cal.	1.00E-02	k	1
Sm	3.90E-04	j, Cal.	2.50E-02	k	1
Eu	2.70E-04	Sup.	8.00E-03	k	1
Gd	2.17E-03	j, Cal.	8.00E-03	k	1
Tb	4.43E-03	j, Cal.	8.00E-03	k	1
Dy	7.22E-03	j, Cal.	8.00E-03	k	1
Y	1.19E-02	j, Cal.	1.20E-02	k	1
Ho	1.14E-02	j, Cal.	9.00E-03	k	1
Er	1.76E-02	j, Cal.	7.00E-03	k	1
Tm	2.55E-02	j, Cal.	1.00E-02	k	1
Yb	3.84E-02	j, Cal.	3.60E-02	k	1
Lu	4.82E-02	j, Cal.	7.00E-03	k	1
Hf	4.46E-01	j, Cal.	1.40E-02	k	1
Stage	6		5, 6		
T (ºC)	1020	l	-		-
P (GPa)	0.08	l	-		-
Fo	-		-		-
Al^{ol}	-		-		-
$X\mathrm{Ti}^{melt}$	-		-		-
Al^{T}	-		-		-
Al^{M1}	-		-		-
Ca^{M2}	-		-		-
Mg^{M2}	-		-		-
Mg^{M1}	-		-		-
Fe^{M1}	-		-		-
XCa	-		-		-
XNa	-		-		-
D_0	0.61	j	-		-
r_0	0.688	j	-		-
E	300	j	-		-
D(Ti)	14.274	l	-		-
Log(fO_2)	-14.54		-		-
Sample/ Experiment	LPUM/0.4-1.5 gl HA02-0.8		-		-

Calculated partition coefficients are indicated in the source column (Cal.). (Sup.) in the source column indicates the partition coefficients were calculated using the lattice strain models in the electronic supplement of this study. Partition coefficients that are not calculated, are taken from partitioning experiments.
Calculation parameters were calculated for mineral compositions from lunar relevant experiments. Studies and experiments that compositions data was sourced from are indicated at the bottom of the table.
Eu partition coefficients for Ol, Opx, Cpx, Plag, and Ilm presented in this table assume an fO_2 equal to the IW redox buffer. The Log($fO2$) of the IW redox buffer for a given temperature was determined using the buffer model from O'Neill and Pownceby (1993).
The LMO solidification stage in which each set of partition coefficients is used is indicated in the Stage row above the calculation parameters
Olivine (Ol), Orthopyroxene (Opx), Clinopyroxene (Cpx), Pigeonite (Pig), Plagioclase (Plag), Ilmenite (Ilm), Quartz (Qtz), Interstitial Melt (Int-Mlt)
[a]McDonough and Sun (1995), [b]Sun and Liang (2013a), [c]Dalou et al. (2012), [d]Sun and Liang (2013b), [e]Fibbrizio et al. (2021), [f]Dygert et al. (2014), [g]Dygert et al. (2020), [h]Snape et al. (2022), [i]Sun et al. (2017), [j]Dygert et al. (2013), [k]Brey et al. (2015), [l]Charlier et al. (2018), [m]Elardo et al. (2011)

The fractionation of Eu in the LMO cumulates is primarily controlled by crystallization and floatation of plagioclase since Eu^{2+} can substitute into the ring site of the feldspar structure normally occupied by Ca^{2+}. Other minerals such as Cpx, Opx, and apatite can also fractionate Eu due to similar substitution effects (Getani and Grove, 1995; Fabbrizio et al., 2021**;** Ji and Dygert, 2024). To assess the effect of fO_2 on Eu fractionation during LMO solidification, we calculated the Eu partition coefficients of Plag, Cpx, and Opx using fO_2 dependent partition coefficient calculators (Dygert et al., 2020, Fabbrizio et al., 2021). For Ol and Ilm, we estimate the effect of fO_2 on Eu partitioning using divalent element (i.e., Mg, Mn, Fe, and Ca) lattice strain models using literature data, REE lattice strain models from previous studies and the fO_2 dependent Eu^{3+} to Eu^{2+} melt distribution calculator from Dygert et al. (2020) (see the supporting text in Appendix B and **Figures B1, B2, and B3** for lattice strain model parameters and results). For Pig and Qtz, the current experimental data sets are insufficient to estimate the Eu^{2+} partitioning behavior using methods similar to this study's Ol and Ilm estimates. Thus, the Eu partition coefficient is calculated using a trivalent element partitioning calculator for Pig and the Eu partition coefficient for Qtz is taken directly from literature (**Table 2.2**).

2.2.3 LMO Solidification Products

As shown in previous studies, progressive solidification of the LMO would result in a heterogeneous major and trace element distribution in the lunar mantle (Snyder et al., 1992; Elkins-Tanton et al., 2011; Lin et al., 2017; Charlier et al., 2018; Rapp and Draper, 2018). Models from this study and previous work (Snyder et al., 1992; Rapp and Draper, 2018) demonstrate that the majority of magma ocean cumulates (~85%) would have sub-

chondritic REE and Hf concentrations (**Figure 2.2a**). Magma ocean cumulates, which form during the last 15% of LMO solidification (including the IBC layer), contain significantly more REE and Hf than early crystallizing LMO cumulates (**Table 2.3**).

Relative to the lunar picritic glasses and KREEP-basalts (**Figure 2.2b**), the early LMO cumulates are HREE-enriched and have elevated $(Yb/Sm)_N$ (**Figure 2.3a**) and $(Lu/Hf)_N$ ratios (**Figure 2.3b**). The REE concentrations and trajectory with respect to $(Yb/Sm)_N$ and $(Lu/Hf)_N$ of LMO cumulates dramatically shift in the last ~15% of magma ocean solidification, becoming progressively less HREE-enriched as plagioclase and high-Ca pyroxenes begin to dominate the cumulate mineral assemblage. This progressive decrease in the degree of HREE enrichment throughout late magma ocean cumulate crystallization drives the elemental ratios toward that of the intermediate-Ti (i.e., yellow picritic glasses) and high-Ti lunar picritic glasses (i.e., orange, red, and black picritic glasses) and produces an IBC layer with similar (albeit slightly higher) $(Yb/Sm)_N$ and $(Lu/Hf)_N$ ratios to most of these picritic glasses (**Figure 2.3**). A MATLAB script, which may be used to model trace element fractionation during LMO solidification can be found in Scholpp and Dygert (2024b).

Table 2.3. Average REE+Hf abundances and ratios for modeled LMO cumulate layers and IBC material assuming 90% plagioclase floatation efficiency.

Element	Layer #1 (ppm)	Layer #1 (CN)	Layer #2 (ppm)	Layer #2 (CN)	Layer #3 (ppm)	Layer #3 (CN)
La	0.0091	0.0387	0.0203	0.0867	0.0434	0.1848
Ce	0.0235	0.0390	0.0565	0.0937	0.1361	0.2256
Pr	0.0036	0.0403	0.0096	0.1081	0.0264	0.2967
Nd	0.0178	0.0393	0.0563	0.1245	0.1491	0.3295
Sm	0.0059	0.0399	0.0278	0.1893	0.0657	0.4468
Eu	0.0024	0.0422	0.0085	0.1513	0.0700	1.2496
Gd	0.0088	0.0450	0.0568	0.2887	0.1488	0.7567
Tb	0.0018	0.0498	0.0127	0.3501	0.0343	0.9458
Dy	0.0138	0.0570	0.1049	0.4322	0.2810	1.1578
Y	0.1035	0.0663	0.7498	0.4806	2.0782	1.3322
Ho	0.0035	0.0636	0.0273	0.4913	0.0728	1.3092
Er	0.0123	0.0772	0.0921	0.5796	0.2475	1.5577
Tm	0.0023	0.0597	0.0160	0.4224	0.0433	1.1461
Yb	0.0181	0.1116	0.1132	0.6968	0.3153	1.9402
Lu	0.0031	0.1293	0.0186	0.7647	0.0518	2.1301
Hf	0.0046	0.0446	0.0264	0.2537	0.0658	0.6329
Lu/Hf	0.6771	2.8977	0.7042	3.0137	0.7864	3.3658
Sm/Nd	0.3304	1.0161	0.4945	1.5208	0.4409	1.3560
Yb/Sm	3.0863	2.7938	4.0658	3.6805	4.7971	4.3425
Ce/Sm	4.0015	0.9758	2.0286	0.4947	2.0709	0.5050

Table 2.3. Continued.

Element	Layer #4 (ppm)	Layer #4 (CN)	Layer #5 (ppm)	Layer #5 (CN)	Layer #6 (ppm)	Layer #6 (CN)
La	0.1239	0.5278	0.4317	1.8395	1.1906	5.0728
Ce	0.4175	0.6921	1.4771	2.4488	3.8800	6.4324
Pr	0.0837	0.9398	0.2984	3.3495	0.7450	8.3612
Nd	0.4888	1.0805	1.7849	3.9454	4.5846	10.1339
Sm	0.2094	1.4233	0.7844	5.3323	2.0966	14.2532
Eu	0.2222	3.9679	0.7504	13.4000	1.6098	28.7461
Gd	0.4080	2.0750	1.4661	7.4571	3.4263	17.4275
Tb	0.0875	2.4117	0.3070	8.4575	0.6686	18.4177
Dy	0.6684	2.7540	2.2959	9.4596	4.7780	19.6868
Y	4.7240	3.0282	15.9005	10.1926	31.3598	20.1024
Ho	0.1628	2.9287	0.5488	9.8702	1.0903	19.6106
Er	0.5236	3.2954	1.7257	10.8601	3.2733	20.6000
Tm	0.0875	2.3160	0.2823	7.4675	0.5175	13.6908
Yb	0.6145	3.7815	1.9303	11.8785	3.4557	21.2661
Lu	0.0976	4.0173	0.3024	12.4438	0.5371	22.1040
Hf	0.1563	1.5026	0.5919	5.6910	3.7543	36.0988
Lu/Hf	0.6247	2.6736	0.5109	2.1866	0.1431	0.6123
Sm/Nd	0.4283	1.3172	0.4394	1.3515	0.4573	1.4065
Yb/Sm	2.9350	2.6569	2.4609	2.2277	1.6482	1.4920
Ce/Sm	1.9939	0.4863	1.8832	0.4592	1.8506	0.4513

Table 2.3. Continued.

Element	IBC #1 (ppm)	IBC #1 (CN)	IBC #2 (ppm)	IBC #2 (CN)
La	0.8936	3.8076	0.3015	1.2848
Ce	2.9132	4.8296	1.0132	1.6797
Pr	0.5596	6.2810	0.2015	2.2620
Nd	3.4458	7.6168	1.2043	2.6620
Sm	1.5782	10.7285	0.5304	3.6054
Eu	1.2662	22.6114	0.4962	8.8612
Gd	2.5852	13.1494	0.9712	4.9402
Tb	0.5053	13.9197	0.2018	5.5580
Dy	3.6172	14.9042	1.5047	6.1999
Y	23.7794	15.2432	10.3789	6.6531
Ho	0.8270	14.8737	0.3586	6.4496
Er	2.4875	15.6548	1.1263	7.0879
Tm	0.3941	10.4249	0.1845	4.8811
Yb	2.6378	16.2325	1.2686	7.8070
Lu	0.4106	16.8989	0.1995	8.2108
Hf	2.8368	27.2766	0.5482	5.2710
Lu/Hf	0.1448	0.6195	0.3640	1.5577
Sm/Nd	0.4580	1.4085	0.4404	1.3544
Yb/Sm	1.6714	1.5130	2.3920	2.1653
Ce/Sm	1.8460	0.4502	1.9104	0.4659

Layer #1: 0-51% LMO solidification, Layer #2: 51-78% LMO solidification, Layer #3: 78-81% LMO solidification, Layer #4: 81-95% LMO solidification, Layer #5: 95-98% LMO solidification, Layer #6: 98-100% LMO solidification.
CN indicates the chondrite normalized values. The CI Chondrite composition reported by Anders and Grevesse (1989) was used for normalization calculations.
IBC #1 represents the composition of IBC material (i.e., average of LMO cumulate compositions from 98-99.5% solidification) assuming no pre-overturn mixing.
IBC #2 represents the composition of IBC material assuming the upper 100 km of the lunar mantle experienced pre-overturn mixing.

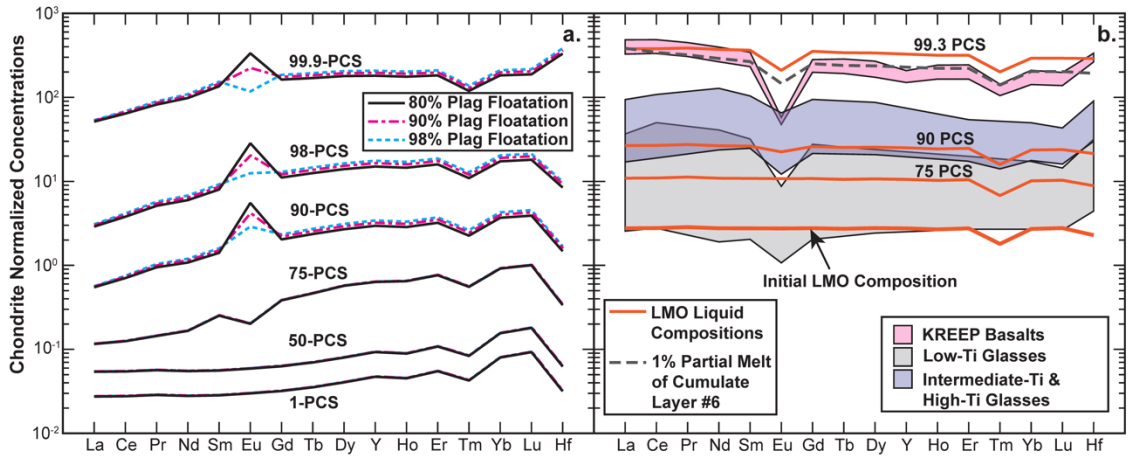


Figure 2.2. Trace element comparison between evolving magma ocean cumulates, lunar picritic glasses, and lunar KREEP basalts. (a) Modeled evolution of LMO cumulates assuming different plagioclase floatation efficiencies. Note the Eu anomaly sign and magnitude depend on the efficiency of plagioclase flotation and assumed fO_2 conditions in the LMO. Here, we assume the fO_2 is IW. (b) Comparison of modeled LMO residual liquids and the compositional ranges of picritic glasses and KREEP basalts. Low-degree partial melt of LMO cumulate layer #6 (i.e., the IBC layer assuming 90% plagioclase floatation) is plotted to show the effect of partial melting on REE trends (also see Figure 2.4). Note that KREEP basalts and many glasses have steeper REE patterns than the LMO residual liquids, suggesting their KREEPy signature cannot result from the direct assimilation of an LMO residual liquid. Partial melting of KREEPy LMO cumulates increases the slope of the REE pattern (dashed gray line), better fitting lunar basalts and suggesting basalt sources contained a KREEP-bearing solid component that precipitated from the late-stage LMO. Partial melting models are discussed further in sections (2.2.4.) and (2.2.5.). Low-Ti picritic glasses: very low-Ti (VLT) glass & green glass groups; Intermediate-Ti picritic glasses: yellow glass group; High-Ti picritic glasses: orange glass, red glass, & black glass groups. The intermediate-Ti and high-Ti picritic glasses are plotted together to declutter the plot as there is significant overlap in their trace element compositions. Lunar picritic glass data was compiled from: Hughes et al., 1990; Shearer et al., 1991; Shearer and Papike, 1993; McIntosh et al., 2024. Lunar KREEP basalt data was compiled from: Neal and Krammer, 2003; Hallis et al., 2014; Borg et al., 2019.

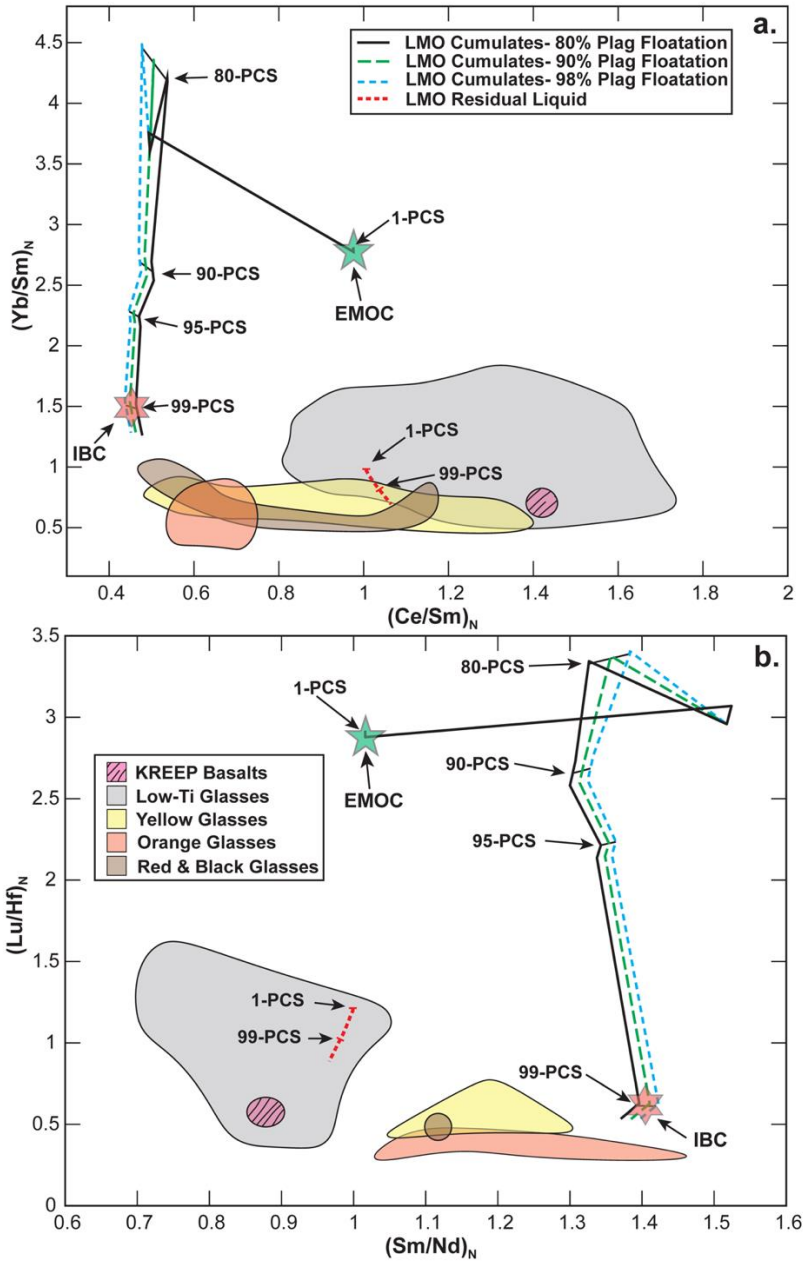


Figure 2.3. Evolution of LMO residual melt and cumulates during fractional crystallization of the LMO compared to picritic lunar glass and basalt compositions. The color and texture of the trend lines indicate plagioclase floatation efficiency. $(Lu/Hf)_N$ and $(Sm/Nd)_N$ are chondrite normalized ratios. References for lunar sample compositions can be found in Figure 2.2. Low-Ti picritic glasses: VLT glass & green glass groups. Percent LMO solidification (PCS), Early Magma Ocean Cumulate (EMOC), Ilmenite-Bearing Cumulate (IBC). These models indicate that the theoretical IBC layer would exhibit similar $(Lu/Hf)_N$ ratios to the intermediate to high-Ti lunar picritic glasses (i.e., yellow, orange, red, and black glasses) while the earliest LMO cumulates plot far from all lunar picritic glass groups.

2.2.4 Eu anomalies of LMO cumulates and cumulate melts

Models from this study indicate that the negative Eu anomaly (i.e., the depletion Eu relative to neighboring REE), which is ubiquitous feature of lunar mare basalt and picritic glass chemistry (Hughes et al., 1990; Shearer et al., 1991; Shearer and Papike, 1993; Neal, 2001; Hallis et al., 2014; McIntosh et al., 2024) (**Figure 2.2b**), is absent in the LMO cumulate pile unless plagioclase floatation is highly efficient (>90%) (**Figure 2.2a**). The 90% floatation efficiency model from this study never generates a negative Eu anomaly in the LMO cumulates (**Figure 2.2a**); however, increasing the amount of interstitial melt in the LMO cumulates or decreasing the fO_2 of the lunar mantle below IW could change this result.

Increasing the amount of interstitial melt in the LMO cumulates to >1% would slightly increase the scale of the Eu anomaly as the abundance of REE in the melt is higher (**Figure 2.2b**). Although increasing the amount of interstitial melt could result in a Eu anomaly at floatation efficiencies ≤90%, the amount of interstitial melt would likely be limited to a couple percent of the total cumulate volume (e.g., 1-5%) at most given the effect of cumulate compaction during crystal settling (Solomatov and Steveson 1993; McKenzie, 2011). This amount of interstitial melt would still fail to explain the scale of the Eu anomaly in lunar mare basalts and picritic glasses at floatation efficiencies <90%. Decreasing the fO_2 of the lunar mantle below IW would increase the impact of plagioclase floatation on the Eu anomaly and could produce a negative Eu anomaly for LMO cumulates assuming 90% floatation efficiency; however, this is still unlikely to

explain the scale of the Eu anomaly in picritic glasses (see section 2.2.5. for further discussion).

Since the picritic glasses also exhibit this Eu anomaly (**Figure 2.2b**) and are minimally fractionated (Delano 1986), the picritic glass mantle sources must also have a negative Eu anomaly or contain residual plagioclase. The glasses are thought to form at depths well below those where plagioclase could be a stable phase (Wagner and Grove, 1997; Elkins-Tanton et al., 2003; Krawczynski and Grove, 2012; Barr and Grove, 2013; Brown and Grove, 2015, also see further discussion below in section 2.3.2.). Thus, without a significant contribution to the Eu anomaly from phases the solidification sequence does not invoke (apatite; see **Figures B4 and B5** for models that demonstrate effects of apatite), plagioclase floatation during LMO solidification and crustal formation must be highly efficient (i.e., >90%) to produce inferred requisite Eu anomalies in the picritic glass source.

2.2.4.1 Residual LMO liquids and their relation to "KREEP"

The modeled residual LMO liquid evolution in this study is generally consistent with previous REE modeling studies (Snyder et al., 1992; Rapp and Draper, 2018), demonstrating that the late magma ocean liquids would be significantly REE enriched similar to KREEPy lunar samples (Warren and Wasson, 1979; Neal and Kramer, 2003; Hallis et al., 2014; Borg et al., 2019) (**Figure 2.2b**). Although the late residual liquids are significantly REE enriched, they are also too MREE and HREE-rich (i.e., they have flat REE patterns) (**Figures 2.2b and 2.3**) to be directly related to the KREEP basalts and other KREEPy lunar materials. In addition, the late LMO residual lquids are too Mg-poor

to be parental to KREEP basalts, or the KREEPiest lunar materials recovered (e.g., Warren and Wasson, 1979; Snyder et al., 1992; Lin et al., 2017; Rapp and Draper, 2018). Assimilation models are incapable of increasing ratios beyond those exhibited by mixing components. Instead, the late LMO KREEPy residual liquid signature is imparted on lunar basalts as a component in their mantle sources (**Figures 2.2 and 2.4**). KREEP basalts and lunar basalts have light-heavy REE ratios exceeding the late LMO residual liquid because partial melting increases the ratio in the hybridized source, as LREEs are incompatible relative to heavier REEs.

2.2.5 Partial Melting Models

To model the effect of partial melting on LMO cumulates and hybridized mantle sources, we use an aggregated fractional melting model Eq. 2.6:

$$C_l^i = C_{S_0}^i \left(\frac{1-(1-F)^{\left(\frac{1}{D_{Bulk}^i}\right)}}{F}\right), \quad (2.6)$$

where $C_{S_0}^i$ represents concentration of a given element i in the initial cumulate, C_l^i is the concentration in the melt that forms, and F is the melt fraction. Given the current lack of information on source mineralogy and non-modal melting behavior, we assume modal melting for all partial melting calculations in this study. This avoids the application of non-modal melting models which are not lunar-relevant (Kinzler and Grove, 1992; Baker and Stolper, 1994; Walter, 1998; Presnall et al., 2002). The bulk partition coefficient (D_{Bulk}^i) values for partial melting equations were calculated using estimated modal mineralogies of the LMO cumulates, downwelling cumulates, or hybridized sources (e.g., Charlier et al. 2018; Mallik et al., 2019).

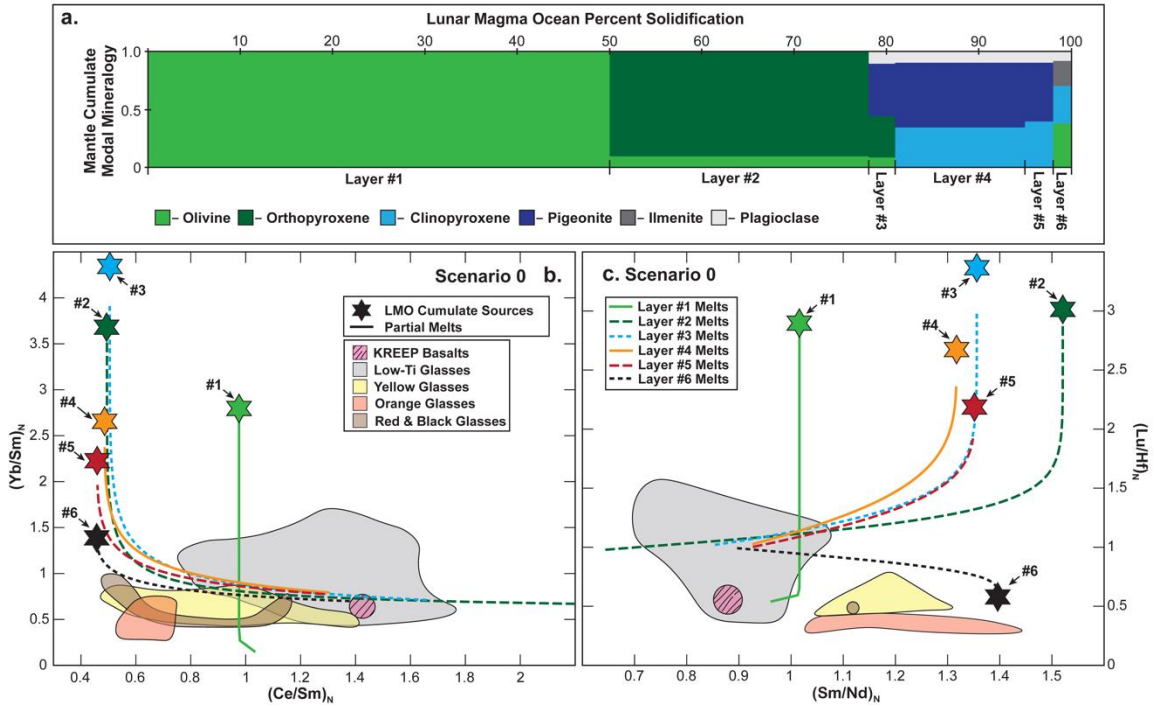


Figure 2.4. Models for partial melting of primary (i.e., unhybridized) LMO cumulates assuming 90% plagioclase floatation (Reference Scenario 0). Panel (a) shows the estimated mineralogy of LMO mantle cumulate layers, assuming 90% of the plagioclase was removed during crustal formation. Panels (b) and (c) show the effect of partial melting on the initial LMO cumulate layers if no hybridization occurred. The cumulate layer number is indicated by the texture and color of the partial melt line and the black numbers next to each cumulate source symbol. LMO cumulate source compositions are the average composition of each cumulate layer from the six stages of LMO solidification (Table 2.3). Modal partial melting of each LMO cumulate layer is modeled from 0.1-30%. $(Lu/Hf)_N$ and $(Sm/Nd)_N$ are chondrite normalized ratios. References for lunar sample compositions can be found in Figure 2.2. Low-Ti picritic glasses: VLT glass & green glass groups. These models demonstrate that partial melting of unhybridized LMO cumulates would not reproduce the $(Yb/Sm)_N$ and $(Lu/Hf)_N$ ratios of intermediate to high-Ti lunar picritic glasses groups. The models also indicate that some low-Ti picritic glasses could be related to unhybridized cumulate melting.

2.2.6 Partial Melting of Initial LMO Cumulates

Partial melting models are presented in a series of Scenarios with increasing complexity. Details of each scenario are summarized in **Table 2.4**. Reference Scenario 0 explores in-situ partial melting of each LMO cumulate layer, assuming 90% plag floatation (**Figure 2.4**, **Tables 2.3 and 2.4**). In the Figures, melting model results are compared to lunar glass compositions using chondrite normalized $(Ce/Sm)_N$, $(Yb/Sm)_N$, $(Lu/Hf)_N$, and $(Sm/Nd)_N$ ratios. The ratios are used as they reveal fractionation associated with lunar differentiation and partial melting while eliminating the dependence of the model results on the elemental concentrations assumed in the bulk Moon (i.e., the extent of refractory element enrichment, e.g., Taylor et al., 2006). The $(Ce/Sm)_N$ and $(Yb/Sm)_N$ ratios reveal the extent of light REE (LREE) and heavy REE (HREE) enrichment or depletion, respectively. The $(Lu/Hf)_N$ and $(Sm/Nd)_N$ ratios reveal how radiogenic parent and daughter isotopes are fractionated during lunar differentiation and subsequent melting.

Scenario 0 simulations demonstrate that partial melting of primary LMO cumulates can account for the REE compositions of many low-Ti lunar picritic glasses. The models also indicate that aside from the extremely low degree melts (i.e., <1%) from layer #1 (the first LMO cumulates), all of the primary LMO cumulate melts have $(Lu/Hf)_N$ and $(Sm/Nd)_N$ ratios that are too high to explain the intermediate- and high-Ti picritic glass compositions.

Table 2.4. Model assumptions for mantle hybridization and partial melting scenarios and associated figures.

	Scenario 0	Scenario #1	Scenario #2
Plagioclase Floatation Efficiency	90%	90%	90%
IBC Composition	From Charlier et al.	IBC #1	IBC #1
Pre-Overturn Mixing	N/a	None	None
IBC Mineralogy	N/a	Garnet-Free	Garnet-Free
IBC Mixing Component	N/a	Solid IBC Material	Solid IBC Material
IBC Partial Melting P-T Conditions	N/a	IBC Material Never Melts	IBC Material Never Melts
EMOC Mixing Component	N/a	Dunite from 0.1 to 51% LMO Solidification	Dunite from 0.1 to 51% LMO Solidification
Hybridized Source Composition	100% Unmixed Cumulates	80% to 98% EMOC and 20% to 2% IBC	80% EMOC to 20% IBC
Hybridized Source Mineralogy	Garnet-Free	Garnet-Free	Garnet-Bearing
Garnet Abundance in IBC or Hybridized Mantle Source	0%	0%	0.25% to 5%
Hybridized Source Partial Melting P-T Conditions	Dependent on the depth of the Cumulate Layer	2 GPa and 1350ºC	2 GPa and 1350ºC
Partial Melting of The Source	0.01% to 30%	0.01% to 30%	0.01% to 30%
Associated Figures	Figure 2.4b-c	Figure 2.8a-c	Figure 2.8d-f

Table 2.4. Continued.

	Scenario #3	Scenario #4	Scenario #5
Plagioclase Floatation Efficiency	90%	90%	90%
IBC Composition	IBC #1	IBC #1	IBC #1
Pre-Overturn Mixing	None	None	None
IBC Mineralogy	Garnet-Free	Garnet-Free	Garnet-Bearing
IBC Mixing Component	IBC Partial Melt @ 25% melting	IBC Partial Melt @ 25% melting	IBC Partial Melt @ 25% melting
IBC Partial Melting P-T Conditions	2 GPa and 1300ºC	2 GPa and 1300ºC	2 GPa and 1300ºC
EMOC Mixing Component	Dunite from 0.1 to 51% LMO Solidification	Dunite from 0.1 to 51% LMO Solidification	Dunite from 0.1 to 51% LMO Solidification
Hybridized Source Composition	80% to 98% EMOC and 20% to 2% IBC	90% EMOC to 10% IBC	90% EMOC to 10% IBC
Hybridized Source Mineralogy	Garnet-Free	Garnet-Bearing	Garnet-Free
Garnet Abundance in IBC or Hybridized Mantle Source	0%	0.25% to 5%	0.25% to 5%
Hybridized Source Partial Melting P-T Conditions	2 GPa and 1350ºC	2 GPa and 1350ºC	2 GPa and 1350ºC
Partial Melting of The Source	0.01% to 30%	0.01% to 30%	0.01% to 30%
Associated Figures	Figure 2.9a-c	Figure 2.9d-f	Figure 2.10a-c

Table 2.4. Continued.

	Scenario #6	Scenario #7
Plagioclase Floatation Efficiency	90%	90%
IBC Composition	IBC #2	IBC #2
Pre-Overturn Mixing	Upper 100 km Of The Lunar Mantle	Upper 100 km Of The Lunar Mantle
IBC Mineralogy	Garnet-Bearing	Garnet-Free
IBC Mixing Component	Solid IBC Material	Solid IBC Material
IBC Partial Melting P-T Conditions	2 GPa and 1300ºC	IBC Material Never Melts
EMOC Mixing Component	N/a	Dunite from 0.1 to 51% LMO Solidification
Hybridized Source Composition	N/a	55% EMOC to 45% IBC
Hybridized Source Mineralogy	Garnet-Bearing	Garnet-Bearing
Garnet Abundance in IBC or Hybridized Mantle Source	0% to 5%	0% to 5%
Hybridized Source Partial Melting P-T Conditions	N/a	2 GPa and 1350ºC
Partial Melting of The Source	0.01% to 30%	0.01% to 30%
Associated Figures	Figure 2.11a-c	Figure 2.11d-f

The primary cumulate melts never achieve $(Lu/Hf)_N$ ratios as low as those of the orange picritic glasses. Melts of layer #1 would be too Ti- and REE-poor to explain the major and trace element compositions of the yellow, red, and black picritic glasses. This suggests that some secondary mantle source hybridization process is required to explain the low $(Lu/Hf)_N$ of at least the orange picritic glasses and most intermediate- and high-Ti lunar picritic glasses.

It should also be noted that while the scenario 0 simulations demonstrate that partial melting of primary LMO cumulates can account for the REE ratios of many low-Ti lunar picritic glasses, this doesn't mean these partial melts could account for the major element compositions or the scale of the Eu anomaly observed in low-Ti picritic glasses (**Figure 2.2b**). If we consider the minimum estimated mantle source Mg#s of low-Ti picritic glasses (~78; calculated using the methods of Scholpp and Dygert, 2024a and references therein), we can rule out primary melts of cumulate layers #4-#6 as the Mg#s of these cumulates likely fall between 16 and 63 based on the experimental mineral compositions and estimated cumulate proportions of Charlier et al. (2018). If we consider the trace element composition of the low-Ti glasses, it is also unlikely that partial melts of cumulate layer #1 (the first 51% of LMO cumulates in this study) could account for the low-Ti glass trace element compositions due to this layer's low overall trace element abundance and lack of a Eu anomaly (**Figure 2.2a**).

While we can reasonably rule out cumulate layers #1, #4, #5, and #6 as the source of low-Ti lunar picritic melts, it is difficult to rule out layers #2 and #3 (cumulates that form between 52% and 82% LMO solidification) based on their estimated major element

chemistry. Each of these layers should have Mg#s ≥80; however, layer #2 is the only layer that could realistically recreate the Eu anomaly (Eu/Eu*: the measured concentration of Eu divided by the interpolated concentration Eu if Eu followed the 3+ REE partitioning trends) observed in the low-Ti lunar picritic glasses without some amount of hybridization (**Figure 2.5**). Melting models for layer #3 indicate that plagioclase floatation efficiency would need to be >99% to produce an Eu/Eu* within the upper range of low-Ti picritic glasses at fO_2s from IW-2 to IW+2 (i.e., two log units above or below the IW redox buffer) (**Figure 2.5**). This holds for models that assume residual plagioclase remained in these cumulate layers (**Figure 2.5a**) and models that assume the cumulate plagioclase metamorphose to Cpx following cumulate compaction (**Figure 2.5b**). Partial melts of layer #2 are unaffected by the floatation efficiency of plagioclase because models from this study assume plagioclase would be absent in this layer (**Figures 2.4a and 2.5b**).

We propose that low-Ti picritic melts could be sourced directly from LMO cumulate layer #2. While some of the low-Ti picritic melts could theoretically be produced by hybridized sources not explored in this study, partial melts of cumulate layer #2 could account for the REE ratios, REE abundances (**Figure B6**), the elevated Mg#s of the lunar low-Ti glass sources, and their low-Ti compositions. Thus, mantle hybridization is not necessarily required to account for the compositions of all low-Ti glasses.

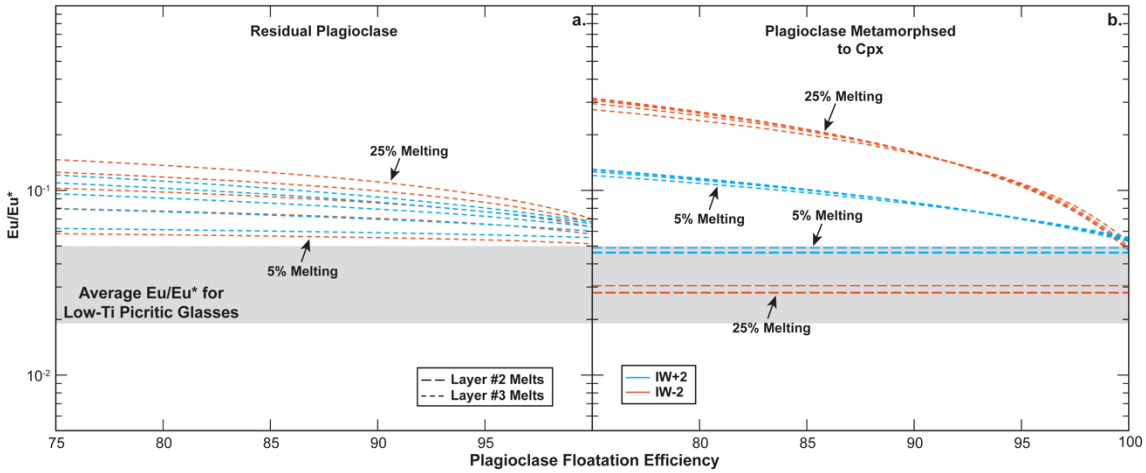


Figure 2.5. Models demonstrating the effect of plagioclase floatation and fO_2 on Eu anomaly (Eu/Eu*) formation in partial melts of LMO cumulates. Dashed lines are melts of magma ocean cumulates; the gray bar shows the mean Eu/Eu* of low-Ti picritic glasses and its standard deviation (i.e., 0.6147±0.2754 (n=43)). (a) Modeled Eu/Eu* for partial melts of cumulate layer #3, assuming plagioclase is residual during melting. (b) modeled Eu/Eu* for partial melts of cumulate layers #2 and #3, assuming the plagioclase in layer #3 metamorphosed to Cpx. All models in this figure show the Eu/Eu* at 5%-25% partial melting for the cumulate layer. Eu* is interpolated using the chondrite normalized concentrations of Sm and Gd (i.e., Sm_N and Gd_N) ($Eu^* = \sqrt{Sm_N \times Gd_N}$). The initial mineralogy of each layer can be found in Figure 2.4a. Without invoking a secondary mantle hybridization process, LMO cumulate layer #2 from this study is the only one that can reasonably account for the major element chemistry and Eu/Eu* observed in lunar low-Ti picritic glasses.

2.3 Mantle Hybridization After Cumulate Mantle Overturn

Simple melting of LMO cumulates described in the previous section failed to reproduce the compositions of most intermediate- and high-Ti lunar picritic glasses. As mentioned in the introduction, LMO solidification would produce a gravitationally unstable density stratification that was relieved by cumulate mantle overturn or sinking of late magma ocean cumulates (the IBC) into early magma ocean cumulates (Hess and Parmentier, 1995; Zhang et al., 2017; Li et al., 2019) (**Figure 2.1**). This sinking would produce mixing and the formation of hybridized mantle sources (Ringwood and Kesson, 1976).

In the following seven Scenarios, we evaluate elemental fractionation after partial melting of sources hybridized by cumulate mantle overturn. The model assumptions for these scenarios are described below and summarized in **Table 2.4**. Five of the seven hybridization models focus on the effects of melting and mixing between EMOC material and a downwelling IBC layer. A sixth model considers the effect of partial melting alone (i.e., no mixing with EMOC material) on a downwelling "thickened" IBC layer that consists of mixed cumulates from the upper 100 km of the magma ocean, produced by small-scale localized sinking of the IBC precipitated from the LMO residual liquid (e.g., Hess and Parmentier, 1995; Parmentier et al., 2002; Li et al., 2019). A seventh model focuses on the effects of mixing between EMOC material and the downwelling "thickened" IBC layer comprising mixed cumulates from the upper 100 km of the magma ocean. Cartoons illustrating the model assumptions are shown in the figures summarizing the results.

2.3.1 Mineralogy of the Downwelling IBC Material

The recent work of Scholpp and Dygert (2024a) indicates that garnet should stabilize in late-crystallizing LMO cumulates during and after hypothesized cumulate overturn events. To test this experimental model and the effect of plagioclase floatation on the mineralogy of IBC brought to higher pressures by overturn, we ran thermodynamic models using the pMELTS algorithm (Ghiorso and Sack, 1995; Ghiorso et al., 2002). The major element composition of the IBC material was estimated using the modal mineral proportions from models in this study (**Tables B1-B3**) and experimental mineral compositions from Charlier et al. (2018). We tested two IBC compositions: IBC #1, which assumes fractional crystallization of the LMO, and IBC #2, an IBC composition that was affected by late LMO cumulate mixing in the upper 100 km of the lunar mantle which occurred during LMO solidification, and before a larger-scale overturn event (**Tables 2.3 and 2.5**). For each model, we set the fO_2 conditions to IW and the P-T conditions to 2 GPa and 1150°C as our goals were to evaluate whether garnet would stabilize in IBC in the lunar mid mantle, and how the floatation efficiency of plagioclase might affect the abundance of garnet.

The pMELTS models indicate that the abundance of garnet in the IBC material is highly dependent on the floatation of plagioclase during LMO solidification (**Figure 2.6**). While both IBC compositions stabilize garnet under the model conditions, IBC #1 produced significantly less garnet, and the models indicate garnet would be absent from the downwelling cumulate if plagioclase floatation efficiencies were above ~95% (**Figure 2.6a**).

Table 2.5. Estimated major element compositions of IBC material for plagioclase floatation efficiencies of 80%, 90%, and 98%.

	IBC #1			IBC #2		
Floatation Efficiency	80%	90%	98%	80%	90%	98%
(wt%)						
SiO_2	31.24	29.55	27.87	48.37	48.46	48.54
TiO_2	13.02	14.09	15.08	1.83	1.99	2.14
Al_2O_3	4.91	2.90	1.13	7.21	4.75	2.41
Cr_2O_3	0.04	0.04	0.04	0.13	0.14	0.16
FeO	40.53	43.72	46.66	19.61	21.41	23.14
MnO	0.42	0.45	0.49	0.23	0.25	0.27
MgO	4.48	4.84	5.18	12.64	13.87	15.05
CaO	4.94	4.17	3.54	9.69	8.96	8.26
Na_2O	0.39	0.21	0.02	0.29	0.16	0.03
K_2O	0.03	0.02	0.00	0.01	0.01	0.00
Total	100.00	100.00	100.00	100.00	100.00	100.00
Mg#	16.46	16.49	16.51	53.47	53.59	53.69

Major element compositions were estimated using the modal mineral proportions from models in this study and experimental mineral compositions from Charlier et al. (2018). IBC #1 represents the composition of IBC material if no pre-overturn mixing occurred. IBC #2 represents the composition of IBC material if pre-overturn mixing occurred in the upper 100 km of the lunar mantle.

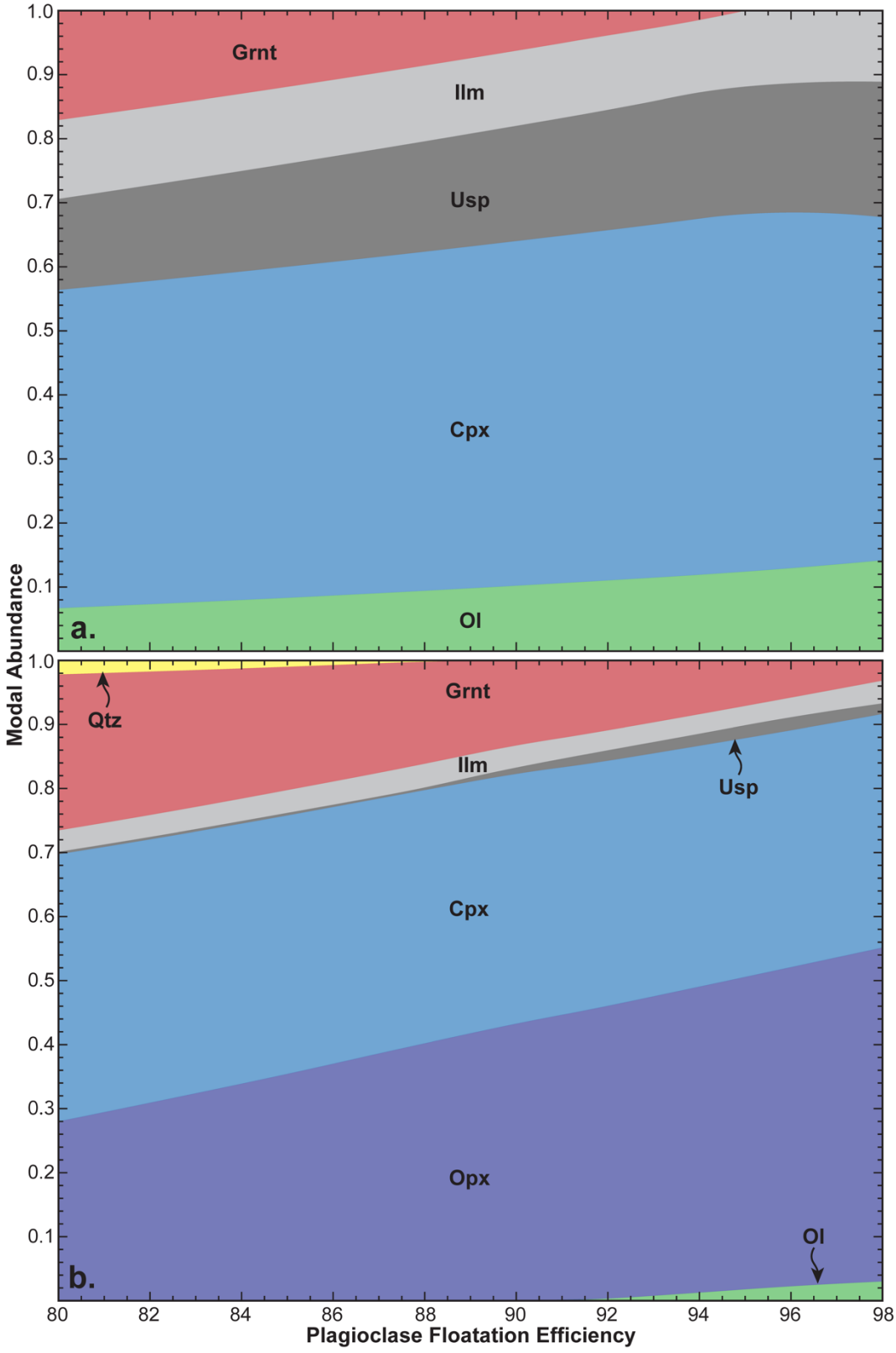
In contrast, the models for IBC #2 indicate that garnet should be stable at all modeled floatation efficiencies (**Figure 2.6b**). While garnet abundance differs between the two modeled IBC compositions, the overall mineralogy of these cumulates also differs remarkably. The models indicate IBC #1 would have a Fe-Ti oxide-rich clinopyroxenitic mineralogy ± garnet (depending on the floatation efficiency). In contrast, IBC #2 would have a relatively Fe-Ti oxide-poor pyroxenitic composition with highly variable garnet abundances (**Figure 2.6**). The difference in Fe-Ti oxide abundances may play an important role in the hybridization process as the melts produced by a hybridized source need to reach ~3-16 wt% TiO_2 depending on the picritic glass group.

2.3.2 Partial Melting of Downwelling IBC

Three of the six models in this study assume partial melting of downwelling IBC occurs during cumulate mantle overturn at an assumed pressure of 2 GPa and temperature of 1300ºC. For partial melts of IBC, we assume the downwelling IBC underwent 25% partial melting to account for the LREE depletion exhibited by the picritic glass source. All partial melting models use LMO cumulate compositions from the 90% plagioclase floatation LMO solidification model for the reasons discussed below.

The minimum floatation efficiency possible during LMO solidification is likely close to 90% because, unlike the low-Ti picritic glasses, the high-Ti picritic glasses can't form directly from partial melting of the early LMO cumulate layers due to their high-Ti content and elevated REE abundances.

Figure 2.6. IBC mineralogy at 1150°C and 2 GPa calculated using thermodynamic models assuming plagioclase floatation efficiencies of 80-98%. (a) Modal mineralogy of the downwelling IBC, assuming no pre-overturn mixing in the upper mantle (i.e., IBC #1). (b) Modal mineralogy of the downwelling IBC, assuming pre-overturn mixing in the upper 100 km of the lunar mantle (i.e., IBC #2). The composition of LMO cumulate material was estimated using the mineral compositions of LMO solidification experiments (Charlier et al., 2018: see Table 2.2 for referenced experiments) and the modal mineral proportions for the initial magma ocean cumulates (Tables B1-B3). Estimated IBC cumulate compositions can be found in Table 2.5. Olivine (Ol), Orthopyroxene (Opx), Clinopyroxene (Cpx), Garnet (Grnt), Ilmenite (Ilm), Ulvöspinel (Usp), Quartz (Qtz). These thermodynamic models demonstrate that plagioclase floatation significantly impacts the stability of garnet in downwelling cumulates at high pressures in the range of estimated lunar melt sources.


Grnt
Ilm
Usp
Cpx
Ol
a.
Qtz
Grnt
Ilm
Usp
Cpx
Opx
Ol
b.
Modal Abundance
Plagioclase Floatation Efficiency
1.0
0.9
0.8
0.7
0.6
0.5
0.4
0.3
0.2
0.1
80
82
84
86
88
90
92
94
96
98

The high-Ti picritic glasses also can't form directly from the late crystallizing IBC (i.e., cumulate Layer #6) because the estimated Mg# of this layer would be too low to produce the high-Ti picritic glasses (see section 2.3.3 for further discussion). This means that their source needs to be hybridized to some extent and contain some amount of material from late crystallizing mantle cumulate layers (cumulate layers #5 and #6) that would be significantly affected by the floatation efficiency plagioclase and early crystallizing Mg-rich material. Partial melting calculations for garnet-free IBC materials and garnet-free hybridized mantle sources indicate that floatation efficiencies >90% would be required for melts to obtain Eu/Eu* values within the range of high-Ti picritic glasses even if the hybridized source is composed of 20% IBC material and 80% LMO cumulate layer #2 material (**Figure 2.7**).

For partial melting of a garnet-free downwelling IBC, we make the simplifying assumption that the plagioclase in the IBC becomes Cpx during overturn. For a garnet-bearing downwelling IBC, we tested variable garnet abundances between 0.25-5%. Thermodynamic models described in section (2.3.1.) indicate that high-pressure decomposition of plagioclase does not form Cpx or garnet in equal proportions, and garnet abundances in IBC material could range from 0% to 9% for plagioclase floatation efficiencies ≥90%. Given the current goals of exploring elemental and isotopic fractionation produced by different hybridized lunar mantle sources and testing the effects of hybridization processes proposed by Schmidt and Kraettlli (2022) and Scholpp and Dygert (2024a), our assumptions are justified.

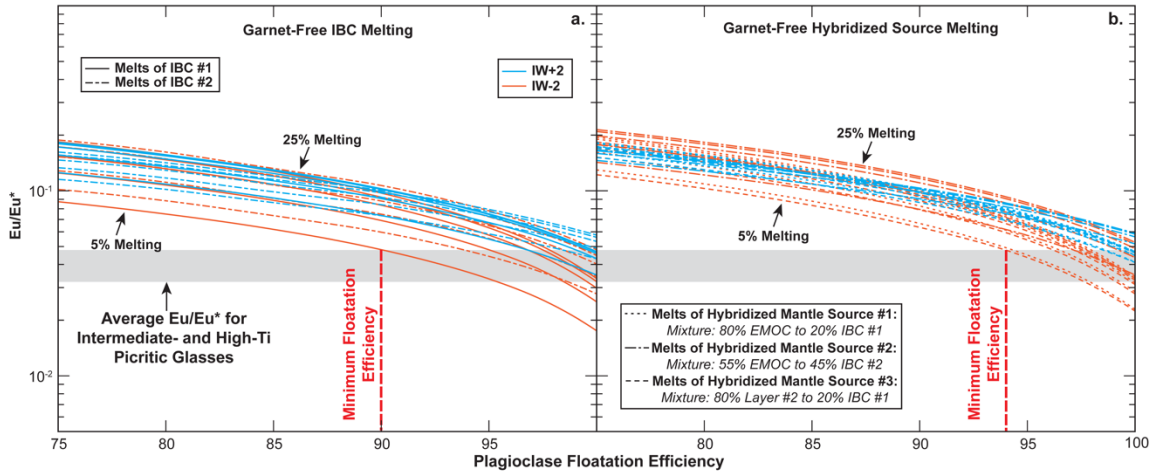


Figure 2.7. Models demonstrating the effect of plagioclase floatation and fO_2 on Eu anomaly (Eu/Eu*) formation in partial melts of garnet-free IBC material and garnet-free hybridized sources. (a) modeled Eu/Eu* for partial melts of overturned IBC material with and without IBC thickening during LMO solidification. The estimated compositions of IBC #1 (i.e., Thin IBC), IBC #2 (Thickened IBC), LMO cumulate layer #1 (i.e., EMOC), and LMO cumulate layer #2 are presented in Table 2.3. (b) modeled Eu/Eu* for partial melts of three hybridized mantle sources. All models in this figure show the Eu/Eu* at 5%-25% partial melting for the cumulate layer. Eu* is interpolated using the chondrite normalized concentrations of Sm and Gd (i.e., Sm_N and Gd_N) ($Eu^* = \sqrt{Sm_N \times Gd_N}$). The grey shaded region represents the average Eu/Eu* of intermediate- and high-Ti picritic glasses (i.e., 0.7737±0.1390 (n=57)). Low-Ti picritic glasses: very low-Ti (VLT) glass & green glass groups. These models demonstrate that regardless of the assumed IBC or hybridized source composition, plagioclase floatation efficiency needs to be >90% efficient to ever produce melts with a Eu/Eu* in the uppermost range of high-Ti picritic glasses.

Making this assumption focuses the model evaluation on the effect of garnet mode and eliminates model dependence on uncertainty related to lunar bulk composition, LMO cumulate modal mineralogy, mineral chemistry, P-T conditions, and reaction stoichiometry. Mineral-melt partition coefficients for the hypothesized IBC are reported in **Table 2.6**.

2.3.3 LMO Cumulate Hybridization

Models from this study that invoke mantle hybridization treat the hybridized mantle source as a simple mixture between IBC partial melts or cumulates and EMOC, which is justified by dissolution-precipitation reactions observed in analog experiments (Scholpp and Dygert, 2024). Hybridization was modeled with a simple mass balance calculation Eq. 2.7:

$$Cs_{Hybrid} = Cl_{IBC}(X_{IBC}) + Cs_{EMOC}(X_{EMOC}), \quad (2.7)$$

where Cs_{Hybrid} is the concentration of a given element in the hybridized source produced during the reaction, Cl_{IBC} is the concentration in the IBC melt or cumulate, Cs_{EMOC} is the concentration in the EMOC, X is the proportion of each composition in the hybridized source.

Snyder et al. (1992) and Hallis et al. (2014) use an 80% EMOC to 20% IBC mixture to explain the source compositions of high-Ti mare basalts; however, those studies assume that the mixture is comprised of cumulates that formed at 86% (early cumulate component) and 95% (IBC component) LMO solidification. As explained below, this mixture is unlikely to represent the components of a hybridized source capable of producing the intermediate-Ti and high-Ti glasses.

Table 2.6. Mineral-melt partition coefficients for partial melting calculations.

Element	Ol (D)	Ol (D)	Ol (D)	ref.	Opx (D)
La	4.59E-06	2.67E-06	3.06E-06	a, Cal.	1.41E-03
Ce	2.52E-05	1.39E-05	1.59E-05	a, Cal.	2.89E-03
Pr	1.03E-04	5.42E-05	6.22E-05	a, Cal.	5.59E-03
Nd	1.63E-04	8.47E-05	9.73E-05	a, Cal.	1.01E-02
Sm	3.69E-04	1.87E-04	2.15E-04	a, Cal.	2.52E-02
Eu	9.46E-04	5.01E-04	5.76E-04	Sup.	1.35E-02
Gd	2.21E-03	1.06E-03	1.22E-03	a, Cal.	4.80E-02
Tb	4.60E-03	2.16E-03	2.48E-03	a, Cal.	6.31E-02
Dy	7.55E-03	3.49E-03	4.01E-03	a, Cal.	8.05E-02
Y	1.25E-02	5.68E-03	6.53E-03	a, Cal.	9.21E-02
Ho	1.20E-02	5.46E-03	6.28E-03	a, Cal.	9.81E-02
Er	1.84E-02	8.28E-03	9.52E-03	a, Cal.	1.15E-01
Tm	2.65E-02	1.18E-02	1.35E-02	a, Cal.	1.31E-01
Yb	3.95E-02	1.73E-02	1.99E-02	a, Cal.	1.44E-01
Lu	4.90E-02	2.14E-02	2.45E-02	a, Cal.	1.56E-01
Hf	4.00E-03	4.00E-03	4.00E-03	b	3.87E-02
Melting	IBC	Hyb. Sr. #1	Hyb. Sr. #2		Hyb. Sr. #1
T (ºC)	1300	1350	1350		1350
P (GPa)	2	2	2		2
Fo	11.4	83.6	85.5	j & k	-
Al^{ol}	0.00078	0.0022	0.0037	j & k	-
$X Ti^{melt}$	-	-	-		0.2249
Al^{T}	-	-	-		0.1088
Al^{M1}	-	-	-		0.0102
Ca^{M2}	-	-	-		0.0906
Mg^{M2}	-	-	-		0.6796
Mg^{M1}	-	-	-		0.8958
Fe^{M1}	-	-	-		0.0434
Ca^{X}	-	-	-		-
D_0	-	-	-		-
r_0	-	-	-		-
E	-	-	-		-
D(Ti)	-	-	-		-
$Log(fO_2)$	-10.75	-10.22	-10.22		-10.22
Sample/ Experiment	LPUM/0.4-1.5 gl HA02-0.8	V984	V1007		V984

Table 2.6. Continued.

Element	Opx (D)	ref.	Cpx (D)	Cpx (D)	Cpx (D)
La	3.02E-03	c, Cal.	1.44E-02	1.51E-02	1.43E-02
Ce	6.21E-03	c, Cal.	2.06E-02	2.12E-02	2.01E-02
Pr	1.20E-02	c, Cal.	2.80E-02	2.86E-02	2.72E-02
Nd	2.17E-02	c, Cal.	3.66E-02	3.71E-02	3.52E-02
Sm	5.34E-02	c, Cal.	5.28E-02	5.30E-02	5.03E-02
Eu	2.81E-02	d, Cal.	1.92E-01	1.80E-01	1.75E-01
Gd	1.01E-01	c, Cal.	6.57E-02	6.54E-02	6.21E-02
Tb	1.31E-01	c, Cal.	7.09E-02	7.04E-02	6.68E-02
Dy	1.66E-01	c, Cal.	7.48E-02	7.42E-02	7.04E-02
Y	1.89E-01	c, Cal.	7.65E-02	7.58E-02	7.19E-02
Ho	2.01E-01	c, Cal.	7.71E-02	7.64E-02	7.25E-02
Er	2.34E-01	c, Cal.	7.81E-02	7.73E-02	7.34E-02
Tm	2.63E-01	c, Cal.	7.80E-02	7.72E-02	7.33E-02
Yb	2.88E-01	c, Cal.	7.71E-02	7.64E-02	7.25E-02
Lu	3.09E-01	c, Cal.	7.58E-02	7.51E-02	7.13E-02
Hf	3.71E-02	c, Cal.	3.81E-02	3.77E-02	3.46E-02
Melting	Hyb. Sr. #2		IBC	Hyb. Sr. #1	Hyb. Sr. #2
T (ºC)	1350		1300	1350	1350
P (GPa)	2		2	2	2
Fo	-		-	-	-
Al^{ol}	-		-	-	-
$X Ti^{melt}$	1.0451	k	-	-	-
Al^{T}	0.0850	k	0.0598	0.1199	0.1010
Al^{M1}	0.0264	k	0.1135	0.0236	0.0151
Ca^{M2}	0.0982	k	0.6571	0.5559	0.5339
Mg^{M2}	0.6981	k	-	-	-
Mg^{M1}	0.8796	k	-	-	-
Fe^{M1}	0.0394	k	-	-	-
Ca^{X}	-		-	-	-
D_0	-		-	-	-
r_0	-		-	-	-
E	-		-	-	-
D(Ti)	-		-	-	-
Log(fO_2)	-10.22		-10.75	-10.22	-10.22
Sample/ Experiment	V1007		LPUM/0.4-1.5 gl HA02-0.8	V984	V1007

Table 2.6. Continued.

Element	ref.	Pig (D)	ref.	Grnt (D)	Grnt (D)	ref.
La	e, Cal.	5.68E-03	f, Cal.	3.41E-03	3.95E-03	a, Cal.
Ce	e, Cal.	1.15E-02	f, Cal.	1.18E-02	1.18E-02	a, Cal.
Pr	e, Cal.	2.05E-02	f, Cal.	3.71E-02	3.24E-02	a, Cal.
Nd	e, Cal.	2.47E-02	f, Cal.	1.06E-01	8.28E-02	a, Cal.
Sm	e, Cal.	3.44E-02	f, Cal.	5.36E-01	3.62E-01	a, Cal.
Eu	d, Cal.	5.84E-02	f, Cal.	9.91E-01	6.42E-01	a, Cal.
Gd	e, Cal.	7.03E-02	f, Cal.	1.74E+00	1.09E+00	a, Cal.
Tb	e, Cal.	9.37E-02	f, Cal.	2.91E+00	1.78E+00	a, Cal.
Dy	e, Cal.	1.14E-01	f, Cal.	4.64E+00	2.81E+00	a, Cal.
Y	e, Cal.	1.37E-01	f, Cal.	6.03E+00	3.64E+00	a, Cal.
Ho	e, Cal.	1.35E-01	f, Cal.	6.83E+00	4.12E+00	a, Cal.
Er	e, Cal.	1.59E-01	f, Cal.	9.39E+00	5.71E+00	a, Cal.
Tm	e, Cal.	1.82E-01	f, Cal.	1.22E+01	7.49E+00	a, Cal.
Yb	e, Cal.	2.10E-01	f, Cal.	1.51E+01	9.41E+00	a, Cal.
Lu	e, Cal.	2.27E-01	f, Cal.	1.79E+01	1.14E+01	a, Cal.
Hf	e, Cal.	6.81E-02	g	6.50E-01	6.50E-01	h
Melting		IBC		IBC	Hyb. Sr. #2	
T (ºC)		-		1300	1350	
P (GPa)		-		2	2	
Fo		-		-	-	
Al^{ol}		-		-	-	
$X\mathrm{Ti}^{melt}$		-		-	-	
Al^{T}	j & k	-		-	-	
Al^{M1}	j & k	-		-	-	
Ca^{M2}	j & k	-		-	-	
Mg^{M2}		-		-	-	
Mg^{M1}		-		-	-	
Fe^{M1}		-		-	-	
Ca^{X}		-		0.7234	0.4674	k
D_0		0.38	f	-	-	
r_0		0.759	f	-	-	
E		198	f	-	-	
D(Ti)		-		-	-	
$\mathrm{Log}(fO_2)$		-		-	-	
Sample/ Experiment		Eu14-17		V986	V1007	

Table 2.6. Continued.

Element	Ilm (D)	Ilm (D)	ref.
La	4.94E-05	6.61E-05	i, Cal.
Ce	1.81E-04	2.33E-04	i, Cal.
Pr	5.35E-04	6.64E-04	i, Cal.
Nd	7.65E-04	9.40E-04	i, Cal.
Sm	1.44E-03	1.74E-03	i, Cal.
Eu	2.79E-03	3.55E-03	Sup.
Gd	5.92E-03	6.82E-03	i, Cal.
Tb	1.06E-02	1.21E-02	i, Cal.
Dy	1.59E-02	1.78E-02	i, Cal.
Y	2.40E-02	2.65E-02	i, Cal.
Ho	2.32E-02	2.57E-02	i, Cal.
Er	3.31E-02	3.62E-02	i, Cal.
Tm	4.48E-02	4.86E-02	i, Cal.
Yb	6.29E-02	6.75E-02	i, Cal.
Lu	7.57E-02	8.07E-02	i, Cal.
Hf	3.73E-01	4.69E-01	i, Cal.
Melting	IBC	Hyb. Sr.	
T (ºC)	1300	1350	
P (GPa)	2	2	
Fo	-	-	
Al^{ol}	-	-	
XTi^{melt}	-	-	
Al^{T}	-	-	
Al^{M1}	-	-	
Ca^{M2}	-	-	
Mg^{M2}	-	-	
Mg^{M1}	-	-	
Fe^{M1}	-	-	
Ca^{X}	-	-	
D_0	0.61	0.61	i
r_0	0.688	0.688	i
E	300	300	i
D(Ti)	2.971	2.971	i
$Log(fO_2)$	-10.75	-10.22	
Sample/ Experiment	NJD-8M	NJD-8M	

Calculated partition coefficients are indicated in the source column (Cal.). (Sup.) in the source column indicates the partition coefficients were calculated using the lattice strain models in the electronic supplement of this study. Partition coefficients that are not calculated, are taken from partitioning experiments.
Calculation parameters were calculated for mineral compositions from lunar relevant experiments. Studies and experiments that compositions data was sourced from are indicated at the bottom of the table.
Eu partition coefficients for Ol, Opx, Cpx, and Ilm presented in this table assume an fO_2 equal to the IW redox buffer. The Log($fO2$) of the IW redox buffer for a given temperature was determined using the buffer model from O'Neill and Pownceby (1993).
The partial melting model in which each set of partition coefficients is used is indicated in the Melting row above the calculation parameters. IBC indicates that the coefficients are used in IBC partial melting models. Hyb. Sr. indicates that the coefficients are used in partial melting models of hybridized mantle sources. Hyb. Sr. #1 is a garnet-free hybridized source. Hyb. Sr. #2 is a garnet-bearing hybridized source. If the hybridized source # is not indicated the partition coefficient set is used in models for both hybridized sources.
Olivine (Ol), Orthopyroxene (Opx), Clinopyroxene (Cpx), Pigeonite (Pig), Garnet (Grnt), Ilmenite (Ilm)
[a]Sun and Liang (2013a), [b]Dalou et al. (2012), [c]Sun and Liang (2013b), [d]Fabbrizio et al. (2021), [e]Dygert et al. (2014), [f]Dygert et al. (2020), [g]Snape et al. (2022), [h]Pertermann et al. (2004), [i]Dygert et al. (2013), [j]Charlier et al. (2018), [k]Mallik et al. (2019)

The implied lunar mantle source pressures suggested by Ol-Opx multi-saturation experiments (i.e., the pressures at which the glasses would be in equilibrium with Ol- and Opx-bearing lunar mantle) are estimated to be between 2.3 GPa and 3.1 GPa for yellow and orange picritic glasses (Krawczynski and Grove, 2012; Brown and Grove, 2015). In addition, the Ol-Opx multi-saturation pressures for red and black glasses are estimated to fall between 1.3 GPa and 2.4 GPa depending on the fO_2 conditions of the lunar mantle (Wagner and Grove, 1997; Krawczynski and Grove, 2012). These multi-saturation pressure estimates indicate that the yellow and orange glasses should be generated at depths of 490-725 km, while the red and black glasses should be generated at depths of 260-525 km. While it is still debated whether the LMO extended to the core-mantle boundary (CMB), the initial LMO cumulates at the picritic glass multi-saturation depths would form between 20-40% solidification (for yellow and orange glasses) and 35-62% solidification (for red and black glasses) assuming the deepest possible magma ocean. If the LMO was shallower, these percentages decrease, and the initial cumulates at those depths would form even earlier in the solidification process. Thus, a hybridized lunar mantle source mixture would most likely contain of the earliest LMO cumulates (dunite or harzburgite and IBC material, Elardo et al., 2011; Lin et al., 2017; Charlier et al., 2018; Rapp and Draper, 2018) as a major component.

The combined enrichment of REE and Hf concentrations and picritic glass-like HREE/LREE ratios of the late-crystallizing LMO cumulates (IBC) are essential to consider when investigating plausible Ti-rich picritic glass sources. With the elevated trace element concentrations in the IBC material (1-30x Chondrite Normalized (CN)

values) and the extremely low concentration of EMOC (0.02-0.2x CN values) (**Table 2.3**), any hybridized EMOC source only needs a minor proportion of IBC material to take on the elevated trace element concentrations and ratios of IBC. This is consistent with calculations presented by Scholpp and Dygert (2024a), which suggest the Mg# of the intermediate-Ti and high-Ti picritic glass sources would likely fall between 65-84 and would be composed primarily of high Mg# EMOC material due to the low Mg# of the hypothetical IBC material (**Table 2.5**).

The EMOC component in this study assumes an averaged composition of cumulates that formed between 1% and 51% LMO solidification, while the IBC component is an averaged composition of cumulates that formed between 98% and 99.5% solidification. In models that assume the hybridized source forms after mixing between IBC partial melts and EMOC (Scenarios #3-#5), we assume the source contains 10% IBC partial melt and 90% EMOC (**Table 2.4**). For models where the IBC is assumed to be unmelted (Scenarios #1-#2), the hybridized source is assumed to contain 20% IBC and 80% EMOC (**Table 2.4**). This divergence in mixing proportions is invoked to account for the effect of partial melting on the abundances of REE and Hf in the assumed IBC component. In IBC partial melts, REE and Hf are enriched relative to the initial IBC cumulate, so it would take less material to create the same level of chemical enrichment in the hybridized source. A comparison of Scenarios #1 and #3 demonstrates the effects of varying these mixing proportions on the trace element ratios in our garnet-free melting models (**Table 2.4**). This tests the possibility that variable mixing

proportions could account for the variation in TiO_2 and REE concentrations between intermediate-Ti and high-Ti picritic glasses.

2.3.4 Partial Melting of Hybridized Mantle Sources

In hybridized source melting calculations, we assume that melting occurs at 2 GPa and 1350ºC. This increase in temperature relative to IBC melting reactions is justified by the refractory nature of the hybridized source, which should be significantly more Mg-rich than the downwelling IBC and would have a higher solidus temperature (e.g., Singletary and Grove, 2008; Thacker et al., 2009; Mallik et al., 2019). When calculating the compositions of partial melts generated by hybridized mantle sources, we use similar mineral proportions and compositions to experiments from Mallik et al., 2019 (V984 for a garnet-free source and V1007 for a garnet-bearing source) (**Table 2.7**). For the garnet-bearing sources, the modal abundances of minerals other than garnet were proportionally adjusted as garnet abundance varies. Mineral-melt partition coefficients and calculation parameters for hybridized source partial melting models are reported in **Table (2.6)**.

2.3.5 Effect of Garnet on Hybridized Source Melt Chemistry

2.3.5.1 Mechanical Mixing with Solid IBC Material

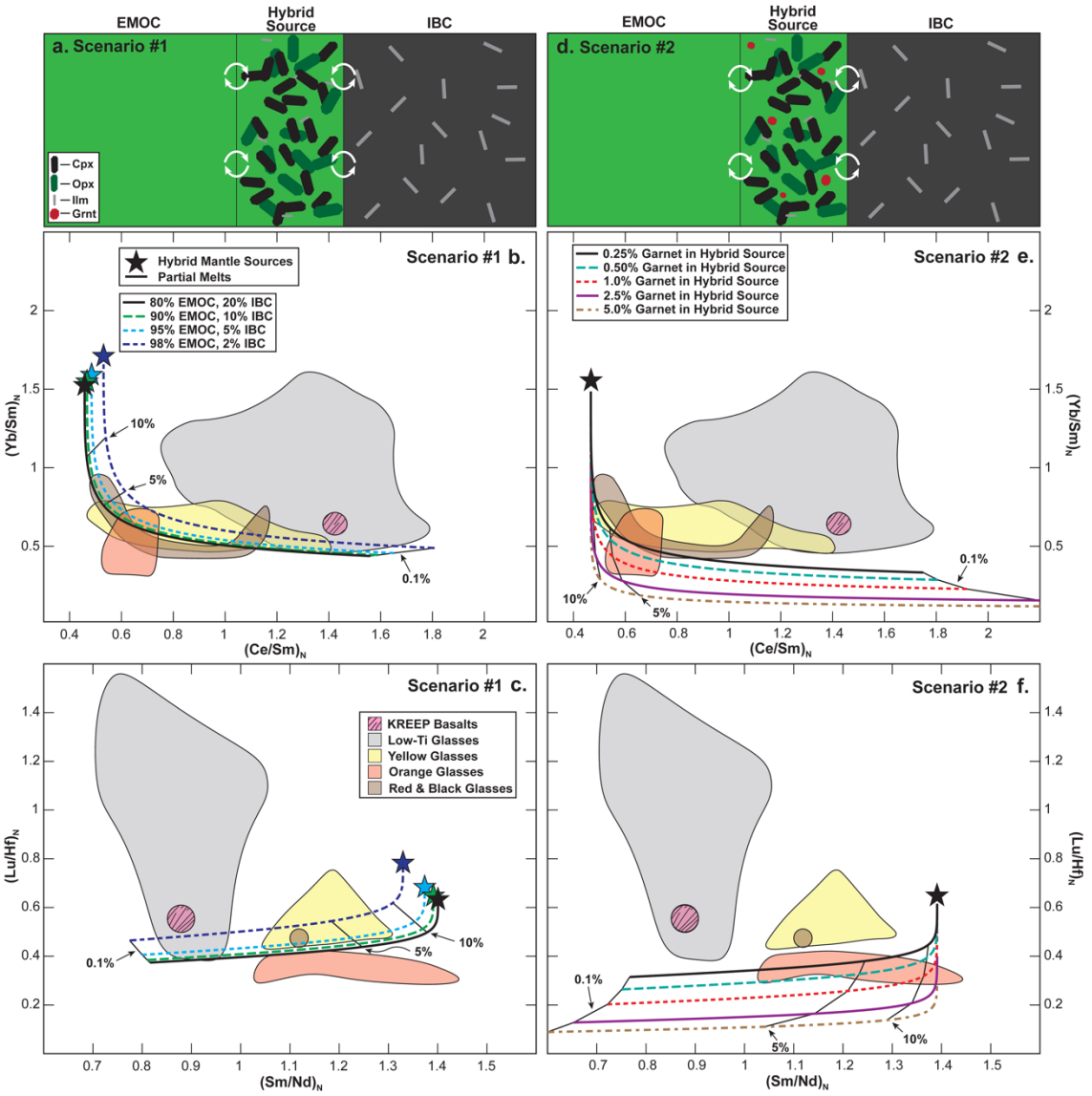
Two models explored the mechanical mixing of IBC into early LMO cumulates without melting (i.e., simple mechanical mixing of solid LMO cumulates). In Scenario #1, garnet was assumed to be absent from the source (**Figure 2.8a-c**).

Table 2.7. Phase proportions of hybridized mantle sources in melting models.

Phases	Garnet-Free Source	Garnet-Bearing Source
Ol	0.243	0.245
Opx	0.419	0.441
Cpx	0.276	0.233
Grnt	0.000	0.012
Ilm	0.062	0.069

Modal mineralogy for a garnet-free source were based on experiment V984 from Mallik et al. (2019)
Modal mineralogy for a garnet-bearing source were based on experiment V984 from Mallik et al. (2019)
Olivine (Ol), Orthopyroxene (Opx), Clinopyroxene (Cpx), Garnet (Grnt), Ilmenite (Ilm)

Figure 2.8. Partial melts of garnet-free and garnet-bearing hybridized sources, assuming that during hybridization, the IBC material was below its solidus and was mechanically mixed into EMOC. Panel (a) shows the mixing end member, mineralogy, and mixing mechanism assumptions for Scenario #1 (Table 2.4). Circling arrows between each endmember and the hybrid source indicate that mechanical mixing occurs to form the source before subsequent partial melting. Panels (b) and (c) show the trend of melts produced by partial melting of a garnet-free hybridized mantle source (Scenario #1). For these models, the proportion of EMOC and IBC material is adjusted to demonstrate the effects of each cumulate reservoir, the hybridized sources, and partial melts. Panel (c) shows the mixing end member, mineralogy, and mixing mechanism assumptions for the Scenario #2 (Table 2.4) hybridization process. Scenario #2 differs from Scenario #1 because the hybridized source for Scenario #2 is garnet-bearing. Panels (b) and (c) show the trend of melts produced by partial melting of a garnet-bearing source (Scenario #2). For these models, the modal abundance of hybridized source garnet varies between 0.25% and 5% to demonstrate the effects of garnet abundance. Stars represent the initial composition of the hybridized source. Black percentages represent the percentage of melting. $(Lu/Hf)_N$ and $(Sm/Nd)_N$ are chondrite normalized ratios. References for lunar sample compositions can be found in the caption to Figure 2.2. Low-Ti picritic glasses: VLT glass & green glass groups. These models demonstrate that garnet-free hybridized mantle sources can account for the trace element patterns in yellow, red, and black picritic glasses; however, garnet-bearing hybridized mantle sources would be required to explain the trace element patterns of lunar orange glasses.

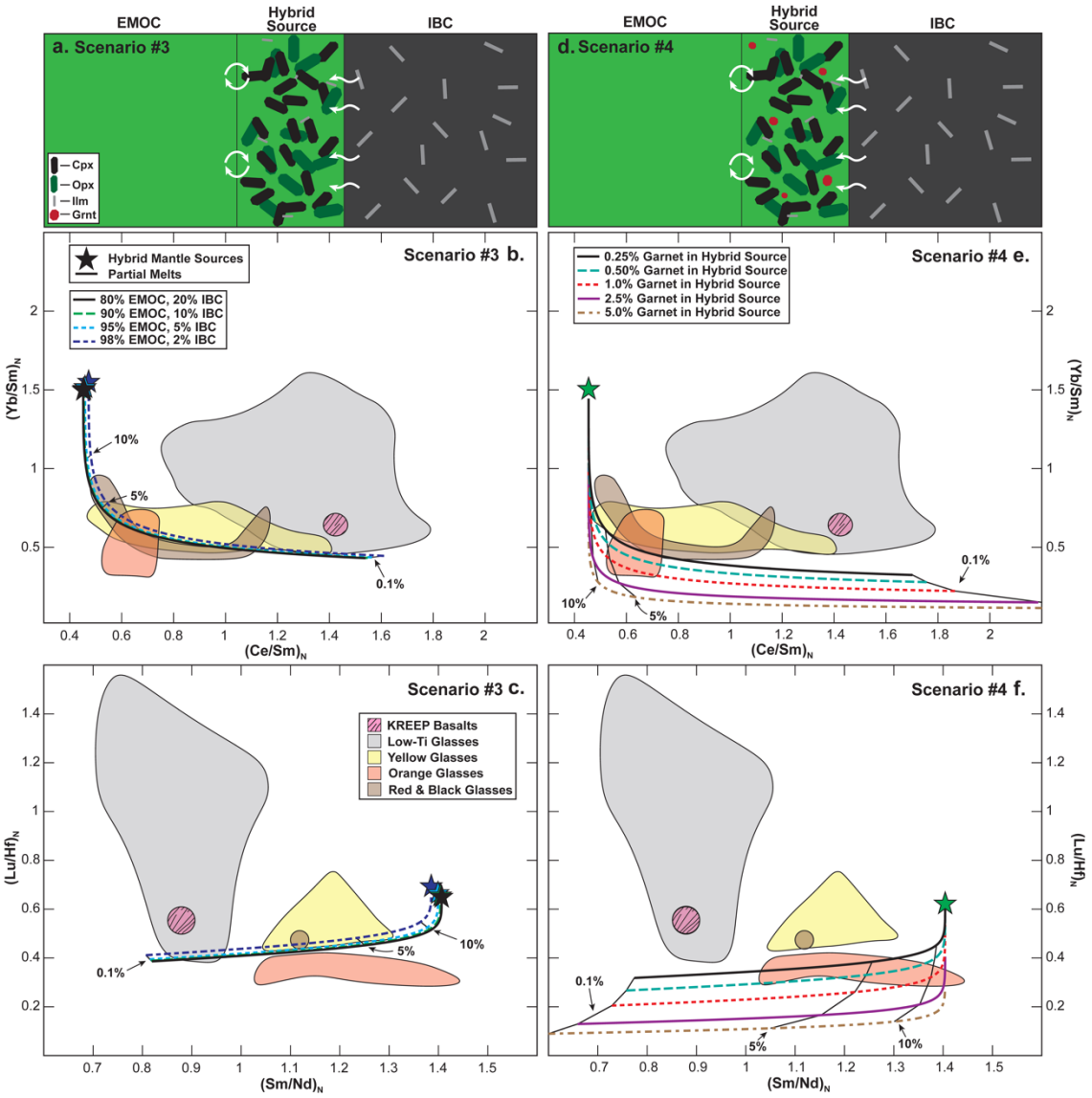

EMOC
Hybrid Source
IBC
a. Scenario #1
Cpx
Opx
Ilm
Grnt
d. Scenario #2
Hybrid Mantle Sources
Partial Melts
80% EMOC, 20% IBC
90% EMOC, 10% IBC
95% EMOC, 5% IBC
98% EMOC, 2% IBC
Scenario #1 b.
10%
5%
0.1%
(Yb/Sm)N
(Ce/Sm)N
0.25% Garnet in Hybrid Source
0.50% Garnet in Hybrid Source
1.0% Garnet in Hybrid Source
2.5% Garnet in Hybrid Source
5.0% Garnet in Hybrid Source
Scenario #2 e.
KREEP Basalts
Low-Ti Glasses
Yellow Glasses
Orange Glasses
Red & Black Glasses
Scenario #1 c.
(Lu/Hf)N
(Sm/Nd)N
Scenario #2 f.

In Scenario #2, garnet was assumed to be present in the source (**Figure 2.8d-f**). The melts produced by (Scenario #1) fit the $(Yb/Sm)_N$ and $(Ce/Sm)_N$ trends of yellow, red, and black glasses remarkably well (**Figure 2.8b**). While there is a notable lack of Hf data for lunar picritic glasses, partial melts produced from this modeled scenario fit the $(Lu/Hf)_N$ and $(Sm/Nd)_N$ data similarly well to the $(Yb/Sm)_N$ and $(Ce/Sm)_N$ data for yellow, red, and black glasses (**Figure 2.8c**). If the proportion of EMOC material in the hybridized source increases, the melting trends fan upwards and across the yellow glass field and towards the low-Ti glass field. Melts from this garnet-free source only overlap with a small portion of the $(Yb/Sm)_N$-$(Ce/Sm)_N$ field for the high-Ti orange glasses and never overlap the $(Lu/Hf)_N$-$(Sm/Nd)_N$ field. Adding garnet to the hybridized source (Scenario #2: **Table 2.4**) results in a significant depletion of HREE (**Figure 2.8e-f**). Melts of this garnet-bearing source overlap with both the $(Yb/Sm)_N$-$(Ce/Sm)_N$ and $(Lu/Hf)_N$-$(Sm/Nd)_N$ fields for orange glasses. These models suggest that 0.25% to 2.5% garnet in a hybridized mantle source could explain the HREE depletion in orange glasses.

2.3.5.2 Garnet-Free IBC

Scenario #3 evaluates mantle sources hybridized by partial melts of garnet-free IBC (**Table 2.4**). These sources can also produce melts that reproduce the $(Yb/Sm)_N$-$(Ce/Sm)_N$ and $(Lu/Hf)_N$-$(Sm/Nd)_N$ trends observed in yellow, red, and black picritic glasses (**Figure 2.9b-c**). The modeled melts trend just below the yellow, red, and black glass fields and just above the orange glass field with respect to $(Lu/Hf)_N$-$(Sm/Nd)_N$ (**Figure 2.9c**).

Figure 2.9. Partial melting models for garnet-free and garnet-bearing sources that were hybridized by partial melts from downwelling garnet-free IBC prior to subsequent melting. Panel (a) shows the mixing end member, mineralogy, and mixing mechanism assumptions for the Scenario #3 (Table 2.4) hybridization process. Panels (b) and (c) show the trend of melts produced by partial melting of a garnet-free hybridized mantle source (Scenario #3). For these models, the proportion of EMOC and IBC material is adjusted to demonstrate the effects of each cumulate reservoir, the hybridized sources, and partial melts. Panel (c) shows the mixing end member, mineralogy, and mixing mechanism assumptions for the Scenario #4 (Table 2.4) hybridization process. Wavy arrows between the IBC and the hybrid source indicate that partial melts interact and mix with EMOC material to form the hybridized source. Panels (b) and (c) show the trend of melts produced by partial melting of a garnet-bearing hybridized mantle source (Scenario #4). For these models, the modal abundance of garnet in the hybridized source varies between 0.25% and 5% to demonstrate the effects of garnet abundance in the hybridized source. Stars represent the initial composition of the hybridized source. Black percentages represent the percentage of melting. $(Lu/Hf)_N$ and $(Sm/Nd)_N$ are chondrite normalized ratios. References for lunar sample compositions can be found in the caption to Figure 2.2. Low-Ti picritic glasses: VLT glass & green glass groups. These models further demonstrate that garnet-free hybridized mantle sources can account for the trace element patterns in yellow, red, and black picritic glasses; however, garnet-bearing hybridized mantle sources would be required to explain the trace element patterns of lunar orange glasses.


EMOC
Hybrid Source
IBC
a. Scenario #3
Cpx
Opx
Ilm
Grnt
d. Scenario #4
Hybrid Mantle Sources
Partial Melts
80% EMOC, 20% IBC
90% EMOC, 10% IBC
95% EMOC, 5% IBC
98% EMOC, 2% IBC
Scenario #3 b.
10%
5%
0.1%
(Yb/Sm)N
(Ce/Sm)N
0.25% Garnet in Hybrid Source
0.50% Garnet in Hybrid Source
1.0% Garnet in Hybrid Source
2.5% Garnet in Hybrid Source
5.0% Garnet in Hybrid Source
Scenario #4 e.
KREEP Basalts
Low-Ti Glasses
Yellow Glasses
Orange Glasses
Red & Black Glasses
Scenario #3 c.
(Lu/Hf)N
(Sm/Nd)N
Scenario #4 f.

Increasing the proportion of EMOC material in the hybridized source shifts the melting trends toward the yellow, red, and black glass fields (**Figure 2.9c**); however, the effect on melts is less significant than that observed in Scenario #1 (**Figure 2.8c**). Melts from this garnet-free hybridized source trend above the majority of orange glass $(Yb/Sm)_N$-$(Ce/Sm)_N$ data and all available $(Lu/Hf)_N$-$(Sm/Nd)_N$ data (**Figure 2.9b-c**). Scenario #4 evaluates the presence of garnet in this hybridized source, resulting in similar levels of HREE depletion as the garnet-bearing solid-solid mixing scenario (Scenario #2) (**Figure 2.9e-d**). Melts of the Scenario #4 garnet-bearing source overlap with both the $(Yb/Sm)_N$-$(Ce/Sm)_N$ and $(Lu/Hf)_N$-$(Sm/Nd)_N$ fields for orange glasses and fall well beneath the yellow, red, and black glass fields.

2.3.5.3 Garnet-Bearing IBC

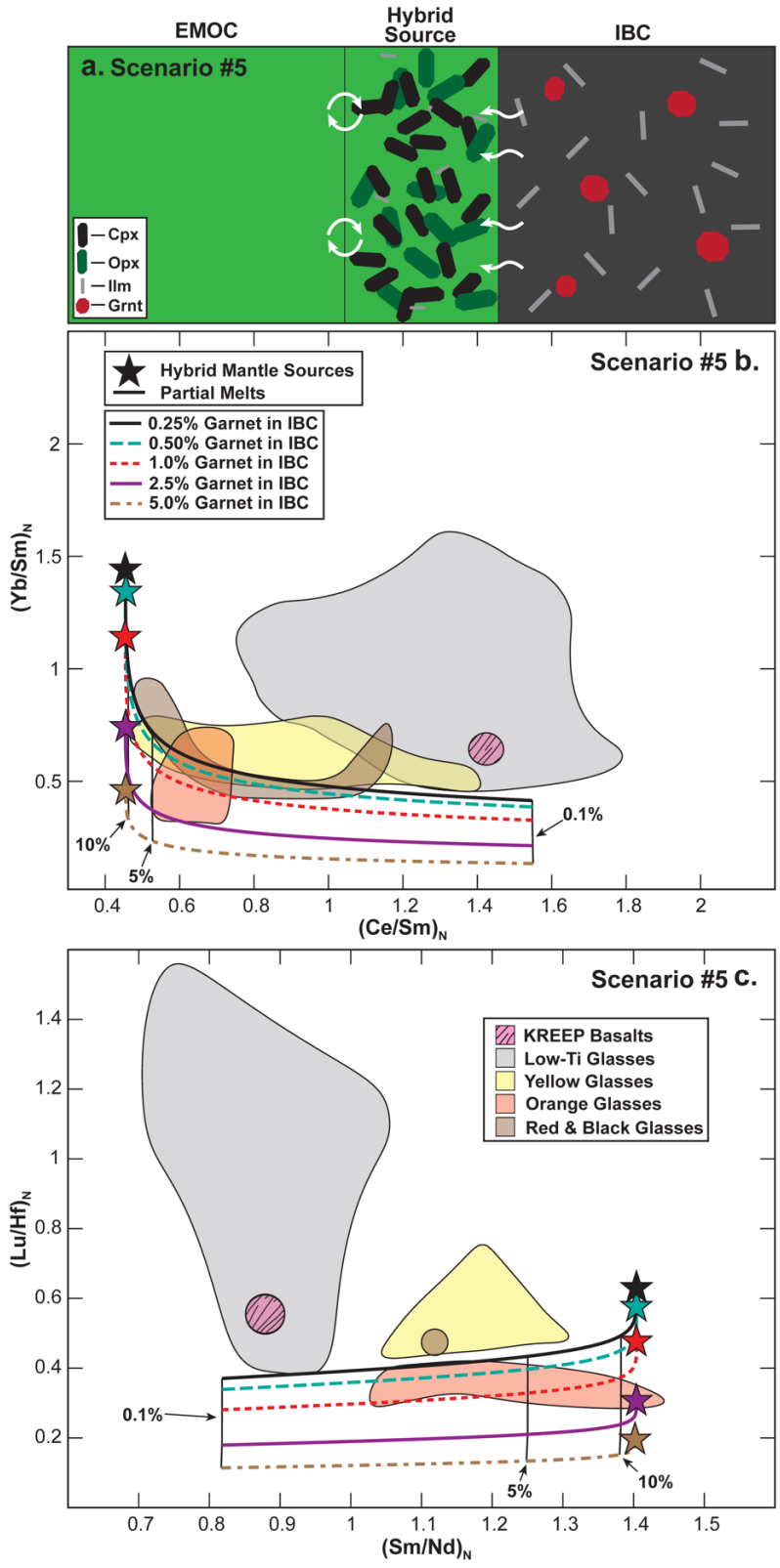
Scenario #5 tests mantle sources hybridized by partial melts of garnet-bearing IBC containing 0.25% to 2.5% garnet. These sources produce similar trace element patterns as garnet-bearing sources hybridized by partial melts from a garnet-free IBC (Scenario #2) (**Figure 2.10**). Scenario #5 hybridized source melts overlap with the fields of some yellow, red, and black glasses and the least HREE-depleted orange glasses in $(Yb/Sm)_N$-$(Ce/Sm)_N$ space if the abundance of garnet in the IBC falls between 0.25% and 1% (**Figure 2.10b**). The most HREE-depleted orange glasses would require 1% to 2.5% garnet in both $(Yb/Sm)_N$-$(Ce/Sm)_N$ and $(Lu/Hf)_N$-$(Sm/Nd)_N$ space (**Figure 2.10c**).

2.3.5.4 Summary of Partial Melting Models Assuming No Late Cumulate Mixing (Scenarios #1-#5)

The hybridization and partial melting models presented above demonstrate that the compositions of yellow, orange, red, and black lunar picritic glasses cannot all be explained by the same hybridization scenario. Regardless of the physical state of the IBC components contributing to the hybridized source (i.e., molten or solid), the yellow, red, and black lunar picritic glasses are fit best by models that assume garnet-free IBC and garnet-free hybridized sources (Scenarios #1 and #3) (**Figures 2.8b-c and 2.9b-c**). The yellow and black glass data are also consistent with progressive melting of a hybridized garnet-free source at extents of melting of 1% to 10%. These scenarios demonstrate that the $(Yb/Sm)_N$-$(Ce/Sm)_N$ and $(Lu/Hf)_N$-$(Sm/Nd)_N$ chemical variation among yellow, red, and black glass data could be related to variations in the proportion of EMOC and IBC material in their respective hybridized sources.

In contrast to the yellow, red, and black glasses, none of the orange glass $(Lu/Hf)_N$ and $(Sm/Nd)_N$ ratios are consistent with melting trends produced by garnet-free source scenarios. The most HREE-depleted orange glass data are better fit by Scenarios #2 and #4 where 0.25-2.5% garnet is in their source (**Figures 2.8e-f and 2.9e-f**), or where garnet was a stable phase in the downwelling IBC that melted and hybridized the deep EMOC material (Scenario #5) (**Figures 2.10b-c**). Thus, the models indicate that garnet is required to explain the orange picritic glass data; however, the location of the garnet (i.e., the hybridized source or the downwelling IBC material) is not revealed by the melting models.

Figure 2.10. Partial melting models for garnet-free hybridized sources that were hybridized by partial melts from a garnet-bearing IBC prior to subsequent melting. Panel (a) shows the mixing end member, mineralogy, and mixing mechanism assumptions for Scenario #5 (Table 2.4). Wavy arrows between the IBC and the hybrid source indicate that partial melts interact and mix with EMOC material to form the hybridized source. Panels (b) and (c) show the trend of melts produced by partial melting of a garnet-bearing hybridized mantle source. For these models, the modal abundance of IBC-hosted garnet varies between 0.25% and 5% to demonstrate the effects of garnet abundance on the garnet-free hybridized source and partial melts generated by that source. Stars represent the initial composition of the hybridized source. Black percentages represent the percentage of melting. $(Lu/Hf)_N$ and $(Sm/Nd)_N$ are chondrite normalized ratios. References for lunar sample compositions can be found in the caption to Figure 2.2. Low-Ti picritic glasses: VLT glass & green glass groups. These models demonstrate that a garnet-bearing IBC could undergo partial melting before source hybridization and still generate the trace element patterns of lunar orange glasses. Whether garnet is a stable phase in the source or the downwelling cumulates, the trace element effects produced are nearly identical when considering secondary melt products (i.e., basalts and picritic glasses), as long as garnet was present.

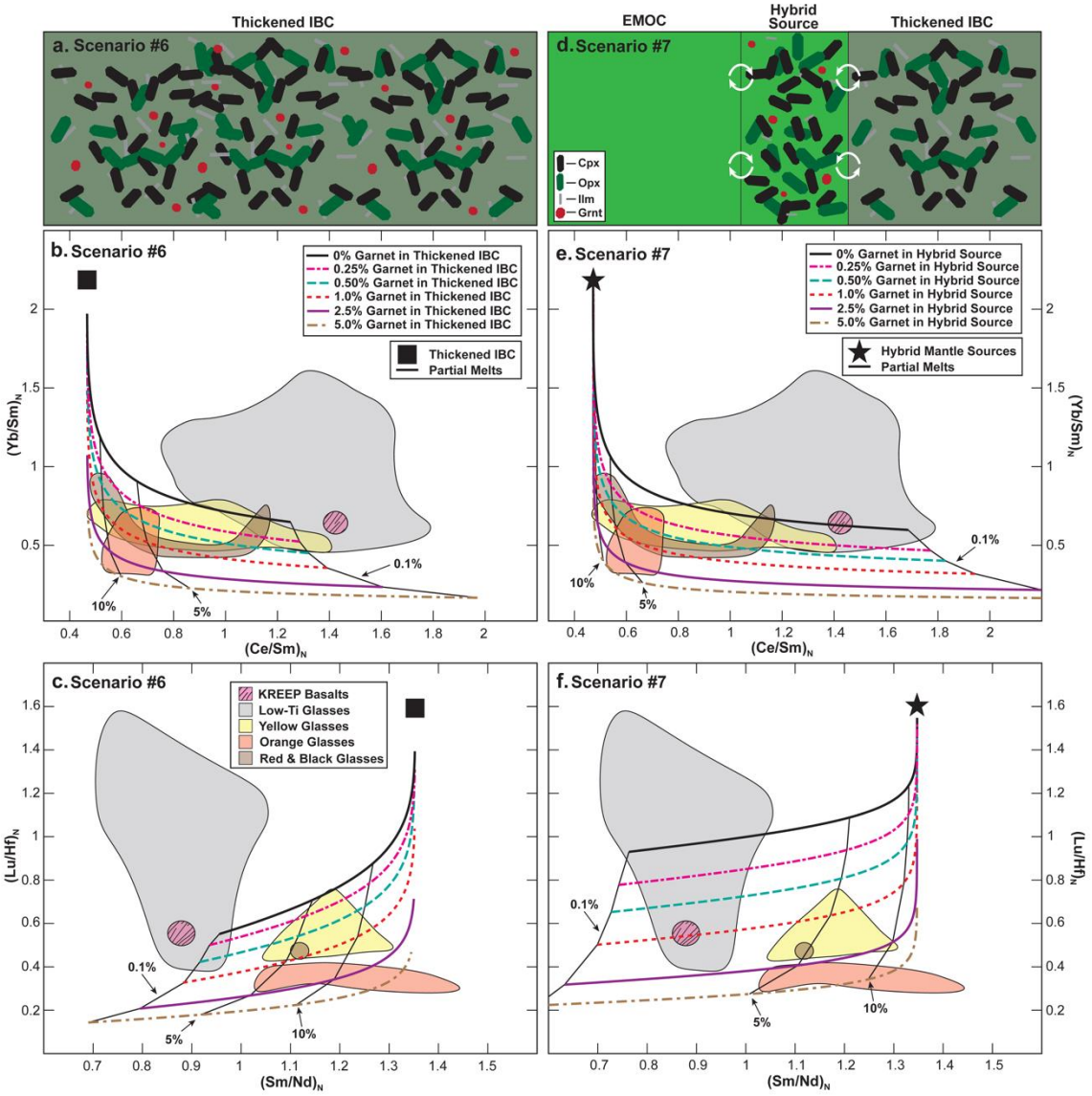

EMOC
Hybrid Source
IBC
a. Scenario #5
Cpx
Opx
Ilm
Grnt
Scenario #5 b.
Hybrid Mantle Sources
Partial Melts
0.25% Garnet in IBC
0.50% Garnet in IBC
1.0% Garnet in IBC
2.5% Garnet in IBC
5.0% Garnet in IBC
(Yb/Sm)N
(Ce/Sm)N
0.1%
10%
5%
Scenario #5 c.
KREEP Basalts
Low-Ti Glasses
Yellow Glasses
Orange Glasses
Red & Black Glasses
(Lu/Hf)N
(Sm/Nd)N
0.1%
5%
10%

2.3.6 Early Mixing During LMO Solidification

Previous studies hypothesized that late LMO cumulate sinking occurred while magma ocean solidification was active, forming a thickened IBC layer before a larger-scale overturn event that transported the IBC material to the lower lunar mantle (Hess and Parmentier, 1995; Parmentier et al., 2002; Li et al., 2019). If the LMO initially extended from the CMB to the lunar surface, and small-scale mixing events occurred, forming a thickened IBC layer of ~100 km, this would imply that the IBC material would consist of cumulates that precipitated between 88% to ~100% LMO solidification. This thickened IBC would have lower overall REE and Hf abundances and higher (Yb/Sm)N and (Lu/Hf)N ratios (**Table 2.3**; **Figure 2.11**) and a higher Mg# than the thin IBC (**Table 2.5**).

The lower minimum estimated mantle Mg#s of intermediate- and high-Ti lunar picritic glasses (e.g., 67.71 and 65.06 respectively) and higher estimated Mg# thickened IBC (~53) make it possible for melts of this thickened IBC to explain the Mg# of the intermediate- and high-Ti lunar picritic glasses. This would require some amount of re-equilibration between the melts and displaced mafic mantle cumulates during their ascent to increase the Mg# (e.g., Klaver et al., 2023; Scholpp and Dygert, 2024a); however, this re-equilibration process would likely have an insignificant effect on the REE+Hf compositions of the melts due to their slow diffusivities (e.g., Cherniak and Liang, 2007; Cherniak, 2010) and high concentrations within the melts (**Figure B7**).

Figure 2.11. Partial melting models for a hybridized source and IBC, assuming a thickened layer of IBC material did not experience melting during the hybridization process (i.e., solid-solid mechanical mixing) prior to subsequent melting. These models assume that the IBC material consists of cumulates that form between 88% and 100% LMO solidification due to small-scale overturn events during LMO solidification (e.g., Figure 2.1). Panel (a) shows the assumption for Scenario #6 (Table 2.4) that a thickened IBC never mixes with the EMOC material. Panels (b) and (c) show the trend of melts produced by partial melting of a thickened garnet-bearing IBC. For these models, the modal abundance of IBC-hosted garnet varies between 0% and 5%. The square represents the initial composition of the thickened IBC. Panel (d) shows the mixing end member, mineralogy, and mixing mechanism assumptions for the Scenario #7 (Table 2.4) hybridization process. Circling arrows between each endmember and the hybrid source indicate that mechanical mixing occurs without partial melting. Panels (e) and (f) show the trend of melts produced by partial melting of a garnet-bearing hybridized mantle source. For these models, the modal abundance of garnet in the hybridized source varies between 0.25% and 5% to demonstrate the effects of garnet abundance in the hybridized source and partial melts generated by that source. The star represents the initial composition of the hybridized source. Black percentages represent the percentage of melting. $(Lu/Hf)_N$ and $(Sm/Nd)_N$ are chondrite normalized ratios. References for lunar sample compositions can be found in Figure 2.2. Low-Ti picritic glasses: VLT glass & green glass groups. These models demonstrate that a garnet-bearing hybridized mantle source would be required to explain the trace element patterns of all lunar picritic glasses if early cumulate mixing occurred during LMO solidification.


Thickened IBC
a. Scenario #6
EMOC
Hybrid Source
Thickened IBC
d. Scenario #7
Cpx
Opx
Ilm
Grnt
b. Scenario #6
0% Garnet in Thickened IBC
0.25% Garnet in Thickened IBC
0.50% Garnet in Thickened IBC
1.0% Garnet in Thickened IBC
2.5% Garnet in Thickened IBC
5.0% Garnet in Thickened IBC
Thickened IBC
Partial Melts
0.1%
10%
5%
(Yb/Sm)N
(Ce/Sm)N
e. Scenario #7
0% Garnet in Hybrid Source
0.25% Garnet in Hybrid Source
0.50% Garnet in Hybrid Source
1.0% Garnet in Hybrid Source
2.5% Garnet in Hybrid Source
5.0% Garnet in Hybrid Source
Hybrid Mantle Sources
Partial Melts
c. Scenario #6
KREEP Basalts
Low-Ti Glasses
Yellow Glasses
Orange Glasses
Red & Black Glasses
(Lu/Hf)N
(Sm/Nd)N
f. Scenario #7

While it may be possible to explain the major element composition of intermediate- and high-Ti lunar picritic glasses with reactive re-equilibration during melt ascent, we propose that mantle hybridization is equally as likely to occur. Scenarios #6 and #7 explore REE and Hf fractionation produced by partial melting of a thickened IBC and partial melting of a source hybridized by this thickened IBC.

2.3.6.1 Partial Melting of a Thickened IBC

Scenario #6 tests the effect of partial melting on a thickened IBC. The melts produced by (Scenario #6) fit the $(Yb/Sm)_N$-$(Ce/Sm)_N$ and $(Lu/Hf)_N$-$(Sm/Nd)_N$ trends of yellow, red, and black glasses remarkably well (**Figure 2.11a-c**) if the abundance of garnet in the thickened IBC falls between 0.25% and 1%. To explain the $(Yb/Sm)_N$-$(Ce/Sm)_N$ and $(Lu/Hf)_N$-$(Sm/Nd)_N$ trends of most orange picritic glasses, 1-5% garnet would be required. The absence of garnet pushes the $(Yb/Sm)_N$ and $(Lu/Hf)_N$ ratios above the trends of yellow, red, and black glasses, indicating garnet would likely be required if a thickened IBC was the source of intermediate- and high-Ti lunar picritic glasses.

2.3.6.2 Partial Melting Source Hybridized by a Thickened IBC

Scenario #7 investigates the effect of partial melting on a source hybridized by a thickened IBC. Due to the lower overall REE and Hf abundances of the thickened IBC (**Table 2.3**), hybridized sources that formed in scenarios that invoke thickened IBC layers would also have to contain more thickened IBC material (i.e., 40-60% based on iterative models) to account for the overall REE and Hf abundances of the intermediate- and high-Ti picritic melts. For Scenario #7, we assume that the hybridized source represents a simple mechanical mixture of 55% EMOC and 45% IBC and uses the same modal

mineralogy from the previous models of garnet-free and garnet-bearing hybridized sources (**Table 2.7**).

In this scenario (i.e., Scenario #7), the hybridized source would have to contain ~5% garnet to account for the $(Yb/Sm)_N$ and $(Lu/Hf)_N$ ratios of the most HREE depleted lunar orange glasses (**Figure 2.11a-c**). In addition, the models indicate that >0.5% garnet would be required to account for the $(Yb/Sm)_N$ and $(Lu/Hf)_N$ ratios of yellow, red, and black picritic glasses. Thus, if pre-overturn mixing occurred and a hybridized source formed, garnet must be present in the hybridized mantle source to generate trace element trends of all intermediate to high-Ti lunar picritic glasses.

2.3.6.3 Summary of Partial Melting Models Assuming Late Cumulate Mixing Occurred (Scenarios #6-#7)

The pre-overturn mixing process would have a significant effect on the overall composition of the IBC, most notably the requirement for residual garnet in the mantle source to explain the $(Yb/Sm)_N$ and $(Lu/Hf)_N$ ratios of most intermediate to high-Ti lunar picritic glasses with and without hybridization. If mantle hybridization occurred, hybridized sources would have to contain 2-3x more IBC material than models that lack late cumulate mixing to account for the overall REE and Hf abundances of intermediate to high-Ti lunar picritic melts. It should also be noted that the amount of garnet required in the lunar mantle to explain the $(Yb/Sm)_N$ and $(Lu/Hf)_N$ ratios of lunar orange picritic glasses roughly doubles in Scenarios #6 and #7 (**Figure 2.11a-c**). Although this is generally consistent with thermodynamic models for the mineralogy of an IBC cumulate that experienced late cumulate mixing (**Figure 2.6b**), the ~5% garnet requirement would

be significantly higher than thermodynamic modeling estimates for a corresponding hybridized source (**Figure B8**).

2.4 Parameters That Could Affect Model Results

2.4.1 LMO Cumulate Mineralogy

Geochemical evidence of garnet in the lunar mantle hinges on the HREE to LREE and HREE to Hf ratios of lunar samples. While garnet is called upon to explain the HREE depleted signatures of some lunar samples in previous studies (Beard et al., 1998; Neal, 2001; Draper et al., 2006), the mineralogy of the IBC material can notably affect these ratios as well. While studies of LMO solidification agree on the early crystallizing phases, these same studies often indicate the mineralogy and modal mineral proportions of late crystallizing cumulates could vary slightly (Snyder et al., 1992; Elardo et al., 2011; Elkins-Tanton et al., 2011; Lin et al., 2016, 2017; Charlier et al., 2018). Crystallization of the LMO generally results in progressive depletion of the $(Lu/Hf)_N$ and $(Yb/Sm)_N$ ratios in the residual magma ocean liquids (**Figure 2.3**). This progressive depletion in the residual LMO liquid results in a related depletion in the LMO cumulates. The chemical evolution of (Lu/Hf)N and (Yb/Sm)N ratios in LMO cumulates and residual liquids are primarily controlled by four late-crystallizing mineral phases: (1) Plag, (2) Cpx, (3) Ilm, (4) Apatite. Here we consider how differing proportions of these phases in the LMO solidification sequence would affect elemental fractionation in the LMO cumulates.

Plagioclase and Cpx are relatively abundant, and the REE partitioning behavior of these minerals differs significantly from other common LMO cumulate phases (**Table**

2.2). The impact of these minerals on cumulate and residual liquid compositions is observable by the significant shift in cumulate (Lu/Hf)N and (Yb/Sm)N ratios around 80% LMO solidification (**Figure 2.3**). Plagioclase produces the most obvious difference in REE partitioning as LREE are more compatible than HREE, which differs from all other LMO cumulate minerals and would appear to have a significant impact on the $(Yb/Sm)_N$ ratios of cumulates and residual liquids (**Table 2.2**) (e.g., Sun et al., 2017; Dygert et al., 2020; Snape et al., 2022; and references therein). While this would affect the $(Yb/Sm)_N$ ratios of LMO mantle cumulate significantly if floatation was relatively inefficient, models from this study assume the majority of Plag is removed from the LMO mantle cumulate piles to form the lunar anorthosite crust, decreasing its overall impact on LMO mantle cumulates.

Since the majority of Plag is removed from late-crystallizing LMO mantle cumulates, Cpx is the primary mineral driving the decrease in modeled $(Lu/Hf)_N$ and $(Yb/Sm)_N$ ratios of mantle cumulates from ~80-95% LMO solidification (**Figure 2.3**). Clinopyroxene has a relatively flat middle REE (MREE: Sm-Ho) to HREE partitioning trend with a decrease in compatibility for LREE from Nd to La. While this partitioning trend does not significantly differ from phases like Ol, Opx, and Pig (**Table 2.2**), these other phases have partitioning trends that steeply increase in elemental compatibility from LREE to HREE (e.g., Sun and Liang, 2013a, 2013b; Dygert et al., 2014, 2020; Snape et al., 2022; Haupt et al., 2024; and references therein). The relatively flat partitioning MREE to HREE trend in Cpx results would likely result in a decreased

$(Yb/Sm)_N$ ratio for the mantle cumulates; however, this is unlikely to account for the $(Lu/Hf)_N$ ratio required to explain the lunar orange glass compositions.

The abundance of Ilm can also significantly impact the Lu/Hf ratios of IBC material. Ilmenite has a notable effect on the $(Lu/Hf)_N$, as it and Qtz are the only phases to crystallize during LMO solidification in which Hf is more compatible than Lu (**Table 2.2**) (e.g., Klemme et al., 2006; Van Kan Parker et al., 2011; Dygert et al., 2013; Shepherd et al., 2022; Snape et al., 2022). The effect of Ilm crystallization on mantle cumulates is evident due to the significant downward shift in mantle cumulate $(Lu/Hf)_N$ ratios between 95% and 99% LMO solidification (**Figure 2.3b**). If the abundance of Ilm in IBC material increased, the $(Lu/Hf)_N$ ratio for the IBC material would decrease slightly. While this could result in a similar signature to residual garnet during partial melting in $(Lu/Hf)_N$ space, it would likely result in the opposite effect in $(Yb/Sm)_N$ space. Yb is significantly more compatible than Sm in Ilm, similar to Ol, Opx, and Pig (**Table 2.2**), so increasing the abundance of Ilm in the IBC would increase the need for garnet in the IBC material or hybridized source to explain the $(Yb/Sm)_N$ ratios of orange glasses.

The experimental results of Rapp and Draper (2018) indicate that apatite could be present in the late-crystallizing LMO cumulates and, specifically, the hypothesized IBC material. The addition of apatite to the IBC material could have a notable effect on the Eu anomaly (see section 2.2.3. for further discussion and **Figure B4**) and the $(Yb/Sm)_N$ ratios given the relatively compatible REE partitioning behavior and generally flat trend from LREE-HREE relative to other LMO cumulate minerals (e.g., Prowatke and Klemme, 2006; Li et al., 2023; Ji and Dygert, 2024). Hf is significantly less compatible

than Lu in apatite, and Lu is considerably more compatible in apatite than Hf is in Ilm (Prowatke and Klemme, 2006; Li et al., 2023). Thus, adding any notable amount of apatite to the IBC would counteract the effects of Ilm and elevate the $(Lu/Hf)_N$ ratio. With this in mind, it is unlikely that a different solidification sequence with an apatite-bearing IBC would explain the low $(Lu/Hf)_N$ and $(Yb/Sm)_N$ ratios observed in orange picritic glasses (**Figure B5**).

2.5 Garnet in the Lunar Mantle

2.5.1 Garnet in a primitive lunar mantle reservoir?

Although the Moon is believed to have formed after a relatively high energy impact, previous studies indicate that the LMO may have been relatively shallow and limited to the upper 1200 km or less of the lunar interior (Solomon and Longhi, 1977; Shearer et al., 2006; Elkins-Tanton et al., 2011; Charlier et al., 2018) based on the estimated cooling rates and crustal thickness of the Moon. This implies that the material underlying the LMO could consist of undifferentiated material that has the same composition as the initial LMO or LMO cumulates that crystallized rapidly and in equilibrium with the LMO liquid via a batch crystallization process (Hess and Parmentier, 1995; Elardo et al., 2011; Charlier et al., 2018; Rapp and Draper, 2018; Jing et al., 2022). If either of these processes occurred, the lower lunar mantle would have a more Al-rich composition than the early crystallizing cumulates (Elardo et al., 2011; Jing et al., 2022; Kraettli et al., 2022). This relatively Al-rich composition of the undifferentiated or batch crystallized lower mantle region would have a greater chance to stabilize garnet at or below the depths where the lunar picritic glasses are sourced (i.e.,

~260-725 km and 1.3-3.1 GPa) (Johnson et al., 2021; Jing et al., 2022); however, the major and trace element systematics demonstrate a primitive garnet-bearing source cannot explain the picritic glass trends.

If we consider the effects of batch crystallization of a well-mixed LMO, the $(Yb/Sm)_N$ and $(Lu/Hf)_N$ ratios of these deep lunar cumulates would be similar to that of the EMOC (i.e., ~2.8 and ~2.9, respectively) regardless of the assumed LMO bulk composition (i.e., LPUM or TWM) (Elardo et al., 2011; Johnson et al., 2021; Jing et al., 2022). The elevated $(Yb/Sm)_N$ and $(Lu/Hf)_N$ ratios in the source would require an abundance of garnet to explain the low $(Yb/Sm)_N$ and $(Lu/Hf)_N$ ratios of the orange picritic glasses. Although a batch crystallized lower lunar mantle would have higher Al_2O_3 contents than a fractionally crystallized lower mantle, the results of Elardo et al. (2011) and Johnson et al. (2021) suggest garnet would be absent or in trace abundances in the lower mantle assuming an LPUM-like bulk LMO. If the Moon had a more TWM-like composition (Kraettli et al., 2022; Jing et al., 2022), garnet may be sufficiently abundant to explain orange glass $(Yb/Sm)_N$ and $(Lu/Hf)_N$ ratios. However, this model would also require addition of a significant Ilm component to account for the TiO_2 contents of the orange glasses since a batch crystallized lower mantle would be incredibly Ti-poor (Wagner and Grove, 1997).

Melts produced garnet-bearing undifferentiated sources would be: (a) REE-poor compared to the intermediate to high-Ti picritic glasses, (b) trending away from the intermediate to high-Ti glasses with respect to their $(Yb/Sm)_N$ and $(Lu/Hf)_N$ ratios, and (c) Ti-poor relative to the intermediate to high-Ti glasses (i.e., the glasses that require

garnet-bearing sources). These traits would require a significant amount of IBC assimilation (dissolution) to overcome, which would likely overprint the HREE-depleted "garnet signature" of these melts.

In conclusion, invoking a primitive layer in the deep Moon is unlikely to model high-Ti glasses successfully. Cumulate overturn is the most straightforward mechanism for explaining the lunar orange glasses' garnet signature and Ti-rich composition. Cumulate overturn provides multiple plausible mechanisms for stabilizing garnet and for imparting the garnet signature onto melts of a hybridized source, and it enriches the TiO_2 contents of the source.

2.5.2 Garnet's Relationship with Cumulate Overturn

All models from this study indicate that garnet in the downwelling IBC material or hybridized mantle source would be required to generate the HREE depletion observed in orange picritic glasses. Based on our model results, <2.5% garnet in the downwelling IBC material or hybridized source would explain the most HREE-depleted orange glasses if no late LMO cumulate mixing occurred (Scenarios #2 and #4, **Figures 2.8e, 2.8f, 2.9e, 2.9f**). This estimate is consistent with the 2% garnet estimate by Beard et al. (1998), who proposed the high-Ti lunar basalt source would be required to explain the Lu/Hf isotope ratios. If late LMO cumulate mixing occurred (Scenarios #6 and #7, **Figure 2.11**), garnet would likely be required to explain the composition of most intermediate to high-Ti lunar glasses given the elevated initial $(Yb/Sm)_N$ and $(Lu/Hf)_N$ ratios of the thickened IBC material**.** Without garnet in the lunar mantle, the bulk LMO would have to exhibit a

HREE and Hf depleted bulk composition to explain the orange picritic glasses and possibly some lunar yellow, red, and black glasses.

Barring the unlikely assumption that the LMO had a pre-existing HREE and Hf depleted composition, the requirement of garnet to explain the HREE depletion in lunar orange glasses does not necessarily indicate that the hybridized source that formed the lunar orange glasses contains garnet. **Figures 2.8, 2.9, and 2.11** demonstrate that a garnet-bearing IBC signature imparted onto a garnet-free hybridized source could produce a similar trend to the garnet-bearing hybridized source if the overall abundance of garnet. Thus, garnet could be present in the downwelling IBC material or the hybridized source and generate similar geochemical signatures in any melts produced by the hybridized source. Given the results of thermodynamic models in this study (**Figure 2.6** and **Figure B8**), we proposed that it is more likely that garnet would be present in the downwelling IBC material; however, further work on high-pressure mantle hybridization and late crystallizing LMO cumulate chemistry is required to evaluate this further.

2.6 Effect of Cumulate Overturn Sm-Nd and Lu-Hf Isotopes

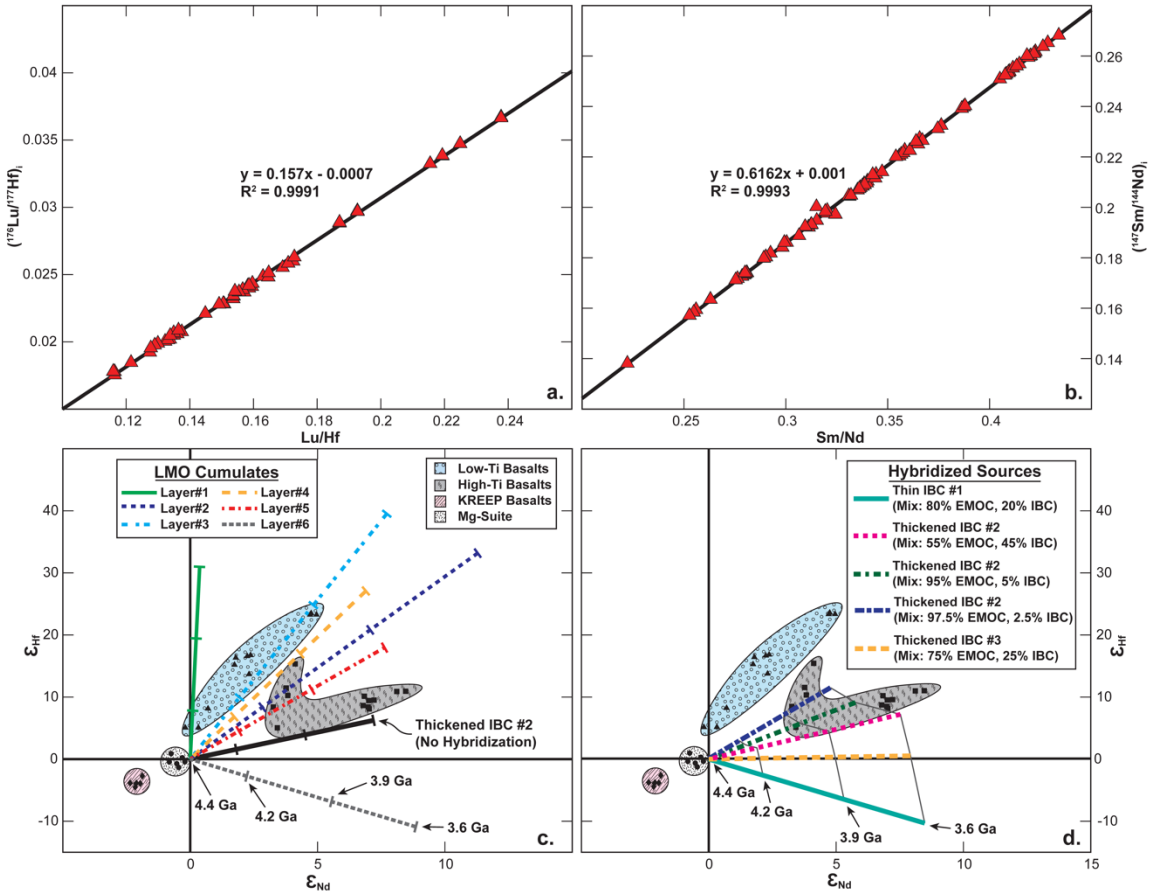
Because the Sm-Nd and Lu-Hf isotopic ratios of intermediate to high-Ti picritic glasses have never been determined and the age of formation for these picritic glasses is unknown, we compare isotopic models to mare basalts to gain a first-order understanding of how hybridization might affect other lunar mantle sources. Due to their long half-lives, the Sm/Nd and Lu/Hf elemental ratios of the lunar sources significantly impact the isotope ratios of these elements. Isotopic and trace element data collected by previous studies (Unruh et al., 1984; Beard et al., 1998; Sprung et al., 2013; Carlson et al., 2014;

Gaffney and Borg, 2014; Boyet et al., 2015; Borg et al., 2019; Marks et al., 2019; Sio et al., 2020; Borg et al., 2020) demonstrate a strong correlation between the age-corrected (initial) isotope ratios and trace element ratios for Sm-Nd and Lu-Hf in lunar samples (**Figure 2.12a-b**). This indicates that the isotopic and elemental ratios for lunar sample sources mirror each other closely (e.g., Beard et al., 1998; Sprung et al., 2013).

To model the isotopic compositions of lunar basalt sources, we assume that the bulk LMO initially had chondritic isotope ratios and solidified by ~4.4 Ga (Sprung et al., 2013; Borg and Carlson, 2023). The decay equation is used to calculate the evolution of each layer of LMO cumulates in $\mathcal{E}_{\mathrm{Nd}}$ and $\mathcal{E}_{\mathrm{Hf}}$ space (**Figure 2.12c**). $\mathcal{E}$ values (i.e., the isotopic composition of the sample relative to the Chondritic Uniform Reservoir (CHUR) at a given time; $\mathcal{E}_{\mathrm{Nd}} = \left(\left(\frac{\left(\frac{^{143}\mathrm{Nd}}{^{144}\mathrm{Nd}}\right)_{\mathrm{sample}} - \left(\frac{^{143}\mathrm{Nd}}{^{144}\mathrm{Nd}}\right)_{\mathrm{CHUR}}}{\left(\frac{^{143}\mathrm{Nd}}{^{144}\mathrm{Nd}}\right)_{\mathrm{CHUR}}}\right) \times 10000\right)$ are calculated using the ratio of the radiogenic decay product and a stable isotope of the produced element (i.e., ^{143}Nd-^{144}Nd for $\mathcal{E}_{\mathrm{Nd}}$ and ^{176}Hf-^{177}Hf for $\mathcal{E}_{\mathrm{Hf}}$). Since the samples' modern isotopic ratios and ages are known, the initial $\mathcal{E}$ values of a given sample are calculated (initial isotope ratios). Initial isotope ratios are not affected by partial melting or fractional crystallization. Since the two isotopes of these heavy elements follow the same partitioning behavior, the initial $\mathcal{E}$ value represents the mantle source itself.

The initial $\mathcal{E}$ values of lunar samples show that low-Ti and high-Ti mare basalt sources fan out across the upper right-hand quadrant of the $\mathcal{E}_{\mathrm{Hf}}$ vs. $\mathcal{E}_{\mathrm{Nd}}$ plot similar to our modeled LMO cumulate layers (**Figure 2.12c**).

Figure 2.12. Comparison of measured and modeled isotopic compositions for lunar mantle sources. Panels (a) and (b) compare the trace element ratios and age-corrected isotope ratios in the same lunar samples. $(^{147}Sm/^{144}Nd)_i$ and $(^{176}Lu/^{177}Hf)_i$ represent the initial isotopic ratio of the lunar samples. Panel (c) compares the calculated isotopic compositions for lunar basalt sources and modeled isotopic compositions for lunar magma ocean cumulates. The initial isotopic composition of the Moon is assumed to be chondritic, and the values of Bouvier et al. (2008) are used in this study. The isotopic model assumes that each reservoir had a chondritic isotope composition at ~4.4 Ga. Evolution lines demonstrate the isotopic evolution of each source over 800 Myr following its formation. Tick marks on each evolution trend correlate with the ages shown along the Layer #6 evolution line. The thick black evolution line represents thickened IBC #2 if no hybridization with the EMOC (i.e., Layer #1) occurs. Panel (d) compares the calculated isotopic compositions for lunar basalt sources and modeled isotopic compositions for hybridized lunar mantle sources following cumulate overturn. Hybridized source lines demonstrate the effect of early cumulate mixing on the isotopic compositions of hybridized mantle sources. IBC #1 assumes no early cumulate mixing, IBC #2 assumes early cumulate mixing between cumulates that form between 88% to 100% LMO solidification, and IBC #3 assumes early cumulate mixing between cumulates that form between 95% to 100% LMO solidification. Small black symbols represent the calculated ε_{Nd} and ε_{Hf} composition of the sources based on measurements from previous studies. Data plotted include mare basalts (Unruh et al., 1984; Beard et al., 1998; Sprung et al., 2013; Borg et al., 2019), KREEP basalts (Sprung et al., 2013; Gaffney and Borg, 2014), Ferroan Anorthosites (FAN) (Boyet et al., 2015; Borg et al., 2019; Marks et al., 2019; Sio et al., 2020; Borg et al., 2020), and Mg-Suite (Carlson et al., 2014; Gaffney and Borg, 2014; Borg et al., 2020) samples. Panels (a) and (b) demonstrate that the trace element and age-corrected isotope ratios of mantle sources for lunar samples strongly correlate, indicating that the process controlling their trace element composition also controls their initial isotopic ratios. Panel (c) demonstrates that LMO cumulate layers would generate a similar fanning pattern to the lunar basalt samples. Panel (d) demonstrates that mantle hybridization processes like those explored in this study could generate similar isotopic trends to the high-Ti lunar basalt samples.


y = 0.157x - 0.0007
R² = 0.9991
a.
Lu/Hf
y = 0.6162x + 0.001
R² = 0.9993
b.
Sm/Nd
LMO Cumulates
Layer#1
Layer#2
Layer#3
Layer#4
Layer#5
Layer#6
Low-Ti Basalts
High-Ti Basalts
KREEP Basalts
Mg-Suite
Thickened IBC #2
(No Hybridization)
4.4 Ga
4.2 Ga
3.9 Ga
3.6 Ga
c.
Hybridized Sources
Thin IBC #1
(Mix: 80% EMOC, 20% IBC)
Thickened IBC #2
(Mix: 55% EMOC, 45% IBC)
Thickened IBC #2
(Mix: 95% EMOC, 5% IBC)
Thickened IBC #2
(Mix: 97.5% EMOC, 2.5% IBC)
Thickened IBC #3
(Mix: 75% EMOC, 25% IBC)
4.4 Ga
4.2 Ga
3.9 Ga
3.6 Ga
d.

Low-Ti mare basalt sources fall between the evolution lines for the first three cumulate layers, while some high-Ti basalt sources fall along the evolution line for layers #2, #4, and #5. Most high-Ti basalt source values fall below the evolution line for layer #5 (i.e., the layer before the IBC). Models demonstrate that mixing between evolved cumulates from layer #6 (i.e., the thin IBC) or a thickened IBC layer and EMOC material (i.e., Layer #1) shift the trend of a hybridized source toward that observed in the high-Ti mare basalt samples (**Figure 2.12d**). The IBC isotope signature will dominate the hybridized source signature owing to the REE and Hf-rich nature of the late crystallizing LMO cumulates. In **Figure 2.12d**, several cases are tested: those where IBC are thickened by early cumulate sinking (as in Scenarios #6 and #7) (Thickened IBC #2), and cases where the IBC layers are produced by fractional crystallization (as in Scenarios #1-#5) (Thin IBC #1) (**Figure 2.12c-d**). The results demonstrate that many hybridization scenarios for these cases could produce the Sm-Nd and Lu-Hf isotopic ratios of the high-Ti mare basalts (**Figure 2.12c**).

2.7 Conclusions

This work attempts to constrain processes producing the geochemical characteristics of lunar picritic glasses using trace element geochemical models. Using experimentally determined LMO cumulate solidification sequences and up-to-date lunar trace element partition coefficients, we model chemical fractionation during LMO solidification, mantle hybridization, and partial melting. Geochemical models of LMO solidification demonstrate that the early-crystallizing cumulates have relatively REE-poor compositions with respect to the lunar picritic glasses and late-crystallizing LMO

cumulates. The LMO solidification models also indicate that LMO residual liquids do not have slopes consistent with KREEP basalts and other lunar materials with a KREEPy signature, implying that assimilation models would fail to produce “KREEP”. The partial melting of LMO cumulate layers or hybridized sources is consistent with samples with KREEPy character. Models testing partial melting of LMO cumulates containing plagioclase suggest that these melts would have the wrong sign of Eu anomaly if plagioclase abundance is elevated in the basalt source cumulates. Thus, plagioclase floatation must be >90% efficient to explain the REE patterns of high-Ti mafic lunar samples.

LMO cumulate melting models demonstrate that partial melting of the primary (i.e., unhybridized) LMO cumulates cannot account for the HREE-depleted compositions of intermediate- and high-Ti lunar picritic glasses. The elevated Ti and REE compositions correlated with the relatively Mg-rich composition of some lunar picritic glasses is evidence of interaction between late-crystallizing (i.e., shallow) and early-crystallizing (i.e., deep) LMO mantle cumulates. Such interactions would be produced by lunar cumulate mantle overturn events, which bring ilmenite-bearing cumulate materials that crystallized from the late LMO into the lunar interior.

The implications for such overturn events for the mineralogy of the lunar mantle were explored in thermodynamic simulations. Garnet stabilization in downwelling IBC material would occur at pressures above ~2 GPa during lunar cumulate overturn events. Partial melting models demonstrate that the HREE-depleted composition of the high-Ti lunar orange glass samples is consistent with a garnet-bearing mantle source. These

models suggest that the location of garnet formation (i.e., in downwelling IBC that fertilizes mantle sources or in the hybridized mantle sources themselves) is less important than the overall abundance of garnet with respect to the generation of HREE-depleted melts.

We explored different mantle hybridization scenarios involving combinations of IBC and early LMO cumulates. Models show that ~0.25-5% garnet would be required to account for the HREE depletion in lunar orange glasses. This is generally consistent with thermodynamic models of a metamorphosed IBC, assuming 90-95% plagioclase floatation during crustal formation. Model parameters and mixing proportions for the hybridization scenarios tested in this study explain multiple geochemical features in high-Ti lunar samples, i.e., their REE enrichment, HFSE enrichment, Eu depletion, HREE depletion, and elevated Mg# relative to high-Ti LMO cumulates as well as their Nd and Hf isotopic compositions. We argue that the orange picritic glasses' garnet signature and high-Ti composition are strong evidence of cumulate overturn during the early lunar formation and differentiation process.

2.8 Acknowledgements

This work was supported by NASA Solar System Workings award 80NSSC20K0467 to ND and a Tennessee Fellowship for Graduate Excellence to JS.

2.9 Open Research Statement

An example of our MATLAB script, which may be used to model trace element fractionation during LMO solidification has been published on Zenodo (Scholpp and Dygert, 2024b). https://doi.org/10.5281/zenodo.14172014

References

Anders, E., and Grevesse, N., 1989, Abundances of the elements: Meteoritic and solar: Geochimica et Cosmochimica Acta, v. 53, p. 197–214, doi:10.1016/0016-7037(89)90286-X.

Baker, M.B., and Stolper, E.M., 1994, Determining the composition of high-pressure mantle melts using diamond aggregates: Geochimica et Cosmochimica Acta, v. 58, p. 2811–2827, doi:10.1016/0016-7037(94)90116-3.

Barr, J.A., and Grove, T.L., 2013, Experimental petrology of the Apollo 15 group A green glasses: Melting primordial lunar mantle and magma ocean cumulate assimilation: Geochimica et Cosmochimica Acta, v. 106, p. 216–230, doi:10.1016/j.gca.2012.12.035.

Beard, B.L., Taylor, L.A., Scherer, E.E., Johnson, C.M., and Snyder, G.A., 1998, The Source Region and Melting Mineralogy of High-Titanium and Low-Titanium Lunar Basalts Deduced from Lu-Hf Isotope Data: Geochimica et Cosmochimica Acta, v. 62, p. 525–544, doi:10.1016/S0016-7037(97)00373-6.

Borg, L.E., and Carlson, R.W., 2023, The evolving chronology of moon formation: Annual Review of Earth and Planetary Sciences, v. 51, p. 25–52.

Borg, L.E., Cassata, W.S., Wimpenny, J., Gaffney, A.M., and Shearer, C.K., 2020, The formation and evolution of the Moon's crust inferred from the Sm-Nd isotopic systematics of highlands rocks: Geochimica et Cosmochimica Acta, v. 290, p. 312–332, doi:10.1016/j.gca.2020.09.013.

Borg, L.E., Gaffney, A.M., Kruijer, T.S., Marks, N.A., Sio, C.K., and Wimpenny, J., 2019, Isotopic evidence for a young lunar magma ocean: Earth and Planetary Science Letters, v. 523, p. 115706, doi:10.1016/j.epsl.2019.07.008.

Bouvier, A., Vervoort, J.D., and Patchett, P.J., 2008, The Lu–Hf and Sm–Nd isotopic composition of CHUR: Constraints from unequilibrated chondrites and implications for the bulk composition of terrestrial planets: Earth and Planetary Science Letters, v. 273, p. 48–57, doi:10.1016/j.epsl.2008.06.010.

Boyet, M., Carlson, R.W., Borg, L.E., and Horan, M., 2015, Sm–Nd systematics of lunar ferroan anorthositic suite rocks: Constraints on lunar crust formation: Geochimica et Cosmochimica Acta, v. 148, p. 203–218, doi:10.1016/j.gca.2014.09.021.

Brey, G.P., Girnis, A.V., Bulatov, V.K., Höfer, H.E., Gerdes, A., and Woodland, A.B., 2015, Reduced sediment melting at 7.5–12 GPa: phase relations, geochemical signals and diamond nucleation: Contributions to Mineralogy and Petrology, v. 170, p. 18, doi:10.1007/s00410-015-1166-z.

Brown, S.M., and Grove, T.L., 2015, Origin of the Apollo 14, 15, and 17 yellow ultramafic glasses by mixing of deep cumulate remelts: Geochimica et Cosmochimica Acta, v. 171, p. 201–215, doi:10.1016/j.gca.2015.09.001.

Cano, E.J., Sharp, Z.D., and Shearer, C.K., 2020, Distinct oxygen isotope compositions of the Earth and Moon: Nature Geoscience, v. 13, p. 270–274, doi:10.1038/s41561-020-0550-0.

Canup, R.M., 2012, Forming a Moon with an Earth-like Composition via a Giant Impact: Science, v. 338, p. 1052, doi:10.1126/science.1226073.

Canup, R.M., 2004, Origin of the terrestrial planets and the Earth-Moon system: Physics Today, v. 57, p. 56–62.

Carlson, R.W., Borg, L.E., Gaffney, A.M., and Boyet, M., 2014, Rb-Sr, Sm-Nd and Lu-Hf isotope systematics of the lunar Mg-suite: the age of the lunar crust and its relation to the time of Moon formation: Philosophical Transactions of the Royal Society A: Mathematical, Physical and Engineering Sciences, v. 372, p. 20130246, doi:10.1098/rsta.2013.0246.

Charlier, B., Grove, T.L., Namur, O., and Holtz, F., 2018, Crystallization of the lunar magma ocean and the primordial mantle-crust differentiation of the Moon: Geochimica et Cosmochimica Acta, v. 234, p. 50–69, doi:10.1016/j.gca.2018.05.006.

Cherniak, D.J., 2010, REE diffusion in olivine: American Mineralogist, v. 95, p. 362–368, doi:10.2138/am.2010.3345.

Cherniak, D.J., and Liang, Y., 2007, Rare earth element diffusion in natural enstatite: Geochimica et Cosmochimica Acta, v. 71, p. 1324–1340, doi:10.1016/j.gca.2006.12.001.

Cohen, L.H., Ito, K., and Kennedy, G.C., 1967, Melting and phase relations in an anhydrous basalt to 40 kilobars: American Journal of Science, v. 265, p. 475, doi:10.2475/ajs.265.6.475.

Dalou, C., Koga, K.T., Shimizu, N., Boulon, J., and Devidal, J.-L., 2012, Experimental determination of F and Cl partitioning between lherzolite and basaltic melt:

Contributions to Mineralogy and Petrology, v. 163, p. 591–609, doi:10.1007/s00410-011-0688-2.

Delano, J.W., 1980, Chemistry and liquidus phase relations of Apollo 15 red glass: implications for the deep lunar interior.: Lunar and Planetary Science Conference Proceedings, v. 1, p. 251–288.

Delano, J.W., 1986, Pristine lunar glasses: Criteria, data, and implications: Journal of Geophysical Research: Solid Earth, v. 91, p. 201–213, doi:10.1029/JB091iB04p0D201.

Draper, D.S., duFrane, S.A., Shearer, C.K., Dwarzski, R.E., and Agee, C.B., 2006, High-pressure phase equilibria and element partitioning experiments on Apollo 15 green C picritic glass: Implications for the role of garnet in the deep lunar interior: Geochimica et Cosmochimica Acta, v. 70, p. 2400–2416, doi:10.1016/j.gca.2006.01.027.

Dygert, N., Draper, D.S., Rapp, J.F., Lapen, T.J., Fagan, A.L., and Neal, C.R., 2020, Experimental determinations of trace element partitioning between plagioclase, pigeonite, olivine, and lunar basaltic melts and an fO2 dependent model for plagioclase-melt Eu partitioning: Geochimica et Cosmochimica Acta, v. 279, p. 258–280, doi:10.1016/j.gca.2020.03.037.

Dygert, N., Liang, Y., and Hess, P., 2013, The importance of melt TiO2 in affecting major and trace element partitioning between Fe–Ti oxides and lunar picritic glass melts: Geochimica et Cosmochimica Acta, v. 106, p. 134–151, doi:10.1016/j.gca.2012.12.005.

Dygert, N., Liang, Y., Sun, C., and Hess, P., 2014, An experimental study of trace element partitioning between augite and Fe-rich basalts: Geochimica et Cosmochimica Acta, v. 132, p. 170–186, doi:10.1016/j.gca.2014.01.042.

Dygert, N., Lin, J.-F., Marshall, E.W., Kono, Y., and Gardner, J.E., 2017, A Low Viscosity Lunar Magma Ocean Forms a Stratified Anorthitic Flotation Crust With Mafic Poor and Rich Units: Geophysical Research Letters, v. 44, p. 11,282-11,291, doi:10.1002/2017GL075703.

Elardo, S.M., Draper, D.S., and Shearer, C.K., 2011, Lunar Magma Ocean crystallization revisited: Bulk composition, early cumulate mineralogy, and the source regions of the highlands Mg-suite: Geochimica et Cosmochimica Acta, v. 75, p. 3024–3045, doi:10.1016/j.gca.2011.02.033.

Elkins Tanton, L.T., Van Orman, J.A., Hager, B.H., and Grove, T.L., 2002, Re-examination of the lunar magma ocean cumulate overturn hypothesis: melting or mixing is required: Earth and Planetary Science Letters, v. 196, p. 239–249, doi:10.1016/S0012-821X(01)00613-6.

Elkins-Tanton, L.T., 2012, Magma Oceans in the Inner Solar System: Annual Review of Earth and Planetary Sciences, v. 40, p. 113–139, doi:10.1146/annurev-earth-042711-105503.

Elkins-Tanton, L.T., Burgess, S., and Yin, Q.-Z., 2011, The lunar magma ocean: Reconciling the solidification process with lunar petrology and geochronology: Earth and Planetary Science Letters, v. 304, p. 326–336, doi:10.1016/j.epsl.2011.02.004.

Elkins-Tanton, L.T., Chatterjee, N., and Grove, T.L., 2003, Experimental and petrological constraints on lunar differentiation from the Apollo 15 green picritic glasses: Meteoritics & Planetary Science, v. 38, p. 515–527, doi:10.1111/j.1945-5100.2003.tb00024.x.

Elkins-Tanton, L.T., and Hager, B.H., 2005, Giant meteoroid impacts can cause volcanism: Earth and Planetary Science Letters, v. 239, p. 219–232, doi:10.1016/j.epsl.2005.07.029.

Fabbrizio, A., Schmidt, M.W., and Petrelli, M., 2021, Effect of fO2 on Eu partitioning between clinopyroxene, orthopyroxene and basaltic melt: Development of a Eu3+/Eu2+ oxybarometer: Chemical Geology, v. 559, p. 119967, doi:10.1016/j.chemgeo.2020.119967.

Frost, B.R., 1991, Chapter 1.Introduction to oxygen fugacity and its petrologic importance, *in* Lindsley, D.H. ed., Petrologic and Magnetic Significance, Berlin, Boston, De Gruyter, p. 1–10, doi:doi:10.1515/9781501508684-004.

Gaetani, G.A., and Grove, T.L., 1995, Partitioning of rare earth elements between clinopyroxene and silicate melt Crystal-chemical controls: Geochimica et Cosmochimica Acta, v. 59, p. 1951–1962, doi:10.1016/0016-7037(95)00119-0.

Gaffney, A.M., and Borg, L.E., 2014, A young solidification age for the lunar magma ocean: Geochimica et Cosmochimica Acta, v. 140, p. 227–240, doi:10.1016/j.gca.2014.05.028.

Ghiorso, M.S., Hirschmann, M.M., Reiners, P.W., and Kress III, V.C., 2002, The pMELTS: A revision of MELTS for improved calculation of phase relations and

major element partitioning related to partial melting of the mantle to 3 GPa: Geochemistry, Geophysics, Geosystems, v. 3, p. 1–35.

Ghiorso, M.S., and Sack, R.O., 1995, Chemical mass transfer in magmatic processes IV. A revised and internally consistent thermodynamic model for the interpolation and extrapolation of liquid-solid equilibria in magmatic systems at elevated temperatures and pressures: Contributions to Mineralogy and Petrology, v. 119, p. 197–212, doi:10.1007/BF00307281.

Giguere, T.A., Taylor, G.J., Hawke, B.R., and Lucey, P.G., 2000, The titanium contents of lunar mare basalts: Meteoritics & Planetary Science, v. 35, p. 193–200, doi:10.1111/j.1945-5100.2000.tb01985.x.

Hallis, L.J., Anand, M., and Strekopytov, S., 2014, Trace-element modelling of mare basalt parental melts: Implications for a heterogeneous lunar mantle: Geochimica et Cosmochimica Acta, v. 134, p. 289–316, doi:10.1016/j.gca.2014.01.012.

Hart, S.R., and Zindler, A., 1986, In search of a bulk-Earth composition: Chemical Geology, v. 57, p. 247–267, doi:10.1016/0009-2541(86)90053-7.

Haskin, L.A., and Warren, P.H., 1991, Lunar chemistry., *in* Lunar sourcebook, v. 4, p. 357–474.

Haupt, C.P., Renggli, C.J., Rohrbach, A., Berndt, J., and Klemme, S., 2024, Experimental Constraints on the Origin of the Lunar High-Ti Basalts: Journal of Geophysical Research: Planets, v. 129, p. e2023JE008239, doi:10.1029/2023JE008239.

Hess, P.C., and Parmentier, E.M., 1995, A model for the thermal and chemical evolution of the Moon's interior: implications for the onset of mare volcanism: Earth and Planetary Science Letters, v. 134, p. 501–514, doi:10.1016/0012-821X(95)00138-3.

Hiesinger, H., and Head, J.W., III, 2006, New Views of Lunar Geoscience: An Introduction and Overview: Reviews in Mineralogy and Geochemistry, v. 60, p. 1–81, doi:10.2138/rmg.2006.60.1.

Hughes, S.S., Delano, J.W., and Schmitt, R.A., 1990, Chemistry of individual mare volcanic glasses: evidence for distinct regions of hybridized mantle and a KREEP component in Apollo 14 magmatic sources.: Lunar and Planetary Science Conference Proceedings, v. 20, p. 127–138.

Ji, D., and Dygert, N., 2023, Trace element partitioning between apatite and silicate melts: Effects of major element composition, temperature, and oxygen fugacity, and implications for the volatile element budget of the lunar magma ocean: Geochimica et Cosmochimica Acta, doi:10.1016/j.gca.2023.11.004.

Jing, J.-J., Lin, Y., Knibbe, J.S., and van Westrenen, W., 2022, Garnet stability in the deep lunar mantle: Constraints on the physics and chemistry of the interior of the Moon: Earth and Planetary Science Letters, v. 584, p. 117491, doi:10.1016/j.epsl.2022.117491.

Johnson, T.E., Morrissey, L.J., Nemchin, A.A., Gardiner, N.J., and Snape, J.F., 2021, The phases of the Moon: Modelling crystallisation of the lunar magma ocean through equilibrium thermodynamics: Earth and Planetary Science Letters, v. 556, p. 116721, doi:10.1016/j.epsl.2020.116721.

Jones, J.H., and Delano, J.W., 1989, A three-component model for the bulk composition of the moon: Geochimica et Cosmochimica Acta, v. 53, p. 513–527, doi:10.1016/0016-7037(89)90402-X.

van Kan Parker, M., Mason, P.R.D., and van Westrenen, W., 2011, Trace element partitioning between ilmenite, armalcolite and anhydrous silicate melt: Implications for the formation of lunar high-Ti mare basalts: Geochimica et Cosmochimica Acta, v. 75, p. 4179–4193, doi:10.1016/j.gca.2011.04.031.

Kinzler, R.J., and Grove, T.L., 1992, Primary magmas of mid-ocean ridge basalts 1. Experiments and methods: Journal of Geophysical Research: Solid Earth, v. 97, p. 6885–6906, doi:10.1029/91JB02840.

Klaver, M., Klemme, S., Liu, X.-N., Hin, R.C., Coath, C.D., Anand, M., Lissenberg, C.J., Berndt, J., and Elliott, T., 2024, Titanium-rich basaltic melts on the Moon modulated by reactive flow processes: Nature Geoscience, v. 17, p. 118–123, doi:10.1038/s41561-023-01362-5.

Klemme, S., Günther, D., Hametner, K., Prowatke, S., and Zack, T., 2006, The partitioning of trace elements between ilmenite, ulvospinel, armalcolite and silicate melts with implications for the early differentiation of the moon: Chemical Geology, v. 234, p. 251–263, doi:10.1016/j.chemgeo.2006.05.005.

Kraettli, G., Schmidt, M.W., and Liebske, C., 2022, Fractional crystallization of a basal lunar magma ocean: A dense melt-bearing garnetite layer above the core? Icarus, v. 371, p. 114699, doi:10.1016/j.icarus.2021.114699.

Krawczynski, M.J., and Grove, T.L., 2012, Experimental investigation of the influence of oxygen fugacity on the source depths for high titanium lunar ultramafic magmas: Geochimica et Cosmochimica Acta, v. 79, p. 1–19, doi:10.1016/j.gca.2011.10.043.

Li, W., Costa, F., Oppenheimer, C., and Nagashima, K., 2023, Volatile and trace element partitioning between apatite and alkaline melts: Contributions to Mineralogy and Petrology, v. 178, p. 9, doi:10.1007/s00410-022-01985-8.

Li, H., Zhang, N., Liang, Y., Wu, B., Dygert, N.J., Huang, J., and Parmentier, E.M., 2019, Lunar Cumulate Mantle Overturn: A Model Constrained by Ilmenite Rheology: Journal of Geophysical Research: Planets, v. 124, p. 1357–1378, doi:10.1029/2018JE005905.

Lin, Y., Tronche, E.J., Steenstra, E.S., and van Westrenen, W., 2017, Evidence for an early wet Moon from experimental crystallization of the lunar magma ocean: Nature Geoscience, v. 10, p. 14–18, doi:10.1038/ngeo2845.

Lin, Y., Tronche, E.J., Steenstra, E.S., and van Westrenen, W., 2016, Solidification Evolution of a Dry Lunar Magma Ocean: Constraints from Experimental Petrology: v. 47, p. 1296.

Longhi, J., 2003, A new view of lunar ferroan anorthosites: Postmagma ocean petrogenesis: Journal of Geophysical Research: Planets, v. 108.

Longhi, J., 2006, Petrogenesis of picritic mare magmas: Constraints on the extent of early lunar differentiation: A Special Issue Dedicated to Larry A. Haskin, v. 70, p. 5919–5934, doi:10.1016/j.gca.2006.09.023.

Longhi, J., Walker, D., Grove, T.L., Stolper, E.M., and Hays, J.F., 1974, The petrology of the Apollo 17 mare basalts.: Lunar and Planetary Science Conference Proceedings, v. 1, p. 447–469.

Lucey, P.G., Taylor, G.J., Hawke, B.R., and Spudis, P.D., 1998, FeO and TiO2 concentrations in the South Pole-Aitken basin: Implications for mantle composition and basin formation: Journal of Geophysical Research: Planets, v. 103, p. 3701–3708, doi:10.1029/97JE03146.

Mallik, A., Ejaz, T., Shcheka, S., and Garapic, G., 2019, A petrologic study on the effect of mantle overturn: Implications for evolution of the lunar interior: Geochimica et Cosmochimica Acta, v. 250, p. 238–250, doi:10.1016/j.gca.2019.02.014.

Marks, N.E., Borg, L.E., Shearer, C.K., and Cassata, W.S., 2019, Geochronology of an Apollo 16 Clast Provides Evidence for a Basin-Forming Impact 4.3 Billion Years Ago: Journal of Geophysical Research: Planets, v. 124, p. 2465–2481, doi:10.1029/2019JE005966.

McDonough, W.F., and Sun, S. -s., 1995, The composition of the Earth: Chemical Evolution of the Mantle, v. 120, p. 223–253, doi:10.1016/0009-2541(94)00140-4.

McIntosh, E.C., Day, J.M.D., McCubbin, F.M., Vander Kaaden, K.E., Hattingh, R., and Porrachia, M., 2024, Revisiting the Petrogenesis of Pyroclastic Glass Bead Deposits at the Apollo 15 and 17 Sites: Journal of Petrology, v. 65, p. egae026, doi:10.1093/petrology/egae026.

McKenzie, D., 2011, Compaction and Crystallization in Magma Chambers: Towards a Model of the Skaergaard Intrusion: Journal of Petrology, v. 52, p. 905–930, doi:10.1093/petrology/egr009.

Neal, C.R., 2001, Interior of the Moon: The presence of garnet in the primitive deep lunar mantle: Journal of Geophysical Research: Planets, v. 106, p. 27865–27885, doi:10.1029/2000JE001386.

Neal, C.R., Hacker, M.D., Snyder, G.A., Taylor, L.A., Liu, Y., and Schmitt, R.A., 1994, Basalt generation at the Apollo 12 site, Part 1: New data, classification, and re-evaluation: Meteoritics, v. 29, p. 334–348.

Neal, C.R., and Kramer, G.Y., 2003, The Composition of KREEP: A Detailed Study of KREEP Basalt 15386, *in* Mackwell, S. and Stansbery, E. eds., Lunar and Planetary Science Conference, Lunar and Planetary Science Conference, p. 2023.

O'Neill, H.St.C., 1991, The origin of the moon and the early history of the earth—A chemical model. Part 2: The earth: Geochimica et Cosmochimica Acta, v. 55, p. 1159–1172, doi:10.1016/0016-7037(91)90169-6.

O'Neill, H.St.C., and Pownceby, M.I., 1993, Thermodynamic data from redox reactions at high temperatures. I. An experimental and theoretical assessment of the electrochemical method using stabilized zirconia electrolytes, with revised values for the Fe-"FeO", Co-CoO, Ni-NiO and Cu-Cu2O oxygen buffers, and new data for the W-WO2 buffer: Contributions to Mineralogy and Petrology, v. 114, p. 296–314, doi:10.1007/BF01046533.

Papike, J.J., Ryder, G., and Shearer, C.K., 1998, Lunar samples: Reviews in Mineralogy and Geochemistry, v. 36, p. 5– 01.

Parmentier, E.M., Zhong, S., and Zuber, M.T., 2002, Gravitational differentiation due to initial chemical stratification: origin of lunar asymmetry by the creep of dense KREEP? Earth and Planetary Science Letters, v. 201, p. 473–480, doi:10.1016/S0012-821X(02)00726-4.

Pertermann, M., Hirschmann, M., Hametner, K., Günther, D., and Schmidt, M.W., 2004, Experimental determination of trace element partitioning between garnet and silica-rich liquid during anhydrous partial melting of MORB-like eclogite: Geochemistry, Geophysics, Geosystems, v. 5.

Presnall, D.C., Gudfinnsson, G.H., and Walter, M.J., 2002, Generation of mid-ocean ridge basalts at pressures from 1 to 7 GPa: Geochimica et Cosmochimica Acta, v. 66, p. 2073–2090, doi:10.1016/S0016-7037(02)00890-6.

Prowatke, S., and Klemme, S., 2006, Trace element partitioning between apatite and silicate melts: Geochimica et Cosmochimica Acta, v. 70, p. 4513–4527, doi:10.1016/j.gca.2006.06.162.

Rapp, J.F., and Draper, D.S., 2018, Fractional crystallization of the lunar magma ocean: Updating the dominant paradigm: Meteoritics & Planetary Science, v. 53, p. 1432–1455, doi:10.1111/maps.13086.

Ringwood, A.E., and Kesson, S.E., 1976, A dynamic model for mare basalt petrogenesis, *in* Lunar and Planetary Science Conference Proceedings, v. 7, p. 1697–1722.

Schmidt, M.W., and Kraettli, G., 2022, Experimental Crystallization of the Lunar Magma Ocean, Initial Selenotherm and Density Stratification, and Implications for Crust Formation, Overturn and the Bulk Silicate Moon Composition: Journal of Geophysical Research: Planets, v. 127, p. e2022JE007187, doi:10.1029/2022JE007187.

Scholpp, J.L., and Dygert, N.J., 2024a, A Geochemical Model for Lunar Magma Ocean Solidification:, https://doi.org/10.5281/zenodo.14172014.

Scholpp, J.L., and Dygert, N., 2024b, Experimental insights into the mineralogy and melt-rock reactions produced by lunar cumulate mantle overturn: Contributions to Mineralogy and Petrology, v. 179, p. 58, doi:10.1007/s00410-024-02134-z.

Shearer, C.K. et al., 2006, Thermal and Magmatic Evolution of the Moon: Reviews in Mineralogy and Geochemistry, v. 60, p. 365–518, doi:10.2138/rmg.2006.60.4.

Shearer, C.K., Elardo, S.M., Petro, N.E., Borg, L.E., and McCubbin, F.M., 2015, Origin Of The Lunar Highlands Mg-Suite: An Integrated Petrology, Geochemistry, Chronology, And Remote Sensing Perspective: v. 100, p. 294–325, doi:10.2138/am-2015-4817.

Shearer, C.K., and Papike, J.J., 1993, Basaltic magmatism on the Moon: A perspective from volcanic picritic glass beads: Geochimica et Cosmochimica Acta, v. 57, p. 4785–4812, doi:10.1016/0016-7037(93)90200-G.

Shearer, C.K., Papike, J.J., Galbreath, K.C., and Shimizu, N., 1991, Exploring the lunar mantle with secondary ion mass spectrometry: a comparison of lunar picritic glass

beads from the Apollo 14 and Apollo 17 sites: Earth and Planetary Science Letters, v. 102, p. 134–147, doi:10.1016/0012-821X(91)90003-Z.

Shepherd, K., Namur, O., Toplis, M.J., Devidal, J.-L., and Charlier, B., 2022, Trace element partitioning between clinopyroxene, magnetite, ilmenite and ferrobasaltic to dacitic magmas: an experimental study on the role of oxygen fugacity and melt composition: Contributions to Mineralogy and Petrology, v. 177, p. 90, doi:10.1007/s00410-022-01957-y.

Singletary, S., and Grove, T., 2008, Origin of lunar high-titanium ultramafic glasses: A hybridized source? Earth and Planetary Science Letters, v. 268, p. 182–189, doi:10.1016/j.epsl.2008.01.019.

Sio, C.K., Borg, L.E., and Cassata, W.S., 2020, The timing of lunar solidification and mantle overturn recorded in ferroan anorthosite 62237: Earth and Planetary Science Letters, v. 538, p. 116219, doi:10.1016/j.epsl.2020.116219.

Snape, J.F., Nemchin, A.A., Johnson, T., Luginbühl, S., Berndt, J., Klemme, S., Morrissey, L.J., and van Westrenen, W., 2022, Experimental constraints on the long-lived radiogenic isotope evolution of the Moon: Geochimica et Cosmochimica Acta, v. 326, p. 119–148, doi:10.1016/j.gca.2022.04.008.

Snyder, G.A., Neal, C.R., Taylor, L.A., and Halliday, A.N., 1997, Anatexis of lunar cumulate mantle in time and space: Clues from trace-element, strontium, and neodymium isotopic chemistry of parental Apollo 12 basalts: Geochimica et Cosmochimica Acta, v. 61, p. 2731–2747, doi:10.1016/S0016-7037(97)00082-3.

Snyder, G.A., Taylor, L.A., and Neal, C.R., 1992, Combined equilibrium and fractional crystallization of a magma ocean and formation of the upper mantle of the Moon, *in* Lunar and Planetary Science Conference, v. 23.

Solomatov, V.S., and Stevenson, D.J., 1993, Kinetics of crystal growth in a terrestrial magma ocean: Journal of Geophysical Research: Planets, v. 98, p. 5407–5418.

Solomon, S.C., and Longhi, J., 1977, Magma oceanography: 1. Thermal evolution.: Lunar and Planetary Science Conference Proceedings, v. 1, p. 583–599.

Springer, W., and Seck, H.A., 1997, Partial fusion of basic granulites at 5 to 15 kbar: implications for the origin of TTG magmas: Contributions to Mineralogy and Petrology, v. 127, p. 30–45, doi:10.1007/s004100050263.

Sprung, P., Kleine, T., and Scherer, E.E., 2013, Isotopic evidence for chondritic Lu/Hf and Sm/Nd of the Moon: Earth and Planetary Science Letters, v. 380, p. 77–87, doi:10.1016/j.epsl.2013.08.018.

Suckale, J., Elkins-Tanton, L.T., and Sethian, J.A., 2012, Crystals stirred up: 2. Numerical insights into the formation of the earliest crust on the Moon: Journal of Geophysical Research: Planets, v. 117, doi:10.1029/2012JE004067.

Sun, C., Graff, M., and Liang, Y., 2017, Trace element partitioning between plagioclase and silicate melt: The importance of temperature and plagioclase composition, with implications for terrestrial and lunar magmatism: Geochimica et Cosmochimica Acta, v. 206, p. 273–295, doi:10.1016/j.gca.2017.03.003.

Sun, C., and Liang, Y., 2013a, Distribution of REE and HFSE between low-Ca pyroxene and lunar picritic melts around multiple saturation points: Geochimica et Cosmochimica Acta, v. 119, p. 340–358, doi:10.1016/j.gca.2013.05.036.

Sun, C., and Liang, Y., 2013b, The importance of crystal chemistry on REE partitioning between mantle minerals (garnet, clinopyroxene, orthopyroxene, and olivine) and basaltic melts: Chemical Geology, v. 358, p. 23–36, doi:10.1016/j.chemgeo.2013.08.045.

Taylor, S.R., 1982, Planetary science: A lunar perspective: Lunar and Planetary Institute Houston, v. 3303.

Taylor, S.R., and Bence, A.E., 1975, Evolution of the lunar highland crust.: Lunar and Planetary Science Conference Proceedings, v. 1, p. 1121–1141.

Taylor, G.J., and Wieczorek, M.A., 2014, Lunar bulk chemical composition: a post-Gravity Recovery and Interior Laboratory reassessment: Philosophical Transactions of the Royal Society A: Mathematical, Physical and Engineering Sciences, v. 372, p. 20130242, doi:10.1098/rsta.2013.0242.

Thacker, C., Liang, Y., Peng, Q., and Hess, P., 2009, The stability and major element partitioning of ilmenite and armalcolite during lunar cumulate mantle overturn: Geochimica et Cosmochimica Acta, v. 73, p. 820–836, doi:10.1016/j.gca.2008.10.038.

Thiemens, M.M., Sprung, P., Fonseca, R.O.C., Leitzke, F.P., and Münker, C., 2019, Early Moon formation inferred from hafnium–tungsten systematics: Nature Geoscience, v. 12, p. 696–700, doi:10.1038/s41561-019-0398-3.

Unruh, D.M., Stille, P., Patchett, P.J., and Tatsumoto, M., 1984, Lu-Hf and Sm-Nd evolution in lunar mare basalts: Journal of Geophysical Research: Solid Earth, v. 89, p. B459–B477, doi:10.1029/JB089iS02p0B459.

Van Orman, J.A., and Grove, T.L., 2000, Origin of lunar high-titanium ultramafic glasses: Constraints from phase relations and dissolution kinetics of clinopyroxene-ilmenite cumulates: Meteoritics & Planetary Science, v. 35, p. 783–794, doi:10.1111/j.1945-5100.2000.tb01462.x.

Wagner, T.P., and Grove, T.L., 1997, Experimental constraints on the origin of lunar high-Ti ultramafic glasses: Geochimica et Cosmochimica Acta, v. 61, p. 1315–1327, doi:10.1016/S0016-7037(96)00387-0.

Walker, D., and Hays, J.F., 1977, Plagioclase flotation and lunar crust formation: Geology, v. 5, p. 425–428, doi:10.1130/0091-7613(1977)5<425:PFALCF>2.0.CO;2.

Walter, M.J., 1998, Melting of Garnet Peridotite and the Origin of Komatiite and Depleted Lithosphere: Journal of Petrology, v. 39, p. 29–60, doi:10.1093/petroj/39.1.29.

Wänke, H., and Dreibus, G., 1982, Chemical and isotopic evidence for the early history of the Earth-Moon system, *in* Springer, p. 322–344.

Warren, P.H., 2005, "New" lunar meteorites: Implications for composition of the global lunar surface, lunar crust, and the bulk Moon: Meteoritics & Planetary Science, v. 40, p. 477–506, doi:10.1111/j.1945-5100.2005.tb00395.x.

Warren, P.H., and Wasson, J.T., 1979, The origin of KREEP: Reviews of Geophysics, v. 17, p. 73–88, doi:10.1029/RG017i001p00073.

Wieczorek, M.A. et al., 2006, The Constitution and Structure of the Lunar Interior: Reviews in Mineralogy and Geochemistry, v. 60, p. 221–364, doi:10.2138/rmg.2006.60.3.

Wieczorek, M.A. et al., 2013, The Crust of the Moon as Seen by GRAIL: Science, v. 339, p. 671–675, doi:10.1126/science.1231530.

Wood, J.A., Dickey Jr, J.S., Marvin, U.B., and Powell, B.N., 1970, Lunar anorthosites and a geophysical model of the moon: Geochimica et Cosmochimica Acta Supplement, v. 1, p. 965.

Yao, L., and Liang, Y., 2012, An Experimental Study of the Solidus of a Hybrid Lunar Cumulate Mantle: Implications for the Temperature at the Core-Mantle Boundary of the Moon, *in* 43rd Annual Lunar and Planetary Science Conference, Lunar and Planetary Science Conference, p. 2258.

Young, E.D., Kohl, I.E., Warren, P.H., Rubie, D.C., Jacobson, S.A., and Morbidelli, A., 2016, Oxygen isotopic evidence for vigorous mixing during the Moon-forming giant impact: Science, v. 351, p. 493, doi:10.1126/science.aad0525.

Zhang, N., Dygert, N., Liang, Y., and Parmentier, E.M., 2017, The effect of ilmenite viscosity on the dynamics and evolution of an overturned lunar cumulate mantle: Geophysical Research Letters, v. 44, p. 6543–6552, doi:10.1002/2017GL073702.

Appendix B

Table B1. Phase proportions in LMO mantle cumulates based on findings from Charlier et al. (2018), assuming 80% plagioclase and 100% quartz floatation efficiency.

Phases	Stage 1	Stage 2	Stage 3	Stage 4	Stage 5	Stage 6
Ol	0.990	0.099	0.083	0.000	0.000	0.352
Opx	0.000	0.891	0.331	0.000	0.000	0.000
Cpx	0.000	0.000	0.000	0.322	0.367	0.281
Pig	0.000	0.000	0.413	0.515	0.459	0.000
Plag	0.000	0.000	0.164	0.153	0.164	0.146
Qtz	0.000	0.000	0.000	0.000	0.000	0.000
Ilm	0.000	0.000	0.000	0.000	0.000	0.211
Melt	0.010	0.010	0.010	0.010	0.010	0.010

*Stage 1: F= 1-0.49, Stage 2: F= 0.49-0.22, Stage 3: F= 0.22-0.19, Stage 4: F= 0.19-0.05, Stage 5: F= 0.05-0.02, Stage 6: F= 0.02-0

Olivine (Ol), Orthopyroxene (Opx), Clinopyroxene (Cpx), Pigeonite (Pig), Plagioclase (Plag), Ilmenite (Ilm), Quartz (Qtz)

Table B2. Phase proportions in LMO mantle cumulates based on findings from Charlier et al. (2018), assuming 90% plagioclase and 100% quartz floatation efficiency.

Phases	Stage 1	Stage 2	Stage 3	Stage 4	Stage 5	Stage 6
Ol	0.990	0.099	0.090	0.000	0.000	0.380
Opx	0.000	0.891	0.360	0.000	0.000	0.000
Cpx	0.000	0.000	0.000	0.349	0.400	0.304
Pig	0.000	0.000	0.450	0.558	0.500	0.000
Plag	0.000	0.000	0.089	0.083	0.089	0.079
Qtz	0.000	0.000	0.000	0.000	0.000	0.000
Ilm	0.000	0.000	0.000	0.000	0.000	0.228
Melt	0.010	0.010	0.010	0.010	0.010	0.010

*Stage 1: F= 1-0.49, Stage 2: F= 0.49-0.22, Stage 3: F= 0.22-0.19, Stage 4: F= 0.19-0.05, Stage 5: F= 0.05-0.02, Stage 6: F= 0.02-0

Olivine (Ol), Orthopyroxene (Opx), Clinopyroxene (Cpx), Pigeonite (Pig), Plagioclase (Plag), Ilmenite (Ilm), Quartz (Qtz)

Table B3. Phase proportions in LMO mantle cumulates based on findings from Charlier et al. (2018), assuming 98% plagioclase and 100% quartz floatation efficiency.

Phases	Stage 1	Stage 2	Stage 3	Stage 4	Stage 5	Stage 6
Ol	0.990	0.099	0.097	0.000	0.000	0.405
Opx	0.000	0.891	0.388	0.000	0.000	0.000
Cpx	0.000	0.000	0.000	0.374	0.431	0.324
Pig	0.000	0.000	0.485	0.598	0.539	0.000
Plag	0.000	0.000	0.019	0.018	0.019	0.017
Qtz	0.000	0.000	0.000	0.000	0.000	0.000
Ilm	0.000	0.000	0.000	0.000	0.000	0.243
Melt	0.010	0.010	0.010	0.010	0.010	0.010

*Stage 1: F= 1-0.49, Stage 2: F= 0.49-0.22, Stage 3: F= 0.22-0.19, Stage 4: F= 0.19-0.05, Stage 5: F= 0.05-0.02, Stage 6: F= 0.02-0

Olivine (Ol), Orthopyroxene (Opx), Clinopyroxene (Cpx), Pigeonite (Pig), Plagioclase (Plag), Ilmenite (Ilm), Quartz (Qtz)

Table B4. Estimated major element compositions of hybridized mantle sources assuming mechanical mixing of unmelted IBC and EMOC components.

	Hybridized Mantle Source #1			Hybridized Mantle Source #2		
Floatation Efficiency	80%	90%	98%	80%	90%	98%
(wt%)						
SiO_2	38.47	38.04	37.65	44.68	44.70	44.72
TiO_2	3.32	3.58	3.83	0.92	0.99	1.06
Al_2O_3	1.32	0.80	0.33	3.67	2.42	1.24
Cr_2O_3	0.22	0.22	0.23	0.21	0.22	0.22
FeO	15.68	16.48	17.22	13.43	14.29	15.11
MnO	0.17	0.18	0.19	0.16	0.17	0.18
MgO	39.36	39.47	39.57	31.85	32.58	33.27
CaO	1.35	1.16	0.98	4.93	4.54	4.17
Na_2O	0.10	0.05	0.01	0.15	0.08	0.02
K_2O	0.01	0.00	0.00	0.01	0.00	0.00
Total	100.00	100.00	100.00	100.00	100.00	100.00
Mg#	81.74	81.02	80.38	80.87	80.25	79.70

Major element compositions were estimated using the modal mineral proportions from models in this study and experimental mineral compositions from and Elardo et al. (2011) and Charlier et al. (2018).

Hybridized Mantle Source #1 was estimated assuming mechanical mixing between IBC #1 (Table 2.4.) and EMOC (i.e., olivine from experiment LPUM 2.015 in Elardo et al. (2011)).

Hybridized Mantle Source #2 was estimated assuming mechanical mixing between IBC #2 (Table 2.4.) and EMOC (i.e., olivine from experiment LPUM 2.015 in Elardo et al. (2011)).

Estimates for scenarios that assume no pre-overturn mixing occurs (i.e., Hybridized Mantle Source #1), assume that the hybridized source is composed of an 80% EMOC to 20% IBC mixture.

Estimates for scenarios that assume pre-overturn mixing occurs (i.e., Hybridized Mantle Source #2), assume that the hybridized source is composed of a 55% EMOC to 45% IBC mixture.

Early-Crystallizing Magma Ocean Cumulate (EMOC)

Lattice Strain Partitioning Model Development Methods and fO_2 Dependent Eu Approximation

To determine how oxygen fugacity (fO_2) affects the partitioning behavior of Eu in olivine and ilmenite, we need to estimate the Eu^{2+} partition coefficient ($D_{Eu^{2+}}$). To approximate the partitioning behavior of divalent Eu in olivine and ilmenite, we use the lattice strain model (Brice, 1975; Blundy and Wood, 1994; Wood and Blundy, 1997):

$$D_j = D_0 \exp\left(\frac{-4\pi E N_A}{RT}\left(\frac{r_0}{2}\left(r_0 - r_j\right)^2 - \frac{1}{3}\left(r_0 - r_j\right)^3\right)\right) \quad \text{(B1)}$$

where D_j is the mineral-melt partition coefficient of element j; D_0 is the partition coefficient for a strain-free substitution; r_0 is the ideal ionic radius for the lattice site; r_j is the ionic radius of the given divalent element (i.e., Mg, Mn, Fe, Ca, etc…); E is the effective Young's modulus of the lattice site; N_A is Avogadro's number; R is the gas constant; and T is the temperature. For both olivine and ilmenite, we use the sixfold ionic radius for divalent ions (Shannon, 1976). To develop the divalent element partitioning models for olivine and ilmenite, we used methods similar to those of Sun and Liang (2013) and compiled large datasets of experimentally determined partitioning data (**Figures B1a and B2a**). For olivine and ilmenite, we fit Eq. (B1) to two or three experiments at a given P-T condition to obtain parameters for D_0, r_0, and E by using nonlinear least squares method to minimize the Chi-square (χ^2) defined below.

$$\chi^2 = \sum_{j=1}^{N} (lnD_j - lnD_j^m)^2, \quad \text{(B2)}$$

where D_j is defined by Eq. (B1); D_j^m is the measured mineral-melt partition coefficient for element j; N is the total number of measured partitioning data used in the fit to the lattice strain model.

These models demonstrate that the D_0 for both olivine and ilmenite is well correlated with the P-T conditions of the experiments, while r_0 and E are relatively consistent regardless of the P-T conditions. Using these observations, we found that the lattice strain parameters D_0, r_0, and E for divalent element partitioning into olivine can be described using the following expressions:

$$\ln D_0^{ol} = a_0^{ol} + a_1^{ol}\left(\frac{10000}{RT}\right) + a_2^{ol}P, \tag{B3}$$

$$r_0^{ol} = a_3^{ol}, \tag{B4}$$

$$E^{ol} = a_4^{ol}, \tag{B5}$$

and the parameters of D_0, r_0, and E for divalent element partitioning into ilmenite can be described using the expressions:

$$\ln D_0^{ilm} = a_0^{ilm} + a_1^{ilm}P\left(\frac{10000}{RT}\right), \tag{B6}$$

$$r_0^{ilm} = a_2^{ilm}, \tag{B7}$$

$$E^{ilm} = a_3^{ilm}, \tag{B8}$$

where P is the pressure (GPa) of crystallization and coefficients $(a_0^{min}, a_1^{min}, \dots, a_4^{min})$ are constants for the respective minerals. Coefficients $(a_0^{min}, a_1^{min}, \dots, a_4^{min})$ were determined using nonlinear least squared regression analysis for olivine and ilmenite by substituting Eqs. (B3)-(B5) and (B6)-(B8) into Eq. (B1), respectively (coefficients reported in **Figures B1a and B2a**). We inverted all coefficients simultaneously through a global inversion of 496 filtered data for olivine and 101 filtered data for ilmenite. As noted by Sun and Liang (2013), the absolute values of the Chi-square Eq. (B2) are

dependent on the number of data used in the inversion, so to better assess the goodness of fit, we calculated the Pearson's Chi-square (χ_P^2):

$$\chi_P^2 = \sum_{j=1}^{N} \frac{(D_j - D_j^m)^2}{D_j}, \quad \text{(B9)}$$

The olivine and ilmenite models for divalent element partitioning were used to estimate the Eu^{2+} partition coefficient ($D_{Eu^{2+}}$) for a sixfold ionic radius (1.17 Å; Shannon, 1976) (see **Figures B1b and B2b** for a schematic). Using the same P-T conditions as the trivalent elements partitioning models within the main text (**Tables 2.2 and 2.6**), we estimated the Eu^{2+} partition coefficients for the modeled olivine and ilmenite (**Figures B1c and B2c**). Using the calculated Eu^{3+} and Eu^{2+} partition coefficients (i.e., $D_{Eu^{3+}}$ and $D_{Eu^{2+}}$) we calculated the combined Eu partition coefficient (D_{Eu}) using the equation from Dygert et al. (2020) below.

$$D_{Eu} = \frac{K \cdot D_{Eu^{2+}} + D_{Eu^{3+}} \cdot (fO_2)^{\frac{1}{4}}}{K + (fO_2)^{\frac{1}{4}}}, \quad \text{(B10)}$$

where K is the equilibrium constant for the $Eu^{3+} \rightarrow Eu^{2+}$ reduction reaction in silicate melts and fO_2 is the oxygen fugacity of the melt. This constant is defined by the equation:

$$K = \frac{[M_{Eu^{2+}}]_{melt} \cdot (fO_2)^{\frac{1}{4}}}{[M_{Eu^{3+}}]_{melt}}, \quad \text{(B11)}$$

where $[M_{Eu^{2+}}]_{melt}$ and $[M_{Eu^{3+}}]_{melt}$ are the mass fraction of Eu^{2+} and Eu^{3+} in the silicate melt. Since K has never been calculated using olivine or ilmenite partitioning data, the fO_2 dependent Eu models in this study use the K of ($9.46 \times 10^{-4} \pm 5.5 \times 10^{-4}$) from Dygert et al. (2020) to approximate the D_{Eu} for olivine or ilmenite (**Figures B1c and B2c**).

Figure B1. Lattice Strain model for divalent element partitioning into olivine and predictive charge dependent Eu partitioning estimate. (a) Comparison of measured mineral-melt partition coefficients for Fe, Mn, and Ca in olivine and predicted partition coefficients using the parameters from this study. (b) Schematic figure showing a calculated lattice strain parabola for the literature data and how the calculated parabolas are used to determine the Eu^{2+} partitioning behavior. (c) Comparison of modeled Eu^{3+} and Eu^{2+} mineral-melt partition coefficients with the estimated Eu partition coefficient at an fO_2 of IW. The trivalent olivine partitioning model of Sun and Liang (2013) was used to calculate the Eu^{3+} partition coefficient. The Log($fO2$) of the IW redox buffer for each given temperature was determined using the IW buffer model from O'Neill and Pownceby (1993) (Tables 2.2 and 2.6). Experimentally determined mineral-melt partitioning data for Fe, Mn, and Ca in olivine from the literature (Kennedy et al., 1993; Tuara et al., 1998; Salters et al., 2002; Wasylenki et al., 2003; Filiberto et al., 2009; Elardo et al., 2011; Dalou et al., 2012; Imai et al., 2012; Krawczynski and Grove, 2012; Barr and Grove, 2013; Davis et al., 2013; Mallmann and O'Neill, 2013; Fonseca et al., 2014; Leitzke et al., 2016; Dygert et al., 2020; Snape et al., 2022; Haupt et al., 2024, Jing et al., 2024).

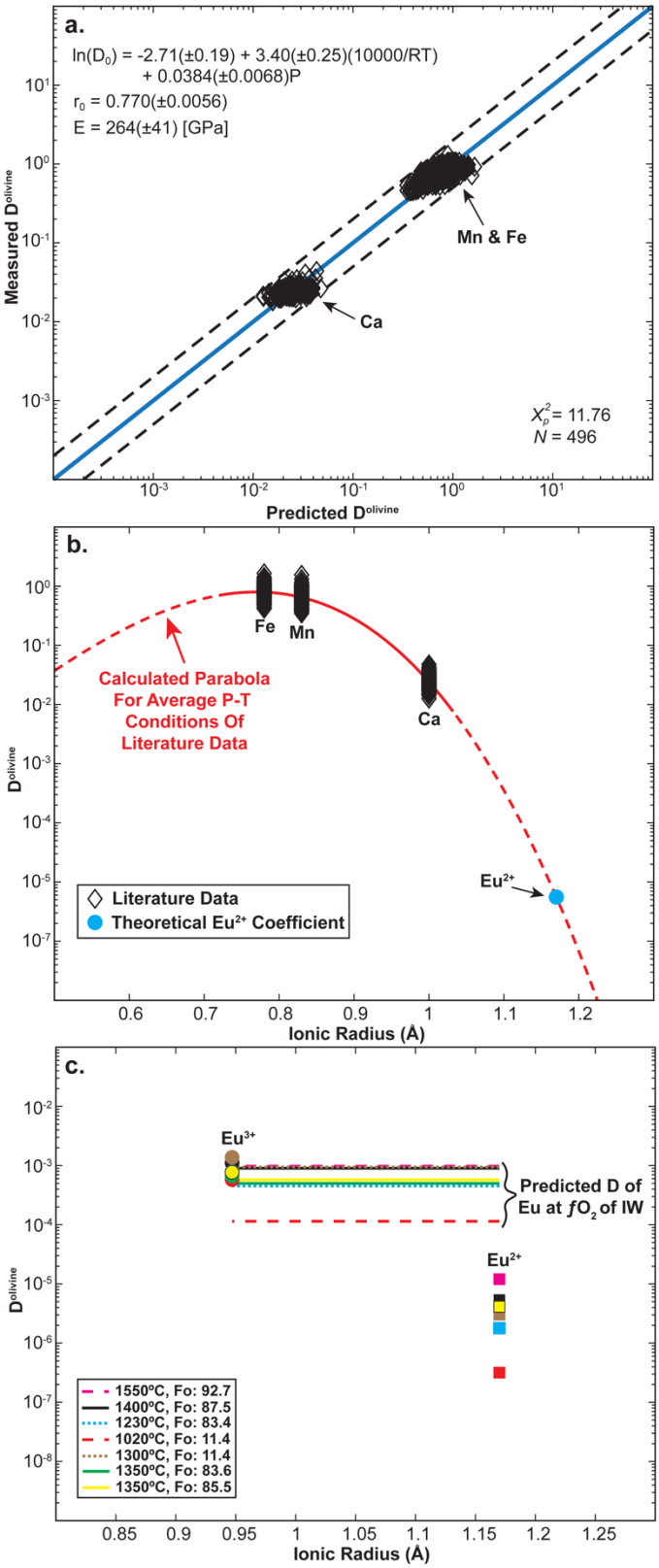
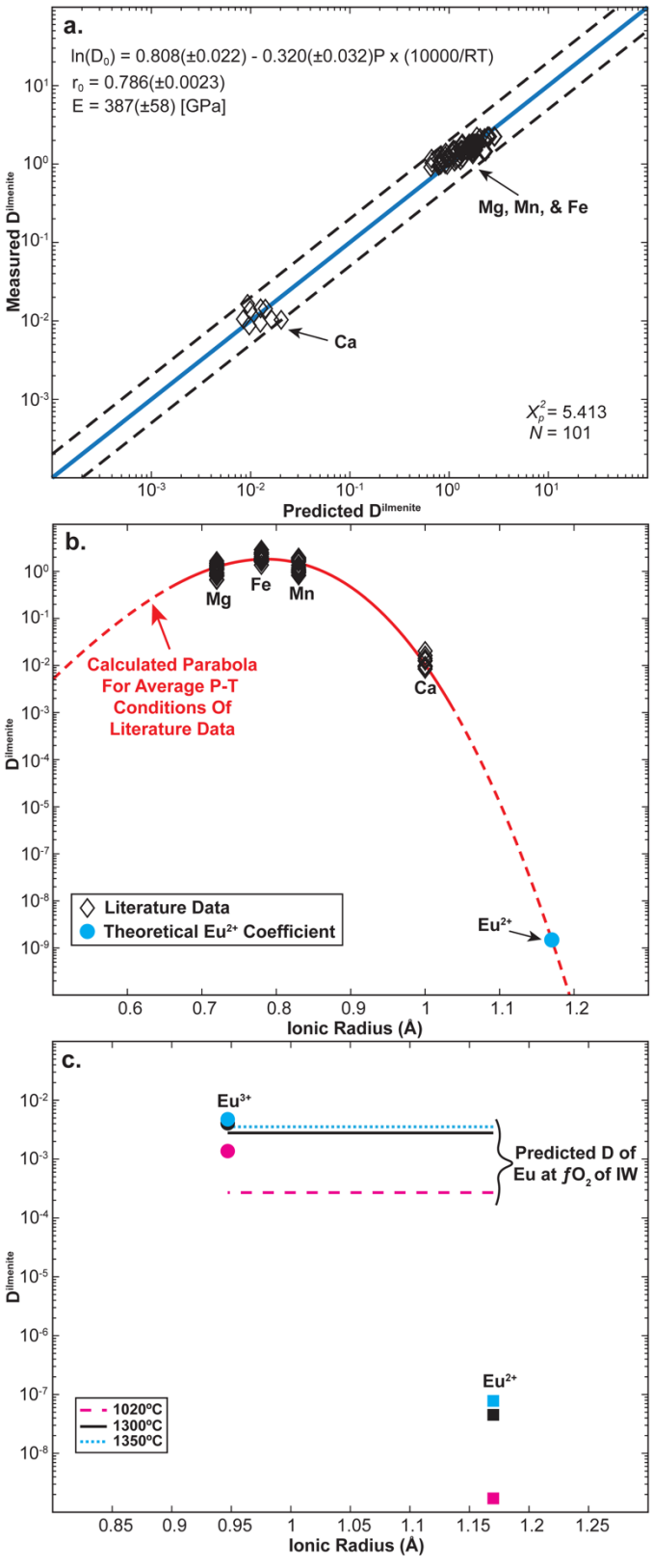

a.
ln(D0) = -2.71(±0.19) + 3.40(±0.25)(10000/RT)
+ 0.0384(±0.0068)P
r0 = 0.770(±0.0056)
E = 264(±41) [GPa]
Mn & Fe
Ca
X2p = 11.76
N = 496
Measured Dolivine
Predicted Dolivine
b.
Fe
Mn
Ca
Calculated Parabola
For Average P-T
Conditions Of
Literature Data
Eu2+
Literature Data
Theoretical Eu2+ Coefficient
Dolivine
Ionic Radius (Å)
c.
Eu3+
Predicted D of
Eu at fO2 of IW
Eu2+
1550°C, Fo: 92.7
1400°C, Fo: 87.5
1230°C, Fo: 83.4
1020°C, Fo: 11.4
1300°C, Fo: 11.4
1350°C, Fo: 83.6
1350°C, Fo: 85.5
Dolivine
Ionic Radius (Å)

Figure B2. Lattice Strain model for divalent element partitioning into ilmenite and predictive charge dependent Eu partitioning estimate. (a) Comparison of measured mineral-melt partition coefficients for Mg, Fe, Mn, and Ca in ilmenite and predicted partition coefficients using the parameters from this study. (b) Schematic figure showing a calculated lattice strain parabola for the literature data and how the calculated parabolas are used to determine the Eu^{2+} partitioning behavior. (c) Comparison of modeled Eu^{3+} and Eu^{2+} mineral-melt partition coefficients with the estimated Eu partition coefficient at an fO_2 of IW. The trivalent ilmenite partitioning model of Dygert et al. (2013) was used to calculate the Eu^{3+} partition coefficient. The Log($fO2$) of the IW redox buffer for each given temperature was determined using the IW buffer model from O'Neill and Pownceby (1993) (Tables 2.2 and 2.6). Experimentally determined mineral-melt partitioning data for Mg, Fe, Mn, and Ca in ilmenite from the literature (McKay et al., 1986; Klemme et al., 2006; Van Kan Parker et al., 2011; Krawczynski and Grove, 2012; Dygert et al., 2013; Leitzke et al., 2016; Charlier et al., 2018; Mallik et al., 2019; Shepherd et al., 2022; Snape et al., 2022).


a.
ln(D0) = 0.808(±0.022) - 0.320(±0.032)P x (10000/RT)
r0 = 0.786(±0.0023)
E = 387(±58) [GPa]
Mg, Mn, & Fe
Ca
X²p = 5.413
N = 101
Measured D^ilmenite
Predicted D^ilmenite
b.
Mg
Fe
Mn
Ca
Calculated Parabola For Average P-T Conditions Of Literature Data
Literature Data
Theoretical Eu²⁺ Coefficient
Eu²⁺
D^ilmenite
Ionic Radius (Å)
c.
Eu³⁺
Predicted D of Eu at fO2 of IW
Eu²⁺
1020°C
1300°C
1350°C
D^ilmenite
Ionic Radius (Å)

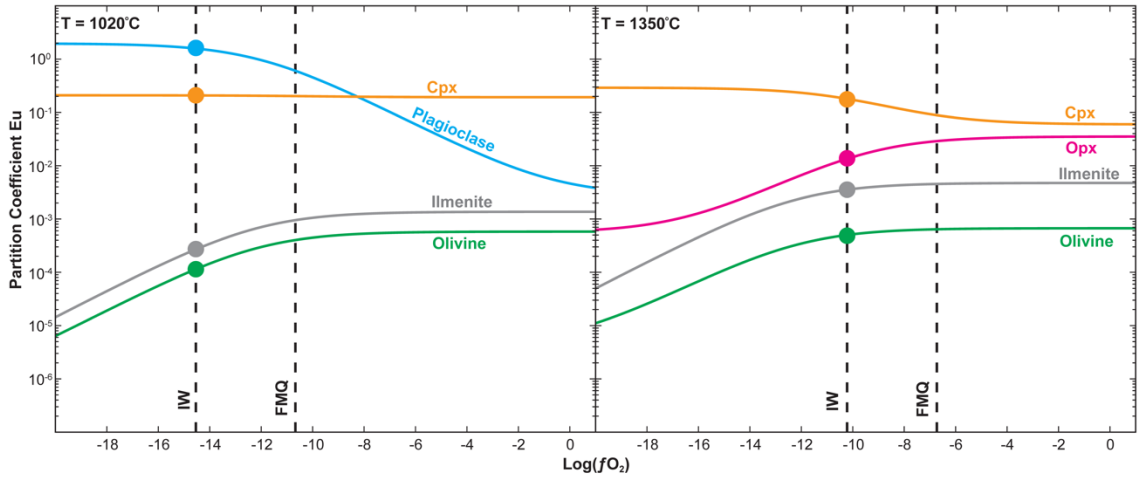


Figure B3. Modeled mineral-melt partitioning behavior of Eu in plagioclase, Opx, Cpx, olivine, and ilmenite at various fO_2 conditions and temperatures. (a) Modeled mineral-melt partitioning behavior of Eu in plagioclase, Cpx, olivine, and ilmenite at 1020°C. The large dots along the mineral partitioning lines in panel (a) correlate with the values reported in Table (2.2). (b) Modeled mineral-melt partitioning behavior of Eu in Cpx, Opx, olivine, and ilmenite at 1350°C. The large dots along the mineral partitioning lines in panel (b) correlate with the values reported in Table (2.6). For plagioclase, Cpx, and Opx, the mineral-melt partitioning models of Dygert et al. (2020) and Fibbrizio et al. (2021). The mineral-melt partitioning models discussed above were used for olivine and ilmenite. The Log($fO2$) of the IW redox buffer for each temperature was determined using the IW buffer model from O'Neill and Pownceby (1993). The Log($fO2$) of the FMQ redox buffer for each temperature was determined using the FMQ buffer model from Frost (1993). Clinopyroxene (Cpx), Orthopyroxene (Opx). The models above demonstrate how both fO_2 conditions and temperatures can significantly affect the partitioning behavior of Eu in magma ocean cumulate minerals. This figure also demonstrates how the fO_2 conditions for redox buffers evolve with temperature. Thus, to accurately model the evolution of Eu during magma ocean solidification, the effect of evolving crystallization temperatures must be accounted for.

Figure B4. Trace element comparison between evolving magma ocean cumulates (with and without Apatite), lunar picritic glasses, and lunar KREEP basalts. (a) modeled LMO cumulate evolution assuming different plagioclase floatation efficiencies and an apatite-free IBC. The dashed light blue line represents the LMO cumulate composition assuming 98% plagioclase floatation and an fO_2 of IW. The dashed green line represents the LMO cumulate composition assuming 98% plagioclase floatation and an fO_2 of IW-2. (b) Comparison of modeled LMO liquids and the compositional ranges of picritic glasses and KREEP basalts. A low-degree partial melt of LMO cumulate layer #6 (i.e., the IBC layer) is plotted to show the effect of partial melting on REE trends in an apatite-free IBC. (c) modeled LMO cumulate evolution assuming different plagioclase floatation efficiencies and an apatite-bearing IBC containing 0.2% apatite. (d) Comparison of modeled LMO liquids and the compositional ranges of picritic glasses and KREEP basalts. A low-degree partial melt of LMO cumulate layer #6 (i.e., the IBC layer) is plotted to show the effect of partial melting on REE trends in an apatite-bearing IBC containing 0.2% apatite. (e) modeled LMO cumulate evolution assuming different plagioclase floatation efficiencies and an apatite-bearing IBC containing 2% apatite. (f) Comparison of modeled LMO liquids and the compositional ranges of picritic glasses and KREEP basalts. A low-degree partial melt of LMO cumulate layer #6 (i.e., the IBC layer) is plotted to show the effect of partial melting on REE trends in an apatite-bearing IBC containing 2% apatite. Partial melting models in panels (b), (d), and (f) assume 90% plagioclase floatation. Low-Ti picritic glasses: very low-Ti (VLT) glass & green glass groups; Intermediate-Ti picritic glasses: yellow glass group; High-Ti picritic glasses: orange glass, red glass, & black glass groups. The intermediate-Ti and high-Ti picritic glasses are plotted together to declutter the plot as there is significant overlap in their trace element compositions. Lunar picritic glass compositions were compiled from (Hughes et al., 1990; Shearer et al., 1991; Shearer and Papike, 1993; McIntosh et al., 2024) and lunar KREEP basalt compositions from (Neal and Krammer, 2003; Hallis et al., 2014; Borg et al., 2019). Apatite partition coefficients were determined using the fO_2 dependent lattice strain partitioning models for hydroxylapatite from Ji and Dygert (2023). Note that in panels (b), (d), and (f), KREEP basalts and many glasses have steeper REE patterns than the LMO residual liquids, suggesting their KREEPy signature cannot result from direct assimilation of an LMO residual liquid regardless of the modal apatite abundance. Partial melting of KREEPy LMO cumulates (i.e., an apatite-free or apatite-bearing IBC layer) increases the slope of the REE pattern (dashed gray line), better fitting lunar basalts and suggesting basalt sources contained a KREEP-bearing solid component that precipitated from the late-stage LMO. It should also be noted that the addition of apatite to the IBC progressively increases the REE abundance in the IBC (a, c, e), but it also has the effect of flattening out the LREE trends of IBC partial melts (b, d, f). Partial melting models are discussed further in the main text.

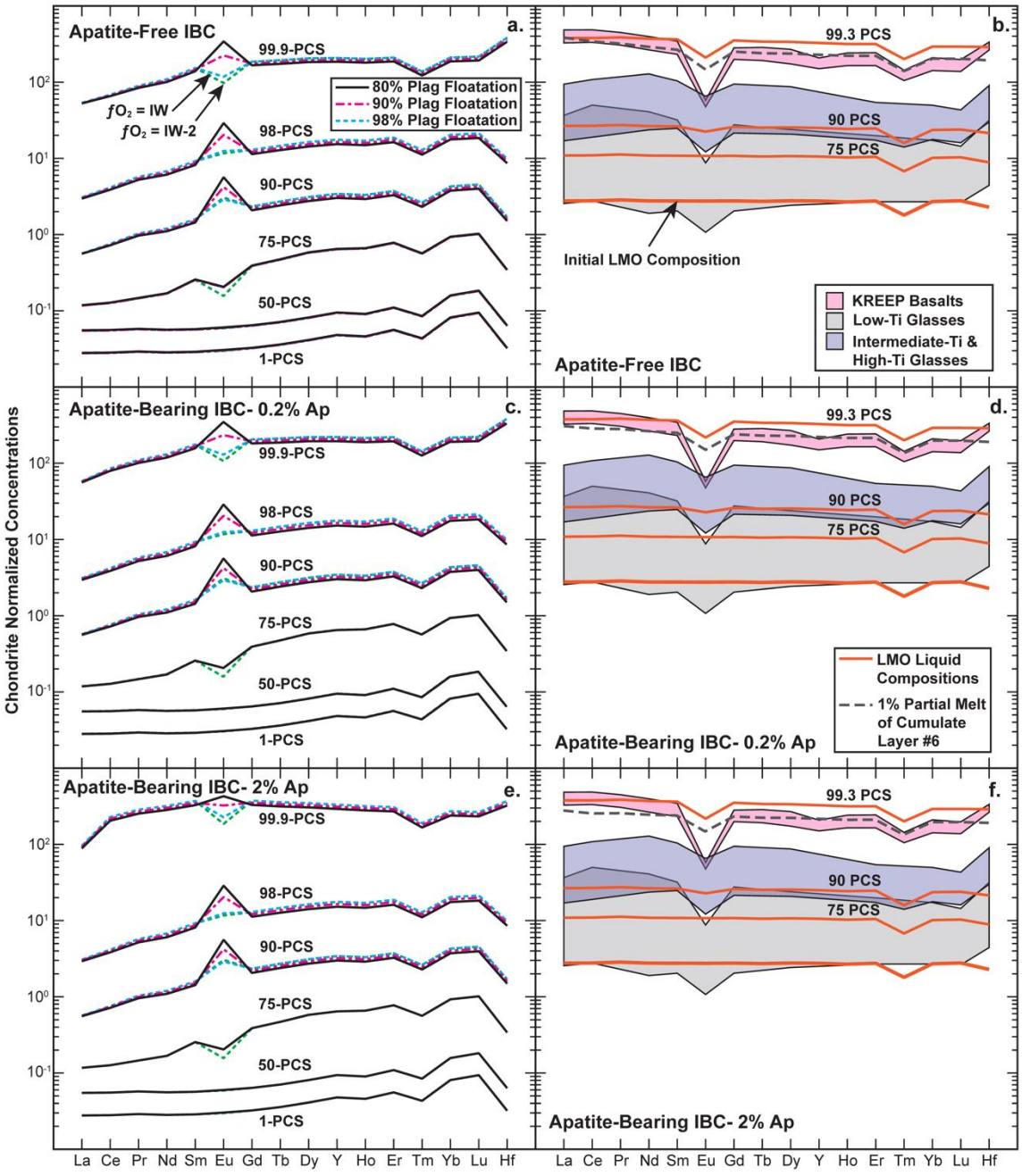
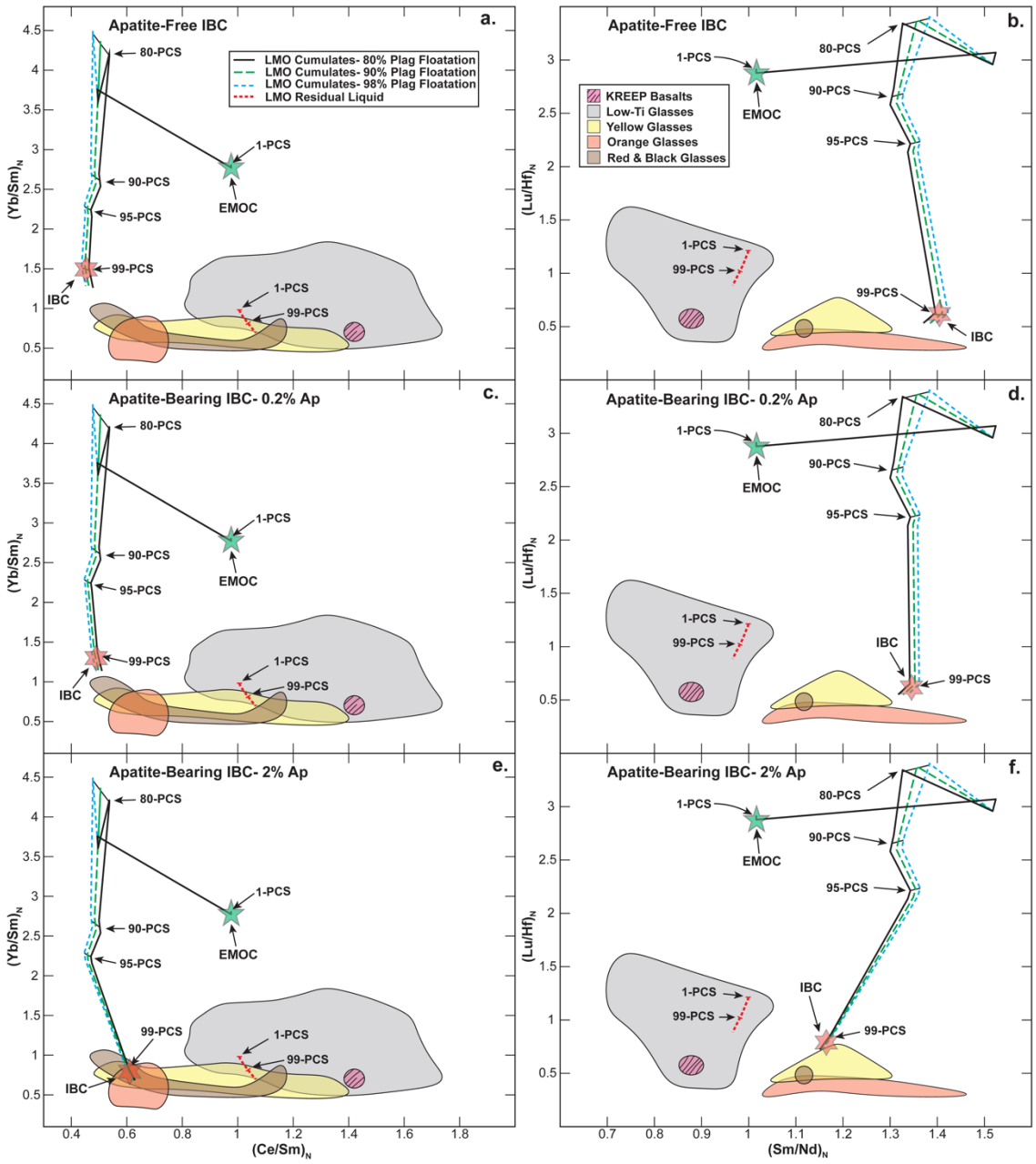

Apatite-Free IBC
a.
99.9-PCS
98-PCS
90-PCS
75-PCS
50-PCS
1-PCS
80% Plag Floatation
90% Plag Floatation
98% Plag Floatation
fO2 = IW
fO2 = IW-2
b.
99.3 PCS
90 PCS
75 PCS
Initial LMO Composition
KREEP Basalts
Low-Ti Glasses
Intermediate-Ti & High-Ti Glasses
Apatite-Free IBC
Apatite-Bearing IBC- 0.2% Ap
c.
d.
LMO Liquid Compositions
1% Partial Melt of Cumulate Layer #6
Apatite-Bearing IBC- 2% Ap
e.
f.
Chondrite Normalized Concentrations
La Ce Pr Nd Sm Eu Gd Tb Dy Y Ho Er Tm Yb Lu Hf

Figure B5. Comparison of LMO residual melt and cumulates during fractional crystallization of the LMO with and without apatite in the IBC layer. The color and texture of the trend lines indicate the plagioclase floatation efficiency. $(Lu/Hf)_N$ and $(Sm/Nd)_N$ are chondrite normalized ratios. Lunar picritic glass compositions were compiled from (Hughes et al., 1990; Shearer et al., 1991; Shearer and Papike, 1993; McIntosh et al., 2024) and lunar KREEP basalt compositions from (Neal and Krammer, 2003; Hallis et al., 2014; Borg et al., 2019). Low-Ti picritic glasses: VLT glass & green glass groups. Percent LMO solidification (PCS), Early Magma Ocean Cumulate (EMOC), Ilmenite-Bearing Cumulate (IBC). Apatite partition coefficients were determined using the fO_2 dependent lattice strain partitioning models for hydroxylapatite from Ji and Dygert (2023). These models indicate that the theoretical IBC layer would exhibit similar $(Lu/Hf)_N$ ratios to the intermediate to high-Ti lunar picritic glasses (i.e., yellow, orange, red, and black glasses) while the earliest LMO cumulates plot far from all lunar picritic glass groups. The addition of apatite to the late crystallizing LMO cumulates drives the $(Lu/Hf)_N$ ratios of the theoretical IBC away from the lunar orange glasses while simultaneously pushing the $(Yb/Sm)_N$ ratios toward the (i.e., yellow, orange, red, and black glasses). This figure highlights the counteracting effects of apatite addition to the late crystallizing LMO cumulates.


a.
Apatite-Free IBC
LMO Cumulates- 80% Plag Floatation
LMO Cumulates- 90% Plag Floatation
LMO Cumulates- 98% Plag Floatation
LMO Residual Liquid
80-PCS
1-PCS
90-PCS
95-PCS
EMOC
99-PCS
IBC
1-PCS
99-PCS
(Yb/Sm)N
b.
Apatite-Free IBC
KREEP Basalts
Low-Ti Glasses
Yellow Glasses
Orange Glasses
Red & Black Glasses
80-PCS
1-PCS
90-PCS
EMOC
95-PCS
1-PCS
99-PCS
99-PCS
IBC
(Lu/Hf)N
c.
Apatite-Bearing IBC- 0.2% Ap
80-PCS
1-PCS
90-PCS
EMOC
95-PCS
99-PCS
IBC
1-PCS
99-PCS
(Yb/Sm)N
d.
Apatite-Bearing IBC- 0.2% Ap
80-PCS
1-PCS
90-PCS
EMOC
95-PCS
1-PCS
99-PCS
IBC
99-PCS
(Lu/Hf)N
e.
Apatite-Bearing IBC- 2% Ap
80-PCS
1-PCS
90-PCS
EMOC
95-PCS
99-PCS
IBC
1-PCS
99-PCS
(Yb/Sm)N
(Ce/Sm)N
f.
Apatite-Bearing IBC- 2% Ap
80-PCS
1-PCS
90-PCS
EMOC
95-PCS
1-PCS
99-PCS
IBC
99-PCS
(Lu/Hf)N
(Sm/Nd)N

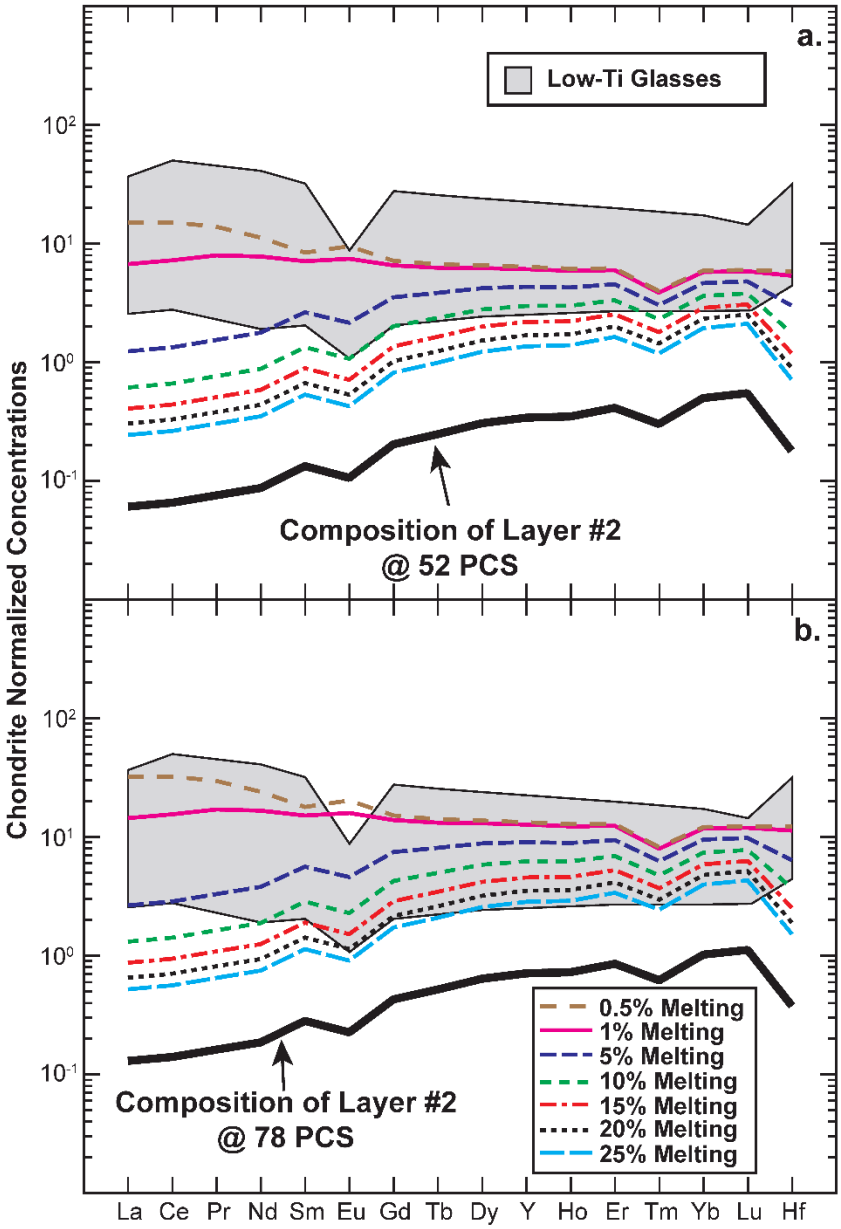
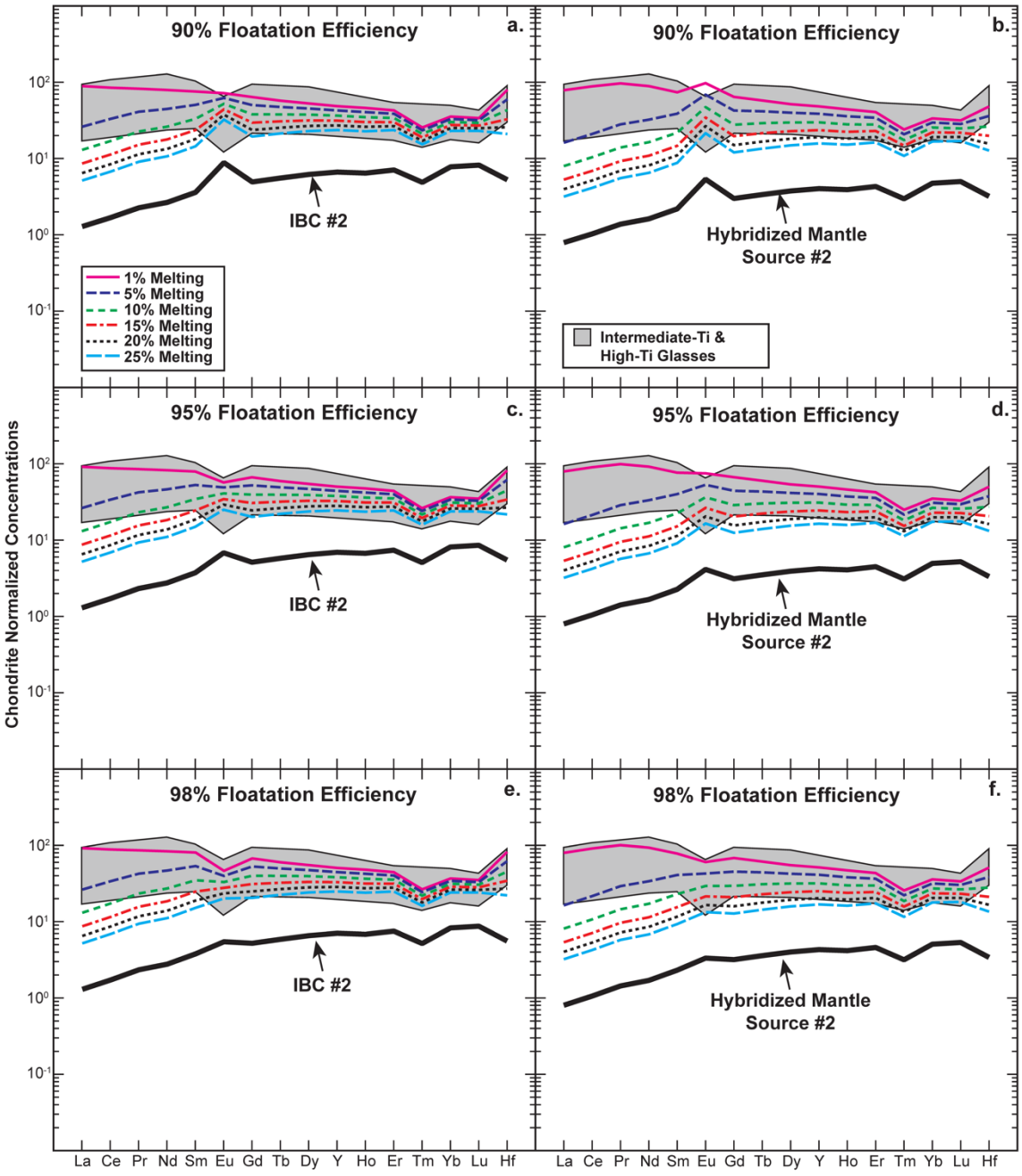


Figure B6. Comparison of modeled LMO mantle cumulate layer #2 partial melts and low-Ti lunar picritic glass compositions. (a) composition of partial melts if early crystallizing portions of LMO cumulate layer #2 were melted. (b) composition of partial melts if late crystallizing portions of LMO cumulate layer #2 were melted. Melting models in this figure assume an LMO fO_2 of IW. These models demonstrate that partial melts of early and late crystallizing portions of LMO cumulate layer #2 can achieve the levels of REE enrichment observed in the Low-Ti picritic glasses. While these models can't account for every geochemical feature of the low-Ti picritic glasses, the models further demonstrate that it is theoretically possible for some of the low-Ti picritic melts to come from an unhybridized portion LMO cumulate layer #2.

Figure B7. Comparison of modeled thickened IBC and hybridized source partial melts with high-Ti lunar picritic glass compositions. (a) composition of partial melts if a garnet-bearing IBC #2 was melted during a cumulate overturn event, assuming a plagioclase floatation efficiency of 90%. (b) composition of partial melts if a garnet-bearing hybridized mantle source #2 was melted following a cumulate overturn event, assuming a plagioclase floatation efficiency of 90%. (c) composition of partial melts if a garnet-bearing IBC #2 was melted during a cumulate overturn event, assuming a plagioclase floatation efficiency of 95%. (d) composition of partial melts if a garnet-bearing hybridized mantle source #2 was melted following a cumulate overturn event, assuming a plagioclase floatation efficiency of 95%. (e) composition of partial melts if a garnet-bearing IBC #2 was melted during a cumulate overturn event, assuming a plagioclase floatation efficiency of 98%. (f) composition of partial melts if a garnet-bearing hybridized mantle source #2 was melted following a cumulate overturn event, assuming a plagioclase floatation efficiency of 98%. For models in panels (b), (d), and (f), we assume hybridized mantle source #2 is composed of a 55% EMOC to 45% IBC #2 mixture. Both models above assume an LMO fO_2 of IW and a garnet abundance of 0.5% in the IBC or hybridized source. These models demonstrate that a garnet-bearing thickened IBC or garnet-bearing hybridized mantle source fertilized by the thickened IBC can still achieve the levels of REE enrichment required to explain the intermediate to high-Ti picritic glasses. These models also highlight the requirement for plagioclase floatation efficiencies of >90% as the partial melts of IBC #2 and hybridized mantle source #2 never develop a negative Eu anomaly in models assuming a plagioclase floatation efficiency of 90%.

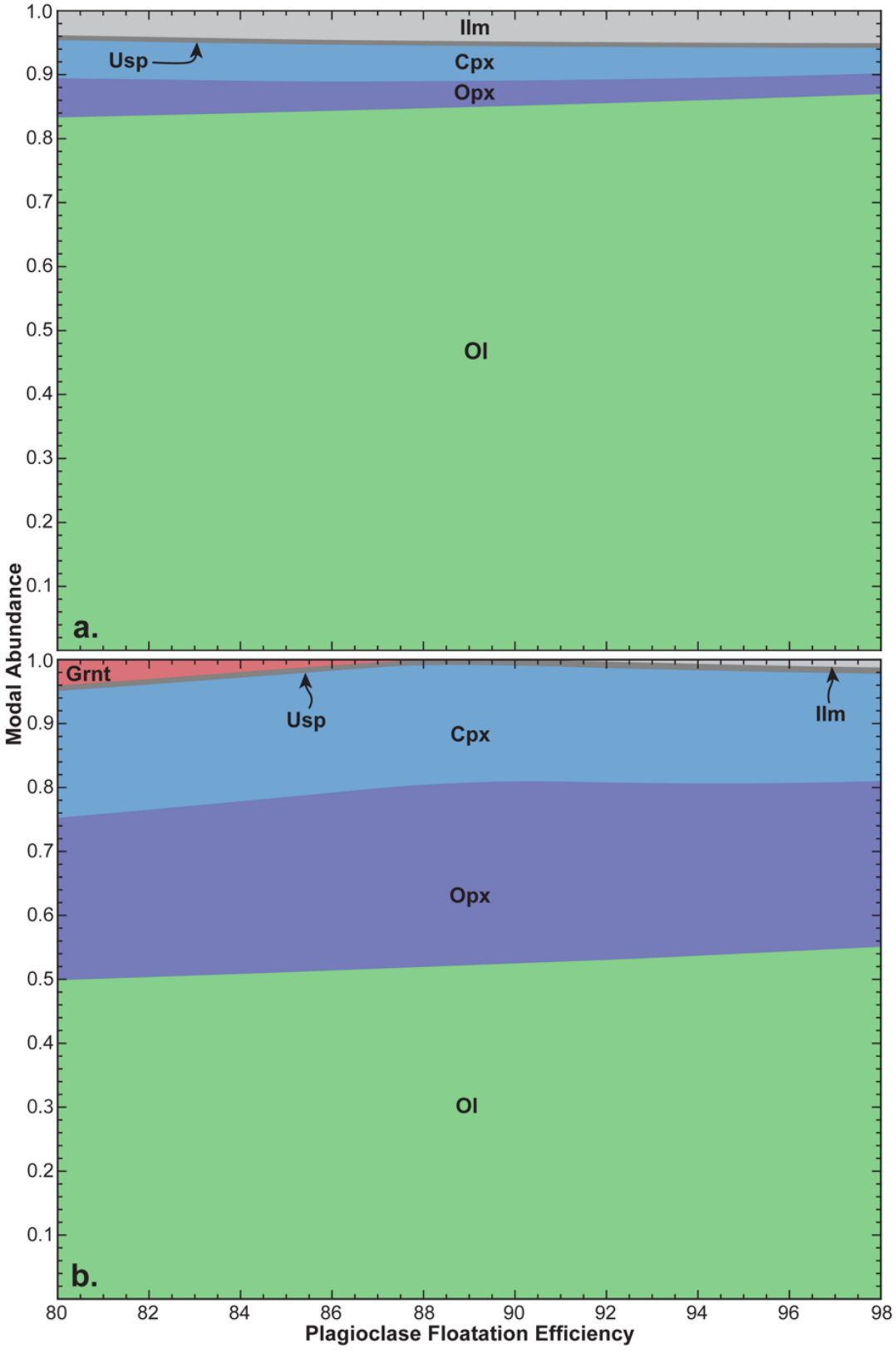

90% Floatation Efficiency
a.
IBC #2
1% Melting
5% Melting
10% Melting
15% Melting
20% Melting
25% Melting
90% Floatation Efficiency
b.
Hybridized Mantle
Source #2
Intermediate-Ti &
High-Ti Glasses
95% Floatation Efficiency
c.
IBC #2
95% Floatation Efficiency
d.
Hybridized Mantle
Source #2
98% Floatation Efficiency
e.
IBC #2
98% Floatation Efficiency
f.
Hybridized Mantle
Source #2
Chondrite Normalized Concentrations
La Ce Pr Nd Sm Eu Gd Tb Dy Y Ho Er Tm Yb Lu Hf

pMELTS Modeling Methods

To test the effect of plagioclase floatation on downwelling hybridized source mineralogy, we ran thermodynamic models using the pMELTS algorithm (Ghiorso and Sack, 1995; Ghiorso et al., 2002). The major element composition of the hybridized source was calculated using the estimated composition of IBC material (**Figure 2.6**) and the olivine composition of experiment LPUM 2.015 from Elardo et al. (2011). We tested two IBC compositions: IBC #1, an IBC composition that wasn't affected by pre-overturn mixing in the upper lunar mantle, and IBC #2, an IBC composition that was affected by pre-overturn mixing in the upper 100 km of the lunar mantle (**Table 2.5**). For each model, we set the fO_2 conditions to IW and the P-T conditions to 2 GPa and 1250°C, as our goals were to determine whether garnet would stabilize in hybridized source compositions at 2 GPa and to consider how the floatation efficiency of plagioclase might affect the abundance of garnet in lunar mantle sources.

The major element composition of hybridized mantle source #1 was estimated assuming mechanical mixing between IBC #1 (**Table 2.4**) and EMOC (**Figure B8a**). For this model, we assume hybridized mantle source #1 comprises an 80% EMOC to 20% IBC #1 mixture (**Table B4**). The major element composition of hybridized mantle source #2 was estimated assuming mechanical mixing between IBC #2 (**Table 2.4**) and EMOC (**Figure B8b**). For this model, we assume hybridized mantle source #2 comprises a 55% EMOC to 45% IBC #2 mixture (**Table B4**).

Figure B8. Thermodynamic models of the hybridized mantle source mineralogy at 1250°C and 2 GPa, assuming mechanical mixing between IBC and EMOC material and plagioclase floatation efficiencies of 80-98%. The modal mineralogy of the hybridized mantle sources in these models varies significantly from the IBC material (Figure 2.6), as the hybridized source is assumed to contain a significant portion of EMOC material. Modal mineralogy of the hybridized mantle source, assuming no pre-overturn mixing in the upper mantle (i.e., IBC #1) (a). Modal mineralogy of the hybridized mantle source, assuming pre-overturn mixing in the upper 100 km of the lunar mantle (i.e., IBC #2) (b). The composition of LMO cumulate material was assumed using the mineral compositions of LMO solidification experiments (Elardo et al., 2011; Charlier et al., 2018: see Table (2.2) for referenced experiments), and the modal mineral proportions for the initial magma ocean cumulates (Tables B1-B3). Estimated hybridized mantle source compositions can be found in Table B4. Olivine (Ol), Orthopyroxene (Opx), Clinopyroxene (Cpx), Garnet (Grnt), Ilmenite (Ilm), Ulvöspinel (Usp). These thermodynamic models demonstrate that garnet is far less likely to stabilize in the hybridized source than the downwelling IBC.


Ilm
Usp
Cpx
Opx
Ol
a.
Grnt
Usp
Ilm
Cpx
Opx
Ol
b.
Modal Abundance
Plagioclase Floatation Efficiency
1.0
0.9
0.8
0.7
0.6
0.5
0.4
0.3
0.2
0.1
80
82
84
86
88
90
92
94
96
98

Appendix B References

Barr, J.A., and Grove, T.L., 2013, Experimental petrology of the Apollo 15 group A green glasses: Melting primordial lunar mantle and magma ocean cumulate assimilation: Geochimica et Cosmochimica Acta, v. 106, p. 216–230, doi:10.1016/j.gca.2012.12.035.

Blundy, J., and Wood, B., 1994, Prediction of crystal–melt partition coefficients from elastic moduli: Nature, v. 372, p. 452–454, doi:10.1038/372452a0.

Borg, L.E., Gaffney, A.M., Kruijer, T.S., Marks, N.A., Sio, C.K., and Wimpenny, J., 2019, Isotopic evidence for a young lunar magma ocean: Earth and Planetary Science Letters, v. 523, p. 115706, doi:10.1016/j.epsl.2019.07.008.

Brice, J.C., 1975, Some thermodynamic aspects of the growth of strained crystals: Journal of Crystal Growth, v. 28, p. 249–253, doi:10.1016/0022-0248(75)90241-9.

Charlier, B., Grove, T.L., Namur, O., and Holtz, F., 2018, Crystallization of the lunar magma ocean and the primordial mantle-crust differentiation of the Moon: Geochimica et Cosmochimica Acta, v. 234, p. 50–69, doi:10.1016/j.gca.2018.05.006.

Dalou, C., Koga, K.T., Shimizu, N., Boulon, J., and Devidal, J.-L., 2012, Experimental determination of F and Cl partitioning between lherzolite and basaltic melt: Contributions to Mineralogy and Petrology, v. 163, p. 591–609, doi:10.1007/s00410-011-0688-2.

Davis, F.A., Humayun, M., Hirschmann, M.M., and Cooper, R.S., 2013, Experimentally determined mineral/melt partitioning of first-row transition elements (FRTE) during

partial melting of peridotite at 3GPa: Geochimica et Cosmochimica Acta, v. 104, p. 232–260, doi:10.1016/j.gca.2012.11.009.

Dygert, N., Draper, D.S., Rapp, J.F., Lapen, T.J., Fagan, A.L., and Neal, C.R., 2020, Experimental determinations of trace element partitioning between plagioclase, pigeonite, olivine, and lunar basaltic melts and an fO2 dependent model for plagioclase-melt Eu partitioning: Geochimica et Cosmochimica Acta, v. 279, p. 258–280, doi:10.1016/j.gca.2020.03.037.

Dygert, N., Liang, Y., and Hess, P., 2013, The importance of melt TiO2 in affecting major and trace element partitioning between Fe–Ti oxides and lunar picritic glass melts: Geochimica et Cosmochimica Acta, v. 106, p. 134–151, doi:10.1016/j.gca.2012.12.005.

Elardo, S.M., Draper, D.S., and Shearer, C.K., 2011, Lunar Magma Ocean crystallization revisited: Bulk composition, early cumulate mineralogy, and the source regions of the highlands Mg-suite: Geochimica et Cosmochimica Acta, v. 75, p. 3024–3045, doi:10.1016/j.gca.2011.02.033.

Filiberto, J., Jackson, C., Le, L., and Treiman, A.H., 2009, Partitioning of Ni between olivine and an iron-rich basalt: Experiments, partition models, and planetary implications: American Mineralogist, v. 94, p. 256–261, doi:10.2138/am.2009.3047.

Frost, B.R., 1991, Chapter 1.Introduction to oxygen fugacity and its petrologic importance, *in* Lindsley, D.H. ed., Petrologic and Magnetic Significance, Berlin, Boston, De Gruyter, p. 1–10, doi:doi:10.1515/9781501508684-004.

Ghiorso, M.S., Hirschmann, M.M., Reiners, P.W., and Kress III, V.C., 2002, The pMELTS: A revision of MELTS for improved calculation of phase relations and major element partitioning related to partial melting of the mantle to 3 GPa: Geochemistry, Geophysics, Geosystems, v. 3, p. 1–35.

Ghiorso, M.S., and Sack, R.O., 1995, Chemical mass transfer in magmatic processes IV. A revised and internally consistent thermodynamic model for the interpolation and extrapolation of liquid-solid equilibria in magmatic systems at elevated temperatures and pressures: Contributions to Mineralogy and Petrology, v. 119, p. 197–212, doi:10.1007/BF00307281.

Hallis, L.J., Anand, M., and Strekopytov, S., 2014, Trace-element modelling of mare basalt parental melts: Implications for a heterogeneous lunar mantle: Geochimica et Cosmochimica Acta, v. 134, p. 289–316, doi:10.1016/j.gca.2014.01.012.

Haupt, C.P., Renggli, C.J., Rohrbach, A., Berndt, J., and Klemme, S., 2024, Experimental Constraints on the Origin of the Lunar High-Ti Basalts: Journal of Geophysical Research: Planets, v. 129, p. e2023JE008239, doi:10.1029/2023JE008239.

Hughes, S.S., Delano, J.W., and Schmitt, R.A., 1990, Chemistry of individual mare volcanic glasses: evidence for distinct regions of hybridized mantle and a KREEP component in Apollo 14 magmatic sources.: Lunar and Planetary Science Conference Proceedings, v. 20, p. 127–138.

Imai, T., Takahashi, E., Suzuki, T., and Hirata, T., 2012, Element partitioning between olivine and melt up to 10GPa: Implications for the effect of pressure: Physics of the Earth and Planetary Interiors, v. 212–213, p. 64–75, doi:10.1016/j.pepi.2012.09.001.

Ji, D., and Dygert, N., 2023, Trace element partitioning between apatite and silicate melts: Effects of major element composition, temperature, and oxygen fugacity, and implications for the volatile element budget of the lunar magma ocean: Geochimica et Cosmochimica Acta, doi:10.1016/j.gca.2023.11.004.

Jing, J.-J., Su, B.-X., Berndt, J., Kuwahara, H., and van Westrenen, W., 2024, Experimental investigation of first-row transition elements partitioning between olivine and silicate melt: Implications for lunar basalt formation: Geochimica et Cosmochimica Acta, v. 373, p. 211–231, doi:10.1016/j.gca.2024.03.028.

van Kan Parker, M., Mason, P.R.D., and van Westrenen, W., 2011, Trace element partitioning between ilmenite, armalcolite and anhydrous silicate melt: Implications for the formation of lunar high-Ti mare basalts: Geochimica et Cosmochimica Acta, v. 75, p. 4179–4193, doi:10.1016/j.gca.2011.04.031.

Kennedy, A.K., Lofgren, G.E., and Wasserburg, G.J., 1993, An experimental study of trace element partitioning between olivine, orthopyroxene and melt in chondrules: equilibrium values and kinetic effects: Earth and Planetary Science Letters, v. 115, p. 177–195, doi:10.1016/0012-821X(93)90221-T.

Klemme, S., Günther, D., Hametner, K., Prowatke, S., and Zack, T., 2006, The partitioning of trace elements between ilmenite, ulvospinel, armalcolite and silicate melts with implications for the early differentiation of the moon: Chemical Geology, v. 234, p. 251–263, doi:10.1016/j.chemgeo.2006.05.005.

Krawczynski, M.J., and Grove, T.L., 2012, Experimental investigation of the influence of oxygen fugacity on the source depths for high titanium lunar ultramafic magmas: Geochimica et Cosmochimica Acta, v. 79, p. 1–19, doi:10.1016/j.gca.2011.10.043.

Leitzke, F.P., Fonseca, R.O.C., Michely, L.T., Sprung, P., Münker, C., Heuser, A., and Blanchard, H., 2016, The effect of titanium on the partitioning behavior of high-field strength elements between silicates, oxides and lunar basaltic melts with applications to the origin of mare basalts: Chemical Geology, v. 440, p. 219–238, doi:10.1016/j.chemgeo.2016.07.011.

Mallik, A., Ejaz, T., Shcheka, S., and Garapic, G., 2019, A petrologic study on the effect of mantle overturn: Implications for evolution of the lunar interior: Geochimica et Cosmochimica Acta, v. 250, p. 238–250, doi:10.1016/j.gca.2019.02.014.

Mallmann, G., and O'Neill, H.St.C., 2013, Calibration of an Empirical Thermometer and Oxybarometer based on the Partitioning of Sc, Y and V between Olivine and Silicate Melt: Journal of Petrology, v. 54, p. 933–949, doi:10.1093/petrology/egt001.

McIntosh, E.C., Day, J.M.D., McCubbin, F.M., Vander Kaaden, K.E., Hattingh, R., and Porrachia, M., 2024, Revisiting the Petrogenesis of Pyroclastic Glass Bead Deposits at the Apollo 15 and 17 Sites: Journal of Petrology, v. 65, p. egae026, doi:10.1093/petrology/egae026.

McKay, G., Wagstaff, J., and Yang, S.-R., 1986, Zirconium, hafnium, and rare earth element partition coefficients for ilmenite and other minerals in high-Ti lunar mare basalts: An experimental study: Journal of Geophysical Research: Solid Earth, v. 91, p. 229–237, doi:10.1029/JB091iB04p0D229.

Neal, C.R., and Kramer, G.Y., 2003, The Composition of KREEP: A Detailed Study of KREEP Basalt 15386, *in* Mackwell, S. and Stansbery, E. eds., Lunar and Planetary Science Conference, Lunar and Planetary Science Conference, p. 2023.

O'Neill, H.St.C., and Pownceby, M.I., 1993, Thermodynamic data from redox reactions at high temperatures. I. An experimental and theoretical assessment of the electrochemical method using stabilized zirconia electrolytes, with revised values for the Fe-"FeO", Co-CoO, Ni-NiO and Cu-Cu2O oxygen buffers, and new data for the W-WO2 buffer: Contributions to Mineralogy and Petrology, v. 114, p. 296–314, doi:10.1007/BF01046533.

Salters, V.J.M., Longhi, J.E., and Bizimis, M., 2002, Near mantle solidus trace element partitioning at pressures up to 3.4 GPa: Geochemistry, Geophysics, Geosystems, v. 3, p. 1–23, doi:10.1029/2001GC000148.

Shannon, R.D., 1976, Revised effective ionic radii and systematic studies of interatomic distances in halides and chalcogenides: Acta Crystallographica Section A, v. 32, p. 751–767, doi:10.1107/S0567739476001551.

Shearer, C.K., and Papike, J.J., 1993, Basaltic magmatism on the Moon: A perspective from volcanic picritic glass beads: Geochimica et Cosmochimica Acta, v. 57, p. 4785–4812, doi:10.1016/0016-7037(93)90200-G.

Shearer, C.K., Papike, J.J., Galbreath, K.C., and Shimizu, N., 1991, Exploring the lunar mantle with secondary ion mass spectrometry: a comparison of lunar picritic glass beads from the Apollo 14 and Apollo 17 sites: Earth and Planetary Science Letters, v. 102, p. 134–147, doi:10.1016/0012-821X(91)90003-Z.

Shepherd, K., Namur, O., Toplis, M.J., Devidal, J.-L., and Charlier, B., 2022, Trace element partitioning between clinopyroxene, magnetite, ilmenite and ferrobasaltic to dacitic magmas: an experimental study on the role of oxygen fugacity and melt composition: Contributions to Mineralogy and Petrology, v. 177, p. 90, doi:10.1007/s00410-022-01957-y.

Snape, J.F., Nemchin, A.A., Johnson, T., Luginbühl, S., Berndt, J., Klemme, S., Morrissey, L.J., and van Westrenen, W., 2022, Experimental constraints on the long-lived radiogenic isotope evolution of the Moon: Geochimica et Cosmochimica Acta, v. 326, p. 119–148, doi:10.1016/j.gca.2022.04.008.

Sun, C., and Liang, Y., 2013, The importance of crystal chemistry on REE partitioning between mantle minerals (garnet, clinopyroxene, orthopyroxene, and olivine) and basaltic melts: Chemical Geology, v. 358, p. 23–36, doi:10.1016/j.chemgeo.2013.08.045.

Taura, H., Yurimoto, H., Kurita, K., and Sueno, S., 1998, Pressure dependence on partition coefficients for trace elements between olivine and the coexisting melts: Physics and Chemistry of Minerals, v. 25, p. 469–484, doi:10.1007/s002690050138.

Wasylenki, L.E., Baker, M.B., Kent, A.J.R., and Stolper, E.M., 2003, Near-solidus Melting of the Shallow Upper Mantle: Partial Melting Experiments on Depleted Peridotite: Journal of Petrology, v. 44, p. 1163–1191, doi:10.1093/petrology/44.7.1163.

Wood, B.J., and Blundy, J.D., 1997, A predictive model for rare earth element partitioning between clinopyroxene and anhydrous silicate melt: Contributions to Mineralogy and Petrology, v. 129, p. 166–181, doi:10.1007/s004100050330.

CHAPTER 3 AN EVALUATION OF THE LUNAR K/TH RATIO USING GEOCHEMICAL MODELING: IMPLICATIONS FOR THE MOON'S THERMAL EVOLUTION

Abstract

The Moon is K-depleted relative to Earth owing to the giant impact event that produced the lunar magma ocean (LMO). As K is a primary heat-producing element (HPE) in planetary interiors, variation in the level of K-depletion can significantly impact lunar thermal evolution and melt production potential. The range of published lunar bulk K abundances is large. Here, we model the chemical fractionation of K and other HPEs (Th and U) during LMO solidification and subsequent partial melting of LMO cumulates. Using measured HPE concentrations in lunar basalts, picritic glasses, crustal cumulates, and remote sensing data, we evaluate the consistency of previous estimates of Th/K with natural samples. We then explore how a Th/K ratio that best fits the natural samples affects long-term lunar thermal evolution. Geochemical models of LMO solidification demonstrate that the K/Th ratio of the initial LMO could range from 450-550 if the floatation efficiency of plagioclase is ≥95%. If plagioclase floatation is less efficient, the LMO's bulk K/Th ratio would need to be lower. Geochemical models also demonstrate that >90% of the lunar HPE budget should initially be concentrated in the lunar crust and upper mantle cumulates following LMO solidification. Thermal evolution models indicate that the degree of K depletion on the Moon would have a more significant impact on lunar thermal evolution than the enrichment of Th or U relative to Earth.

3.1 Introduction

The concentration and distribution of heat-producing elements (HPEs) (K, U, and Th) within planetary interiors determine their thermal evolution (Laneuville et al., 2013, 2018; Criss and Hofemeister, 2016). The volatile nature of K at high temperatures and the

incompatible partitioning behavior of all HPEs makes their concentrations and distributions sensitive to processes like planetary accretion, high energy impacts, and fractional crystallization during planetary magma ocean solidification, all of which the Moon is thought to have experienced (Lodders, 2003; Canup, 2004, 2008; Wang and Jacobsen, 2016a, 2016b; Li et al., 2020). Previous studies conclude that like Earth, the Moon is K depleted and U and Th enriched relative to chondritic meteorites (Ringwood and Kesson, 1977; Ringwood, 1986; Taylor et al., 2006; Taylor and Wieczorek, 2014; Wang and Jacobsen, 2016a, 2016b; Seigler et al., 2022) (**Table 3.1**); however, estimated abundances of HPEs have not been tested in the context of recent lunar magma ocean (LMO) solidification and mantle melting models (e.g., Scholpp and Dygert, *in review*).

Previous studies of lunar HPE concentrations often employ a combination of geophysical and geochemical constraints to estimate the abundance of refractory elements indirectly, then estimate the initial volatile elements using sample-based linear regressions (Hagerty et al., 2006; Taylor et al., 2006; Taylor and Wieczorek, 2014). Lunar HPE concentrations have also been estimated using the Urey ratio (the ratio between internal heat production and the total surface heat loss) determined via remote sensing measurements (Seigler et al., 2022). Both methods depend on implicit assumptions (e.g., crustal thickness, crustal composition, crustal thermal conductivity, mare basalt source compositions, distribution of HPEs within the Moon), which are poorly constrained in some cases and could affect the HPE estimates if they differ from current estimates (e.g., Taylor et al., 2006; Taylor and Wieczorek, 2014) (**Table 3.1**).

Table 3.1. Comparison of assumed present day bulk moon HPE concentrations from previous studies.

Th (ppm)	U (ppm)	K (ppm)	K/Th	Source	Study
0.0335	0.0090	3770	112537.31	CHUR	Anders and Grevesse (1989)
0.0795	0.0203	240	3018.87	Bulk Silicate Earth	McDonough and Sun (1995)
0.1240	0.0310	310	2500.00	Bulk Silicate Earth	Turcotte and Schubert (2002)
0.1100	0.0275	94.25	856.82	Bulk Silicate Moon	Taylor et al. (2006)
0.0795	0.0203	36.90	464.15	Bulk Silicate Moon	Taylor and Wieczorek (2014)
0.0790	0.0214	42.72	540.62	Bulk Silicate Moon	Seigler et al. (2022)

CHUR- Chondritic Uniform Reservoir

Due to the complexities that the poorly constrained isotope concentrations present, few studies have attempted to model the impacts of radiogenic heating (Gagnepain-Beyneix et al., 2006; Laneuville et al., 2013, 2018; Zhang et al., 2013; Zhao et al., 2019; Zhang et al., 2022). No published model for the distribution of HPEs throughout the Moon accounts for the effects of fractional crystallization during LMO solidification. Existing studies make the following simplifying assumptions about the HPE distributions: (1) HPEs are evenly distributed throughout the lunar mantle (Gagnepain-Beyneix et al., 2006) or (2) HPEs are all concentrated in the ilmenite-bearing cumulates (IBC) or remaining urKREEP melt near the end of solidification (Laneuville et al., 2013, 2018; Zhang et al., 2013; Zhao et al., 2019; Zhang et al., 2022). The latter assumption enables workers to treat the IBC as a mobile heat-producing layer in models that attempt to account for cumulate overturn (Laneuville et al., 2013, 2018; Zhang et al., 2013; Zhao et al., 2019; Zhang et al., 2022). While both assumptions are unrealistic, assuming the HPEs are concentrated in the IBCs is more consistent with the results of studies that model the distribution of incompatible elements such as REEs (Snyder et al., 1992; Scholpp and Dygert, *in review*). Because K, Th, and U are highly incompatible in lunar constituent minerals (except for K in plagioclase), they will likely have similar distributions to the REEs.

Here, we model the HPE composition of LMO cumulates and cumulate derived partial melts using methods similar to those used by Scholpp and Dygert (*in review*). We use experimentally determined LMO cumulate solidification sequences (Charlier et al., 2018) and up-to-date lunar trace element partition coefficients to model chemical

fractionation during LMO solidification and post-solidification partial melting. We compare the modeled LMO cumulate and cumulate melt compositions assuming different bulk Moon HPE estimates to lunar samples to assess the viability of previous estimated lunar HPE budgets. We find that the bulk LMO likely had a relatively low K/Th ratio, as concluded by more recent studies. We then explore the implications of this lower K/Th ratio on the lunar HPE budget and lunar thermal evolution using heat conduction models.

3.2 Geochemical Modeling

3.2.1 Modeling Parameters for LMO Solidification

Radiogenic element concentrations (^{232}Th, ^{235}U, ^{238}U, and ^{40}K) in the LMO cumulates were determined assuming Rayleigh fractionation using the methods discussed in Appendix C. The crystallization sequence assumed in this study is identical to the sequence used by Scholpp and Dygert (*in review*). This sequence is based on the experimental results of Charlier et al. (2018) and assumes that LMO solidification occurs in a six-stage progression of fractionating phases. Olivine is the only crystallization phase from $F = 1$ to $F = 0.49$, Ol and Opx crystallize from $F = 0.49$ to $F = 0.22$, Ol, Opx, pigeonite (Pig), and Plag crystallize from $F = 0.22$ to $F = 0.19$, and Cpx (i.e., augite), Pig, and Plag crystallize from $F = 0.19$ to $F = 0.05$. The last two stages of solidification are assumed to crystallize Cpx, Pig, Plag, and quartz (Qtz) from $F = 0.05$ to $F = 0.02$, and fayalitic Ol, Cpx, Plag, Qtz, and Ilm crystallize from $F = 0.02$ to $F = 0$. Models from this study also assume 100% quartz floatation and 95% plagioclase floatation during crustal formation based on the REE partitioning models discussed in Scholpp and Dygert (*in review*) (**Table 3.2**).

Table 3.2. Phase proportions in LMO cumulates based on results from Charlier et al. (2018), assuming 95% plagioclase and 100% quartz floatation efficiency.

Phases	Stage 1	Stage 2	Stage 3	Stage 4	Stage 5	Stage 6
Ol	0.990	0.099	0.094	0.000	0.000	0.395
Opx	0.000	0.891	0.377	0.000	0.000	0.000
Cpx	0.000	0.000	0.000	0.364	0.419	0.316
Pig	0.000	0.000	0.472	0.583	0.524	0.000
Plag	0.000	0.000	0.047	0.043	0.047	0.041
Qtz	0.000	0.000	0.000	0.000	0.000	0.237
Ilm	0.000	0.000	0.000	0.000	0.000	0.000
Melt	0.010	0.010	0.010	0.010	0.010	0.010

*Stage 1: F= 1-0.49, Stage 2: F= 0.49-0.22, Stage 3: F= 0.22-0.19, Stage 4: F= 0.19-0.05, Stage 5: F= 0.05-0.02, Stage 6: F= 0.02-0

Olivine (Ol), Orthopyroxene (Opx), Clinopyroxene (Cpx), Pigeonite (Pig), Plagioclase (Plag), Ilmenite (Ilm), Quartz (Qtz)

3.2.2 Radiogenic Element Partitioning

The U, Th, and K partition coefficients for each mineral phase during solidification were compiled from experimental studies of terrestrial and lunar synthetic analogs (Nash and Crecraft, 1985; Van Kan Parker et al., 2011; Leitzke et al., 2016; Snape et al., 2022; Haupt et al., 2024) or they were calculated using lattice strain-based partitioning models (Sun et al., 2017).

In general, published data are adequate for modeling HPE fractionation during LMO solidification; however, the abundance of K is often at or below the detection limit (i.e., the measured concentrations of K are within error of zero) in measured olivines in published experimental mineral-melt partitioning studies. Thus, K partitioning between olivine and melt was calculated using a lattice strain-based partitioning model fit to Li and Na partitioning data (see Appendix C). Mineral-melt partition coefficient and compositional calculation parameter assumptions are reported in **Table 3.3** and are plotted relative to the literature data in **Figures C1 and C3**.

3.3 Modeled HPE Distributions and Ratios

3.3.1 Lunar HPE Distribution

Models demonstrate that after LMO solidification, >90% of the lunar HPE budget is initially concentrated in the anorthosite crust, and the upper mantle cumulates (those that formed between 80% and 99.9% solidification) (**Figure 3.1a**). This means that much of the lunar radiogenic heat production potential is initially concentrated close to the crust-mantle boundary; however, the heat-producing elements are not distributed evenly across the crustal and upper mantle reservoirs.

Table 3.3. Mineral-melt partition coefficients for Th, U, and K used in magma ocean solidification models.

Element	Ol (D)	ref.	Opx (D)	ref.	Cpx (D)	ref.	Pig (D)	ref.	Plag (D)	Plag (D)
Th	6.13E-06	a	3.78E-05	a	1.47E-02	c	6.50E-03	c	9.10E-04	9.10E-04
U	1.26E-05	a	7.12E-04	a	1.14E-02	c	8.20E-03	c	5.60E-04	5.60E-04
K	4.02E-09	Est.	2.20E-03	b	3.50E-03	c	1.92E-02	d	4.12E-01	5.02E-01
Stage	1, 2, 3, 6	-	2, 3	-	4, 5, 6	-	3, 4, 5, 6	-	3	4
T (ºC)	-	-	-	-	-	-	-	-	1215	1130
P (GPa)	-	-	-	-	-	-	-	-	0.5	0.3
*X*Ca	-	-	-	-	-	-	-	-	0.9406	0.8833
*X*Na	-	-	-	-	-	-	-	-	0.0594	0.1138
Sample/ Experiment	-	-	-	-	-	-	-	-	LPUM88 HAO2-5	LPUM/02-5 HA02-3

Table 3.3. Continued.

Element	Plag (D)	Plag (D)	ref.	Ilm (D)	ref.	Qtz (D)	ref.	Core (D)	ref.	Int-Mlt (D)
Th	9.10E-04	9.10E-04	e	4.30E-04	b	9.00E-03	f	3.86E-05	g	1
U	5.60E-04	5.60E-04	e	1.90E-03	b	2.80E-02	f	5.65E-05	g	1
K	6.44E-01	6.10E-01	e, Cal.	3.32E-02	d	1.40E-02	f	5.62E-03	h	1
Stage	5	6	-	6	-	5, 6	-	-	-	All Stages
T (ºC)	1040	1020	-	-	-	-	-	-	-	-
P (GPa)	0.15	0.08	-	-	-	-	-	-	-	-
*XC*a	0.8029	0.7445	-	-	-	-	-	-	-	-
*X*Na	0.1916	0.2424	-	-	-	-	-	-	-	-
Sample/ Experiment	LPUM/02-3 gl HAO4-1.5	LPUM/0.4-1.5 gl HA02-0.8	i	-	-	-	-	-	-	-

Calculated partition coefficients are indicated in the source column (Cal.). Partition coefficients that are not calculated, are measurements from partitioning experiments or estimated as indicated by the (Est.) label in the ref. column. Estimated partition coefficients were determined using lattice strain partitioning models presented in Appendix C.

Calculation parameters were calculated for mineral compositions from lunar relevant experiments. Studies and experiments that compositions data was sourced from are indicated at the bottom of the table.

The LMO solidification stage in which each set of partition coefficients is used is indicated in the Stage row above the calculation parameters.

Olivine (Ol), Orthopyroxene (Opx), Clinopyroxene (Cpx), Pigeonite (Pig), Plagioclase (Plag), Ilmenite (Ilm), Quartz (Qtz), Interstitial Melt (Int-Mlt)

[a]Leitzke et al. (2016), [b]Van Kan Parker et al. (2011), [c]Haupt et al. (2024), [d]Snape et al. (2022), [e]Sun et al. (2017), [f]Nash and Crecraft (1985), [g]Faure et al. (2020), [h]Steenstra et al. (2018), [i]Charlier et al. (2018)

The modeled distributions indicate that >60% of the lunar K budget was contained within the lunar crust, mainly in the lower crust. In contrast, the crust would contain <11% of the total Th and U budgets. Most of the lunar Th and U budget is concentrated in the uppermost mantle cumulates (the last 5% of LMO mantle cumulates). The upper mantle cumulates also contain >30% of the lunar K budget; however, this value would vary depending on the assumed plagioclase floatation efficiency.

The modeled elemental heat production for each terrestrial and lunar HPE budget considered (McDonough and Sun, 1995; Turcotte and Schubert, 2002; Taylor et al., 2006; Taylor and Wieczorek, 2014; Seigler et al., 2022) demonstrates that varying the overall abundance of Th and U has less of an effect than varying the overall abundance of K (**Figure 3.1d**). For terrestrial HPE budgets with K/Th ratios >2000, K produces the most radiogenic heat until ~0.8 Ga (**Figure 3.1b**). For lunar HPE budgets with K/Th ratios <900, the contribution from K to the total radiogenic heat production is far less significant than the combined heat production of Th and U (**Figure 3.1b**). Considering the distribution of heat-producing elements in the late-crystallizing crustal and mantle reservoirs, the crust would produce a significant amount of heat if the Moon had an HPE budget similar to estimated terrestrial budgets (**Figure 3.1b-d**). In contrast, the most recent lunar HPE budget estimates are so K-depleted that the lower crust would produce negligible heat relative to the overall diffusive heat flux leaving the Moon (**Figures 3.1b and 3.1d**). These models highlight the importance of constraining the lunar HPE budget, specifically the degree of K depletion in the Moon.

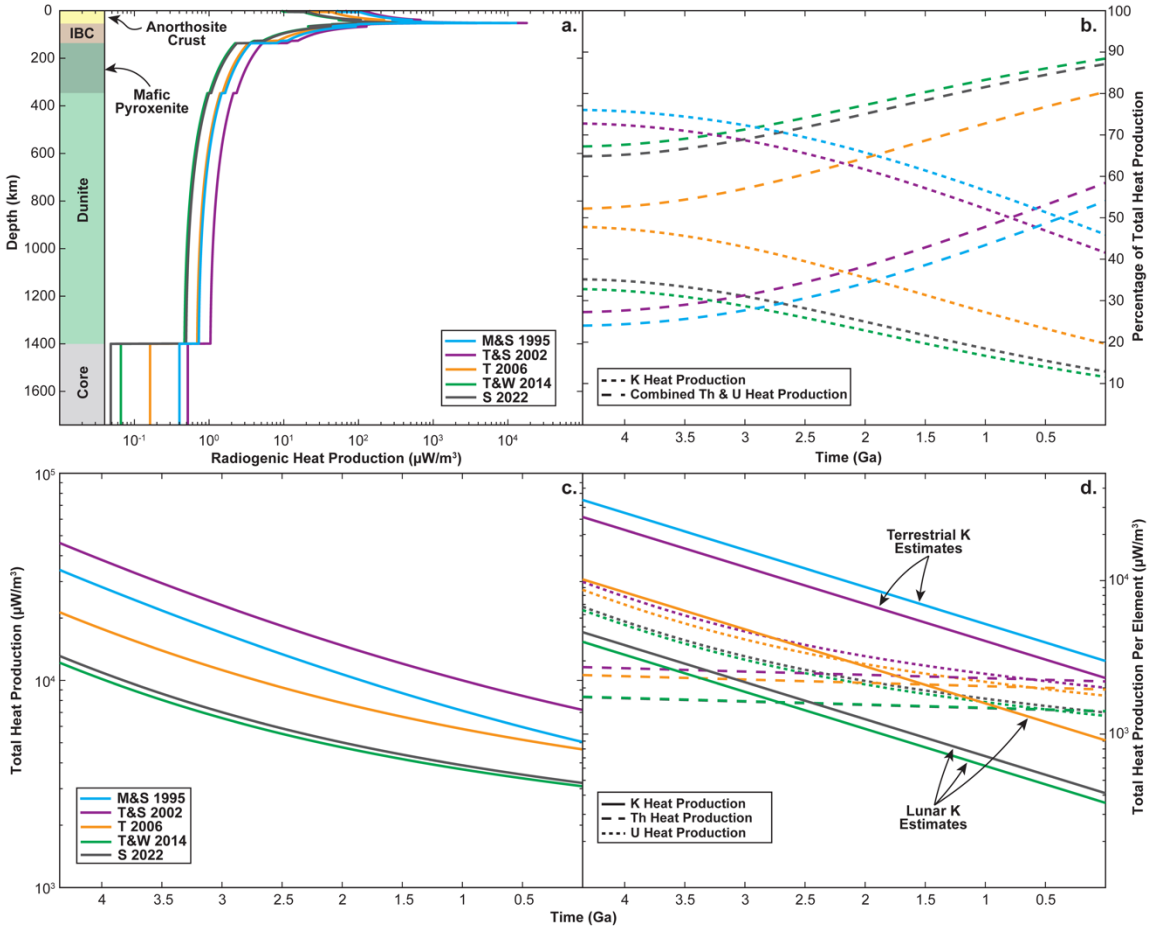


Figure 3.1. Distribution of Heat Producing Elements (HPE) and heat production potential following LMO solidification if the LMO extends to the lunar core-mantle boundary. (a) radiogenic heat production potential across the lunar mantle, assuming the lunar core, mantle cumulates, and anorthosite crust following LMO solidification if the Moon contained previous lunar or terrestrial HPE budgets. The assumed lunar stratigraphy for the models is shown in the sub-panel on the left side of (a). (b) Evolution of each HPE's proportional heat throughout the bulk Moon as a function of time. (c) Evolution of the total radiogenic heat production across the lunar crust and mantle. (d) Evolution of each HPE's radiogenic heat production across the lunar crust and mantle. Heat production calculations were conducted using the HPE budgets found in Table 3.1 and heat production and elemental decay parameters in Table 3.4. M&S 1995: McDonough and Sun (1995), T&S 2002: Turcotte and Schubert (2002), T 2006: Taylor et al. (2006), T&W 2014: Taylor and Wieczorek (2014), S 2022: Seigler et al. (2022). This figure demonstrates that fractional crystallization of the LMO would significantly impact the distribution of HPE throughout the lunar crust and mantle. The figure also shows how significantly the depletion or enrichment of each HPE affects lunar radiogenic heat production over geologic timescales.

3.3.2 Constraining The Lunar K/Th Ratio

The models for energy production with respect to time (**Figures 3.1b-d**) demonstrate the large variation between the Earth's and Moon's K budgets would have a far more significant effect on the total heat production than the variation in the estimated U and Th budgets. This is primarily related to the degree of elemental variation between the Earth and Moon **Table 3.1**. Given the significant variation in estimated K budgets and relatively minor variation in estimated U and Th budgets, we focus on constraining the ratio of K relative to U and Th, which should reveal the most information about the degree of lunar K depletion and the impact this depletion would have on lunar thermal evolution.

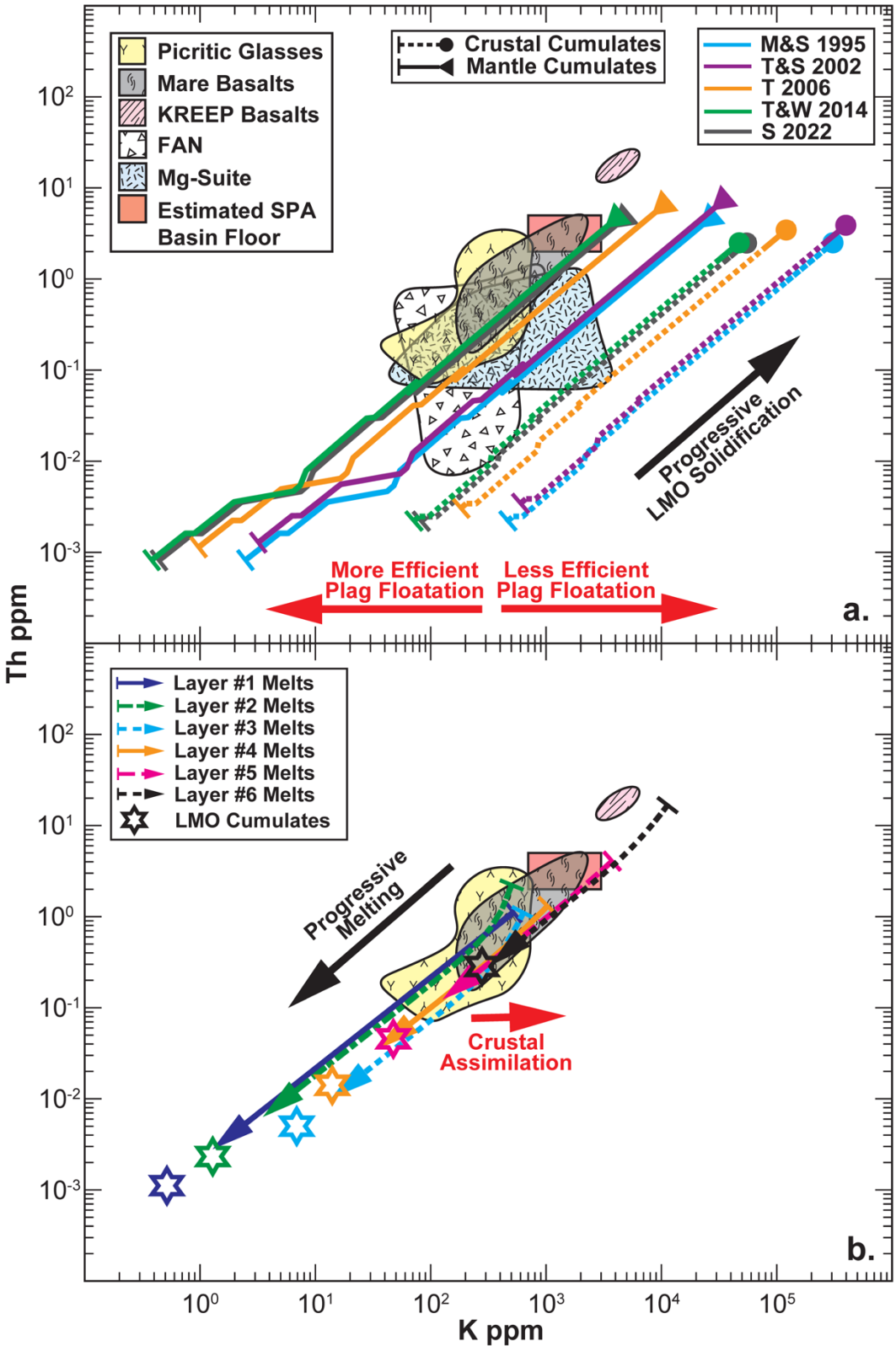
Considering the partitioning behavior of the HPEs (**Table 3.1**), Th and U should mirror one another as the difference between their partition coefficients is typically less than an order of magnitude. This differs significantly for K as its partition coefficient differs from the Th and U coefficients by as much as four orders of magnitude, depending on the phase. This means that LMO crystallization will primarily fractionate K from Th and U. Given the negligible difference in estimated U/Th ratios from previous studies (i.e., 0.2613±0.0094: McDonough and Sun, 1995; Turcotte and Schubert, 2002; Taylor et al., 2006; Taylor and Wieczorek, 2014; Seigler et al., 2022), we focus on constraining the K/Th ratio of the LMO.

Solidification models from this study unsurprisingly demonstrate that the estimated terrestrial K/Th ratios from McDonough and Sun (1995) and Turcotte and Schubert (2002) would generate mantle and crustal LMO cumulates that are far too high

(too K-rich) when compared to the ratios in lunar crustal cumulates, mare basalts, picritic glasses (**Figure 3.2a**), and South Pole Aitken (SPA) basin floor deposits. The lunar K/Th ratio proposed by Taylor et al. (2006) would generate mantle and crustal LMO cumulates that fall within the range of some lunar melts and crustal samples but are too K-rich to be consistent with most lunar samples. The ratios estimated by Taylor and Wieczorek (2014) and Seigler et al. (2022) best fit the ratios exhibited by lunar mafic melts and crustal cumulates. They fit the lunar sample compositions even better if more efficient plagioclase floatation is assumed (**Figure 3.2a**). This exercise suggests a lunar K/Th ratio of 450 to 550 is consistent with the range of K/Th ratios observed in lunar melts and crustal samples if plagioclase floatation was highly efficient; however, post-LMO solidification melting and emplacement processes (i.e., reactive re-equilibration during ascent and crustal assimilation) must also be considered.

Since the lunar mare basalts and picritic glasses are melts derived from the lunar mantle, the effects of partial melting must be considered. Here, we assume a bulk Moon HPE budget of Taylor and Wieczorek (2014) and treat the average composition of each LMO cumulate layer as a theoretical source composition (**Figure 3.2b**). We also assume that these lunar mantle sources lack residual plagioclase they crystallized with because the relatively compatible behavior of K in plagioclase would significantly affect the melt trajectories, and previous studies on lunar mantle melting consistently conclude that the mafic lunar melts originate from depths below the plagioclase stability field (Wagner and Grove, 1997; Elkins-Tanton et al., 2003; Krawczynski and Grove, 2012; Barr and Grove, 2013; Brown and Grove, 2015).

Figure 3.2. Comparison of the Th and K abundances observed in lunar samples with geochemical models for LMO solidification and mantle cumulate partial melting. (a) modeled mantle and crustal cumulate Th and K abundances as LMO solidification progresses. All models in this figure assume a plagioclase floatation efficiency of 95% during LMO solidification. The red arrows in panel (a) show how more or less efficient plagioclase floatation would affect the mantle cumulate composition. (b) Models for partial melting of LMO cumulate sources assuming a bulk Moon HPE budget proposed by Taylor and Wieczorek (2014). Partial melting models assume modal fractional melting of a plagioclase-free unhybridized source, and melts represent aggregated modal partial melts. The red arrow in panel (b) shows the trajectory of melts affected by crustal assimilation. The black arrow in panel (b) shows the trajectory of partial melts as the extent of melting increases. Data for lunar picritic glasses was compiled from: Hughes et al., 1990; Shearer et al., 1991; Shearer and Papike, 1993; McIntosh et al., 2024. Data for lunar Mare and KREEP basalts was compiled from: Ryder and Schuraytz, 2001; Neal and Krammer, 2003; Zeigler et al., 2005; Hallis et al., 2014; Borg et al., 2019. Data for lunar Mg-Suite samples was compiled from: Taylor et al., 1972; Kent et al., 2017; Cao et al., 2021; Fu et al., 2021; He et al., 2024. Data for ferroan anorthosites (FAN) was compiled from: Norman et al., 2003, 2010; Nyquist et al., 2006, Borg et al., 2020; Sio et al., 2020. Estimated South Pole Aitken (SPA) basin floor compositional ranges were taken from Moriarty et al. (2021). Initial LMO HPE budgets modeled in this figure can be found in Table 3.1. M&S 1995: McDonough and Sun (1995), T&S 2002: Turcotte and Schubert (2002), T 2006: Taylor et al. (2006), T&W 2014: Taylor and Wieczorek (2014), S 2022: Seigler et al. (2022). This figure demonstrates that the K/Th ratio of the Moon needs to be ≤550 to fit the Th and K abundances in both crustal cumulates or mantle-derived melts. The figure also demonstrates that the K/Th ratio of the partial melts is similar to mantle sources.


Picritic Glasses
Mare Basalts
KREEP Basalts
FAN
Mg-Suite
Estimated SPA Basin Floor
Crustal Cumulates
Mantle Cumulates
M&S 1995
T&S 2002
T 2006
T&W 2014
S 2022
Progressive LMO Solidification
More Efficient Plag Floatation
Less Efficient Plag Floatation
a.
Layer #1 Melts
Layer #2 Melts
Layer #3 Melts
Layer #4 Melts
Layer #5 Melts
Layer #6 Melts
LMO Cumulates
Progressive Melting
Crustal Assimilation
b.
Th ppm
K ppm
10^{2}
10^{1}
10^{0}
10^{-1}
10^{-2}
10^{-3}
10^{0}
10^{1}
10^{2}
10^{3}
10^{4}
10^{5}

Accordingly, we remove plagioclase from the assumed modal mineralogy of LMO cumulate layers 3-6 and proportionally adjust the other mineral abundances to determine the bulk partition coefficients of each cumulate source. We apply modal fractional melting models to explore the chemical variations during melting (see Scholpp and Dygert (*in review*) for details).

The melting models demonstrate that partial melting of the LMO cumulates does not significantly fractionate the K/Th ratio of the melt if the melt sources were plagioclase-free. Given the similarity between the K/Th ratios of LMO cumulates (**Figure 3.2a**), reactive re-equilibration during accent through the lunar mantle would likely have negligible effects on a partial melts' K/Th ratio. Thus, a lunar melt's K/Th ratio is likely representative of the mantle source from which it was derived. It should also be noted that crustal assimilation would drive the K/Th ratios of the mantle melts away from the observed lunar melt array, like the Mg-Suite sample array (**Figure 3.2a**). Considering the composition of lunar melts (i.e., basalt and picritic glasses), we conclude the initial LMO K/Th ratio was similar to the ~464 estimates of Taylor and Wieczorek (2014) as long as plagioclase floatation efficiencies were ≥95%. If plagioclase floatation were less efficient, the initial LMO K/Th ratio would need to be <464 to account for the K added by the retained plagioclase. Thus, the Moon likely started with a low radiogenic heat potential relative to Earth (**Figure 3.1b**). Below, we explore the effect of this low K/Th ratio on the lunar thermal evolution and how cumulate overturn may extend or shorten the period over which lunar mantle melting could occur.

3.4 Thermal Evolution Models

3.4.1 Thermal Diffusion and Heat Production Model

For the thermal evolution models in this study, the finite-difference approximations for Fickian diffusion within a radially symmetric sphere from Ford Versypt (2012) and Ford Versypt and Braatz (2014) were used. The diffusion equations were modified to account for internal heat generation through radioactive decay following Özisik (1993):

$$\frac{1}{r^2}\frac{\partial}{\partial r}\left(r^2 \propto_i \frac{\partial T}{\partial r}\right) = \frac{\partial T}{\partial t}, \text{ if } r \neq 0, \tag{3.1}$$

$$\frac{2\propto_i}{r}\frac{\partial T}{\partial r} + \frac{\partial}{\partial r}\left(\propto_i \frac{\partial T}{\partial r}\right) = \frac{\partial T}{\partial t}, \text{ if } r \neq 0, \tag{3.2}$$

$$\frac{2\propto_i}{r}\frac{\partial T}{\partial r} + \frac{\partial \propto_i}{\partial r}\frac{\partial T}{\partial r} + \propto_i \frac{\partial^2 T}{\partial r^2} = \frac{\partial T}{\partial t}, \text{ if } r \neq 0, \tag{3.3}$$

where T is the temperature (K), t is time in seconds, and r_i is the scaled radius of the sphere at an interval i within a spherical grid. $r_i = i \cdot \Delta r$ and $\Delta r = 1$, $\propto_i$ is the dimensionless diffusivity at an interval i. The dimensionless diffusivity is:

$$\propto_i = \frac{\kappa_i \Delta t}{\Delta \hat{r}^2} \tag{3.4}$$

where κ_i is the diffusivity of the material (m^2/s) at a given interval i, $\Delta \hat{r}_i$ reflects the dimensional grid spacing (i.e., $\Delta \hat{r} = (\hat{r}_{i+1} - \hat{r}_i)$) in (m), and Δt is the timestep. To use the numerical approximations from Ford Versypt and Braatz (2014), the central operator notation where the operator δ_{ir} centered in the r dimension at the position r_i over an interval of $i\Delta r$ applied to $T(r_i, t)$ must be used:

$$\delta_{ir} T(r_i, t) = T\left(r_i + \frac{1\Delta r}{2}, t\right) - T\left(r_i - \frac{1\Delta r}{2}, t\right) \approx \bar{T}_{i+\frac{1}{2}}(t) - \bar{T}_{i-\frac{1}{2}}(t) \tag{3.5}$$

where $\bar{T}_i(t) \approx T(r_i, t)$ and $\bar{T}_i$ is the cell center temperature at a given grid point interval i. If $\propto_i$ was constant, a common finite difference discretization scheme for diffusion in a spherical geometry (Crank, 1975; Carslaw and Jaeger, 1986, Özisik, 1993; Morton and Mayer, 2005; Ford Versypt and Braatz, 2014) could be used:

$$\frac{\propto_i}{i\Delta r^2}\delta_{2r}T(r_i,t) + \frac{\propto_i}{\Delta r^2}\delta_r\left(\delta_r T(r_i,t)\right) = \frac{\propto_i}{i\Delta r^2}\delta_{2r}T(r_i,t) + \frac{\propto_i}{\Delta r^2}\delta_r\left(T\left(r_i + \frac{\Delta r}{2}, t\right) - T\left(r_i - \frac{\Delta r}{2}, t\right)\right), \quad (3.6)$$

$$\frac{\propto_i}{i\Delta r^2}\delta_{2r}T(r_i,t) + \frac{\propto_i}{\Delta r^2}\delta_r\left(T\left(r_i + \frac{\Delta r}{2}, t\right) - T\left(r_i - \frac{\Delta r}{2}, t\right)\right) \approx \frac{\propto_i}{i\Delta r^2}\left(\bar{T}_{i+1}(t) - \bar{T}_{i-1}(t)\right) + \frac{\propto_i}{\Delta r^2}\left(\bar{T}_{i+1}(t) - 2i\bar{T}_i(t) + \bar{T}_{i-1}(t)\right), \quad (3.7)$$

$$\frac{\propto_i}{i\Delta r^2}\left(\bar{T}_{i+1}(t) - \bar{T}_{i-1}(t)\right) + \frac{\propto_i}{\Delta r^2}\left(\bar{T}_{i+1}(\mathrm{t}) - 2i\bar{T}_i(t) + \bar{T}_{i-1}(t)\right) \approx \frac{\propto_i}{i\Delta r^2}\left((i+1)\bar{T}_{i+1}(t) - 2i\bar{T}_i(t) + (i-1)\bar{T}_{i-1}(t)\right), \quad (3.8)$$

Thus,

$$\frac{\partial T_i(t)}{\partial t} = \frac{\propto_i}{i\Delta r^2}\left((i+1)\bar{T}_{i+1}(t) - 2i\bar{T}_i(t) + (i-1)\bar{T}_{i-1}(t)\right), \text{ if } i = 1,2,\ldots N-1 \text{ and } t > 0 \quad (3.9)$$

However, this study assumes that the $\propto_i$ is not constant, it must be assumed that the cell center diffusivity changes for grid point i:

$$\frac{\propto(r_i,t)}{i\Delta r^2}\delta_{2r}T(r_i,t) + \frac{1}{\Delta r^2}\delta_r\left(\propto(r_i,t)\delta_r T(r_i,t)\right) = \frac{\propto(r_i,t)}{i\Delta r^2}\delta_{2r}T(r_i,t) + \frac{1}{\Delta r^2}\delta_r\left(\propto(r_i,t)T\left(r_i + \frac{\Delta r}{2}, t\right) - T\left(r_i - \frac{\Delta r}{2}, t\right)\right), \quad (3.10)$$

$$\frac{\propto(r_i,t)}{i\Delta r^2}\delta_{2r}T(r_i,t) + \frac{1}{\Delta r^2}\delta_r\left(\propto(r_i,t)T\left(r_i + \frac{\Delta r}{2}, t\right) - T\left(r_i - \frac{\Delta r}{2}, t\right)\right) \approx \frac{A_i}{i\Delta r^2}\left(\bar{T}_{i+1}(t) - \bar{T}_{i-1}(t)\right) + \frac{A_{i+\frac{1}{2}}}{\Delta r^2}\left(\bar{T}_{i+1}(t) - \bar{T}_i(t)\right) + \frac{A_{i-\frac{1}{2}}}{\Delta r^2}\left(\bar{T}_{i-1}(t) - \bar{T}_i(t)\right), \quad (3.11)$$

where $\propto_i \approx A_i$, $A_{i+\frac{1}{2}} \approx \frac{A_i + A_{i+1}}{2}$, and $A_{i-\frac{1}{2}} \approx \frac{A_i + A_{i-1}}{2}$. This means that the temperature derivative:

$$\frac{\partial T_i(t)}{\partial t} = \frac{A_i}{2i\Delta r^2}\left((i+2)\bar{T}_{i+1}(t) - 2i\bar{T}_i(t) + (i-2)\bar{T}_{i-1}(t)\right) + \frac{A_{i+1}}{2\Delta r^2}\left(\bar{T}_{i+1}(t) - \bar{T}_i(t)\right) + \frac{A_{i-1}}{2\Delta r^2}\left(\bar{T}_{i-1}(t) - \bar{T}_i(t)\right), \quad \text{if } i = 1,2,\ldots N-1 \text{ and } t > 0 \tag{3.12}$$

The temperature change at the center of the sphere (where $r = 0$ and $i = 0$) can be determined by applying the boundary condition $\frac{\partial T(0,t)}{\partial r} = 0$:

$$\frac{\partial T(0,t)}{\partial t} = \lim_{r\to 0}\left(\frac{2\propto_i}{r}\frac{\partial T}{\partial r} + \frac{\partial}{\partial r}\left(\propto_i \frac{\partial T}{\partial r}\right)\right), \tag{3.13}$$

$$\frac{\partial T(0,t)}{\partial t} = \lim_{r\to 0}\left(\frac{2\propto_i \frac{\partial T}{\partial r}}{r}\right) + \frac{\partial}{\partial r}\left(\propto_i \frac{\partial T}{\partial r}\right), \tag{3.14}$$

The first term of Eq. 3.14 gives an indeterminate form of $\frac{0}{0}$ that can be solved using l'Hôpital's rule:

$$\lim_{r\to 0}\left(\frac{2\propto_i \frac{\partial T}{\partial r}}{r}\right) = \lim_{r\to 0}\left(\frac{\frac{\partial}{\partial r}(2\propto_i \frac{\partial T}{\partial r})}{\frac{\partial}{\partial r}r}\right), \tag{3.15}$$

$$\lim_{r\to 0}\left(\frac{2\propto_i \frac{\partial T}{\partial r}}{r}\right) = 2\frac{\partial}{\partial r}(\propto_i \frac{\partial T}{\partial r}), \tag{3.16}$$

This result substituted into Eq. 3.14 yields:

$$\lim_{r\to 0}\left(\frac{2\propto_i}{r}\frac{\partial T}{\partial r} + \frac{\partial}{\partial r}\left(\propto_i \frac{\partial T}{\partial r}\right)\right) = 3\frac{\partial}{\partial r}(\propto_i \frac{\partial T}{\partial r}), \tag{3.17}$$

$$\lim_{r\to 0}\left(\frac{2\propto_i}{r}\frac{\partial T}{\partial r} + \frac{\partial}{\partial r}\left(\propto_i \frac{\partial T}{\partial r}\right)\right) = 3 \propto_i \frac{\partial^2 T}{\partial r^2}, \tag{3.18}$$

The central difference approximation to the spatial derivatives is:

$$\frac{3\propto_i}{\Delta r^2}\delta_r\left(\delta_r T(r_i,t)\right) = \frac{3\propto_i}{\Delta r^2}\delta_r\left(T\left(r_i + \frac{\Delta r}{2}, t\right) - T\left(r_{i-1} - \frac{\Delta r}{2}, t\right)\right), \tag{3.19}$$

$$\frac{3\propto_i}{\Delta r^2}\delta_r\left(T\left(r_i+\frac{\Delta r}{2},t\right)-T\left(r_{i-1}-\frac{\Delta r}{2},t\right)\right)\approx\frac{3\propto_i}{\Delta r^2}\left(\bar{T}_{i+1}(t)-2\bar{T}_i(t)+\bar{T}_{i-1}(t)\right), \quad (3.20)$$

and since this study assumes a radially symmetric sphere around the origin:

$$\frac{\partial T(0,t)}{\partial r}\approx\frac{\delta_{2r}T(r_i,t)}{2\Delta r}\approx\frac{\bar{T}_i(t)-\bar{T}_{i-1}(t)}{2\Delta r}=0 \quad (3.21)$$

and $\bar{T}_{i+1}$ can be substituted for $\bar{T}_{i-1}$ at $r=0$ to obtain:

$$\frac{\partial T_i(t)}{\partial t}=\frac{6A_i\left(\bar{T}_{i+1}(t)-\bar{T}_i(t)\right)}{\Delta r^2} \quad (3.22)$$

This study assumes that the surface temperature is fixed at 250 K such that Eqs. 3.12 and 3.22 can be used to solve for the thermal evolution at a given radius r_i. To account for radiogenic heat production over time a heat production term is added to Eq. 3.12 (Özisik, 1993):

$$\frac{\partial T_i(t)}{\partial t}=\frac{A_i}{2i\Delta r^2}\left((i+2)\bar{T}_{i+1}(t)-2i\bar{T}_i(t)+(i-2)\bar{T}_{i-1}(t)\right)+\frac{A_{i+1}}{2\Delta r^2}\left(\bar{T}_{i+1}(t)-\bar{T}_i(t)\right)+$$

$$\frac{A_{i-1}}{2\Delta r^2}\left(\bar{T}_{i-1}(t)-\bar{T}_i(t)\right)+A_iG_i(t),\ \text{if } i=1,2,\dots N-1 \text{ and } t>0 \quad (3.23)$$

where $G_i(t)$ represents the energy production coefficient for a given interval of i and a given time. If n represents the time interval from $n=1,2,\dots,Nt$ and i represent the radius interval from $i=0,1,\dots,N$, the energy production coefficient is:

$$G_i^n=\frac{\Delta\hat{r}^2g_i^n}{K_i} \quad (3.24)$$

where g_i^n is the total energy (J) produced by decay for ^{232}Th, ^{235}U, ^{238}U, and ^{40}K over a time step Δt for a given radius, and K_i is the thermal conductivity at interval i. Total energy (J) produced by decay g_i^n is calculated for every time interval n by calculating the difference in radiogenic heat potential of each element for a given r_i. The variation in radiogenic heat potential between time intervals $n-1$ and n is used to determine the

energy (J) produced per element for time interval n. The parameters for energy production per decay of ^{232}Th, ^{235}U, ^{238}U, and ^{40}K were taken from Ruedas (2017) (**Table 3.4**). In summary:

$$T_i^n - T_i^{n-1} =$$

$$\begin{cases} \frac{6A_i\left(\bar{T}_{i+1}^{n-1} - \bar{T}_i^{n-1}\right)}{\Delta r^2}, & \text{if } i = 0 \\ \frac{A_i}{2i\Delta r^2}\left((i+2)\bar{T}_{i+1}^{n-1} - 2i\bar{T}_i^{n-1} + (i-2)\bar{T}_{i-1}^{n-1}\right) + \frac{A_{i+1}}{2\Delta r^2}\left(\bar{T}_{i+1}^{n-1} - \bar{T}_i^{n-1}\right) \dots \\ \quad + \frac{A_{i-1}}{2\Delta r^2}\left(\bar{T}_{i-1}^{n-1} - \bar{T}_i^{n-1}\right) + A_i G_i^n, & \text{if } i = 1,2,\dots,N-1 \\ 0, & \text{if } i = N \end{cases} \quad (3.25)$$

This numerical model has been successfully tested against the analytical solution to the heat production-conduction model of Hevey and Sanders (2006) (**Figure C4**).

3.4.2 Density, Conductivity, and Heat Capacity Assumptions

To simplify the problem, the Moon is broken into three layers: crustal cumulates, mantle cumulates, and core. Each layer is assigned a constant value for heat capacity, thermal diffusivity, and density to avoid additional uncertainty related to model-dependent mineral abundance, density, and composition variations. The thermal conductivity and heat capacity constants for crustal and mantle cumulate layers were determined using the reported thermal conductivity and heat capacities of the minerals that comprise each layer (Waples and Waples, 2004). The crustal and mantle densities were assumed to be equal to anorthite and olivine, respectively. We apply the thermal conductivity, heat capacity, and density values used by Zhang et al. (2013) and Li et al. (2019) for the lunar core. Model assumptions are reported in **Table 3.5**.

Table 3.4. Atomic Mass (u), Half-life ($T_{1/2}$), Present-Day Fractional Abundance (X_{iso}), Heat-Effective Decay Energy per Atom (E_H), and Specific Heat Production (H) of ^{40}K, ^{232}Th, ^{235}U, and ^{238}U from Ruedas (2017).

Isotope	u (a.m.u.)	$T_{1/2}$ (Myr)	X_{iso}	E_H (J)	H (W/kg)
^{40}K	39.9639982	1,248	0.0001167	1.084E-13	2.876E-05
^{232}Th	232.0380537	14,000	1	6.476E-12	2.637E-05
^{235}U	235.0439282	704	0.0072045	7.110E-12	5.684E-04
^{238}U	238.0507870	4,468	0.9927955	7.634E-12	9.495E-05

Table 3.5. Parameter assumptions used in thermal evolution calculations in this study.

Term	Symbol	Units	Value
Radius of Moon	R	km	1740
Radius of Outer Core	R_{core}	km	340
Radius of Lower Crust	R_{crust}	km	1688
Crustal Thermal Conductivity	K	W $m^{-1}K^{-1}$	1.68
Mantle Thermal Conductivity	K	W $m^{-1}K^{-1}$	5
Core Thermal Conductivity	K	W $m^{-1}K^{-1}$	50
Crustal Specific Heat Capacity	C_P	J $kg^{-1}K^{-1}$	762
Mantle Specific Heat Capacity	C_P	J $kg^{-1}K^{-1}$	830
Core Specific Heat Capacity	C_P	J $kg^{-1}K^{-1}$	800
Crustal Density	ρ	kg m^{-3}	2760
Mantle Density	ρ	kg m^{-3}	3400
Core Density	ρ	kg m^{-3}	7800
Crustal Thermal Diffusivity	κ	m^2 s^{-1}	7.99E-07
Mantle Thermal Diffusivity	κ	m^2 s^{-1}	1.77E-06
Core Thermal Diffusivity	κ	m^2 s^{-1}	8.01E-06
Ambient Temperature	T_0	K	250

3.4.3 P-T Conditions of the Lunar Mantle

Following magma ocean solidification, the terrestrial anhydrous peridotite solidus model from Katz et al. (2003) is assumed as the initial temperature Eq. (3.26):

$$T_r = 1085.7 + 132.9P_r - 5.1P_r^2 \quad (3.26)$$

where T_r is the solidus temperature (°C) at a given radius (r) within the Moon, P_r is the pressure (GPa) at that radius. The lunar pressure gradient model from Elkins-Tanton et al. (2011) is applied Eq. 3.27:

$$P_r = (-1.522 \times 10^{-6})r^2 + (-8.963 \times 10^{-5})r + 4.7 \quad (3.27)$$

where r is the radius (km) within the Moon.

3.4.4 HPE and Thermal Distributions Before and After Overturn

Thermal models in this study test three lunar HPE budgets with K/Th ratios of 464 and U/Th ratios of 0.2613 based on the findings of this study and previous studies (Taylor and Wieczorek, 2014; Seigler et al., 2022). These HPE budgets assume high-Th (0.11 ppm), moderate-Th (0.0795 ppm), and low-Th (0.0432 ppm) compositions to evaluate the effect of changing the Th abundance within the range of lunar and terrestrial estimates. We also test a fourth reference scenario with a K/Th ratio of 3019 and moderate-Th (0.0795 ppm) to evaluate how much the low lunar K/Th ratio favored by geochemical models in this study would affect the lunar thermal evolution relative to a terrestrial K/Th ratio.

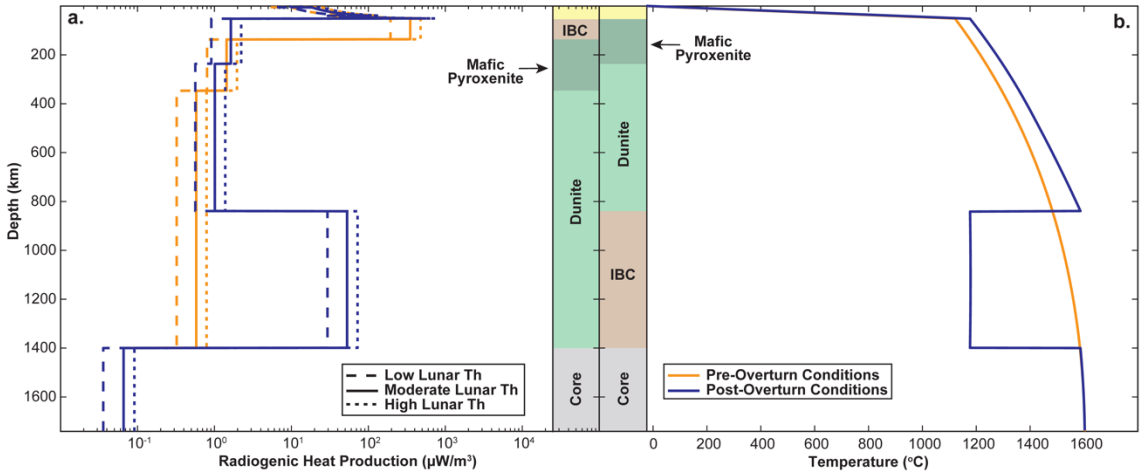


Figure 3.3. Pre- and post-overturn HPE (a) and temperature (b) distributions tested in this study. The assumed lunar stratigraphy for the models which assume overturn did not occur are shown in the sub-panel on the right side of (a). The assumed lunar stratigraphy for the models that assume overturn occurred is shown in the sub-panel on the left side of (b).

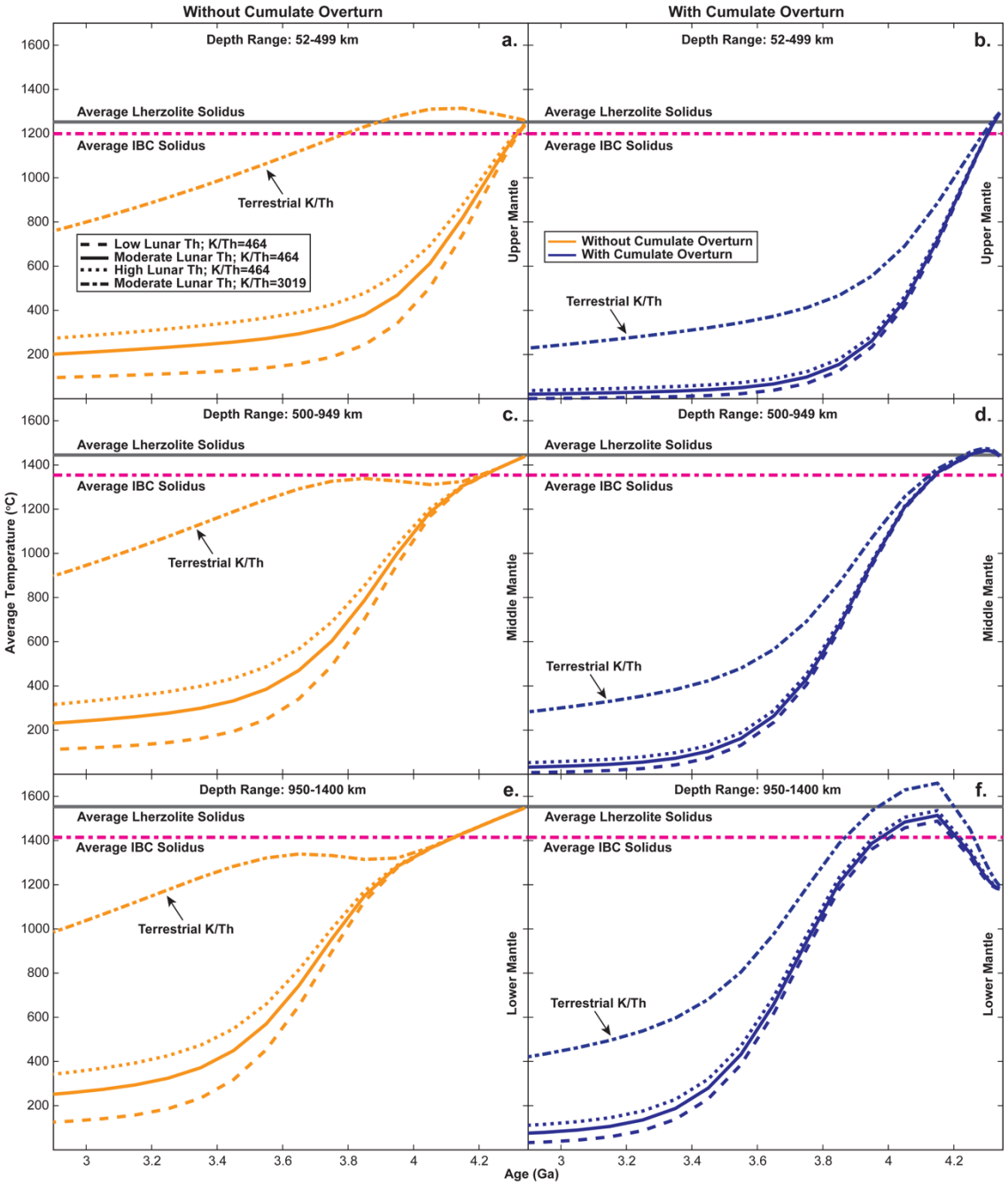
We simplify the HPE distribution and assume the mantle cumulates comprise three layers: (1) an early mantle dunite layer (i.e., stage 1 cumulates), (2) a mafic pyroxenite layer (i.e., stage 2 cumulates), and (3) an IBC layer (stage 3-6 cumulates, **Table 3.1** and **Figure 3.3**). We also assume that the HPE budget of these layers is evenly distributed across them. Making the simplifying assumption that density does not change after overturn, the radiogenic heat production per km in the lunar interior changes according to the volume of the IBC layer prior to and after overturn (**Figure 3.3a**).

For overturn models in this study, overturn is assumed to be 100% efficient and occurs quickly enough that there is negligible thermal exchange during the overturn process. Thus, the post-overturn thermal structure shifts the thermal gradient of the lower lunar mantle layers upward. The IBC is assumed to have a temperature equal to the average temperature of cumulate layers 3-6 before cumulate overturn (**Figure 3.3b**).

3.5 Thermal Modeling Results

The model results depend on the initial thermal structure, HPE distribution, and K/Th ratio. In cases where overturn does not occur and the Moon has a K/Th ratio of 464, the lunar mantle reaches subsolidus temperatures relatively quickly (i.e., by 4.3-3.9 Ga, depending on the depth) due to the K-depleted composition of the Moon (**Figure 3.4**). Changing the Th abundance within the range of lunar and terrestrial estimates has a relatively negligible effect on short-term thermal evolution.

Figure 3.4. Post 4.35 Ga thermal evolution of the upper (top row), middle (middle row), and lower lunar mantle (bottom row) for scenarios with and without lunar cumulate overturn (left and right columns). The terrestrial K/Th model assumes an Earth-like ratio of 3019. The three other models assume this study's preferred lunar K/Th ratio (i.e., 464) and test various Th abundances (i.e., various degrees of refractory element enrichment or depletion). All models in this figure assume the U/Th ratio of 0.2613 for each HPE budget. The average lherzolite and IBC solidus temperatures for the given depth ranges are represented by the horizontal solid (Lherzolite) and dashed (IBC) lines. The lherzolite solidus temperatures were determined using Eq.'s 3.26 and 3.27. The IBC solidus was determined using the experimentally determined IBC solidus from (Scholpp and Dygert, 2024) (see Appendix C and Figure C5 for further discussion). This figure shows how the overturn of late crystallizing LMO cumulates would be required to initiate lunar mantle melting if the Moon had a highly K-depleted composition, as suggested by this study. The figure also shows that another heat production or retention mechanism is likely required for the Moon to produce mantle melts after ~3.88 Ga, as radiogenic heating alone fails to maintain long-term melting even if we assume an Earth-like K/Th ratio.


Without Cumulate Overturn
With Cumulate Overturn
Depth Range: 52-499 km
a.
b.
Average Lherzolite Solidus
Average IBC Solidus
Terrestrial K/Th
Low Lunar Th; K/Th=464
Moderate Lunar Th; K/Th=464
High Lunar Th; K/Th=464
Moderate Lunar Th; K/Th=3019
Without Cumulate Overturn
With Cumulate Overturn
Upper Mantle
Depth Range: 500-949 km
c.
d.
Middle Mantle
Depth Range: 950-1400 km
e.
f.
Lower Mantle
Average Temperature (°C)
Age (Ga)

In cases where overturn does not occur and the Moon has an Earth-like K/Th ratio of 3019, the lunar mantle reaches subsolidus temperatures at a similar rate to the model with less K in the middle and lower mantle; however, the effects of lower crustal and upper mantle cumulate heat production reheat the upper mantle and keep the upper mantle partially molten until ~3.8 Ga (**Figure 3.4**). This upper mantle heating also creates a downward propagating thermal pulse in the mantle, which peaks at ~4.15 Ga in the upper mantle (**Figure 3.4a**), ~3.8 Ga in the middle mantle (**Figure 3.4c**), and ~3.6 Ga in the lower mantle (**Figure 3.4e**). These model results demonstrate that the depletion of K on the Moon would significantly affect the thermal evolution.

In cases where overturn occurs, two mechanisms could induce lunar mantle melting at different depths (**Figure 3.4b, 3.4d, 3.4f**). The first mechanism (i.e., decompression melting) would primarily affect the upper mantle (i.e., 52-499 km depth) as the lower mantle cumulates are displaced by the overturning cumulates and ascend into the upper mantle where mantle pressures are lower (**Figure 3.4b**). This event would likely be short-lived (i.e., 4.35-4.28 Ga regardless of the K/Th ratio); however, it should be noted that the occurrence of this melting event is not only dependent on the initial cumulate temperatures but also on the rate of overturn. Thus, 3D dynamic overturn models, which account for the rate of downwelling and material displacement, are required to determine whether this event would occur. The second mechanism (i.e., radiogenic heating) would primarily affect the middle and lower lunar mantle (i.e., 500-1400 km depth) as the cold but HPE-rich IBC material began to heat up in the lower mantle (**Figure 3.4d and 3.4f**). This heating process should result in melting; however,

the model results indicate that the melts would be constrained to IBC material or hybridized peridotites unless the lunar K/Th ratio was more Earth-like or the overturned cumulates experienced significant conductive heating during overturn. This melting event would last slightly longer (i.e., ~4.32-3.88 Ga for a K/Th ratio of 464 or ~4.32-3.80 Ga for a K/Th ratio of 3019) than the earlier melting period as the heat produced by radioactive decay would need to diffuse through the overlying lunar mantle material.

Another notable feature of cases where overturn occurs, is the lower temperatures throughout the lunar mantle at ~3 Ga relative to the cases without overturn (**Figure 3.4)**. This decrease in long-term mantle temperatures likely occurs for two reasons: (1) cooling of the lunar core by the overturned cumulates, and (2) the upper mantle cumulates thermally insulate the lunar mantle if overturn doesn't occur. Cooling of the lunar core would occur quickly because the metallic core has a much higher thermal diffusivity than the mantle (i.e., the core should cool off or heat up faster than the mantle) (**Table 3.5**). This means that overturn effectively carries an extra layer of cold material beneath the overturned cumulates that must be heated by radioactive decay. Without overturn, the HPE-rich upper mantle cumulates thermally insulate the upper mantle due to their high radiogenic heat output. This insulating effect is best demonstrated by comparing the models that assume an Earth-like K/Th ratio with and without overturn (**Figure 3.4**). In the model that assumes no cumulate overturn occurs, the radiogenic heat produced by the upper mantle cumulates heats the mantle from above. The lower crustal heating adds to this insulating effect; however, this effect is primarily related to the upper mantle

cumulates because the downward propagating thermal pulse from the upper mantle is absent in the model that assumes overturn occurred.

The models presented in this study are informative when thinking about how the cumulate overturn and the degree of K depletion would affect the lunar thermal evolution; however, the results of these models aren't necessarily representative of the actual lunar thermal history. If we consider the average ages of lunar Mg-Suite samples (4.30±0.11 Ga; Bogard et al., 1975; Hinthorne et al., 1975; Huneke and Wasserburg, 1975; Husain and Schaeffer; 1975; Turner and Cadogan, 1975; Lugmair et al., 1976; Nakamura et al., 1976; Oberli et al., 1978; Carlson and Lugmair 1981; Aeschlimann et al., 1982; Nyquist et al., 1982; Compston et al., 1984; Meyer et al., 1989; Shih et al., 1993; Carlson et al., 2014; Borg et al., 2019), lunar KREEP basalts (3.92±0.07 Ga; Sprung et al., 2013; Gaffney and Borg, 2014; Borg et al., 2019), high-Ti mare basalts (3.72±0.06 Ga; Evensen et al., 1973; Huneke et al, 1973; Kirsten et al., 1973; Tera et al., 1974; Kirsten and Horn, 1974; Lugmair et al., 1975; Nyquist et al., 1974; Turner and Cadogan, 1975; Murthy and Coscio, 1976; Schaeffer, 1977; Unruh et al., 1984; Paces et al., 1991; Beard et al., 1997; Sprung et al., 2013; Borg et al., 2019), low-Ti mare basalts (3.28±0.10 Ga; Unruh et al., 1984; Sprung et al., 2013; Borg et al., 2019), and the recently recovered Chang'e 6 (2.83±0.005 Ga; Cui et al., 2024; Zhang et al., 2024) and Chang'e 5 basalts (2.03±0.004 Ga; Li et al., 2021), it is evident that the history of mafic lunar volcanism covers a ~2.27 Gyr period following the Moon's formation. In addition to this period of mafic volcanism, geophysical studies of the lunar mantle indicate that the Moon likely contains a solid core surrounded by a molten or partially molten layer of

material (Wieczorek et al., 2006; Weber et al., 2011). The model results from this study indicate that mantle melting should last for ~0.55 Gyr following lunar formation regardless of the assumed K/Th ratio (**Figure 3.4**) (i.e., our modeled Moon would solidify long before the isotopic dates and geophysical data suggest it should). Thus, there must be other heat production or heat retention mechanisms that models in this study don't account for.

3.6 Mechanisms That Could Prolong Lunar Thermal Evolution

The model results for cases with and without cumulate overturn suggest that radiogenic heating alone couldn't account for the protracted history of lunar basaltic volcanism if the HPE were symmetrically distributed throughout the lunar mantle; however, this may change given different model parameters. One parameter that could significantly affect the thermal evolution models is the assumed thermal diffusivity of the lunar crust. Models in this study assume that the crustal layer has a constant thermal diffusivity equal to anorthite; however, variations in the crustal density with depth would directly affect the thermal diffusivity. Previous studies indicate that the porosity of the lunar crust decreases with depth due to the lunar impact history (Toksöz et al., 1978; Hörz et al., 1991; Wieczorek et al., 2013). This would directly affect the density and thermal diffusivity of the lunar crust, resulting in a lower density and diffusivity for the upper crust and a higher density and diffusivity for the lower crust (Smoluchowski, 1981; Siegler and Smrekar, 2014; Henke et al., 2016). Depending on the density and porosity profiles you assume for the average lunar crust, this could significantly impact heat retention.

Another parameter that could affect the thermal evolution models is the latent heat released during core solidification (Laneuville et al., 2014). The heat produced by this process would likely be significantly lower than the heat produced by radiogenic decay; however, in cases where overturn occurs, the heat released by crystallization of the cooling core would decrease the effect of overturn on the core temperatures. This means less radiogenic heat from the overturned cumulates would be lost to the rapidly cooling core, and more heat would go towards heating the lunar mantle.

The most straightforward mechanism to extend the lunar thermal evolution might be to decrease the efficiency of cumulate overturn. This would adjust the distribution of HPE throughout the Moon by retaining some of the upper mantle cumulates near the crust-mantle boundary and transferring a smaller portion of these cumulates deep within the lunar mantle. Based on the models from this study (**Figure 3.4**), this may extend the lunar thermal evolution in two ways: (1) it would minimize the cooling effect of cumulate overturn on the lower mantle, and (2) it would leave a more of the HPE-rich cumulates in the upper mantle where they could thermally insulate the lunar mantle.

It should also be noted that other mechanisms like the asymmetric redistribution of HPE due to large-scale cumulate overturn events (Zhong et al., 2000; Laneuville et al., 2013, 2018; Moriarty et al., 2021; Zhang et al., 2022) or shock heating during multiple large basin-forming impacts (Perera et al., 2018; Rolf et al., 2017; Jones et al., 2022) could also aid in extending the lunar thermal evolution. These mechanisms for producing heat are highly model dependent (e.g., the mechanism that initiated overturn, mantle rheologic properties at the time of overturn or impact, impact rate, etc… can all

significantly alter the distribution of elements or heat produced by impacts) so we avoid further speculation on their overall impact. In reality, a combination of multiple mechanisms discussed above is likely required to explain the protracted history of lunar volcanism and the possibly present-day molten state of material around the modern lunar core; however, each mechanism needs to be tested by future thermal models.

3.7 Conclusions

This work attempts to constrain the K/Th ratio of the initial lunar magma ocean. Using experimentally determined LMO cumulate solidification sequences and up-to-date lunar trace element partition coefficients, we model chemical fractionation during LMO solidification and post-solidification partial melting. Geochemical models of LMO solidification demonstrate that the K/Th ratio of the initial LMO could range from 450-550 if the floatation efficiency of plagioclase is ≥95%. If plagioclase floatation is less efficient, the K/Th ratio of the LMO would have to decrease such that the crystallizing cumulates have similar K/Th ratios to mantle-derived lunar melts (i.e., mare basalts and picritic glasses) as secondary partial melts should have similar K/Th ratios to their respective mantle sources.

Thermal evolution models from this study demonstrate that the degree of K depletion on the Moon has a far more significant impact on lunar thermal evolution than the degree of possible Th and U enrichment relative to Earth. Thermal evolution models that assume cumulate overturn occurred indicate that two separate mantle melting events could occur if overturn occurs quickly: (1) an early decompression melting event in the

upper mantle and (2) a later radiogenic heating-induced melting event in the middle and lower lunar mantle caused by the displaced and HPE-rich IBC material.

References

Aeschlimann, U., Eberhardt, P., Geiss, J., Grogler, N., Kurtz, J., and Marti, K., 1982, On the Age of Cumulate Norite 78236: an 39AR-40AR Study, *in* Lunar and Planetary Science Conference, Lunar and Planetary Science Conference, p. 1–2.

Anders, E., and Grevesse, N., 1989, Abundances of the elements: Meteoritic and solar: Geochimica et Cosmochimica Acta, v. 53, p. 197–214, doi:10.1016/0016-7037(89)90286-X.

Barr, J.A., and Grove, T.L., 2013, Experimental petrology of the Apollo 15 group A green glasses: Melting primordial lunar mantle and magma ocean cumulate assimilation: Geochimica et Cosmochimica Acta, v. 106, p. 216–230, doi:10.1016/j.gca.2012.12.035.

Beard, B.L., Taylor, L.A., Scherer, E.E., Johnson, C.M., and Snyder, G.A., 1998, The Source Region and Melting Mineralogy of High-Titanium and Low-Titanium Lunar Basalts Deduced from Lu-Hf Isotope Data: Geochimica et Cosmochimica Acta, v. 62, p. 525–544, doi:10.1016/S0016-7037(97)00373-6.

Bogard, D.D., Nyquist, L.E., Bansal, B.M., Wiesmann, H., and Shih, C.Y., 1975, 76535: An old lunar rock: Earth and Planetary Science Letters, v. 26, p. 69–80, doi:10.1016/0012-821X(75)90178-8.

Borg, L.E., Cassata, W.S., Wimpenny, J., Gaffney, A.M., and Shearer, C.K., 2020, The formation and evolution of the Moon's crust inferred from the Sm-Nd isotopic systematics of highlands rocks: Geochimica et Cosmochimica Acta, v. 290, p. 312–332, doi:10.1016/j.gca.2020.09.013.

Borg, L.E., Gaffney, A.M., Kruijer, T.S., Marks, N.A., Sio, C.K., and Wimpenny, J., 2019, Isotopic evidence for a young lunar magma ocean: Earth and Planetary Science Letters, v. 523, p. 115706, doi:10.1016/j.epsl.2019.07.008.

Brown, S.M., and Grove, T.L., 2015, Origin of the Apollo 14, 15, and 17 yellow ultramafic glasses by mixing of deep cumulate remelts: Geochimica et Cosmochimica Acta, v. 171, p. 201–215, doi:10.1016/j.gca.2015.09.001.

Canup, R.M., 2008, Accretion of the Earth: Philosophical Transactions of the Royal Society A: Mathematical, Physical and Engineering Sciences, v. 366, p. 4061–4075, doi:10.1098/rsta.2008.0101.

Canup, R.M., 2004, Dynamics of Lunar Formation: Annual Review of Astronomy and Astrophysics, v. 42, p. 441–475, doi:https://doi.org/10.1146/annurev.astro.41.082201.113457.

Cao, H., Ling, Z., Chen, J., Fu, X., and Zou, Y., 2021, Petrography, mineralogy, and geochemistry of a new lunar magnesian feldspathic meteorite Northwest Africa 11460: Meteoritics & Planetary Science, v. 56, p. 1857–1889, doi:10.1111/maps.13741.

Carlson, R.W., Borg, L.E., Gaffney, A.M., and Boyet, M., 2014, Rb-Sr, Sm-Nd and Lu-Hf isotope systematics of the lunar Mg-suite: the age of the lunar crust and its relation to the time of Moon formation: Philosophical Transactions of the Royal Society A: Mathematical, Physical and Engineering Sciences, v. 372, p. 20130246, doi:10.1098/rsta.2013.0246.

Carlson, R.W., and Lugmair, G.W., 1981, Sm-Nd age of lherzolite 67667: implications for the processes involved in lunar crustal formation: Earth and Planetary Science Letters, v. 56, p. 1–8, doi:10.1016/0012-821X(81)90112-6.

Carslaw, H.S., and Jaeger, J.C., 1986, Conduction of heat in solids: Conduction of heat in solids,.

Compston, W., Williams, I.S., and Meyer, C., 1984, U-Pb geochronology of zircons from lunar breccia 73217 using a sensitive high mass-resolution ion microprobe: Journal of Geophysical Research: Solid Earth, v. 89, p. B525–B534, doi:10.1029/JB089iS02p0B525.

Crank, J., 1975, The mathematics of diffusion: Oxford university press.

Criss, R.E., and Hofmeister, A.M., 2016, Conductive cooling of spherical bodies with emphasis on the Earth: Terra Nova, v. 28, p. 101–109, doi:10.1111/ter.12195.

Cui, Z. et al. A sample of the Moon's far side retrieved by Chang'e-6 contains 2.83-billion-year-old basalt: Science, v. 0, p. eadt1093, doi:10.1126/science.adt1093.

Elkins-Tanton, L.T., Burgess, S., and Yin, Q.-Z., 2011, The lunar magma ocean: Reconciling the solidification process with lunar petrology and geochronology: Earth and Planetary Science Letters, v. 304, p. 326–336, doi:10.1016/j.epsl.2011.02.004.

Elkins-Tanton, L.T., Chatterjee, N., and Grove, T.L., 2003, Experimental and petrological constraints on lunar differentiation from the Apollo 15 green picritic glasses: Meteoritics & Planetary Science, v. 38, p. 515–527, doi:10.1111/j.1945-5100.2003.tb00024.x.

Evensen, N.M., Murthy, V.R., and Coscio, Jr., M.R., 1973, Rb-Sr ages of some mare basalts and the isotopic and trace element systematics in lunar fines: Lunar and Planetary Science Conference Proceedings, v. 4, p. 1707.

Faure, P., Bouhifd, M.A., Boyet, M., Manthilake, G., Clesi, V., and Devidal, J.-L., 2020, Uranium and thorium partitioning in the bulk silicate Earth and the oxygen content of Earth's core: Geochimica et Cosmochimica Acta, v. 275, p. 83–98, doi:10.1016/j.gca.2020.02.010.

Ford Versypt, A.N., 2012, Modeling of controlled-release drug delivery from autocatalytically degrading polymer microspheres: University of Illinois at Urbana-Champaign.

Ford Versypt, A.N., and Braatz, R.D., 2014, Analysis of finite difference discretization schemes for diffusion in spheres with variable diffusivity: Computers & Chemical Engineering, v. 71, p. 241–252, doi:10.1016/j.compchemeng.2014.05.022.

Fu, X., Cao, H., Chen, J., Hou, X., Ling, Z., Xu, L., Zou, Y., Tang, C., and Hsu, W., 2021, Petrology and geochemistry of lunar feldspathic meteorite Northwest Africa 11111: Insights into the lithology of the lunar farside highlands: Meteoritics & Planetary Science, v. 56, p. 1829–1856, doi:10.1111/maps.13743.

Gaffney, A.M., and Borg, L.E., 2014, A young solidification age for the lunar magma ocean: Geochimica et Cosmochimica Acta, v. 140, p. 227–240, doi:10.1016/j.gca.2014.05.028.

Gagnepain-Beyneix, J., Lognonné, P., Chenet, H., Lombardi, D., and Spohn, T., 2006, A seismic model of the lunar mantle and constraints on temperature and mineralogy:

Physics of the Earth and Planetary Interiors, v. 159, p. 140–166, doi:10.1016/j.pepi.2006.05.009.

Garrick-Bethell, I., Nimmo, F., and Wieczorek, M.A., 2010, Structure and Formation of the Lunar Farside Highlands: Science, v. 330, p. 949–951, doi:10.1126/science.1193424.

Hagerty, J.J., Shearer, C.K., and Vaniman, D.T., 2006, Heat-producing elements in the lunar mantle: Insights from ion microprobe analyses of lunar pyroclastic glasses: Geochimica et Cosmochimica Acta, v. 70, p. 3457–3476, doi:10.1016/j.gca.2006.04.013.

Hallis, L.J., Anand, M., and Strekopytov, S., 2014, Trace-element modelling of mare basalt parental melts: Implications for a heterogeneous lunar mantle: Geochimica et Cosmochimica Acta, v. 134, p. 289–316, doi:10.1016/j.gca.2014.01.012.

Haupt, C.P., Renggli, C.J., Rohrbach, A., Berndt, J., and Klemme, S., 2024, Experimental Constraints on the Origin of the Lunar High-Ti Basalts: Journal of Geophysical Research: Planets, v. 129, p. e2023JE008239, doi:10.1029/2023JE008239.

He, Q. et al., 2024, Petrogenesis of magnesian troctolitic granulite clasts from Chang'e -5 drilling sample: Implications for the origin of ejecta material from lunar highlands: Icarus, v. 408, p. 115853, doi:10.1016/j.icarus.2023.115853.

Henke, S., Gail, H.-P., and Trieloff, M., 2016, Thermal evolution and sintering of chondritic planetesimals: A&A, v. 589, doi:10.1051/0004-6361/201527687.

Hevey, P.J., and Sanders, I.S., 2006, A model for planetesimal meltdown by 26Al and its implications for meteorite parent bodies: Meteoritics & Planetary Science, v. 41, p. 95–106, doi:10.1111/j.1945-5100.2006.tb00195.x.

Hinthorne, J.R., Conrad, R., and Andersen, C.A., 1975, Lead-Lead Age and Trace Element Abundances in Lunar Troctolite 76535, *in* Lunar and Planetary Science Conference, Lunar and Planetary Science Conference, v. 6, p. 373.

Hörz, F., Grieve, R., Heiken, G., Spudis, P., and Binder, A., 1991, Lunar Surface Processes, *in* Heiken, G.H., Vaniman, D.T., and French, B.M. eds., Lunar Sourcebook, A User's Guide to the Moon, p. 61–120.

Hughes, S.S., Delano, J.W., and Schmitt, R.A., 1990, Chemistry of individual mare volcanic glasses: evidence for distinct regions of hybridized mantle and a KREEP component in Apollo 14 magmatic sources.: Lunar and Planetary Science Conference Proceedings, v. 20, p. 127–138.

Huneke, J.C., Jessberger, E.K., Podosek, F.A., and Wasserburg, G.J., 1973, $^{40}Ar/^{39}Ar$ measurements in Apollo 16 and 17 samples and the chronology of metamorphic and volcanic activity in the Taurus-Littrow region: Lunar and Planetary Science Conference Proceedings, v. 4, p. 1725.

Huneke, J.C., and Wasserburg, G.J., 1975, Trapped 40Ar in Troctolite 76535 and Evidence for Enhanced 40Ar-39Ar Age Plateaus, *in* Lunar and Planetary Science Conference, Lunar and Planetary Science Conference, v. 6, p. 417.

Husain, L., and Schaeffer, O.A., 1975, Lunar evolution: The first 600 million years: Geophysical Research Letters, v. 2, p. 29–32, doi:10.1029/GL002i001p00029.

Jones, M.J., Evans, A.J., Johnson, B.C., Weller, M.B., Andrews-Hanna, J.C., Tikoo, S.M., and Keane, J.T. A South Pole–Aitken impact origin of the lunar compositional asymmetry: Science Advances, v. 8, p. eabm8475, doi:10.1126/sciadv.abm8475.

van Kan Parker, M., Mason, P.R.D., and van Westrenen, W., 2011, Experimental study of trace element partitioning between lunar orthopyroxene and anhydrous silicate melt: Effects of lithium and iron: Chemical Geology, v. 285, p. 1–14, doi:10.1016/j.chemgeo.2011.02.007.

Katz, R.F., Spiegelman, M., and Langmuir, C.H., 2003, A new parameterization of hydrous mantle melting: Geochemistry, Geophysics, Geosystems, v. 4, doi:10.1029/2002GC000433.

Kent, J.J., Brandon, A.D., Joy, K.H., Peslier, A.H., Lapen, T.J., Irving, A.J., and Coleff, D.M., 2017, Mineralogy and petrogenesis of lunar magnesian granulitic meteorite Northwest Africa 5744: Meteoritics & Planetary Science, v. 52, p. 1916–1940, doi:10.1111/maps.12898.

Kirsten, T., and Horn, P., 1974, 39Ar-40Ar-Chronology of the Taurus-Littrow Region II: A 4.28 b.y. Old Troctolite and Ages of Basalts and Highland Breccias, *in* Lunar and Planetary Science Conference, Lunar and Planetary Science Conference, v. 5, p. 419.

Kirsten, T., Horn, P., and Heymann, D., 1973, Chronology of the Taurus-Littrow region I: Ages of two major rock types from the Apollo 17-site: Earth and Planetary Science Letters, v. 20, p. 125–130, doi:10.1016/0012-821X(73)90149-0.

Laneuville, M., Taylor, J., and Wieczorek, M., 2018, Distribution of radioactive heat sources and thermal history of the Moon: Journal of Geophysical Research: Planets, v. 123, p. 3144–3166, doi:10.1029/2018JE005742.

Laneuville, M., Wieczorek, M.A., Breuer, D., Aubert, J., Morard, G., and Rückriemen, T., 2014, A long-lived lunar dynamo powered by core crystallization: Earth and Planetary Science Letters, v. 401, p. 251–260, doi:10.1016/j.epsl.2014.05.057.

Laneuville, M., Wieczorek, M., Breuer, D., and Tosi, N., 2013, Asymmetric thermal evolution of the Moon: Journal of Geophysical Research: Planets, v. 118, p. 1435–1452, doi:10.1002/jgre.20103.

Leitzke, F.P., Fonseca, R.O.C., Michely, L.T., Sprung, P., Münker, C., Heuser, A., and Blanchard, H., 2016, The effect of titanium on the partitioning behavior of high-field strength elements between silicates, oxides and lunar basaltic melts with applications to the origin of mare basalts: Chemical Geology, v. 440, p. 219–238, doi:10.1016/j.chemgeo.2016.07.011.

Li, Q.-L. et al., 2021, Two-billion-year-old volcanism on the Moon from Chang'e-5 basalts: Nature, v. 600, p. 54–58, doi:10.1038/s41586-021-04100-2.

Li, M., Huang, S., Petaev, M.I., Zhu, Z., and Steffen, J.H., 2020, Dust condensation in evolving discs and the composition of planetary building blocks: Monthly Notices of the Royal Astronomical Society, v. 495, p. 2543–2553, doi:10.1093/mnras/staa1149.

Li, H., Zhang, N., Liang, Y., Wu, B., Dygert, N.J., Huang, J., and Parmentier, E.M., 2019, Lunar Cumulate Mantle Overturn: A Model Constrained by Ilmenite

Rheology: Journal of Geophysical Research: Planets, v. 124, p. 1357–1378, doi:10.1029/2018JE005905.

Lodders, K., 2003, Solar System Abundances and Condensation Temperatures of the Elements: The Astrophysical Journal, v. 591, p. 1220, doi:10.1086/375492.

Lugmair, G.W., Kurtz, J.P., Marti, K., and Scheinin, N.B., 1976, The Low-Sm/Nd Region of the Moon: Evolution and History of a Troctolite and a KREEP Basalt, *in* Lunar and Planetary Science Conference, Lunar and Planetary Science Conference, v. 7, p. 509.

Lugmair, G.W., Scheinin, N.B., and Marti, K., 1975, Sm-Nd Age of Apollo 17 Basalt 75075: Two-Stage Igneous Processes in Mare Basalt Genesis, *in* Lunar and Planetary Science Conference, Lunar and Planetary Science Conference, v. 6, p. 531.

McDonough, W.F., and Sun, S. -s., 1995, The composition of the Earth: Chemical Evolution of the Mantle, v. 120, p. 223–253, doi:10.1016/0009-2541(94)00140-4.

McIntosh, E.C., Day, J.M.D., McCubbin, F.M., Vander Kaaden, K.E., Hattingh, R., and Porrachia, M., 2024, Revisiting the Petrogenesis of Pyroclastic Glass Bead Deposits at the Apollo 15 and 17 Sites: Journal of Petrology, v. 65, p. egae026, doi:10.1093/petrology/egae026.

Meyer, C., Williams, I.S., and Compston, W., 1989, $^{207}Pb/^{206}Pb$ Ages of Zircon-containing Rock Fragments Indicate Continuous Magmatism in the Lunar Crust from 4350 to 3900 Million Years, *in* LPI Editorial Board ed., 20th Lunar and Planetary Science Conference, LPI Contributions, v. 698, p. 73.

Moriarty III, D.P., Watkins, R.N., Valencia, S.N., Kendall, J.D., Evans, A.J., Dygert, N., and Petro, N.E., 2021, Evidence for a Stratified Upper Mantle Preserved Within the South Pole-Aitken Basin: Journal of Geophysical Research: Planets, v. 126, p. e2020JE006589, doi:10.1029/2020JE006589.

Morton, K.W., and Mayers, D.F., 2005, Numerical solution of partial differential equations: an introduction: Cambridge university press.

Murthy, V.R., and Coscio, Jr., M.R., 1976, Rb-Sr ages and isotopic systematics of some Serenitatis mare basalts.: Lunar and Planetary Science Conference Proceedings, v. 2, p. 1529–1544.

Nakamura, N., Tatsumoto, M., Nunes, P.D., Unruh, D.M., Schwab, A.P., and Wildeman, T.R., 1976, 4.4 b.y.-old clast in Boulder 7, Apollo 17: a comprehensive chronological study by U-Pb, Rb-Sr and Sm-Nd methods.: Lunar and Planetary Science Conference Proceedings, v. 2, p. 2309–2333.

Nash, W.P., and Crecraft, H.R., 1985, Partition coefficients for trace elements in silicic magmas: Geochimica et Cosmochimica Acta, v. 49, p. 2309–2322, doi:10.1016/0016-7037(85)90231-5.

Neal, C.R., and Kramer, G.Y., 2003, The Composition of KREEP: A Detailed Study of KREEP Basalt 15386, *in* Mackwell, S. and Stansbery, E. eds., Lunar and Planetary Science Conference, Lunar and Planetary Science Conference, p. 2023.

Norman, M.D., Borg, L.E., Nyquist, L.E., and Bogard, D.D., 2003, Chronology, geochemistry, and petrology of a ferroan noritic anorthosite clast from Descartes breccia 67215: Clues to the age, origin, structure, and impact history of the lunar

crust: Meteoritics & Planetary Science, v. 38, p. 645–661, doi:10.1111/j.1945-5100.2003.tb00031.x.

Norman, M.D., Duncan, R.A., and Huard, J.J., 2010, Imbrium provenance for the Apollo 16 Descartes terrain: Argon ages and geochemistry of lunar breccias 67016 and 67455: Geochimica et Cosmochimica Acta, v. 74, p. 763–783, doi:10.1016/j.gca.2009.10.024.

Nyquist, L.E., 1982, Radiometric ages and isotopic systematics of pristine plutonic lunar rocks, *in* Walker, D. and McCallum, I.S. eds., Magmatic Processes of Early Planetary Crusts: Magma Oceans and Stratiform Layered Intrusions, p. 114.

Nyquist, L.E., Bansal, B.M., Wiesmann, H., and Jahn, B.M., 1974, Taurus-Littrow Chronology: Implications for Early Lunar Crustal Development, *in* Lunar and Planetary Science Conference, Lunar and Planetary Science Conference, v. 5, p. 565.

Nyquist, L., Bogard, D., Yamaguchi, A., Shih, C.-Y., Karouji, Y., Ebihara, M., Reese, Y., Garrison, D., McKay, G., and Takeda, H., 2006, Feldspathic clasts in Yamato-86032: Remnants of the lunar crust with implications for its formation and impact history: A Special Issue Dedicated to Larry A. Haskin, v. 70, p. 5990–6015, doi:10.1016/j.gca.2006.07.042.

Oberli, F., McCulloch, M.T., Tera, F., Papanastassiou, D.A., and Wasserburg, G.J., 1978, Early Lunar Differentiation Constraints from U-Th Sm-Nd and Rb-Sr Model Age, *in* Lunar and Planetary Science Conference, Lunar and Planetary Science Conference, p. 832–834.

Özısık, M.N., 1993, Finite-difference Methods, *in* Heat conduction, John Wiley & Sons, p. 436–501.

Paces, J.B., Nakai, S., Neal, C.R., Taylor, L.A., Halliday, A.N., and Lee, D.-C., 1991, A strontium and neodymium isotopic study of Apollo 17 high-Ti mare basalts: Resolution of ages, evolution of magmas, and origins of source heterogeneities: Geochimica et Cosmochimica Acta, v. 55, p. 2025–2043, doi:10.1016/0016-7037(91)90040-C.

Parmentier, E.M., Zhong, S., and Zuber, M.T., 2002, Gravitational differentiation due to initial chemical stratification: origin of lunar asymmetry by the creep of dense KREEP? Earth and Planetary Science Letters, v. 201, p. 473–480, doi:10.1016/S0012-821X(02)00726-4.

Perera, V., Jackson, A.P., Elkins-Tanton, L.T., and Asphaug, E., 2018, Effect of Reimpacting Debris on the Solidification of the Lunar Magma Ocean: Journal of Geophysical Research: Planets, v. 123, p. 1168–1191, doi:10.1029/2017JE005512.

Ringwood, A.E., 1986, Terrestrial origin of the Moon: Nature, v. 322, p. 323–328, doi:10.1038/322323a0.

Ringwood, A.E., and Kesson, S.E., 1977, Basaltic magmatism and the bulk composition of the moon: The moon, v. 16, p. 425–464, doi:10.1007/BF00577902.

Rolf, T., Zhu, M.-H., Wünnemann, K., and Werner, S.C., 2017, The role of impact bombardment history in lunar evolution: Icarus, v. 286, p. 138–152, doi:10.1016/j.icarus.2016.10.007.

Ruedas, T., 2017, Radioactive heat production of six geologically important nuclides: Geochemistry, Geophysics, Geosystems, v. 18, p. 3530–3541, doi:10.1002/2017GC006997.

Ryder, G., and Schuraytz, B.C., 2001, Chemical variation of the large Apollo 15 olivine-normative mare basalt rock samples: Journal of Geophysical Research: Planets, v. 106, p. 1435–1451, doi:10.1029/2000JE001368.

Schaeffer, O.A., Massey, H.S.W., Brown, G.M., Eglinton, G., Runcorn, S.K., and Urey, H.C., 1997, Lunar chronology as determined from the radiometric ages of returned lunar sample: Philosophical Transactions of the Royal Society of London. Series A, Mathematical and Physical Sciences, v. 285, p. 137–143, doi:10.1098/rsta.1977.0049.

Scholpp, J.L., and Dygert, N.J., in review, Tace Element and Isotopic Evolution of the Lunar Interior During Magma Ocean Solidification, Cumulate Overturn, and Subsequent Melting: Insights into Lunar Melt Sources: Journal of Geophysical Research: Planets,.

Shearer, C.K., and Papike, J.J., 1993, Basaltic magmatism on the Moon: A perspective from volcanic picritic glass beads: Geochimica et Cosmochimica Acta, v. 57, p. 4785–4812, doi:10.1016/0016-7037(93)90200-G.

Shearer, C.K., Papike, J.J., Galbreath, K.C., and Shimizu, N., 1991, Exploring the lunar mantle with secondary ion mass spectrometry: a comparison of lunar picritic glass beads from the Apollo 14 and Apollo 17 sites: Earth and Planetary Science Letters, v. 102, p. 134–147, doi:10.1016/0012-821X(91)90003-Z.

Shih, C.-Y., Nyquist, L.E., Dasch, E.J., Bogard, D.D., Bansal, B.M., and Wiesmann, H., 1993, Ages of pristine noritic clasts from lunar breccias 15445 and 15455: Geochimica et Cosmochimica Acta, v. 57, p. 915–931, doi:10.1016/0016-7037(93)90178-Y.

Siegler, M.A., and Smrekar, S.E., 2014, Lunar heat flow: Regional prospective of the Apollo landing sites: Journal of Geophysical Research: Planets, v. 119, p. 47–63, doi:10.1002/2013JE004453.

Siegler, M., Warren, P., Franco, K.L., Paige, D., Feng, J., and White, M., 2022, Lunar Heat Flow: Global Predictions and Reduced Heat Flux: Journal of Geophysical Research: Planets, v. 127, p. e2022JE007182, doi:10.1029/2022JE007182.

Sio, C.K., Borg, L.E., and Cassata, W.S., 2020, The timing of lunar solidification and mantle overturn recorded in ferroan anorthosite 62237: Earth and Planetary Science Letters, v. 538, p. 116219, doi:10.1016/j.epsl.2020.116219.

Smoluchowski, R., 1981, Amorphous ice and the behavior of cometary nuclei: \apjl, v. 244, p. L31–L34, doi:10.1086/183473.

Snape, J.F., Nemchin, A.A., Johnson, T., Luginbühl, S., Berndt, J., Klemme, S., Morrissey, L.J., and van Westrenen, W., 2022, Experimental constraints on the long-lived radiogenic isotope evolution of the Moon: Geochimica et Cosmochimica Acta, v. 326, p. 119–148, doi:10.1016/j.gca.2022.04.008.

Snyder, G.A., Taylor, L.A., and Neal, C.R., 1992, Combined equilibrium and fractional crystallization of a magma ocean and formation of the upper mantle of the Moon, *in* Lunar and Planetary Science Conference, v. 23.

Sprung, P., Kleine, T., and Scherer, E.E., 2013, Isotopic evidence for chondritic Lu/Hf and Sm/Nd of the Moon: Earth and Planetary Science Letters, v. 380, p. 77–87, doi:10.1016/j.epsl.2013.08.018.

Steenstra, E.S., Agmon, N., Berndt, J., Klemme, S., Matveev, S., and van Westrenen, W., 2018, Depletion of potassium and sodium in mantles of Mars, Moon and Vesta by core formation: Scientific Reports, v. 8, p. 7053, doi:10.1038/s41598-018-25505-6.

Sun, C., Graff, M., and Liang, Y., 2017, Trace element partitioning between plagioclase and silicate melt: The importance of temperature and plagioclase composition, with implications for terrestrial and lunar magmatism: Geochimica et Cosmochimica Acta, v. 206, p. 273–295, doi:10.1016/j.gca.2017.03.003.

Taylor, S.R., Kaye, M., Muir, P., Nance, W., Rudowski, R., and Ware, N., 1972, Composition of the lunar uplands: Chemistry of Apollo 14 samples from Fra Mauro: Lunar and Planetary Science Conference Proceedings, v. 3, p. 1231.

Taylor, S.R., Taylor, G.J., and Taylor, L.A., 2006, The Moon: A Taylor perspective: A Special Issue Dedicated to Larry A. Haskin, v. 70, p. 5904–5918, doi:10.1016/j.gca.2006.06.262.

Taylor, G.J., and Wieczorek, M.A., 2014, Lunar bulk chemical composition: a post-Gravity Recovery and Interior Laboratory reassessment: Philosophical Transactions of the Royal Society A: Mathematical, Physical and Engineering Sciences, v. 372, p. 20130242, doi:10.1098/rsta.2013.0242.

Tera, F., Papanastassiou, D.A., and Wasserburg, G.J., 1974, Isotopic evidence for a terminal lunar cataclysm: Earth and Planetary Science Letters, v. 22, p. 1–21, doi:10.1016/0012-821X(74)90059-4.

Toksöz, M.N., Hsui, A.T., and Johnston, D.J., 1978, Thermal evolutions of the terrestrial planets: The moon and the planets, v. 18, p. 281–320, doi:10.1007/BF00896484.

Turcotte, D.L., and Schubert, G., 2002, Geodynamics: Cambridge university press.

Turner, G., and Cadogan, P.H., 1975, The history of lunar bombardment inferred from ^{40}Ar-^{39}Ar dating of highland rocks.: Lunar and Planetary Science Conference Proceedings, v. 2, p. 1509–1538.

Unruh, D.M., Stille, P., Patchett, P.J., and Tatsumoto, M., 1984, Lu-Hf and Sm-Nd evolution in lunar mare basalts: Journal of Geophysical Research: Solid Earth, v. 89, p. B459–B477, doi:10.1029/JB089iS02p0B459.

Wagner, T.P., and Grove, T.L., 1997, Experimental constraints on the origin of lunar high-Ti ultramafic glasses: Geochimica et Cosmochimica Acta, v. 61, p. 1315–1327, doi:10.1016/S0016-7037(96)00387-0.

Wang, K., and Jacobsen, S.B., 2016a, An estimate of the Bulk Silicate Earth potassium isotopic composition based on MC-ICPMS measurements of basalts: Geochimica et Cosmochimica Acta, v. 178, p. 223–232, doi:10.1016/j.gca.2015.12.039.

Wang, K., and Jacobsen, S.B., 2016b, Potassium isotopic evidence for a high-energy giant impact origin of the Moon: Nature, v. 538, p. 487–490, doi:10.1038/nature19341.

Waples, D.W., and Waples, J.S., 2004, A review and evaluation of specific heat capacities of rocks, minerals, and subsurface fluids. Part 1: Minerals and nonporous rocks: Natural resources research, v. 13, p. 97–122.

Weber, R.C., Lin, P.-Y., Garnero, E.J., Williams, Q., and Lognonné, P., 2011, Seismic Detection of the Lunar Core: Science, v. 331, p. 309–312, doi:10.1126/science.1199375.

Wieczorek, M.A. et al., 2006, The Constitution and Structure of the Lunar Interior: Reviews in Mineralogy and Geochemistry, v. 60, p. 221–364, doi:10.2138/rmg.2006.60.3.

Wieczorek, M.A. et al., 2013, The Crust of the Moon as Seen by GRAIL: Science, v. 339, p. 671–675, doi:10.1126/science.1231530.

Zeigler, R.A., Korotev, R.L., Jolliff, B.L., and Haskin, L.A., 2005, Petrography and geochemistry of the LaPaz Icefield basaltic lunar meteorite and source crater pairing with Northwest Africa 032: Meteoritics & Planetary Science, v. 40, p. 1073–1101, doi:10.1111/j.1945-5100.2005.tb00174.x.

Zhang, Q.W.L. et al., 2024, Lunar farside volcanism 2.8 billion years ago from Chang'e-6 basalts: Nature, doi:10.1038/s41586-024-08382-0.

Zhang, N., Ding, M., Zhu, M.-H., Li, H., Li, H., and Yue, Z., 2022a, Lunar compositional asymmetry explained by mantle overturn following the South Pole–Aitken impact: Nature Geoscience, v. 15, p. 37–41, doi:10.1038/s41561-021-00872-4.

Zhang, N., Dygert, N., Liang, Y., and Parmentier, E.M., 2017, The effect of ilmenite viscosity on the dynamics and evolution of an overturned lunar cumulate mantle: Geophysical Research Letters, v. 44, p. 6543–6552, doi:10.1002/2017GL073702.

Zhang, N., Parmentier, E.M., and Liang, Y., 2013, A 3-D numerical study of the thermal evolution of the Moon after cumulate mantle overturn: The importance of rheology and core solidification: Journal of Geophysical Research: Planets, v. 118, p. 1789–1804, doi:10.1002/jgre.20121.

Zhang, W., Zhang, N., and Li, H., 2022b, Abundances of lunar heat-producing elements constrained by a 3-D numerical model of titanium-rich basaltic eruption: Chin. J. Geophys, v. 65, p. 119–136.

Zhao, Y., de Vries, J., van den Berg, A.P., Jacobs, M.H.G., and van Westrenen, W., 2019, The participation of ilmenite-bearing cumulates in lunar mantle overturn: Earth and Planetary Science Letters, v. 511, p. 1–11, doi:10.1016/j.epsl.2019.01.022.

Zhong, S., Parmentier, E.M., and Zuber, M.T., 2000, A dynamic origin for the global asymmetry of lunar mare basalts: Earth and Planetary Science Letters, v. 177, p. 131–140, doi:10.1016/S0012-821X(00)00041-8.

Appendix C

Geochemical Models for Magma Ocean Solidification and Cumulate Partial Melting

Trace element fractionation during LMO crystallization was modeled assuming Rayleigh fractionation using Eq.'s C1 and C2:

$$C_L^i = C_{L_0}^i F^{(D_{Bulk}^i - 1)}\,, \tag{C1}$$

$$C_S^i = C_L^i \times D_{Bulk}^i\,, \tag{C2}$$

where C_L^i represents the concentration of element i, $C_{L_0}^i$ is the composition of the initial liquid, C_S^i represents the concentration in the solid, F is the fraction of melt remaining, and D_{Bulk}^i is the bulk partition coefficient between crystals and liquid. For an assemblage of phases, D_{Bulk}^i can be calculated with Eq. C3:

$$D_{Bulk}^i = D_\alpha^i(X_\alpha) + D_\beta^i\left(X_\beta\right) + D_\gamma^i\left(X_\gamma\right) + \ldots, \tag{C3}$$

where D_α^i is the partition coefficient for element i in phase α, X_α is the modal proportion of phase a in the group of crystallizing phases. Fractional crystallization assumes that crystals form within the LMO and settle out to form cumulates at the base of the magma ocean. By definition, in a fractional crystallization scenario, crystals in the cumulate pile are not in equilibrium with the magma ocean residual liquid except at the moment they form. To conserve mass, D_{Bulk}^i in this model must account for previously removed crystallizing phases as the magma ocean evolves. Recalculating the D_{Bulk}^i at intervals j after a first interval a:

$$D_{Comb}^{i,ab} = \frac{D_{Bulk}^{i,a}(1-F_a) + D_{Bulk}^{i,b}(F_a - F)}{(1-F)}, \tag{C4}$$

$$D_{Comb}^{i,abc} = \frac{D_{Bulk}^{i,a}(1-F_a) + D_{Bulk}^{i,b}(F_a - F_b) + D_{Bulk}^{i,c}(F_b - F)}{(1-F)}, \tag{C5}$$

and so forth, where $D_{Bulk}^{i,j}$ is the bulk partition coefficient for a given element during a part of the crystallization sequence at an extent of melt F. For the first interval a, the melt fraction at which crystallization interval a ends is F_a. $D_{Comb}^{i,ab}$ represents the combined bulk partition coefficient for a second crystallization interval b, crystallization sequence b occurs for melt fractions between F_a and F_b. $D_{Comb}^{i,abc}$ represents the combined bulk partition coefficient for a third crystallization interval c, crystallization interval c occurs for melt fractions between F_b and F_c.

To model the effect of partial melting on LMO cumulates and hybridized mantle sources, we use an aggregated fractional melting model Eq. C6:

$$C_l^i = C_{S_0}^i \left(\frac{1-(1-F)^{\left(\frac{1}{D_{Bulk}^i}\right)}}{F}\right), \quad \text{(C6)}$$

where $C_{S_0}^i$ represents concentration of a given element i in the initial cumulate, C_l^i is the concentration in the melt that forms, and F is the melt fraction. Given the current lack of information on source mineralogy and non-modal melting behavior, we assume modal melting for all partial melting calculations in this study.

Mineral-Melt Partitioning

K partitioning between olivine and melt was estimated using a lattice strain-based partitioning model to fit Li and Na partitioning data. This was done because the abundance of K is often at or below the detection limit (i.e., the measured concentrations of K are within error of zero) in olivine grains from previous mineral-melt partitioning studies. In addition, the partitioning behavior of Li and Na (i.e., other 1+ elements) exhibit systematic partitioning trends with respect to pressure and temperature across

multiple studies, and the abundance of these elements is often above their respective detection limits. The partitioning behavior of K in olivine was approximated using the lattice strain model (Brice, 1975; Blundy and Wood, 1994; Wood and Blundy, 1997):

$$D_j = D_0 \exp\left(\frac{-4\pi E N_A}{RT}\left(\frac{r_0}{2}\left(r_0 - r_j\right)^2 - \frac{1}{3}\left(r_0 - r_j\right)^3\right)\right) \quad \text{(C7)}$$

where D_j is the mineral-melt partition coefficient of element j; D_0 is the partition coefficient for a strain-free substitution; r_0 is the ideal ionic radius for the lattice site; r_j is the ionic radius of the given element (e.g., Li, Na, K, Rb, Cs); E is the effective Young's modulus of the lattice site; N_A is Avogadro's number; R is the gas constant; and T is the temperature (Kelvin). We use the sixfold ionic radius for monovalent ions (Shannon, 1976). To develop the monovalent element partitioning model for olivine, we used methods similar to those of Sun and Liang (2013) and compiled a large dataset of experimentally determined partitioning data (**Figure C1**). Eq. C7 was fit simultaneously through a global inversion of 87 experimentally determined observations for olivine to obtain expressions for D_0, r_0, and E. A nonlinear least squares method was utilized minimizing the Pearson's Chi-square (χ^2) defined below.

$$\chi_P^2 = \sum_{j=1}^{N} \frac{(D_j - D_j^m)^2}{D_j}, \quad \text{(C8)}$$

where D_j is the predicted partition coefficient for element j; D_j^m is the measured mineral-melt partition coefficient; N is the total number of measured partitioning data used in the fit to the predictive model. Iteratively testing models to calculate how potential experimental and chemical parameters affect partitioning behavior, we found the lattice

strain parameters D_0, r_0, and E for monovalent element partitioning into olivine are best described using the following expressions:

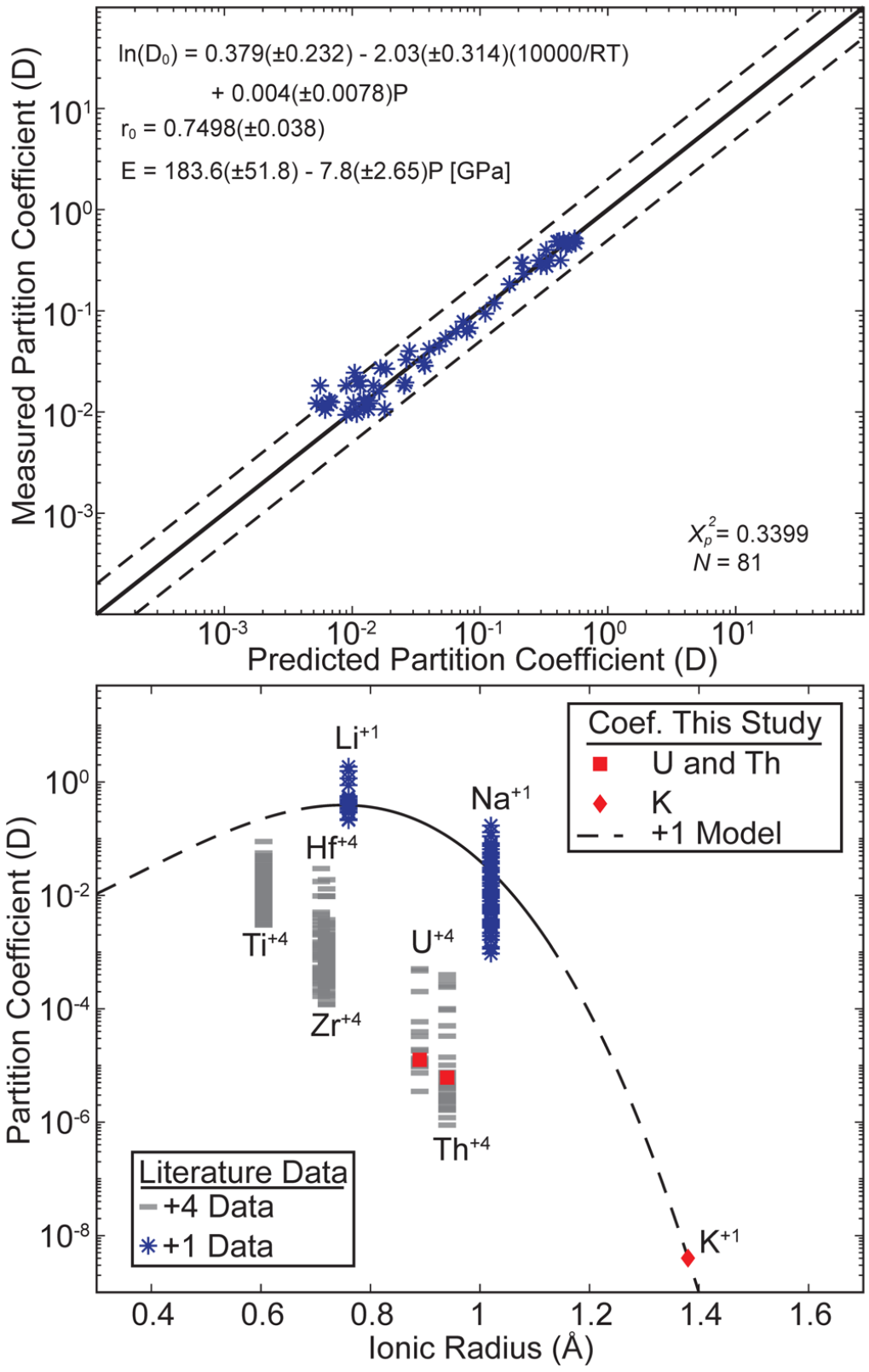
$$\ln D_0^{ol} = a_0^{ol} + a_1^{ol}\left(\frac{10000}{RT}\right) + a_2^{ol}P, \quad \text{(C9)}$$

$$r_0^{ol} = a_3^{ol}, \quad \text{(C10)}$$

$$E^{ol} = a_4^{ol} + a_5^{ol}P, \quad \text{(C11)}$$

where P is the pressure (GPa) of crystallization and coefficients ($a_0^{ol}, a_1^{ol}, \ldots, a_5^{ol}$) are constants for the respective minerals. Coefficients ($a_0^{ol}, a_1^{ol}, \ldots, a_5^{ol}$) were determined using nonlinear least squared regression analysis for olivine by substituting Eqs. C9-C11 into Eq. C7, respectively (coefficients reported in **Figure C1**).

Figure C1. Comparison between the literature data and the olivine mineral-melt coefficients used in this study. The partitioning behavior of K used in the numerical simulations is approximated using the model presented in panel (a) at the average experimental conditions from the literature data. Literature data was compiled from: Shimizu et al., 1982; Kennedy et al., 1993; Dun and Sen 1994; Suzuki and Akago, 1995; Brenan et al., 1998; Taura et al., 1998; Salters et al., 2002; Zanetti et al., 2003; McDade et al., 2003; Wasylenki et al., 2003; Filiberto et al. 2009; Ottolini et al., 2009; Elardo et al., 2011; Dalou et al., 2012; Imai et al., 2012; Davis et al., 2013; Mallmann and O'Neill, 2013; Fonseca et al., 2014; Wijbrans et al., 2015; Leitzke et al., 2016; Dygert et al., 2020; Chen et al., 2022; Snape et al., 2022; Haupt et al., 2024; Jing et al., 2024.


ln(D0) = 0.379(±0.232) - 2.03(±0.314)(10000/RT)
+ 0.004(±0.0078)P
r0 = 0.7498(±0.038)
E = 183.6(±51.8) - 7.8(±2.65)P [GPa]
Measured Partition Coefficient (D)
Predicted Partition Coefficient (D)
Xp2 = 0.3399
N = 81
Partition Coefficient (D)
Ionic Radius (Å)
Coef. This Study
U and Th
K
+1 Model
Literature Data
+4 Data
+1 Data
Li+1
Na+1
K+1
Hf+4
Ti+4
Zr+4
U+4
Th+4

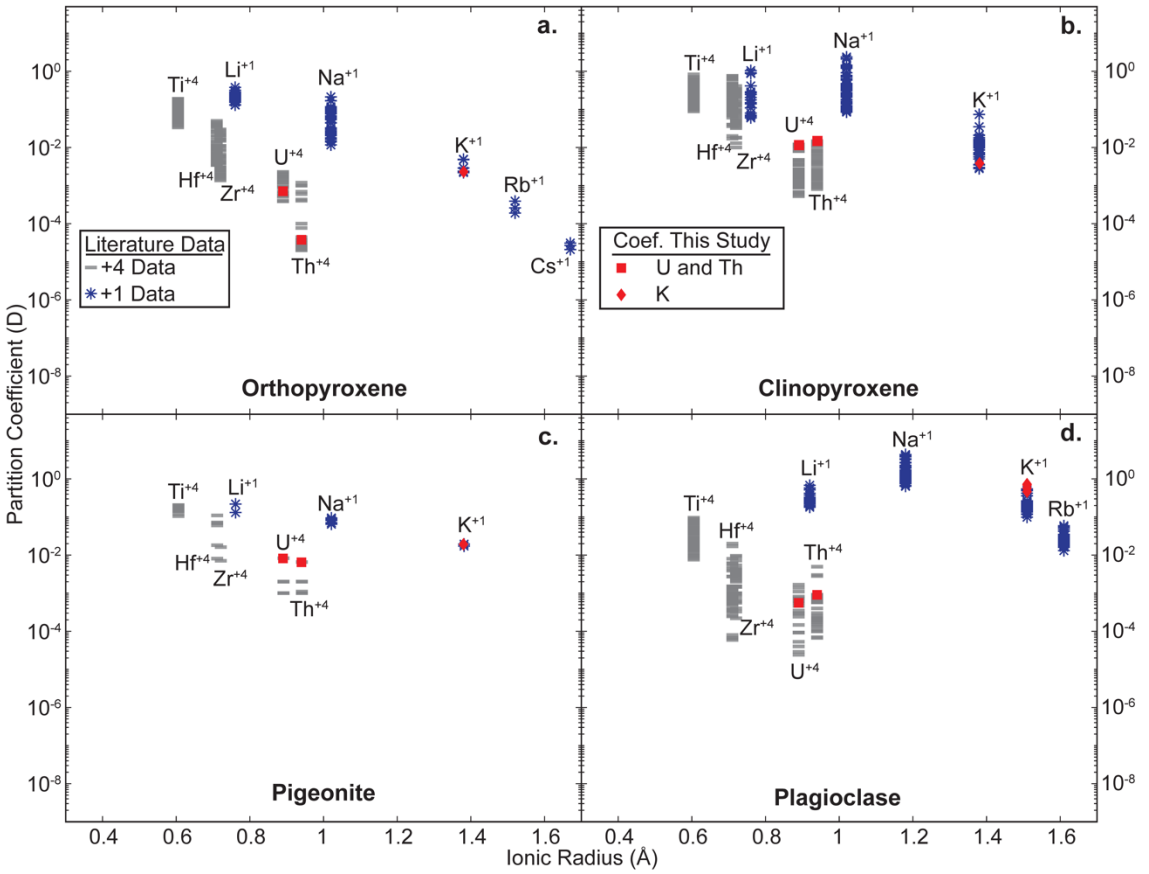


Figure C2. Comparison between the literature data and the silicate mineral-melt coefficients used in this study. Mineral is indicated in each panel. Literature data on orthopyroxene mineral-melt partitioning presented in this figure was compiled from: Van Kan Parker et al., 2010, 2011a, 2011b; Frei et al. 2009; Ottolini et al., 2009; Elardo et al., 2011; Dalou et al., 2012; Yao et al., 2012; Davis et al., 2013; Sun and Liang, 2013; Fonseca et al., 2014; Sharp et al. 2015; Leitzke et al., 2016; Mallik et al., 2019; Fibbrizio et al., 2021; Snape et al., 2022; Haupt et al., 2024. Literature data on clinopyroxene mineral-melt partitioning presented in this figure was compiled from: Chamorro et al., 2002; Klemme et al., 2002; Ottolini et al., 2009; Hill et al., 2011; Suzuki et al., 2012; Yao et al., 2012; Dalou et al., 2012; Davis et al., 2013; Dygert et al., 2014; Leitzke et al., 2016; Mallik et al., 2019; Fibbrizio et al., 2021; Snape et al., 2022; Shepherd et al., 2022; Haupt et al., 2024. Literature data on pigeonite mineral-melt partitioning presented in this figure was compiled from: Filiberto et al. 2009; Dygert et al., 2020; Snape et al., 2022; Haupt et al., 2024. Literature data on plagioclase mineral-melt partitioning presented in this figure was compiled from: Bindeman and Davis, 2000; Ainger-Torres et al., 2007; Tepley et al., 2010; Sharp et al., 2015; Wijbrans et al., 2015; Sun et al. 2017; Schoneveld, 2018; Schoneveld and O'Neill, 2019; Dygert et al., 2020; Snape et al., 2022; Haupt et al., 2024.

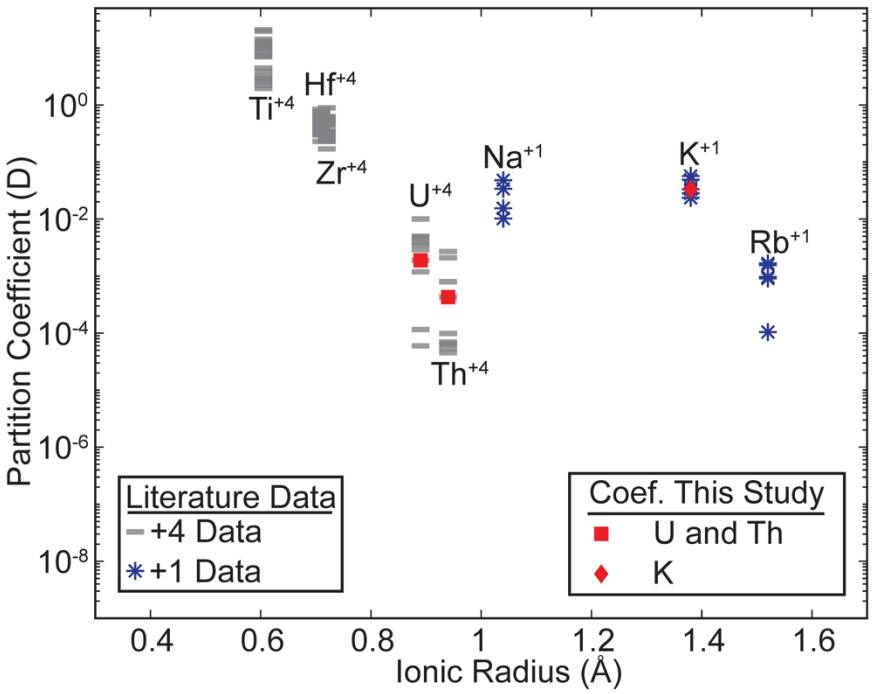


Figure C3. Comparison between the literature data and the ilmenite mineral melt coefficients used in this study. Literature data on ilmenite mineral-melt partitioning presented in this figure was compiled from: Mckay et al., 1986; Klemme et al., 2006; Van Kan Parker et al., 2011; Krawzyncski and Grove, 2012; Dygert et al., 2013; Leitzke et al., 2016; Charlier et al., 2018; Shepherd et al., 2022; Snape et al., 2022.

Table C1. Values used in calculating the temperatures shown in Figure (C4).

Term	Symbol	Units	Value
Diameter of body	d	km	40
Thermal Conductivity	K	W $m^{-1}K^{-1}$	2.1
Specific Heat Capacity	C_P	J $kg^{-1}K^{-1}$	837
Density	ρ	kg m^{-3}	3300
Thermal Diffusivity	κ	m^2 s^{-1}	7.60E-07
Decay Constant	λ	yr^{-1}	9.50E-07
Initial power per unit volume	A_0	W m^{-3}	6.40E-04
Initial power per unit mass	H_0	W kg^{-1}	1.90E-07
Ambient temperature	T_0	K	250

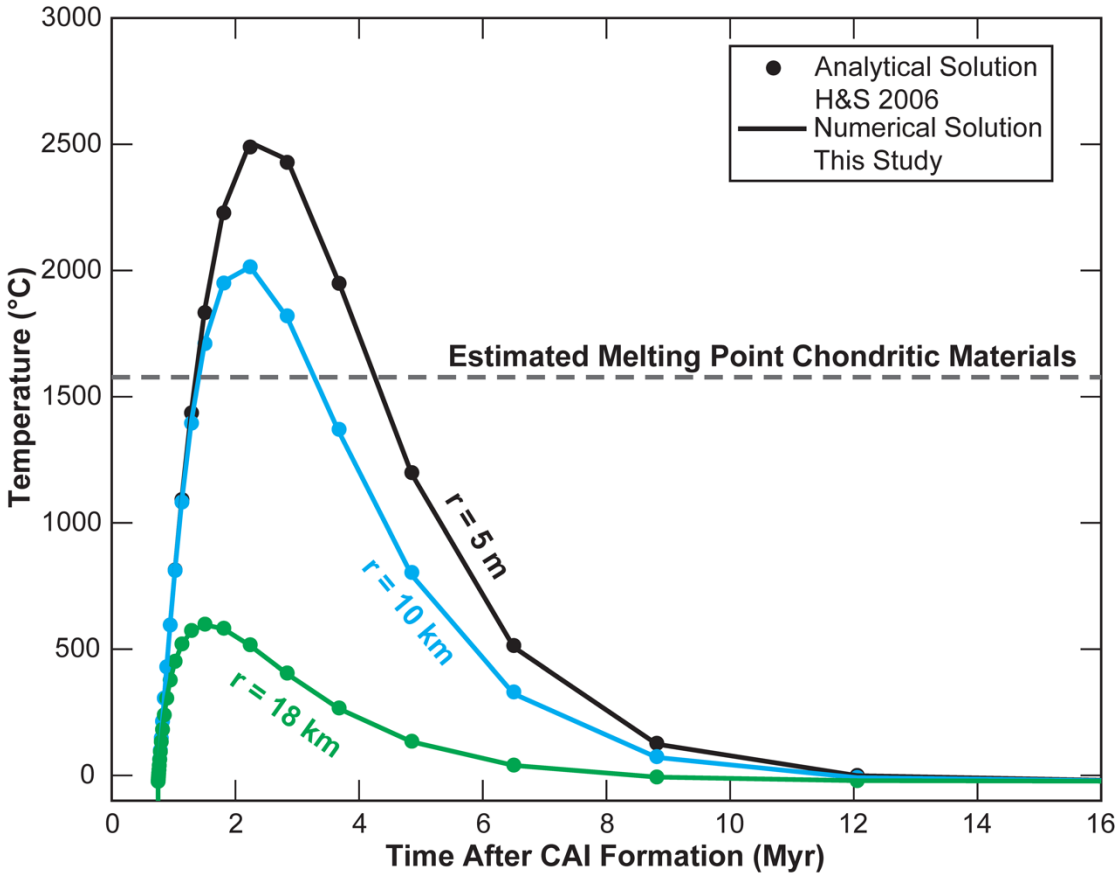


Figure C4. Comparison of the analytical heat conduction-heat production model used by Hevey and Sanders (2006) (H&S 2006) and the numerical model used in this study. Models in this figure calculate the thermal evolution of a 40 km wide spherical body that accreted 0.75 Myr after CAI formation. The models assume that ^{26}Al is the only heat producing element and the parameter used to calculate the thermal evolution of this body were taken from Hevey and Sanders (2006) (Table C1). The figure demonstrates that the previously published analytical models and the numerical model used in this study are in excellent agreement with one assuming the same starting conditions.

IBC Solidus Model

The estimated IBC solidus from Scholpp and Dygert (2024) was parameterized using a second order polynomial fit **Figure (C5)**:

$$T_r = 1034.6(\pm 3.83) + 143.2(\pm 4.80)P_r - 12.5(\pm 1.10)P_r^2 \qquad \text{(C12)}$$

where T_r is the solidus temperature (°C) at a given radius (r) within the moon, P_r is the pressure (GPa) at that radius.

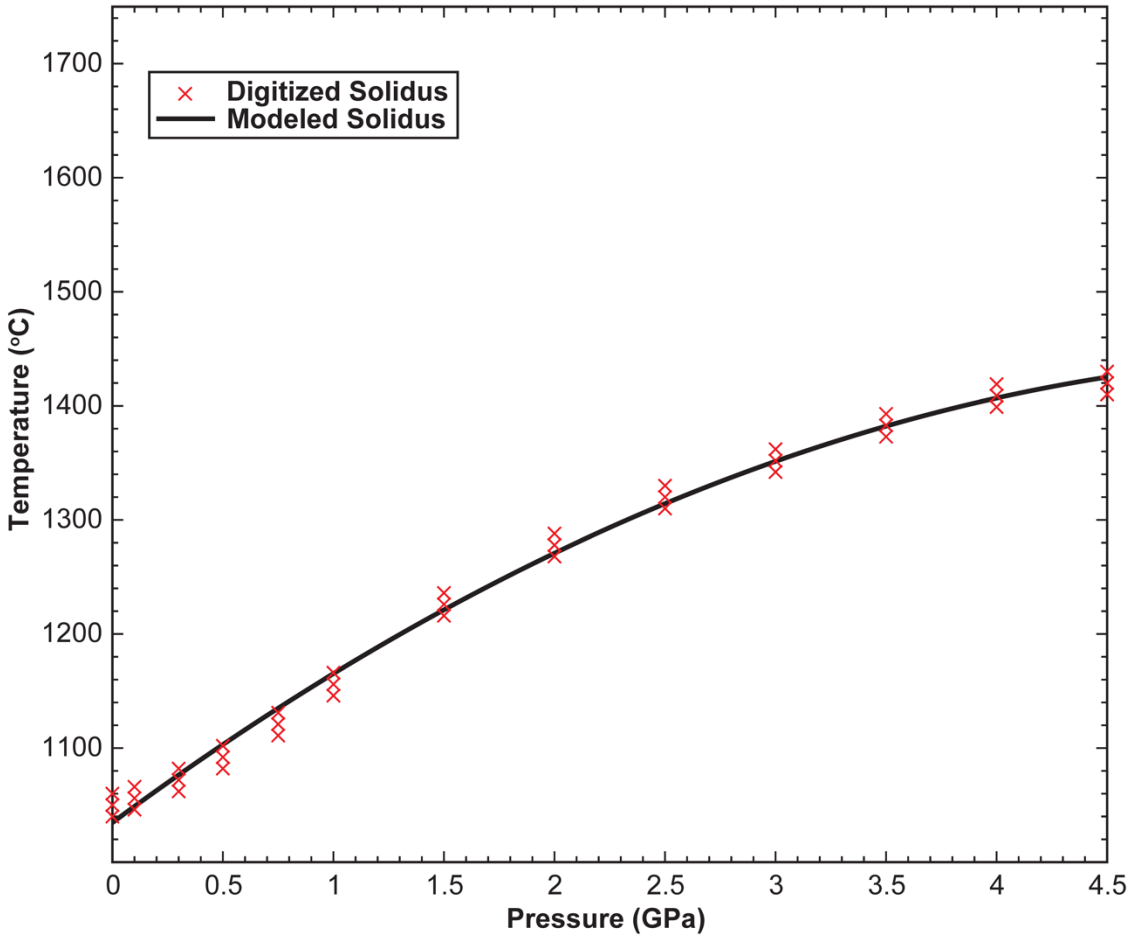


Figure C5. Modeled IBC solidus based on the experimentally determined IBC solidus from Scholpp and Dygert (2024). Digitized data set includes the experimentally determined solidus temperature and two error points for each given pressure. Modeled solidus line is defined by Eq. C12.

References Appendix C

Aigner-Torres, M., Blundy, J., Ulmer, P., and Pettke, T., 2007, Laser Ablation ICPMS study of trace element partitioning between plagioclase and basaltic melts: an experimental approach: Contributions to Mineralogy and Petrology, v. 153, p. 647–667, doi:10.1007/s00410-006-0168-2.

Bindeman, I.N., and Davis, A.M., 2000, Trace element partitioning between plagioclase and melt: investigation of dopant influence on partition behavior: Geochimica et Cosmochimica Acta, v. 64, p. 2863–2878, doi:10.1016/S0016-7037(00)00389-6.

Blundy, J., and Wood, B., 1994, Prediction of crystal–melt partition coefficients from elastic moduli: Nature, v. 372, p. 452–454, doi:10.1038/372452a0.

Brenan, J.M., Neroda, E., Lundstrom, C.C., Shaw, H.F., Ryerson, F.J., and Phinney, D.L., 1998, Behaviour of boron, beryllium, and lithium during melting and crystallization: constraints from mineral-melt partitioning experiments: Geochimica et Cosmochimica Acta, v. 62, p. 2129–2141, doi:10.1016/S0016-7037(98)00131-8.

Brice, J.C., 1975, Some thermodynamic aspects of the growth of strained crystals: Journal of Crystal Growth, v. 28, p. 249–253, doi:10.1016/0022-0248(75)90241-9.

Chamorro, E.M., Brooker, R.A., Wartho, J.-A., Wood, B.J., Kelley, S.P., and Blundy, J.D., 2002, Ar and K partitioning between clinopyroxene and silicate melt to 8 GPa: Geochimica et Cosmochimica Acta, v. 66, p. 507–519, doi:10.1016/S0016-7037(01)00784-0.

Charlier, B., Grove, T.L., Namur, O., and Holtz, F., 2018, Crystallization of the lunar magma ocean and the primordial mantle-crust differentiation of the Moon:

Geochimica et Cosmochimica Acta, v. 234, p. 50–69, doi:10.1016/j.gca.2018.05.006.

Chen, S., Ni, P., Zhang, Y., and Gagnon, J., 2022, Trace element partitioning between olivine and melt in lunar basalts: v. 107, p. 1519–1531, doi:10.2138/am-2022-7971.

Dalou, C., Koga, K.T., Shimizu, N., Boulon, J., and Devidal, J.-L., 2012, Experimental determination of F and Cl partitioning between lherzolite and basaltic melt: Contributions to Mineralogy and Petrology, v. 163, p. 591–609, doi:10.1007/s00410-011-0688-2.

Davis, F.A., Humayun, M., Hirschmann, M.M., and Cooper, R.S., 2013, Experimentally determined mineral/melt partitioning of first-row transition elements (FRTE) during partial melting of peridotite at 3GPa: Geochimica et Cosmochimica Acta, v. 104, p. 232–260, doi:10.1016/j.gca.2012.11.009.

Dunn, T., and Sen, C., 1994, Mineral/matrix partition coefficients for orthopyroxene, plagioclase, and olivine in basaltic to andesitic systems: A combined analytical and experimental study: Geochimica et Cosmochimica Acta, v. 58, p. 717–733, doi:10.1016/0016-7037(94)90501-0.

Dygert, N., Draper, D.S., Rapp, J.F., Lapen, T.J., Fagan, A.L., and Neal, C.R., 2020, Experimental determinations of trace element partitioning between plagioclase, pigeonite, olivine, and lunar basaltic melts and an fO2 dependent model for plagioclase-melt Eu partitioning: Geochimica et Cosmochimica Acta, v. 279, p. 258–280, doi:10.1016/j.gca.2020.03.037.

Dygert, N., Liang, Y., and Hess, P., 2013, The importance of melt TiO2 in affecting major and trace element partitioning between Fe–Ti oxides and lunar picritic glass melts: Geochimica et Cosmochimica Acta, v. 106, p. 134–151, doi:10.1016/j.gca.2012.12.005.

Dygert, N., Liang, Y., Sun, C., and Hess, P., 2014, An experimental study of trace element partitioning between augite and Fe-rich basalts: Geochimica et Cosmochimica Acta, v. 132, p. 170–186, doi:10.1016/j.gca.2014.01.042.

Elardo, S.M., Draper, D.S., and Shearer, C.K., 2011, Lunar Magma Ocean crystallization revisited: Bulk composition, early cumulate mineralogy, and the source regions of the highlands Mg-suite: Geochimica et Cosmochimica Acta, v. 75, p. 3024–3045, doi:10.1016/j.gca.2011.02.033.

Filiberto, J., Jackson, C., Le, L., and Treiman, A.H., 2009, Partitioning of Ni between olivine and an iron-rich basalt: Experiments, partition models, and planetary implications: American Mineralogist, v. 94, p. 256–261, doi:10.2138/am.2009.3047.

Fonseca, R.O.C., Mallmann, G., Sprung, P., Sommer, J.E., Heuser, A., Speelmanns, I.M., and Blanchard, H., 2014, Redox controls on tungsten and uranium crystal/silicate melt partitioning and implications for the U/W and Th/W ratio of the lunar mantle: Earth and Planetary Science Letters, v. 404, p. 1–13, doi:10.1016/j.epsl.2014.07.015.

Frei, D., Liebscher, A., Franz, G., Wunder, B., Klemme, S., and Blundy, J., 2009, Trace element partitioning between orthopyroxene and anhydrous silicate melt on the

lherzolite solidus from 1.1 to 3.2 GPa and 1,230 to 1,535°C in the model system Na2O–CaO–MgO–Al2O3–SiO2: Contributions to Mineralogy and Petrology, v. 157, p. 473–490, doi:10.1007/s00410-008-0346-5.

Haupt, C.P., Renggli, C.J., Rohrbach, A., Berndt, J., and Klemme, S., 2024, Experimental Constraints on the Origin of the Lunar High-Ti Basalts: Journal of Geophysical Research: Planets, v. 129, p. e2023JE008239, doi:10.1029/2023JE008239.

Hevey, P.J., and Sanders, I.S., 2006, A model for planetesimal meltdown by 26Al and its implications for meteorite parent bodies: Meteoritics & Planetary Science, v. 41, p. 95–106, doi:10.1111/j.1945-5100.2006.tb00195.x.

Hill, E., Blundy, J.D., and Wood, B.J., 2011, Clinopyroxene–melt trace element partitioning and the development of a predictive model for HFSE and Sc: Contributions to Mineralogy and Petrology, v. 161, p. 423–438, doi:10.1007/s00410-010-0540-0.

Imai, T., Takahashi, E., Suzuki, T., and Hirata, T., 2012, Element partitioning between olivine and melt up to 10GPa: Implications for the effect of pressure: Physics of the Earth and Planetary Interiors, v. 212–213, p. 64–75, doi:10.1016/j.pepi.2012.09.001.

Jing, J.-J., Su, B.-X., Berndt, J., Kuwahara, H., and van Westrenen, W., 2024, Experimental investigation of first-row transition elements partitioning between olivine and silicate melt: Implications for lunar basalt formation: Geochimica et Cosmochimica Acta, v. 373, p. 211–231, doi:10.1016/j.gca.2024.03.028.

van Kan Parker, M., Liebscher, A., Frei, D., van Sijl, J., van Westrenen, W., Blundy, J., and Franz, G., 2010, Experimental and computational study of trace element distribution between orthopyroxene and anhydrous silicate melt: substitution mechanisms and the effect of iron: Contributions to Mineralogy and Petrology, v. 159, p. 459–473, doi:10.1007/s00410-009-0435-0.

van Kan Parker, M., Mason, P.R.D., and van Westrenen, W., 2011a, Experimental study of trace element partitioning between lunar orthopyroxene and anhydrous silicate melt: Effects of lithium and iron: Chemical Geology, v. 285, p. 1–14, doi:10.1016/j.chemgeo.2011.02.007.

van Kan Parker, M., Mason, P.R.D., and van Westrenen, W., 2011b, Trace element partitioning between ilmenite, armalcolite and anhydrous silicate melt: Implications for the formation of lunar high-Ti mare basalts: Geochimica et Cosmochimica Acta, v. 75, p. 4179–4193, doi:10.1016/j.gca.2011.04.031.

Kennedy, A.K., Lofgren, G.E., and Wasserburg, G.J., 1993, An experimental study of trace element partitioning between olivine, orthopyroxene and melt in chondrules: equilibrium values and kinetic effects: Earth and Planetary Science Letters, v. 115, p. 177–195, doi:10.1016/0012-821X(93)90221-T.

Klemme, S., Blundy, J.D., and Wood, B.J., 2002, Experimental constraints on major and trace element partitioning during partial melting of eclogite: Geochimica et Cosmochimica Acta, v. 66, p. 3109–3123, doi:10.1016/S0016-7037(02)00859-1.

Klemme, S., Günther, D., Hametner, K., Prowatke, S., and Zack, T., 2006, The partitioning of trace elements between ilmenite, ulvospinel, armalcolite and silicate

melts with implications for the early differentiation of the moon: Chemical Geology, v. 234, p. 251–263, doi:10.1016/j.chemgeo.2006.05.005.

Krawczynski, M.J., and Grove, T.L., 2012, Experimental investigation of the influence of oxygen fugacity on the source depths for high titanium lunar ultramafic magmas: Geochimica et Cosmochimica Acta, v. 79, p. 1–19, doi:10.1016/j.gca.2011.10.043.

Leitzke, F.P., Fonseca, R.O.C., Michely, L.T., Sprung, P., Münker, C., Heuser, A., and Blanchard, H., 2016, The effect of titanium on the partitioning behavior of high-field strength elements between silicates, oxides and lunar basaltic melts with applications to the origin of mare basalts: Chemical Geology, v. 440, p. 219–238, doi:10.1016/j.chemgeo.2016.07.011.

Mallik, A., Ejaz, T., Shcheka, S., and Garapic, G., 2019, A petrologic study on the effect of mantle overturn: Implications for evolution of the lunar interior: Geochimica et Cosmochimica Acta, v. 250, p. 238–250, doi:10.1016/j.gca.2019.02.014.

Mallmann, G., and O'Neill, H.St.C., 2013, Calibration of an Empirical Thermometer and Oxybarometer based on the Partitioning of Sc, Y and V between Olivine and Silicate Melt: Journal of Petrology, v. 54, p. 933–949, doi:10.1093/petrology/egt001.

McDade, P., Blundy, J.D., and Wood, B.J., 2003, Trace element partitioning on the Tinaquillo Lherzolite solidus at 1.5GPa: Diffusion and Partitioning in Planetary Interiors, v. 139, p. 129–147, doi:10.1016/S0031-9201(03)00149-3.

McDonough, W.F., and Sun, S. -s., 1995, The composition of the Earth: Chemical Evolution of the Mantle, v. 120, p. 223–253, doi:10.1016/0009-2541(94)00140-4.

McKay, G., Wagstaff, J., and Yang, S.-R., 1986, Zirconium, hafnium, and rare earth element partition coefficients for ilmenite and other minerals in high-Ti lunar mare basalts: An experimental study: Journal of Geophysical Research: Solid Earth, v. 91, p. 229–237, doi:10.1029/JB091iB04p0D229.

Ottolini, L., Laporte, D., Raffone, N., Devidal, J.-L., and Le Fèvre, B., 2009, New experimental determination of Li and B partition coefficients during upper mantle partial melting: Contributions to Mineralogy and Petrology, v. 157, p. 313–325, doi:10.1007/s00410-008-0336-7.

Salters, V.J.M., Longhi, J.E., and Bizimis, M., 2002, Near mantle solidus trace element partitioning at pressures up to 3.4 GPa: Geochemistry, Geophysics, Geosystems, v. 3, p. 1–23, doi:10.1029/2001GC000148.

Scholpp, J.L., and Dygert, N., 2024, Experimental insights into the mineralogy and melt-rock reactions produced by lunar cumulate mantle overturn: Contributions to Mineralogy and Petrology, v. 179, p. 58, doi:10.1007/s00410-024-02134-z.

Schoneveld, L.E., 2018, Partitioning of Trace Elements Between Plagioclase, Clinopyroxene and Melt [Ph.D.]: The Australian National University (Australia), 299 p., https://utk.idm.oclc.org/login?url=https://www.proquest.com/dissertations-theses/partitioning-trace-elements-between-plagioclase/docview/2083996420/se-2?accountid=14766.

Schoneveld, L., and O'Neill, H.St.C., 2019, The influence of melt composition on the partitioning of trace elements between anorthite and silicate melt: Contributions to Mineralogy and Petrology, v. 174, p. 13, doi:10.1007/s00410-019-1548-8.

Shannon, R.D., 1976, Revised effective ionic radii and systematic studies of interatomic distances in halides and chalcogenides: Acta Crystallographica Section A, v. 32, p. 751–767, doi:10.1107/S0567739476001551.

Sharp, M., Righter, K., and Walker, R.J., 2015, Estimation of trace element concentrations in the lunar magma ocean using mineral- and metal-silicate melt partition coefficients: Meteoritics & Planetary Science, v. 50, p. 733–758, doi:10.1111/maps.12396.

Shepherd, K., Namur, O., Toplis, M.J., Devidal, J.-L., and Charlier, B., 2022, Trace element partitioning between clinopyroxene, magnetite, ilmenite and ferrobasaltic to dacitic magmas: an experimental study on the role of oxygen fugacity and melt composition: Contributions to Mineralogy and Petrology, v. 177, p. 90, doi:10.1007/s00410-022-01957-y.

Shimizu, H., Sangen, K., and Masuda, A., 1982, Experimental study on rare-earth element partitioning in olivine and clinopyroxene formed at 10 and 20kb for basaltic systems: GEOCHEMICAL JOURNAL, v. 16, p. 107–117, doi:10.2343/geochemj.16.107.

Siegler, M., Warren, P., Franco, K.L., Paige, D., Feng, J., and White, M., 2022, Lunar Heat Flow: Global Predictions and Reduced Heat Flux: Journal of Geophysical Research: Planets, v. 127, p. e2022JE007182, doi:10.1029/2022JE007182.

Snape, J.F., Nemchin, A.A., Johnson, T., Luginbühl, S., Berndt, J., Klemme, S., Morrissey, L.J., and van Westrenen, W., 2022, Experimental constraints on the

long-lived radiogenic isotope evolution of the Moon: Geochimica et Cosmochimica Acta, v. 326, p. 119–148, doi:10.1016/j.gca.2022.04.008.

Sun, C., Graff, M., and Liang, Y., 2017, Trace element partitioning between plagioclase and silicate melt: The importance of temperature and plagioclase composition, with implications for terrestrial and lunar magmatism: Geochimica et Cosmochimica Acta, v. 206, p. 273–295, doi:10.1016/j.gca.2017.03.003.

Sun, C., and Liang, Y., 2013a, Distribution of REE and HFSE between low-Ca pyroxene and lunar picritic melts around multiple saturation points: Geochimica et Cosmochimica Acta, v. 119, p. 340–358, doi:10.1016/j.gca.2013.05.036.

Sun, C., and Liang, Y., 2013b, The importance of crystal chemistry on REE partitioning between mantle minerals (garnet, clinopyroxene, orthopyroxene, and olivine) and basaltic melts: Chemical Geology, v. 358, p. 23–36, doi:10.1016/j.chemgeo.2013.08.045.

Suzuki, T., and Akaogi, M., 1995, Element partitioning between olivine and silicate melt under high pressure: Physics and Chemistry of Minerals, v. 22, p. 411–418, doi:10.1007/BF00200318.

Suzuki, T., Hirata, T., Yokoyama, T.D., Imai, T., and Takahashi, E., 2012, Pressure effect on element partitioning between minerals and silicate melt: Melting experiments on basalt up to 20GPa: Physics of the Earth and Planetary Interiors, v. 208–209, p. 59–73, doi:10.1016/j.pepi.2012.07.008.

Taura, H., Yurimoto, H., Kurita, K., and Sueno, S., 1998, Pressure dependence on partition coefficients for trace elements between olivine and the coexisting melts:

Physics and Chemistry of Minerals, v. 25, p. 469–484, doi:10.1007/s002690050138.

Taylor, S.R., Taylor, G.J., and Taylor, L.A., 2006, The Moon: A Taylor perspective: A Special Issue Dedicated to Larry A. Haskin, v. 70, p. 5904–5918, doi:10.1016/j.gca.2006.06.262.

Taylor, G.J., and Wieczorek, M.A., 2014, Lunar bulk chemical composition: a post-Gravity Recovery and Interior Laboratory reassessment: Philosophical Transactions of the Royal Society A: Mathematical, Physical and Engineering Sciences, v. 372, p. 20130242, doi:10.1098/rsta.2013.0242.

Tepley, F.J., Lundstrom, C.C., McDonough, W.F., and Thompson, A., 2010, Trace element partitioning between high-An plagioclase and basaltic to basaltic andesite melt at 1 atmosphere pressure: Lithos, v. 118, p. 82–94, doi:10.1016/j.lithos.2010.04.001.

Turcotte, D.L., and Schubert, G., 2002, Geodynamics: Cambridge university press.

Wasylenki, L.E., Baker, M.B., Kent, A.J.R., and Stolper, E.M., 2003, Near-solidus Melting of the Shallow Upper Mantle: Partial Melting Experiments on Depleted Peridotite: Journal of Petrology, v. 44, p. 1163–1191, doi:10.1093/petrology/44.7.1163.

Wijbrans, C.H., Klemme, S., Berndt, J., and Vollmer, C., 2015, Experimental determination of trace element partition coefficients between spinel and silicate melt: the influence of chemical composition and oxygen fugacity: Contributions to Mineralogy and Petrology, v. 169, p. 45, doi:10.1007/s00410-015-1128-5.

Wood, B.J., and Blundy, J.D., 1997, A predictive model for rare earth element partitioning between clinopyroxene and anhydrous silicate melt: Contributions to Mineralogy and Petrology, v. 129, p. 166–181, doi:10.1007/s004100050330.

Yao, L., Sun, C., and Liang, Y., 2012, A parameterized model for REE distribution between low-Ca pyroxene and basaltic melts with applications to REE partitioning in low-Ca pyroxene along a mantle adiabat and during pyroxenite-derived melt and peridotite interaction: Contributions to Mineralogy and Petrology, v. 164, p. 261–280, doi:10.1007/s00410-012-0737-5.

Zanetti, A., Tiepolo, M., Oberti, R., and Vannucci, R., 2004, Trace-element partitioning in olivine: modelling of a complete data set from a synthetic hydrous basanite melt: Trace element fingerprinting: laboratory studies and petrogenetic processes, v. 75, p. 39–54, doi:10.1016/j.lithos.2003.12.022.

CONCLUSIONS

Experimental petrology, geochemical modeling, and kinetic modeling are valuable tools for understanding the formation and evolution of planetary bodies. This work presented high-pressure and high-temperature petrologic experiments, in combination with kinetic and geochemical models, to study the physical and chemical evolution of the Moon.

Lunar Mantle Hybridization During Cumulate Overturn

High-pressure and high-temperature petrologic experiments were conducted to explore the chemical reactions that occur during lunar cumulate overturn, as downwelling IBC melts and mushes interact with early crystallizing mafic cumulates. Experiments conducted at near solidus conditions show that metamorphic changes in the downwelling IBC stabilize garnet in the IBC at pressures around 2 GPa during cumulate mantle overturn events. These near solidus experiments also reveal solid-state diffusive exchange between the IBC material and dunite. In supersolidus experiments, a dissolution-precipitation reaction is observed, where dunite dissolves and forms a hybrid melt ± clinopyroxene, depending on the experimental conditions. Similar chemical processes may govern the hybridization of the lunar mantle.

The supersolidus experiments also demonstrate that the rate of dunite dissolution depends on pressure, temperature, and the saturation state of olivine in the hybridizing melt. Kinetic exchange models suggest that the formation of substantial hybridized lunar mantle sources over geologically relevant timescales may require mechanical mixing, in addition to the chemical reactions identified in this study. This depends on the scale of

downwelling plumes that develop within the Moon's interior during cumulate mantle overturn.

Magma Ocean Solidification And The Formation Of Lunar Basalt Sources

Using experimentally derived LMO cumulate solidification sequences and up-to-date lunar trace element partition coefficients, we model the chemical fractionation of trace elements during magma ocean solidification, mantle hybridization, and mantle partial melting. Our geochemical models of LMO solidification show that the early-crystallizing cumulates are depleted in REE compared to the late-crystallizing Ti-rich LMO cumulates, high-Ti lunar basalts, and high-Ti picritic glasses.

Models of partial melting of late-crystallizing LMO cumulates and hybridized sources suggest that these melts would exhibit an incorrect Eu anomaly (i.e., positive instead of negative) if plagioclase flotation were <90% efficient. Further, partial melting simulations show that melting unhybridized LMO cumulates cannot explain the HREE-depleted compositions observed in intermediate- and high-Ti lunar picritic glasses. The elevated Ti and REE content, coupled with the relatively Mg-rich composition of certain lunar picritic glasses, points to interaction between late-crystallizing (shallow) and early-crystallizing (deep) LMO cumulates. Such interactions likely result from lunar cumulate mantle overturn events, which bring ilmenite-bearing cumulates that crystallized from the late LMO into the interior of the Moon.

Thermodynamic simulations were conducted to examine the effect of cumulate overturn on lunar mantle mineralogy. In agreement with petrologic experiments, these simulations show that garnet stabilizes in downwelling IBC material at pressures above

~2 GPa during lunar cumulate overturn events. Partial melting models suggest that the HREE-depleted composition of lunar orange glass samples is consistent with a garnet-bearing mantle source. These models imply that the exact location of garnet formation (whether in downwelling IBC that fertilizes mantle sources or within hybridized mantle sources) is less critical than the overall abundance of garnet in generating HREE-depleted melts. The models indicate that 0.25-5% garnet is required to account for the HREE depletion observed in high-Ti lunar orange glasses. This is consistent with thermodynamic models of a metamorphosed IBC, assuming 90-95% plagioclase flotation during crustal formation.

The model parameters and mixing ratios for the hybridization scenarios tested in this study help explain several key geochemical features of high-Ti lunar samples, such as their REE enrichment, HFSE enrichment, Eu depletion, HREE depletion, and elevated Mg# relative to high-Ti LMO cumulates, as well as their Nd and Hf isotopic signatures. We conclude that the garnet signature and high-Ti composition of the orange picritic glasses provide compelling evidence for cumulate overturn events during the early stages of lunar formation and differentiation.

Concentration And Distribution Of Lunar Heat Producing Elements

Using experimentally determined LMO cumulate solidification sequences and current lunar trace element partition coefficients, we aim to constrain the K/Th ratio of the initial lunar magma ocean. Geochemical models of LMO solidification suggest that the K/Th ratio of the initial LMO could range from 450-550, assuming plagioclase flotation efficiency is ≥95%. If plagioclase flotation is less efficient, the K/Th ratio of the

LMO would need to decrease so that the crystallizing cumulates have K/Th ratios comparable to those of mantle-derived lunar melts (e.g., mare basalts and picritic glasses), as secondary partial melts are expected to reflect the K/Th ratios of their respective mantle sources.

Thermal evolution models from this study show that the degree of K depletion on the Moon plays a much more significant role in lunar thermal evolution than the potential Th and U enrichment relative to Earth. Models assuming cumulate overturn suggest that two mechanisms could trigger mantle melting if overturn occurs relatively quickly: (1) decompression melting in the upper mantle as lower mantle cumulates are displaced, and (2) radiogenic heating-induced melting in the middle and lower lunar mantle due to the overturned, HPE-rich IBC material.

VITA

Jesse Scholpp was born in Tampa, Florida. He found his love of geology and volcanology during an introductory geology course as a freshman in college, which led him to leave Florida Gulf Coast University for the University of South Florida (USF), where he majored in geology. During his time at USF, he discovered his interest in geochemistry and igneous petrology after working with Dr. Jeffrey Ryan on a research project documenting the mineralogy and chemical compositions of boninite lavas to understand the petrogenetic history of magmas during subduction initiation. He presented his research at multiple geologic research conferences, and in 2018, he received the Excellence in Student Research Award from the Council on Undergraduate Research. He earned his Bachelor of Science in Geology at USF in the spring of 2018 and started graduate school at Utah State University (USU) in the fall of 2018, working with Dr. John Shervais. For his M.S., he continued his research on volcanism and mantle melting during subduction initiation. In 2019, he received the Lipman Research Award from the Geologic Society of America. Jesse earned his Master of Science from USU and submitted his research for publication in the summer of 2020. He started his Philosophical Doctorate at the University of Tennessee (UT) in the fall of 2020 as a Tennessee Fellow for Graduate Excellence, working with Dr. Nicholas Dygert, exploring his interest in experimental petrology, geochemical modeling, mantle geochemistry, and the evolution of planetary volcanism. In 2021, Jesse was selected to be a shipboard scientist on International Ocean Discovery Program (IODP) Expedition 391. Following IODP Expedition 391, he acquired over $200,000 of research funding from the National

Science Foundation (NSF), which funded his research and the research of multiple undergraduate research assistants. During his Ph.D., Jesse led five projects, three of which were presented in his dissertation. His research included trips to research facilities in South Africa, Canada, Spain, and Japan. He presented his work at the Lunar and Planetary Science Conference in 2022, 2023, and 2024, and the IODP Expedition 391 Post-Cruise Meeting in 2024. He gave an invited talk for the Research Activities Supporting Science and Lunar Exploration (RASSLE) team meeting. He authored and coauthored eight peer-reviewed publications, one Wikipedia page, and nine conference presentations during his time at the University of Tennessee. In 2024, Jesse received the Career Development Award from the Lunar and Planetary Science Institute and the Graduate Professional Promise Award from the University of Tennessee Department of Earth, Environmental, and Planetary Sciences.